Cranfield University

James K. Lander

Designing with z-pins: locally reinforced composite structures

School of Applied Science

PhD

Cranfield University

School of Applied Science
Department of Materials – Composites Centre

PhD Thesis

Academic Year 2008-2009

James K. Lander

Designing with z-pins: locally reinforced composite structures

Supervisor: Professor Ivana K. Partridge

November 2008

This thesis is submitted in partial fulfilment of the requirements for the Degree of Doctor of Philosophy

Abstract

This thesis describes specific new applications of Z-Fibre® pinning and focuses the attention onto the failure modes of locally reinforced (z-pinned) structures. Design implications of the use of localised reinforcement on structures, rather than laboratory coupons, are considered.

Z-pinning reinforcement is applied to cylindrical crash tubes and I-section patch joints manufactured from woven carbon / epoxy pre-pregs. Z-pinning is shown to improve the Specific Energy Absorption (SEA) of the crash tubes by up to 76 %, the exact amount depending on the tube geometry. For the I-section patch joints, an initial increase in ultimate load carrying capability due to z-pin use is observed and, as the quantity of z-pins increases, a change in failure mode is induced. Z-pinning is also shown to enhance the damage tolerance of these. The ability to predict major changes to the structural response due to use of z-pins, and design for them accordingly, is the next step in the understanding of the technology.

The design element of this study is contained in the development of a new Finite Element model using cohesive interface elements. The provision of mode II input data for this model comes from End Loaded Split (ELS) testing of the woven laminates and continued development of the Z-shear test. A new analysis for quantifying the crack sliding displacement, based on the ELS test, is developed. Z-shear testing has shown that the z-pin 'mode II' fracture energy is strongly affected by the amount of mode I opening of the shear surfaces. Here, new data are obtained for a fully constrained, pure mode II case. Using this modelling tool, changes in failure mode due to z-pin use can be predicted. Verification is provided by a new simulation of the I-section patch joint geometry.

To my parents, Jan and Keith
for their support and encouragement.

Acknowledgements

I would like to express my gratitude, first and foremost, to Professor Ivana Partridge for giving me the opportunity to work at Cranfield University for this PhD. Your advice, support and guidance throughout this work were immeasurable and I am both grateful and proud to have studied under your supervision.

I would like to say thankyou to Dr. Alex Skordos for the many long mornings, afternoons and evenings spent working on the FE models. You have been so generous with your time and encouragement, I cannot thank you enough.

To Dr. Denis Cartié for the standards you set in carrying out and presenting experimental work. Your company during the numerous company visits and presentations has been much appreciated. To Jim for all your assistance with the manufacturing work and the many last minute jobs which kept me going.

To my colleagues Dr. Andrea Marasco and Dr. Giuseppe Dell'Anno for showing me the way through the final stages of the PhD and to all the friends I have made at Cranfield: Jeremy, Iain, Christian, Harry, Andrea, Mehdi, Marco, Giuse, Pietro, Guido, Giovanni, Evandro, Giuliano, Giuseppe, Andy, David, Silvia, Johannes, Ben and all the footballers. A special thankyou is reserved for my two 'assistants' Fulvio and Laurent. It was a real pleasure to work with you guys.

To my family, Jono, Chris, Mark, Grandma and Grandad and lastly to Maria del Mar whose love, unending patience and understanding have made all of this possible.

Contents

List of figures

Nomenclature

a	Crack length
a_0	Initial crack length
a_c	Calculated crack length
b	Width
c_r	Empirical constant
C	Compliance
C_0	Load line compliance
D	Diameter
E	Energy
E_{bulk}	Bulk Young's modulus
E_{11}, E_{XX}	Major axis Young's modulus
E_{22}, E_{YY}	Transverse Young's modulus
E_{33}, E_{ZZ}	Normal Young's modulus
E_f	Flexural modulus
F	Force
F	Large deflection correction used in ELS analysis
G, G_{12}	Shear modulus
G_{IC}	Critical strain energy release rate (or delamination toughness) for Mode I
G_{IIC}	Critical strain energy release rate (or delamination toughness) for Mode II
h	Specimen half thickness for ELS and DCB tests
K_{IC}	Critical stress intensity factor for Mode I
L	Length
m	Slope of the C vs. a^3 plot from mode II ELS test
m_1	Initial mass

m_2	Final mass
N	Load block correction used in ELS analysis
P	Load
Strength_C	Compressive strength
Strength_S	Shear strength
Strength_T	Tensile strength
t	Specimen thickness
Tg	Glass transition temperature
α	Z-pinning area fraction (areal density)
δ	Deflection (or displacement)
δ_{CT}	Displacement at the crack tip
Δ_{II}	Mode II delamination length correction
Δ_{a0}	Sliding displacement relative to the initial crack position
Δ_{clamp}	Clamping correction for the ELS test
Δ_x	Sliding displacement at any point x along the cracked region
v	Poisson's ratio
ν_i	Stress component for the FEA element in the i local coordinate
θ_{CT}	Rotation of the ELS beam at the crack tip
θ_x	Rotation of the beam at any point x along the cracked region
σ_p	Z-pinned laminate tensile strength
σ_o	Unpinned laminate tensile strength

Abbreviations

AEC	Albany Engineered Composites
BMI	Bismaleimide
BSI	British Standard Institute
CAD	Computer aided design
CAI	Compression after impact
CBT	Corrected beam theory
CBTE	Corrected beam theory with effective crack length
CF	Carbon fibre
CoDA	Component Design Analysis (laminate analysis software)
DCB	Double cantilever beam
E-glass	Electrical grade glass
ECM	Experimental compliance method
ELS	End loaded split (mode II delamination test method)
ENF	End notched flexure (mode II delamination test method)
FE	Finite element
FEA	Finite element analysis
ISO	International Standards Organisation
LVDT	Linear variable differential transformer
MPC	Multi point constraint
NASA	National Aeronautics and Space Administration
OSS	One sided stitching
PEI	Polyetherimide
PES	Polyethersulfone
PMI	Polymethacrylimide
PTFE	Polytetrafluoroethylene

R-curve	Resistance curve
RCS	Rear crash structure
RTP	Room temperature and pressure
S-glass	Silica glass
SBT	Simple beam theory
SEA	Specific energy absorption
SEM	Scanning electron microscope
SENF	Stabilised end notched flexure
SiC	Silicone carbide
UAZ	Ultrasonically assisted Z-Fibre™ insertion
UD	Unidirectional
VCCT	Virtual crack closure technique
3PB	3 point bend (test)
4ENF	4 point end notched flexure (test)

Chapter 1

General introduction

This thesis describes specific new applications of Z-Fibre® pinning to thermosetting polymer matrix / continuous fibre composites and focuses the attention onto the failure modes of locally reinforced (z-pinned) structures. Whilst previous work on z-pinning in the author's group has concentrated largely on establishing the structure-property relationships in flat z-pinned laboratory coupons [1-12], the purpose of this study was to consider the design implications of the use of localised reinforcement on more complex structures.

The particular structures used here are cylindrical crash tubes made from 8, 12 or 16 plies of 977-6 / 6K8H / T800 pre-preg and an I-section patch joint made from 914 / 6K5H / T300 or 8552 / 3K8H / HTA pre-preg. All Z-pin preforms used in the study were either supplied by Albany Int. (USA) or made in-house from bismaleimide / CF rodstock, also supplied by Albany Int. The crash tubes, with and without circumferential bands of z-pins, were tested in end-on impact. The I-sections, with and without z-pin reinforced patches, were tested in longitudinal tension and post-impact tension. The differences in failure modes between reinforced and unreinforced specimens were

established and the ‘transitions’ between them were located in terms of the reinforcement parameters.

The design element of the study is contained in the development of a new Finite Elements model of the I-section structures, using the MSC.Marc software suite, with cohesive interface elements. The aim is to provide a user-friendly design tool for predicting the effects of z-pinning on the response of the structure to loading.

Transverse shear testing of single z-pins was required in order to establish the traction laws defining the response of the interface elements in the model and highlighted the need for close control of the manufacturing quality.

The background to z-pinning technology is given in Chapter 2, as an update on existing reviews of the through-the-thickness reinforcement technologies and within the wider context of toughness enhancement in aerospace grade composites.

The full range of materials used in this study is detailed in Chapter 3. The standard, commercially available ‘preform’, containing z-pins ready for insertion, is introduced here. The pre-preg material systems are given special attention; mechanical properties for the fibre and resin components for each material are compared along with the cure cycles used.

The full z-pinning manufacture process, from pultrusion of the raw rodstock material through to the insertion of z-pins and subsequent cure of the through-thickness reinforced laminate, is described in Chapter 4. This work is the first in which z-pin preforms manufactured outside the United States have been used. A z-pin insertion head mounted on a 6-axis robotic arm has provided this opportunity. Special attention is given to the commissioning of this unique system and its use in manufacturing both z-pin preforms and pin reinforced cores.

Chapter 5 details the methodologies for the full range of experimental tests carried out for this work. These include the structural tests described earlier and laboratory coupon

scale ELS, Z-shear and 3 point bend tests used to provide data from which the traction responses for FE interface element use could be developed.

The results obtained from the crash tube and I-section joint structure tests are presented in Chapter 6. These tests highlight the performance benefits that a structure specific, tailored z-pinning approach could offer in the future and some initial proposals for these two structures in particular.

The advantages of structurally tailored z-pinning arrangements can only be fully realised by the development of new design tools which allow the consideration of this technology during the structural design stage. Chapter 7 highlights a user-friendly finite element approach which facilitates the prediction the meso-scale mode II z-pinning response. An in depth description is given of the test data analysis and subsequent implementation for a virtual representation of the z-pinning mode II response.

The interface elements developed to represent the mode II z-pinning response are used in a finite element representation of the I-section patch joints structures. Chapter 8 details the development of the geometric representation of this structure through to the predicted mechanical response under loading.

The penultimate chapter gives a critique of the key details within this study. Comparison is made in areas where similar testing work has been conducted previously. The author gives his opinions on areas of this study which proved problematic and proposes new solutions where possible.

Chapter 10 lists the main conclusions drawn from this work and suggests areas in which future work should be focussed.

Chapter 2

Toughening techniques for fibre reinforced polymer matrix composites

The search for enhancement of toughness of thermoset matrix composites has seen modifications of the two individual components, the matrix and the reinforcement as well as various attempts at interface control.

A wide range of technologies exist for toughening composites through the modification of the reinforcement. For dry reinforcement and resin infused material systems 3D weaving, z-anchoring, stitching and tufting provide a means of reinforcing the through-the-thickness direction. Here, all of these technologies are summarised along with a more detailed account of z-pinning which is the dominant technology for through thickness reinforcement of pre-preg materials. The z-pinning technology has been extended to sandwich core structures which are introduced as a background for discussion later in this work. Finally, a review of published finite element and analytical modelling methodologies relevant to this work are discussed.

2.1 Matrix toughening

One of the earliest attempts to enhance the toughness of composite systems was the addition of rubber particles to thermosetting matrices [13]. Energy absorbing damage mechanisms including void coalescence, particle cavitation, shear banding, crack blunting and crazing [14,15] gave rubber modified matrices significantly increased toughness with minimal stiffness reduction. Inclusion of thermoplastic materials as toughening agents was developed to cater for high temperature requirements (above 120 °C). Thermostable PES [16] and PEI [17] for these applications were used extensively in the 1980s during which time the morphology of these modified resins was afforded special attention [18,19]. Ultimately, the limiting factor for toughness, using these additive methods, was found to be due to the high level of cross-linking within the host matrix itself [20].

The full benefit of toughened matrices is exploited when the fibre arrangement in a composite can be modified to leave a free zone or 'interleaf' [21]. Thermoplastic interleaves were shown to be beneficial when placed as thin layers in pre-preg systems [22]. They [23,24] were developed to address limitations found for thermoset interleaves which included failure of the interleaf-bulk matrix interface and buckling failure of the continuous fibre reinforcement [25,26]. Tough adhesive films were also trialled in a similar manner to interleaving for pre-preg systems [27]. For these methods, mode I fracture toughness has been measured to be ten times greater and seven times greater for mode II compared with non-interleaved laminates [28]. However, these improvements were at the expense of compression properties and the potential for saving weight. Self-same resin interleaf modification has shown promise [22,29].

The economy of dry fabrics and liquid resin infusion processing is of particular appeal to the aerospace industry. Spraying tough particulates or 'binders' directly onto the dry reinforcement has been developed to overcome the difficulties for injecting tough (intrinsically viscous) resins [30]. Embedding soluble thermoplastic fibres within the reinforcement architecture is another promising recent development [31-33]. Both these

processes allow the tough additives to dissolve into the matrix after the resin injection phase. Structures manufactured using these techniques fly on aircraft today [34,35].

2.2 Toughening through reinforcement modification by…

2.2.1 3D knitting, weaving and braiding

Three dimensional weaving of reinforcing fibres stands out as a technology as it is the only means of achieving a truly 3D fibre structure. The technologies detailed in subsequent sections are all methods of enhancing basic 2D fibre arrangements. The 3D weaving of composite reinforcement today has been facilitated through modification of traditional 2D textile weaving machinery.

Knitted, woven and braided are the three types of 3D fibre structure available. Knitted preforms consist of a complex, interlocked arrangement of reinforcement loops [36]. Woven preforms consist of traditional warp and weft tow arrangements bound together by an additional set of binder yarns [37]. A braided preform consists of a non-orthogonal pattern of diagonally overlapped reinforcement [38].

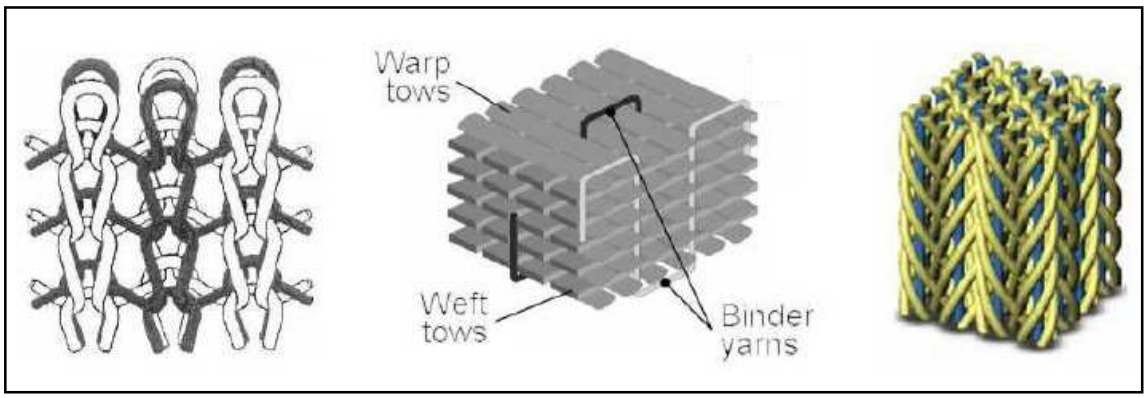

Figure 2.1 – Knitted, woven and braided 3D arrangements (from left to right) courtesy Dell'Anno

For woven preforms, structuring the fibre architecture in three dimensions has been shown to provide increased fracture toughness and damage tolerance [36,39].

Significant improvements in impact properties [40] and interlaminar toughness [41] compared to equivalent 2D laminates have been recorded. The microstructure of 3D composites which contains many resin-rich areas and distortion to in-plane fibre tows [42] is attributed as the cause for reduced tensile and compressive performance [36,43]. The microstructure is strongly influenced by the manufacturing parameter [44]. To date, little published information exists on the mechanical performance of braided and knitted preforms.

These three types of preform offer relative simplicity in manufacture. The preforms can be produced to near-net shape, placed in a mould or on a tool and infused with resin. This is simpler than laying up dry reinforcement in-situ prior to the use of liquid resin moulding techniques. Knitted fabrics offer improved drapability over standard plain weave fabrics, allowing them to be shaped to complex curvatures. This benefit is offset by a limit on the maximum fibre volume fraction attainable which is typically around 40% [45,46].

Examples of 3D components are usually found in niche applications. Dowty Propellers UK use a glass / carbon hybrid braid for manufacture of their propeller blades [47,48] which fly on the Hercules C-130J military transport aircraft.

Figure 2.2 – Dowty Propellers manufactured 3D braided propeller blades on the Hercules C-130J

2.2.2 Z-anchoring

The Z-anchor® process is a newly developed technique for modifying dry fibre preforms to include a network of fibres in the thickness direction [49,50]. Using specially designed needles, a controlled percentage of fibres can be pushed through the dry fibre preform stack to create physical links with adjacent layers. The stack is infused with resin once this is completed; permeability in the thickness direction is enhanced as a result of Z-anchoring [49]. Improvements in compression-after-impact (CAI) strength and interlaminar fracture toughness are claimed to be 35 % and 144 % respectively. The orientation of the out-of-plane fibres is not perpendicular to the bulk preform but close to 45°. Although no specific references are made in the literature, the needles are expected to cause a significant amount of damage to the fibre reinforcement.

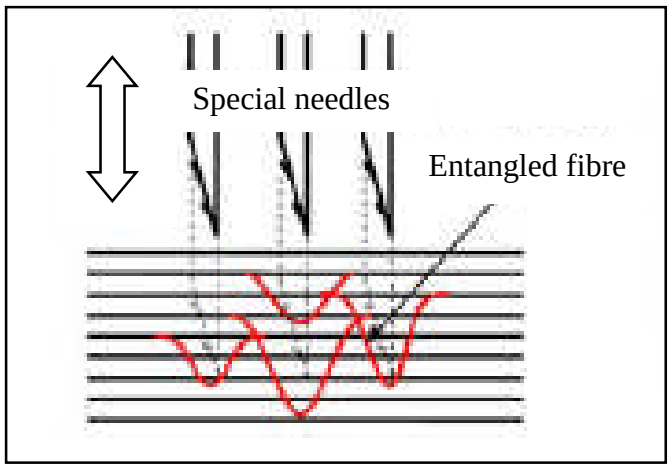

Figure 2.3 – Schematic of the Z-anchor® technique adapted from [50]

2.2.3 Stitching

Stitching has evolved from the age old textiles industry to find application in reinforcing composite materials. Stitching for composites manufacture is used with dry fibre reinforcement prior to liquid resin infusion processing. It involves the through thickness insertion of up to two threads from opposite sides of the dry fibre stack. A range of fibrous, high tensile strength materials have been used for threads such as aramid, Kevlar, glass and most recently carbon [36,51,52]. The vast majority of stitching applications are for reinforcement of dry fibre preforms but stitching of pre-pregs has

been trialled and reported in literature [53]. Passing the needle through viscous pre-preg layers presents great challenges and is generally considered problematic. Stitching architectures are varied also; three of the most common interlocking arrangements are shown in Figure 2.4.

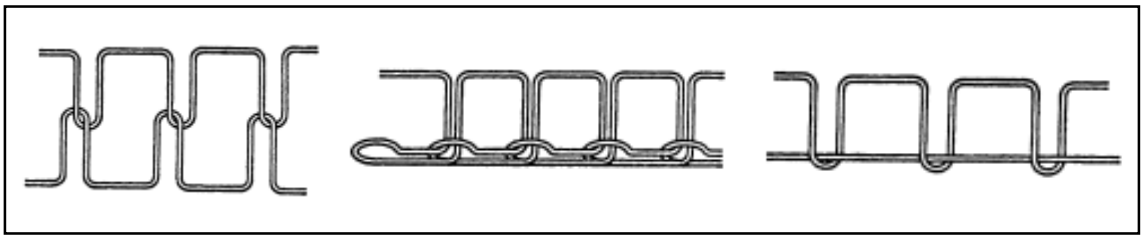

Figure 2.4 – Lock stitch, modified lock stitch and chain stitch (left to right) from [54]

The stitching technology offers economy of cost and weight in conjunction with out of autoclave processing methods and has encouraged investigation since the 1980s [55,56]. More technologically advanced sewing machines have been developed for the composites industry, driven by the aerospace industries need for high quality and reproducibility. Automated production lines have been developed for stitching large parts. In the late 1980s, NASA and Boeing developed a full scale automated stitching process for the production of composite wing structures [57]. These new computer controlled machines operate at a rate of 3200 stitches per minute and can reinforce 13 m by 2.5 m panels up to thicknesses of 35 mm.

Figure 2.5 – NASA and Boeing's advanced stitching machine

Fifteen fold increases in mode I delamination toughness have been published compared to non-stitched controls [58]. Stitching has also been reported to enhance delamination

toughness under mode II conditions between eight and fifteen times compared to non-stitched controls [53,59-61]. This broad range of mode II delamination toughness enhancement arises from the difficulty in quantifying the effects of a range of stitching parameters. Stitch stiffness and strength, thread type and diameter, stitching density, pattern, laminate thickness and the stitch-matrix interaction all play a role. Finite element modelling [60-66] has been used to address these issues by predicting their effects on both material and structural behaviour.

The majority of investigations on the mechanical performance effects of stitching agree that stitching is detrimental to the in-plane properties of the final composite [53,67]. The one exception to this is for CAI strength. For a carbon / epoxy composite reinforced by stitching using a Kevlar fibre thread CAI strength was recorded to be twice that of the unstitched control [68]. In general however, in plane properties such as tension and compressive strength are affected by the disturbance stitching causes to the fibre reinforcement; damage or breakage of the fibre reinforcement as the needle passes through occurs frequently. Damage is more prevalent in tight reinforcement stacks and in pre-pregs. The presence of the stitch itself promotes resin rich regions [67] in the final composite and can cause waviness in the fibre reinforcement plane. The tension of the stitch can cause waviness in the thickness direction also, especially on the surface. The reduction of in-plane properties caused by stitching varies between studies, for similar reasons to those mentioned previously; 45 – 55 % reductions to tensile and compressive strengths have been reported [67]. If stitching lines can be aligned with the direction of applied load then stitching offers improved creep performance in carbon / epoxy composites [69]. When subjected to impact stitched composites are able to contain damage compared to unstitched controls although they are more susceptible to penetration [70].

2.2.4 One sided stitching and tufting

The key advantage of one sided stitching (OSS) and tufting is that access to the underside of the dry fibre preform, as is required for stitching, is not needed. This opens up a new range of applications, especially in large composite structures, which can be

reinforced on their mould tooling. Stitching had previously been limited to relatively simple, open geometries with easy access to both sides of the preform. Only recently, in the last decade has the standard stitching approach been modified to overcome these limitations [71-74]. As with stitching beforehand, OSS and tufting are borrowed technologies from the textiles industry and adapted for composite applications. OSS is already used on the new Airbus A380 aircraft for reinforcing the rear pressure bulkhead [75,76]. Details of the various OSS geometries (multi-thread chain, blind and chain stitch) can be found in [71,77,78] respectively. The OSS and tufting technologies have a distinct separation in that tufting is the only single side access method which uses a single needle; OSS always requires two even if a single thread is used. The reduced potential for fibre reinforcement damage and disturbance this offers makes it a desirable technology.

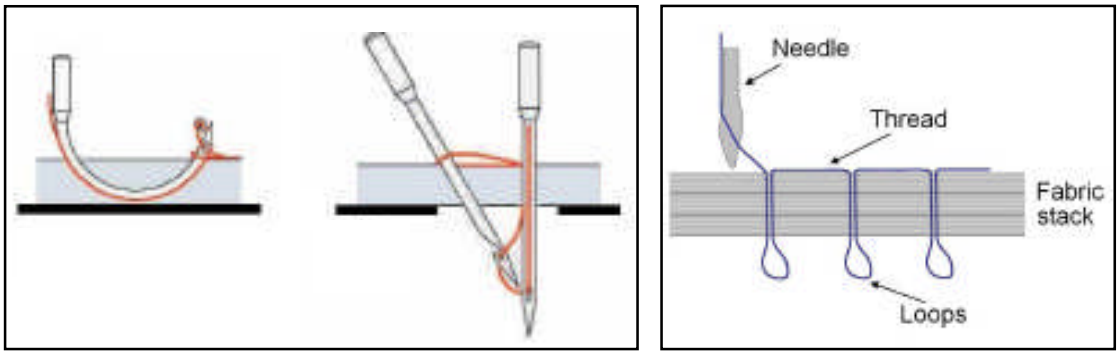

Figure 2.6 – Schematics of needle paths for OSS (left) and tufting (right) from [79]

The first PhD thesis on tufting was completed this year by Dell'Anno [79] from which the following summary of the tufting technology is taken. Tufting has its roots in an ancient method for carpet manufacture and is the insertion of a single yarn through layers of a dry fabric preform using a single, hollow needle. The insertion can be total or partial, orthogonal to the preform surface or angled. When the needle penetrates the whole preform thickness, a loop of yarn is formed on the underside of the structure. The loops are not tied or interlocked and the tufts remain in position due to frictional forces.

Dell'Anno traced the earliest example of tufting in published literature back as far as 1973 [80] although tufting equipment has only been available commercially in the last decade. The new generation of tufting 'head' can be mounted on robotic arm or gantry

systems [81]. Tufting is stated to be able to reinforce up to 40 mm thick preforms, twice the capability of OSS. A virtually unlimited thickness can be tufted if a multiple laying up process is used [72,82]. Tufting also offers an advantage over stitching in that it causes less waviness of the fibre reinforcement and therefore the knock-down to in-plane mechanical properties can be expected to be less. Due to the fact that tufting is a new process, in this context, published literature is limited to technical information [76,83,84] and comparative studies against other through-thickness reinforcement technologies [77,85-88]. Although there is currently no published database on the mechanical performance of tufted composites, positive effects of tufting on fracture toughness have been reported for composite T-joints [89].

2.2.5 Z-pinning

In the author's research group alone, eleven MSc [3-12,89] and two PhD [1,2] theses have been completed on the topic of z-pinning. Mouritz has published the most recent review on z-pinned composite laminates [90]. These extensive works give a thorough review of published literature up to the end of 2007 and provide background reading for the current work. The manufacture of z-pinned composites is covered in detail in Chapter 4.

2.2.5.1 The history of z-pinning

Huang et al [91] reported the first use of rods for reinforcing polymer laminates in 1978. Short, steel pins were inserted at ± 45° angles to provide through-thickness reinforcement for carbon / epoxy laminates. This first use of z-axis rods provided a 73% increase in strength for short beam shear test specimens. Major advancements in this technology did not occur until the late 1980s. The US based company Foster-Miller Inc. investigated this through-the-thickness reinforcement concept and, over a ten year period, pioneered a method to insert pins into laminates [92]. In the mid 1990s Foster-Miller formed a spin-off company, Aztex Inc., to handle z-pinning exclusively. The technique we call z-pinning today was patented in 1998 [93]. Aztex Inc. was responsible for developing more controlled insertion techniques, integrating z-pins into

sandwich constructions (given special attention in Section 2.2.5.5), and promoting their application into complex structures. At the beginning of the authors work in 2004 Aztex Inc. was the sole supplier of the z-pin product around the world. In 2006, Aztex Inc. was bought by Albany Int. and is now part of the Albany Engineered Composites (AEC) group. AEC continues to be the sole manufacturer and provider of z-pin products for commercial use.

2.2.5.2 Research to date

Figure 2.7 shows the geographical locations of the major contributors to z-pinning research based solely on published literature in the public domain.

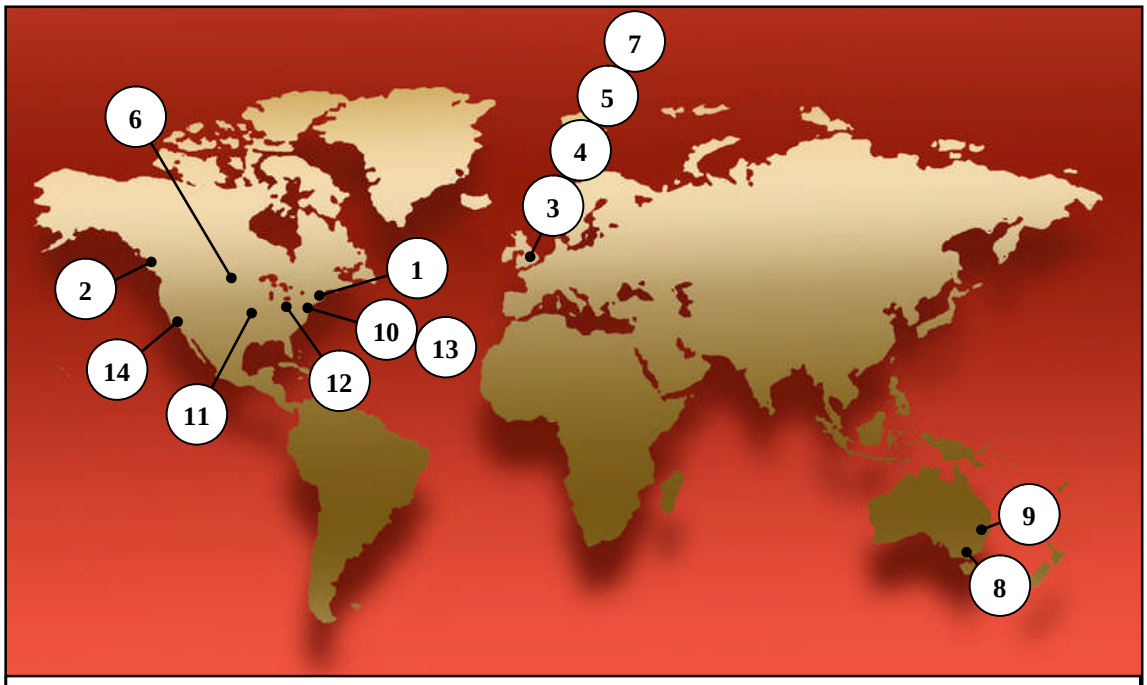

(1) Aztex Inc.	**(2)** Boeing	**(3)** Cambridge University
(4) Cranfield University	**(5)** Imperial College	**(6)** North Dakota State University
(7) QinetiQ	**(8)** RMIT Melbourne	**(9)** Sydney University
(10) UMBC University	**(11)** University of Missouri	**(12)** USAF Research Laboratory
(13) NASA	**(14)** Rockwell	

Figure 2.7 – Major contributors to z-pinning research around the world

2.2.5.3 Z-pinning characterization

Firstly, it is almost impossible to insert z-pins perpendicular to the laminate; there will always be a small angle of inclination or offset. An extensive characterisation study has been carried out by Chang [94] to characterise the z-pinning process which includes an assessment of the offset angle for z-pin diameters of 0.28 and 0.51 mm (Figure 2.8).

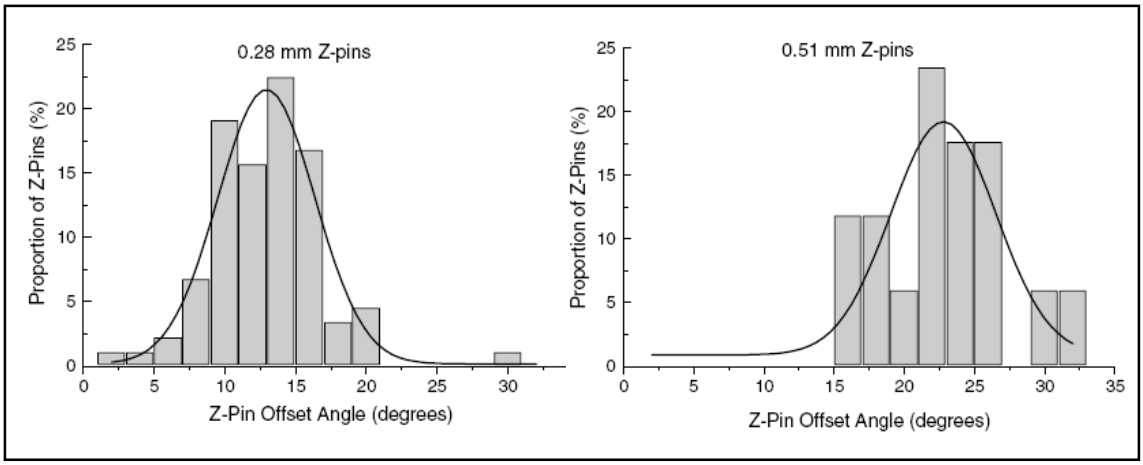

Figure 2.8 – Distribution of z-pin offset angle adapted from [95]

Figure 2.9 identifies the various manufacturing steps which contribute to the total misalignment.

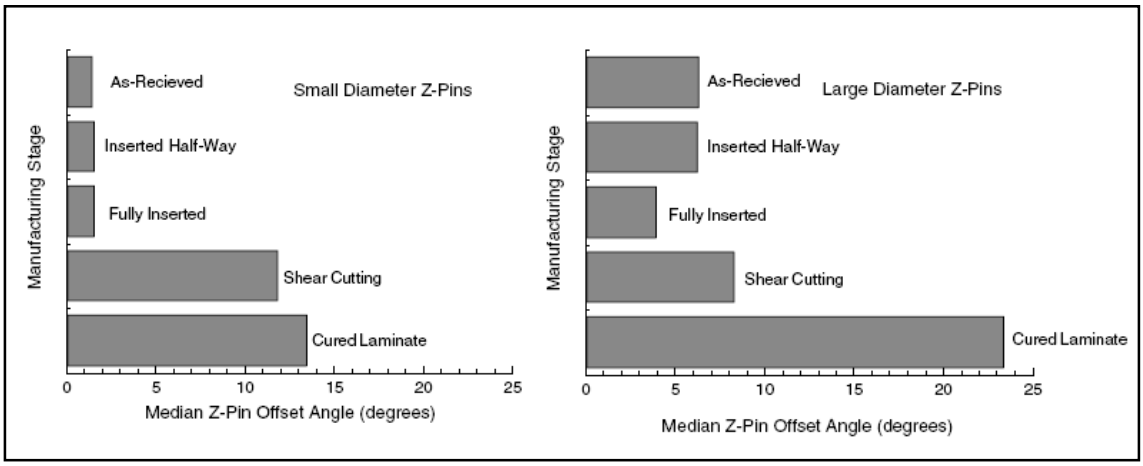

Figure 2.9 – Manufacture steps contribution to z-pin offset angle from [95]

Z-pinning can alter the microstructure of laminates in a number of ways. In order to understand the effects to laminate properties the microstructural changes caused by the insertion of z-pins must first be understood. The first and most obvious of these changes

is fibre waviness near the z-pins [94,96,97]. Fibre waviness, as shown in Figure 2.10, alters the in-plane mechanical properties of the z-pinned laminate.

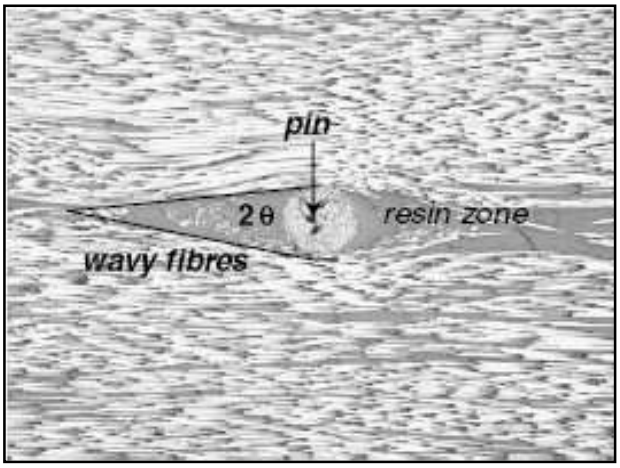

Figure 2.10 – Fibre waviness and resin rich zones around a z-pin adapted from [90]

Resin rich zones have been reported extensively [95,96,98,99]and are formed in the regions vacated by the displaced fibres. Resin rich zone geometry varies with z-pin content and diameter and can affect mechanical properties. Resin channels formed by coalescence of multiple resin rich regions can occur if z-pins are very closely spaced. Z-pinning also causes crimping of the reinforcement fibres in the through-thickness direction by bending forces exerted during insertion.

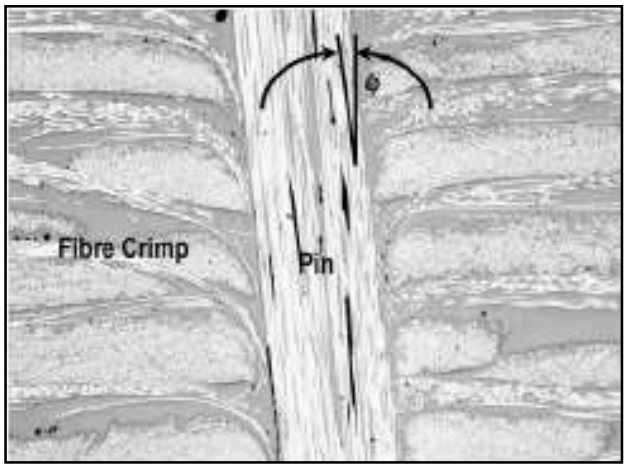

Figure 2.11 – Fibre crimping from [90]

Fibre crimp is limited to the region immediately surrounding the z-pins but it does have a negative effect on compressive strength [100-102]. Fibre breakage due to z-pinning is limited but has been observed [98,103]. The cure process after z-pins have been inserted

into pre-preg laminates affects the z-pin / laminate bond. At elevated temperatures the difference in thermal expansion coefficients leads to residual stresses which are sufficient to cause partial or complete fracture of the bond-line [104].

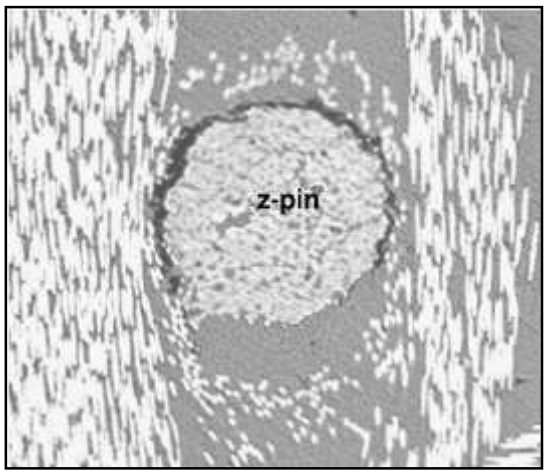

Figure 2.12 – Z-pin / laminate bond-line fracture due to residual cure stresses from [90]

The final microstructural alteration to the host laminate cause by z-pinning is swelling which reduces its local fibre volume content [92,95,99]. Swelling increases with z-pin volume content. Swelling is reported to be caused by two effects; the first, expansion of the laminate to accommodate the z-pins and second, resistance against compaction by the pins coming into contact with mould surfaces [95].

The delamination toughness improvement that z-pinning provides results in laminates with increased resistance to impact, greater damage tolerance and joint strength [1,105-136]. Z-pinning is not so effective at resisting crack initiation [103,111,126,137] but shows great effectiveness in retarding longer cracks [1,105,108-113,119-121,126,128]. The rate of crack propagation can also be controlled by z-pinning [110]. Under mode I loading conditions, the z-pin toughening mechanism is by pull-out of the pins [1,109,112,113,127,138]. Under mode II loading conditions, a number of mechanisms are involved including elastic shear deformation, de-bonding, snubbing and, if the delamination surfaces are free to open, shear-induced pullout [109,113,121,123,124,139].

Impact tests have shown that z-pinning reduces the amount of delamination damage for a range of projectiles [92,99,105,111,120,137,140-142]. This can be as much as 50 %. As a result of this post impact properties are conserved [1,103,137,142].

Mouritz [90] comments that "most research into z-pinned laminates has focussed on the benefits... the adverse effects of z-pinning have received less attention." Several studies have been performed which have reported reductions to elastic properties [95,96,103,111,143-146], strength [92,95,98,103,105,111,145-148] and fatigue properties [95,145,146]. Most relevant to this work is the effect on the elastic properties which are decreased gradually as the z-pin content increases. Unidirectional laminates are most affected; for other laminates, the reduction is related to the percentage of fibres aligned with the applied loading direction. For standard aerospace industry laminate lay-ups the in-plane modulus reduction is usually less than 10 %. Strength properties for z-pinned laminates can be calculated accurately due to a linear relationship with z-pin content. Simple models exist for predicting z-pinned laminate strengths in tension, compression and flexure [95,145,146].

2.2.5.4 Z-pinning applications

Z-pinning is used in high performance automotive and aerospace applications; two of the largest markets for pre-preg materials. Formula 1 racing teams now make considerable use of the z-pinning technology for reinforcing highly loaded structures in their racing cars. Jaguar Racing was one of the first teams to take advantage of the benefits of z-pinning using it to reinforce the roll hoop of its R3 car in 2000 [97]. Possibly the largest consumer of z-pins is the US Air Force which uses 5 m^2 of z-pins on its Northrop F18E/F aircraft as a replacement for over 4500 titanium fasteners. The use of z-pins is reported to result in a 17 kg weight and US$ 83,000 saving per aircraft [149].

Figure 2.13 – Jaguar Racing R3 with position of roll hoop circled (top) and Northrop F18 (bottom)

2.2.5.5 Pin reinforced sandwich cores

The z-pinning technology has been extended to sandwich constructions. The simplest way this has been done is by inserting z-pins straight through a composite skin / core sandwich lay-up prior to cure [105,150,151]. This is a direct transfer of the z-pinning method for monolithic laminates to sandwich constructions. The rest of this section will concentrate on the more advanced type of pin reinforced sandwich structures which are known as X-Cor and K-Cor.

X-Cor and K-Cor were originally developed to replace honeycomb products, used extensively in the aerospace and automotive industries, by providing improved durability and damage tolerance [152]. These through thickness reinforced products use Z-Fiber® reinforcement developed and patented by Aztex Inc. The composite z-pins used for X-Cor and K-Cor are manufactured by the same process as for z-pin rodstock detailed in Chapter 4. However, the constituent materials used for these pins vary according to the product (see Table 4-5).

For both core types, the process in which pins are inserted into the foam core is an automated one using an insertion head and a computer controlled X-Y gantry system as shown in Figure 2.14. The full insertion methodology is discussed in Chapter 4. Closed cell polymethacrylimide (PMI) foams are typically used for the core for their temperature resistance and the fact that they can facilitate economic liquid moulding procedures.

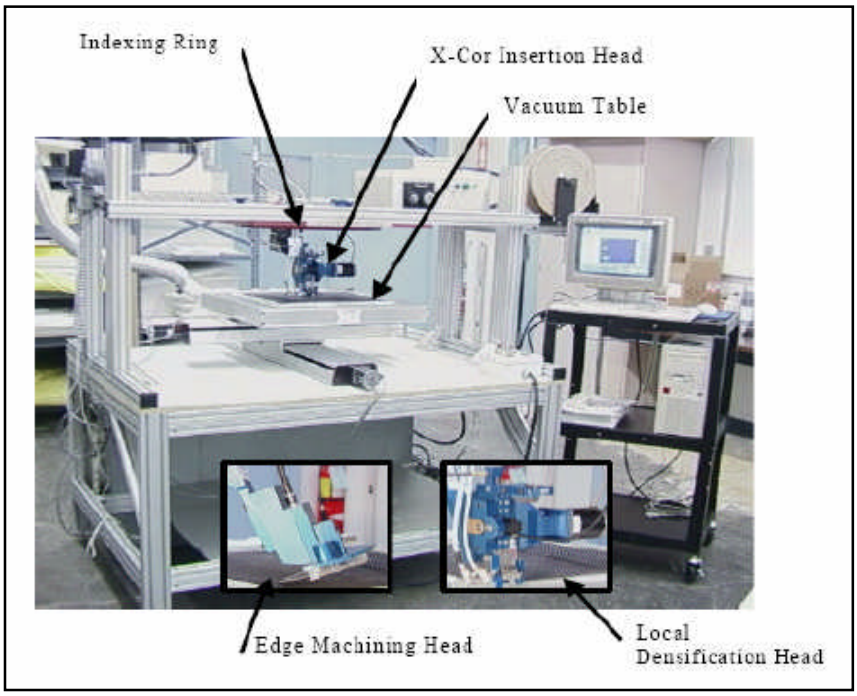

Figure 2.14 – Automated pin insertion machine for manufacture of pin reinforced cores from [153]

After pin insertion, both core types are in the X-Cor configuration (see Figure 2.15). K-Cor undergoes an additional step in which the pin reveal lengths on both sides are simultaneously thermo-formed flush with the foam surface. A heated press is used for this; the K-Cor rodstock is not fully cured at this stage so that the pins do not fracture during the process. The fullest account of the manufacture steps for these cores is given in [152].

In X-Cor sandwich constructions the pin tips are designed to pierce the skins. X-Cor is specifically suited to composite pre-preg or resin infused skins. In this case the skins are cured in situ, the pins are anchored in each skin to produce a through-thickness mechanical link. In K-Cor sandwich constructions the flattened pin tips facilitate

bonding to the full range of skin materials. If composite skins are used then they are usually pre-cured prior to bonding.

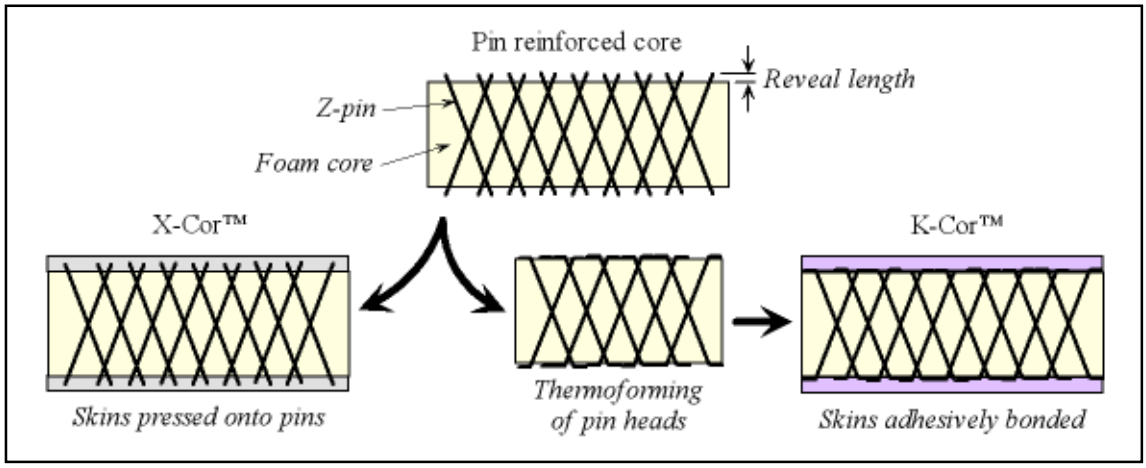

Figure 2.15 – Pin reinforced X-Cor and K-Cor structures and terminology

A considerable advantage of these z-pinned structures is the possibility of removing the foam completely to leave a partially hollow core leaving only the pin structure linking the two skins. The increased core accessibility is attracting growing interest [154] and they represent a conceptually similar, lighter weight alternative to metal truss structures [155,156].

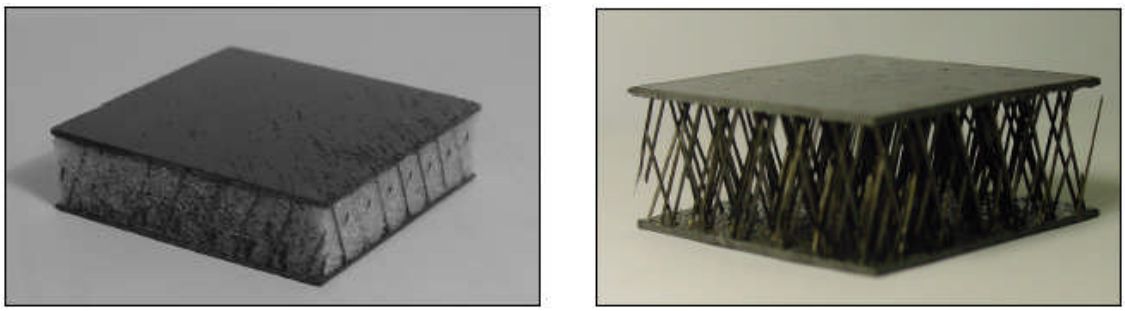

Figure 2.16 – Foam filled (left) and hollow (right) X-Cor structure courtesy of Marasco

Marasco [152,157] writes that "the uniqueness of these pin reinforced structures is their flexibility to meet a variety of design specifications." The ability to select the foam type, different pin materials and geometries and the positioning of the reinforcing pins gives wide scope for design. The angle at which the reinforcing pins are inserted can be tailored to balance the compressive and shear response of the sandwich construction.

Using these pin reinforced cores a similar performance to that of honeycomb can be achieved with an insertion angle between 20° and 30° [99,153].

There is a growing market for pin-reinforced core technology particularly in the United States. X-Cor technology is known to be used in the front fuselage region of the Boeing-Sikorsky RAH-66 Comanche helicopter for its superior damage tolerance over the previous honeycomb structure. Additionally, the X-Cor design allows a 10 % weight and 25 % manufacture cost saving over the honeycomb base-line [152].

Figure 2.17 – Boeing-Sikorsky RAH-66 Comanche makes use of X-Cor technology

2.3 Modelling z-pin reinforcement

The attempts being made to model the properties of z-pinned laminates are increasing in number, based on literature published since 2000. Modelling the delamination properties of z-pinned laminates has complications due to the numerous microscopic and mesoscopic failure mechanisms which occur. These mechanisms exist over a wide range of scales which is particularly challenging for FE computations.

For the modelling of z-pins, several large scale bridging fracture models have been developed to calculate the mode I [90,108,116,127-134,136,158], mode II [117,122,124,125] and mixed mode [122,124,125] delamination toughness of z-pinned laminates [90]. Jain et al [62] developed a model for discontinuous, through-thickness stitches which can also be applied to z-pinning.

Analysis of mode I performance is by far the most extensively covered. In all cases these models are based around the double cantilever beam (DCB) geometry in which the beam deflections and the crack opening displacement are calculated from Euler-Bernoulli beam theory. Three types of modelling approaches have been used for mode I analysis. Bridging laws are used to calculate the z-pin traction force and these laws have been developed by treating the pins as elastic inflexible rods [108,115,116,118,127,128,132-136,158], elastic flexible rods [130,131] or discrete springs [129]. The bridging laws themselves are formed from experimental pull-out tests on single or multi-pin specimens. The bridging laws are material specific and must therefore be obtained for the specific z-pin / laminate type. Interlaminar fracture toughness can be calculated using linear elastic fracture mechanics. Despite the existence of this range of mode I models only those by Cartie et al [108] and by Liu et al [127] have been verified against experimental data.

For other modes of loading, analytical models have been developed to evaluate the effects of z-pinning. For example, an analytical model to calculate the local buckling strength of a delaminated composite beam under edgewise compression showed that z-pins are expected to increase the post-impact buckling strength [159]. Models to recreate the z-pinning effect in structural elements such as T-joints and novel cruciform stiffener joints have also been developed [160,161]. Several models exist, based on large scale bridging mechanics, for the calculation of the ultimate strength of z-pinned lap joints [121,162].

Of particular relevance to this work are the modelling approaches developed for z-pin mode II performance [117,121,122,124,125,163]. The bridging laws, as for mode I models, need to be obtained from experimental tests. At Cranfield University the Z-shear test has been adopted for obtaining single pin bridging laws under mode II loading conditions [2,6]. Mode II delamination testing of z-pinned laminates is complicated by the fact that to date no standard test configuration has been agreed upon. Previously the favoured mode II testing arrangement was the End Notched Flexure (ENF) test [2,163] however recent work by the ESIS TC4 group [164-167] in particular has seen the End loaded Split (ELS) configuration come to the fore [168-170]. The models for the

behaviour of z-pins under mode II loading conditions of particular note are those by Cox [122,124] and by Allegri [171] although the two disagree on the specifics of the fracture of the pins if opening displacement is constrained. It is the author's opinion that these works are difficult to implement at present due to the fact that the analytical methodologies for both require parameters that cannot be measured experimentally. These parameters are for the foundation of the pin in the laminate material. There is a need for an easy to implement FE approach which can be used to assist in the design of z-pinned components subjected to mode II loading.

To conclude, the only published modelling attempt for pin reinforced cores was produced by Marasco [152]. This first attempt aimed to reproduce the experimentally measured linear elastic response of K-Cor and X-Cor structures under out-of-plane shear loading conditions. The model underestimated the experimental shear rigidity by ~20% but showed that such FE models could be used as tools for optimising pin positioning. Current work at Cranfield University continues to develop improved analysis tools for pin reinforced core structures.

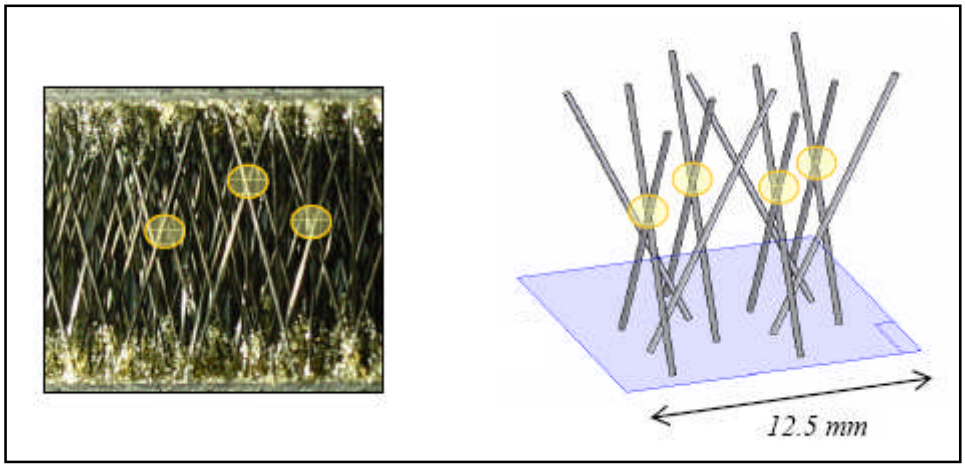

Figure 2.18 – Marasco's FE model unit cell of the pin reinforcement structure in sandwich cores; occurrence of pin contacts are highlighted in the real structure (left) and unit cell (right)

Chapter 3

Materials

This chapter details all of the materials used to manufacture experimental test specimens and structures used in this work.

Users should be aware of the safety guidelines which accompany all of these materials and ensure that the correct safety equipment is used when handling them. This is to minimise personal risk and prevent contamination of the materials themselves.

3.1 Fibres

The following table summarises the properties, as listed by the manufacturer, for a range of reinforcing fibres included in the composite systems used in this work and which are detailed hereafter. For woven materials, thousands of these fibres are grouped together into tows and subsequently woven together to form a fabric. Fibres in unidirectional (UD) materials are simply aligned parallel in the same plane. Both of these reinforcement architectures can then be fully wetted out with resin to create layers of composite known as pre-pregs.

Fibre type	T300	HTA	T800	E-5
Material	Carbon	Carbon	Carbon	E-glass
Manufacturer	Toray	TohoTenax	Toray	unknown
Filament diameter (μm)	7	7	5	4 to 13
Tensile strength (MPa)	3530	3950	5490	2000
Tensile modulus (GPa)	230	238	294	80
Elongation at break (%)	1.5	1.7	1.9	2.0
Density (g/cm^3)	1.76	1.76	1.81	2.55

Table 3-1 – Properties for reinforcing fibre types

3.2 Z-pins and z-pin preform

Z-pins (also known as Z-Fiber®) are thin, rigid rods for through-the-thickness reinforcement of pre-preg laminates. Individual pins are cut from a long pultruded length of cured T300 / bismaleimide (BMI) rodstock which is twisted during the pultrusion process to give it a near circular cross-section.

Z-pins are manufactured solely by Albany International, formally Aztex Inc. and supplied in foam carrier preforms. Two z-pin diameters are available, 0.28mm and 0.51

mm. Both of these diameters are available in a range of areal densities from 0.5% to 4%; the array of z-pins is almost always square.

Figure 3.1 – Z-pin rodstock spools (200 mm diameter)

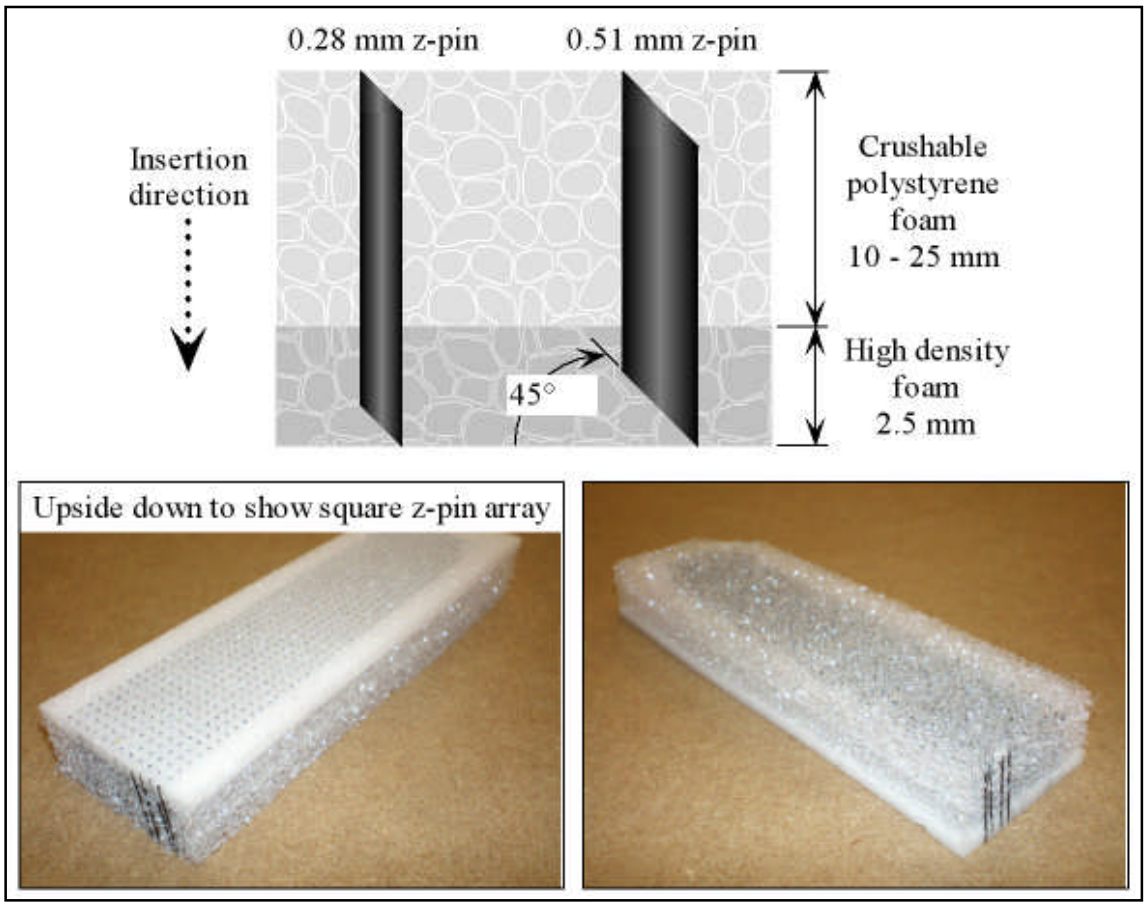

Figure 3.2 – Schematic of z-pin preform

The most commonly used areal density for this study was 2% which equates to a pin-to-pin spacing of 1.8 mm (pin-to-pin spacing denotes the distance between neighbouring z-pin axial centres). The foam preforms allow the areal density of z-pins to be controlled and maintain their vertical alignment. Figure 3.2 shows the constituent parts which make up a z-pin preform as supplied, although not drawn to scale. Z-pins are cut with a sharp, 45° chamfer to assist insertion.

For the experimental work described in this report, only T300 / BMI z-pins were used, T300 refers to the type of carbon fibre and the BMI resin system is CytecFiberite 5250-4. The glass transition temperature (Tg) of this resin system is sufficiently high so as to maintain the integrity of the z-pins during the cure processing of the pre-preg systems through which they are inserted. (200 – 270 °C from [172]) For the manufacture of all z-pinned components described in this report the z-pins were inserted through the full thickness of the laminate using a handheld ultrasonic horn. Full thickness insertion was deemed to be complete when it was not possible to insert the z-pins any further; this probably resulted in local crushing of the chamfer length.

Cranfield University recently acquired a robotic facility which allowed the author to manufacture a limited quantity of his own preform. The major advantage of this was to allow the production of tailored preforms where the areal density, pin length and most importantly the individual pin positions and orientations could be fully controlled. This capability and a full description of the z-pin insertion process are given in Chapter 4.

3.3 Foams

Figure 3.3 shows the two foam types required for the production of z-pin preform, low density, crushable polystyrene (top) and high density Rohacell LastaFoam (bottom). The high density base foam does not crush during the insertion process and is present to assist in the trimming of the exposed z-pin heads once insertion is complete. The crushed preform including both of these materials is discarded once the z-pin insertion process is complete as these foams serve no mechanical purpose.

Figure 3.3 – Z-pin preform foams

Additionally, Rohacell is the preferred supplier of foam materials for reinforced core products (X-Cor™ and K-Cor™) in which case they do serve an important load carrying role and for which their physical, mechanical and thermal properties are optimised.

3.4 Pre-pregs

These materials were stored in the freezer in a sealed bag whilst not in use to prevent degradation and premature cure. Prior to use these materials were allowed to fully defrost before removal from their sealed bag to prevent the pick up of moisture.

3.4.1 HexPly® 914 / 6K5H / T300

This aerospace grade carbon/epoxy woven pre-preg system, supplied by Hexcel Composites, was used to manufacture I-section test elements and flat laminate specimens for delamination testing. This composite system consists of a 914 formulated epoxy matrix reinforced with a five harness weave of T300 type carbon fibre tows. A summary of typical cured 914 matrix properties as supplied by the manufacturer is given in Table 3-2.

Tensile strength	47.7 MPa
Tensile modulus	3.9 GPa
Tensile strain	1.5 %
Poisson's ratio	0.4
Calculated shear modulus	1.4 GPa
Compression strength	180 MPa
Toughness (K_{IC})	0.7 MPa$\sqrt{m}$
Toughness (G_{IC})	103 J/m^2
Glass transition temperature (Tg)	190 °C
Cured density	1.3 g/cm^3

Table 3-2 – Cured properties for neat 914 resin

This material was vacuum bagged (1 bar) and autoclave cured according to the manufacturer's recommended cure cycle, a summary of which is given in Table 3-3.

Heat-up rate	2 to 5 °C/min
Dwell at 120 - 135°C	1 hour
Cure temperature	175 °C
Cure pressure	700 kN/m^2 (7 bar)
Cure time	1 hour
Post-cure required	Yes

Table 3-3 – 914 woven pre-preg cure cycle

Upon completion of this cure cycle the composite parts were placed, free standing, in an oven and post-cured for 4 hours at 190°C.

3.4.2 HexPly® 8552 / 3K8H / HTA

This aerospace grade, carbon / toughened epoxy woven pre-preg, supplied by Hexcel Composites, was used to manufacture I-section test elements and flat laminate specimens for delamination testing. This composite system consists of an 8552 formulated epoxy matrix reinforced with an eight harness weave of HTA type carbon fibre tows. A summary of typical cured 8552 matrix properties as supplied by the manufacturer is given in Table 3-4.

Tensile strength	121 MPa
Tensile modulus	4.7 GPa
Toughness (G_{IC})	679 J/m^2 from [173]
Glass transition temperature (Tg)	200 °C
Cured density	1.3 g/cm^3

Table 3-4 – Cured properties for neat 8552 epoxy resin

This material was vacuum bagged (1 bar) and autoclave cured according to the manufacturer's recommended cure cycle, a summary of which is given in Table 3-5.

Heat-up rate	1 to 3 °C/min
Dwell at 110 °C	1 hour
Cure temperature	180 °C
Cure pressure	700 kN/m^2 (7 bar)
Cure time	2 hours
Post-cure required	No

Table 3-5 – 8552 woven pre-preg cure cycle

3.4.3 Cycom 977-6 / 6K8H / T800

Cycom 977-6 aerospace grade woven pre-preg was used to manufacture the crash tubes reported in this study. This composite consists of a 977-6 epoxy matrix reinforced with an eight harness weave of T800 type carbon fibre tows. Typical neat 977-6 matrix properties as given by the manufacturer are listed in Table 3-6.

Compression strength	179.3 MPa
Flexural strength	154.5 MPa
Flexural modulus	3.9 GPa
Toughness (K_{IC})	1.6 MPa$\sqrt{m}$
Toughness (G_{IC})	638 J/m^2
Glass transition temperature (Tg)	190 °C
Cured density	1.3 g/cm^3

Table 3-6 – Cured properties for neat 977-6 epoxy resin

Heat-up rate	2 °C/min
Cure temperature	135 °C
Cure pressure	310 to 609 kN/m^2 (3.1 to 6.9 bar)
Cure time	3 hours
Post-cure required	No

Table 3-7 – 977-6 woven pre-preg cure cycle

The manufacturer's parameters for a standard autoclave cure of this material are given in Table 3-7. Parts to be cured should be vacuum bagged and a full vacuum applied however, for the crash tube manufacture, the vacuum bag was replaced with a thermally activated shrink tape to provide consolidation.

3.4.4 HexPly® 913G / UD and 913G / 4H

These two glass / epoxy systems were selected to manufacture shear specimens because they offered the advantage that the carbon z-pins could be seen inside the composite. Two E-glass reinforcement architectures were used, unidirectional tape and a 4 harness satin woven fabric. The matrix was consistent between the two, Hexcel Composites 913 epoxy. Properties for cured 913 epoxy resin are detailed in Table 3-8, and the manufacturer's recommended cure cycle is given in Table 3-9.

Tensile strength	65.5 MPa
Tensile modulus	3.4 GPa
Glass transition temperature (Tg)	131 °C
Cured density	1.23 g/cm^3

Table 3-8 – Cured properties for neat 913 epoxy resin

Heat-up rate	2 to 8 °C/min
Cure temperature	125 °C
Cure pressure	700 kN/m^2 (7 bar)
Cure time	1 hour
Post-cure required	No

Table 3-9 - 913 pre-preg cure cycle

Hexcel 913 uncured epoxy, when heated, is very prone to hazardous exotherms and must be treated with extreme caution. In the worst case it can cause a severe fire risk, to a lesser extent it can lead to darkening of the matrix colour which in this case was undesirable as it would reduce visibility of the z-pins. To avoid this the slowest heat-up rate was used and the recommended cure cycle was modified to include two dwell periods, one at 60 °C for 1 hour and the second at 100 °C for 1 hour.

3.5 Miscellaneous

3.5.1 Structil® EA 9685

An empty region exists in the geometry of the pre-preg I-sections, where the web meets either flange which needs to be filled. Structil® EA 9685 epoxy was one material selected for this purpose as it could be thermo-formed to the required shape and co-cured with the 914 / 6K5H / T300 pre-preg.

3.5.2 Hexcel 8552 / 12K / IM7 single tow

For I-sections manufactured using the 8552 / 3K8H / HTA pre-preg the noodle region was filled with a twisted length of six 8552 / 12K / IM7 pre-preg tows which were pressed into shape by hand. The identical resin systems allowed the noodle to be co-cured with the I-sections. The use of twisted tows for filling noodle regions is understood to give superior performance compared to epoxy fillers in terms of maintaining shape and mechanical performance [174].

3.5.3 Araldite® 420 A/B

All bonding of test structures to test jigs and tabbing of test specimens was carried out using this epoxy adhesive. Araldite® 420, supplied by Huntsman [175], is a two-component paste adhesive suitable for aerospace materials and applications. The two components are mixed (4 parts hardener per 10 parts epoxy by weight), applied to the prepared bonding surfaces and oven cured at 70 °C for 2 hours. The shear strength of this adhesive at ambient temperature as stated by the manufacturer is 37 MPa. Removal of test jig parts and tabs from tested specimens is possible by heating the adhesive to 150 °C. At this temperature the adhesive degrades and the bonded parts can be separated with a firm tap.

Chapter 4

Manufacturing: methodology and considerations

This chapter details the procedure and processes used to manufacture all of the test specimens and structures used in this work.

A special focus is placed on the recently acquired robotic facility which was used to manufacture some tailor made z-pin preforms and for which a programming code was developed for the manufacture of X-Cor and K-Cor materials. Additionally, the quality of z-pins from raw material rod-stock through to insertion into a laminate is discussed.

4.1 Z-pin insertion apparatus and procedure

Insertion of z-pins into un-cured, pre-preg composite parts is a relatively straight forward process in theory but is influenced greatly by operator skill. In the previous chapter it was stated that the material used for manufacturing z-pins is a pultruded T300 / BMI composite rod. In principle, a wide range of materials can be used to manufacture z-pins so long as they can be manufactured as a thin rod and have the rigidity and strength to survive the insertion process. Materials known to have been tried in the past for through thickness reinforcement, in a similar manner to z-pinning, include silicone carbide / bismaleimide (SiC / BMI), S-glass / epoxy, titanium, stainless steel and aluminium. Diameters of z-pins made from these alternative materials range from 0.15 mm to 1 mm.

4.1.1 Introduction to z-pin preform manufacture and preparation

Z-pins are supplied in foam preforms which provide a means by which the areal density and orientation of the individual pins can be controlled. The manufacture of the preform is itself a two stage process originally developed by Aztex Inc. [99]. Firstly, a pultrusion process allows a continuous, small diameter composite rodstock to be drawn and coiled on a spool. The second part is the insertion of this rodstock into a two part foam block.

In the pultrusion process, T300 carbon fibre tows are drawn through a bath of liquid BMI resin held at an elevated temperature to maintain its fluidity. Typically, a 1k (1000 individual filaments) tow of T300 carbon fibres is used to produce 0.28 mm diameter rodstock and a 3k T300 tow is used for 0.51 mm diameter rodstock. The carbon fibre tow exits the bath and is subsequently drawn through a die (either 0.28 mm or 0.51 mm diameter) and immediately enters a long oven. The length of the oven is sufficient that the resin hardens, but does not fully cure, prior to being wound onto a spool. The winding process also introduces a twist into the material which serves to produce a near circular cross-section of the rodstock. Once on the spool the T300 / BMI rodstock is post-cured. Other than passing through the die, there is no consolidation of the material

during the cure, a process which is usually associated with composite manufacturing. This has quality implications which are described later in Section 4.1.4.

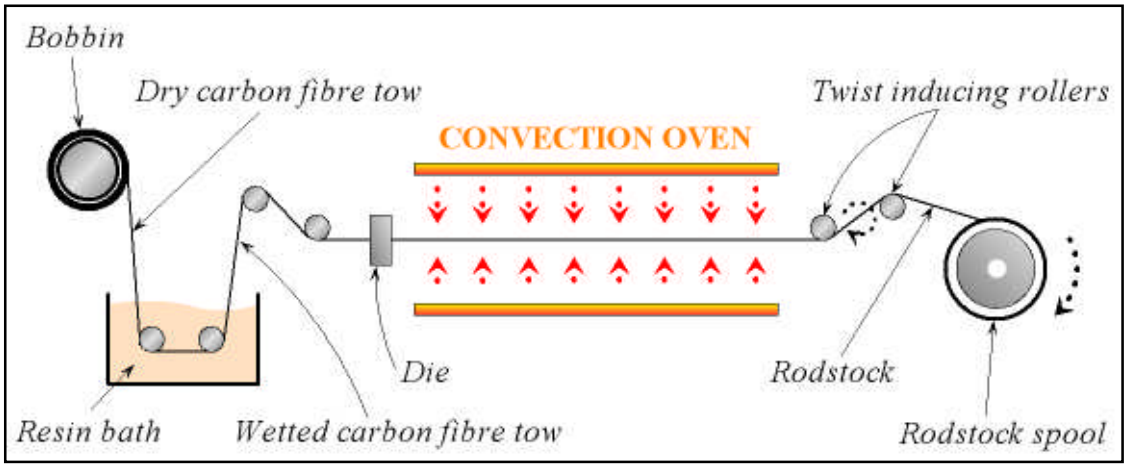

Figure 4.1 – Z-pin rodstock pultrusion process

The process in which the rodstock is inserted into the two part foam block is an automated one where the length of z-pin, the areal density, and the orientation is controlled. For standard z-pin preform the orientation of the z-pins is always vertical, however, it would be possible to alter this. The z-pin preforms are manufactured upside-down, with the high density foam on top, as this provides the best support for the z-pins as they are inserted, reducing the likelihood of deviation from the desired insertion orientation.

The method for rodstock insertion into the foam block is as follows: the rodstock spool is mounted onto an insertion head which is motor driven by two axis gantry. The rodstock is passed through a set of rollers driven by the insertion head which pushes a length of rodstock into the foam block. The rodstock is cut with a shear cutter, slightly above the foam surface, at a 45º angle to give the required z-pin length. The angle at which the pins are cut mainly helps the pin to pierce the foam, and ultimately the composite pre-preg laminate, but also minimises carbon fibre filament breakage and distortion. The protruding length of pin is pushed down flush with the foam surface by a stamper set at a short distance behind the cutter. The stamper is positioned behind the insertion tip so that the two functions can run simultaneously to reduce process time. In

current production, Albany Int. run machines which make use of an array of insertion heads capable of inserting 8 pins per second.

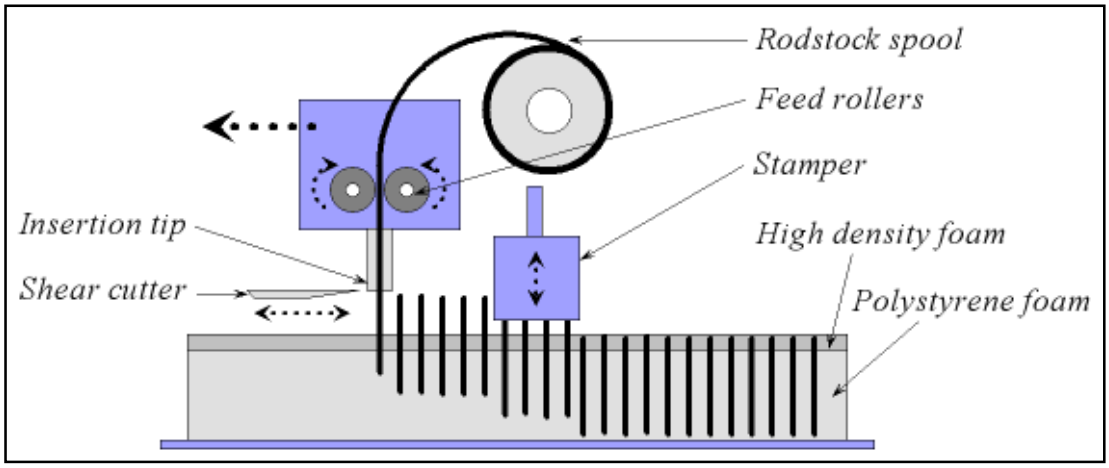

Figure 4.2 – Albany Int. z-pin preform manufacture schematic

With the preform made, it is cut to size prior to insertion of the z-pins into the composite pre-preg laminate. At Cranfield University, the author learnt an additional step which improves the quality during the insertion process. The non-laminate facing surface of the foam block, the surface on which the ultrasonic insertion horn is applied, is covered with a thermally stable adhesive tape. This tape helps to prevent pins vibrating out of the preform once the ultrasonic insertion horn is activated. This is more of a problem for small z-pin diameters and high areal densities. The adhesive tape must be thermally stable to withstand heating caused by the ultrasonic equipment. When done correctly, loss of no more than one pin per square inch of preform is normal and has been typical for the author's work.

4.1.2 Laminate preparation for z-pin insertion

In reality, very little has to be done to prepare pre-preg laminates for z-pinning. The laminate must obviously be uncured and must be allowed to reach room temperature, at least, if it has been kept in freezer storage previously. The specific fibre architecture and resin type of the laminate will affect the z-pin insertion process. Tightly woven fabric architectures and high viscosity resins can make insertion more difficult; naturally some material systems lend themselves to z-pinning more than others. If insertion is proving

troublesome then a couple of steps can be taken to prepare the laminate for easier insertion. Warming the laminate, to about 35 ºC, usually helps to soften the resin sufficiently to allow an easier passage through for the z-pins. Tight fabric architectures cannot really be avoided, however, and to help z-pins pass through these usually requires some adjustment to the pressure and application time of the ultrasonic insertion equipment. It is preferable to de-bulk the pre-preg laminate prior to insertion of z-pins but, on occasion, if the fabric architecture is not allowing the pins to pass through then this step can be omitted.

4.1.3 Z-pin insertion

Two methods for insertion of z-pins into uncured pre-preg laminates exist, the Ultrasonic Assisted Z-Fibre™ Insertion method (UAZ™) and the autoclave insertion method. The autoclave method was initially developed by Aztex Inc. to insert large areas of pins in one go.

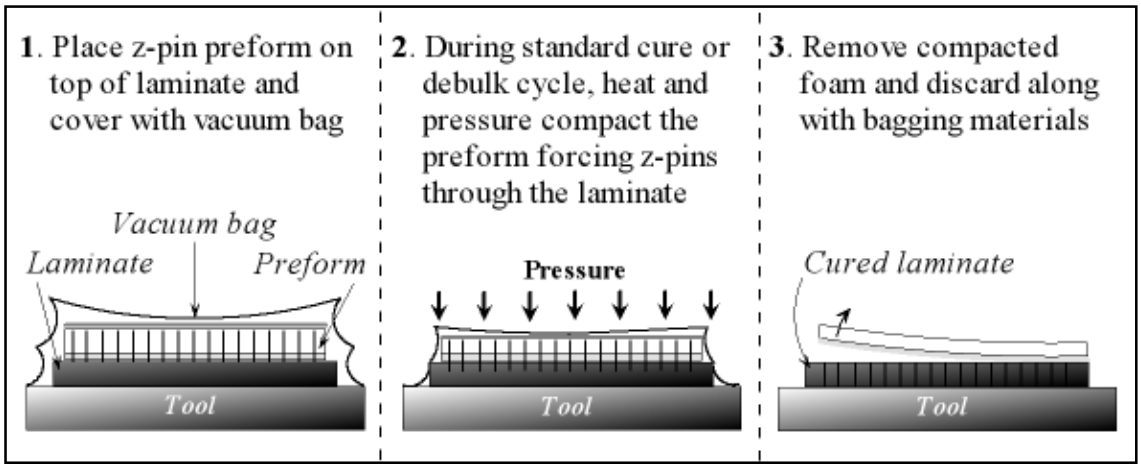

Figure 4.3 – Autoclave z-pin insertion process (adapted from [1])

The preform is placed on top of the uncured laminate and a rigid pressure plate placed on top of the preform. The heat provided by the autoclave softens the resin and the pressure applied compacts the preform pushing the z-pins into the laminate. Because of the high pressures required to compact large areas of preform only low areal densities can generally be used. This method is now rarely used and for all work described in this report the UAZ™ method of insertion was used.

UAZ™ insertion of z-pins offers the benefit that it is completely separate from the laminate cure process and therefore insertion parameters can be optimised without any effects on future processing of the laminate. Furthermore, access to only one side of the laminate is required for z-pin insertion making this technique particularly suitable for composite components laid up on moulding tools.

4.1.3.1 The UAZ™ insertion apparatus

The ultrasonic apparatus consists of a power supply, a transducer, a signal booster and an insertion horn. The transducer is a 20 kHz type with a maximum amplitude of 20 μm at 100 % output. The transducer setting can be adjusted depending on the ease with which z-pins pass through the laminate. If insertion is proving difficult then more power can be used. The insertion horn can be supplied with a range of footprint sizes and shapes depending on the area to be reinforced and its accessibility. The size used for all the work here was 25 x 25 mm. The horn can either be a handheld unit as shown in Figure 4.4, mounted on a gantry and controlled via an automated system (see Figure 4.5) or mounted on a robotic arm system.

Figure 4.4 – Handheld UAZ™ insertion apparatus

The transducer is included in the handheld unit and the horn screwed directly into it. Between the horn and the transducer an insulating collar is placed to prevent shorting out of the electrical components should the horn come into contact with a conductive surface whilst activated.

The gantry operated horn system at Cranfield University was also available for use. The gantry system offers advantages if the z-pins are to be inserted to a controlled depth whilst it also insures that the horn is applied perpendicular to the laminate at all times.

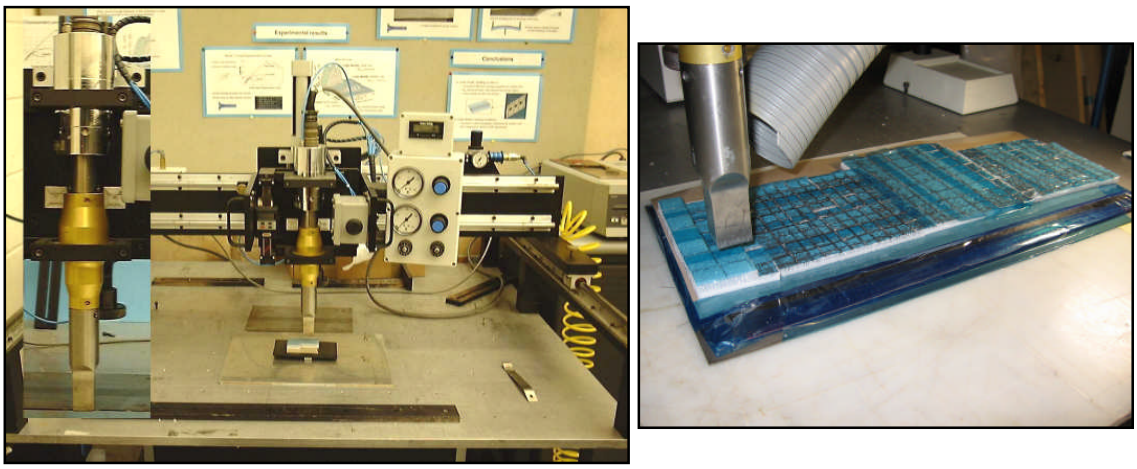

Figure 4.5 – Cranfield University's gantry insertion system

The gantry system is considered by some to offer a greater level of repeatability of the insertion process, a view not shared by the author. The system is cumbersome, mainly due to the level of downward pressure on the horn being out of the control of the operator. Further details regarding the gantry controlled insertion system can be found in [1,2]. For all work described here the z-pins were inserted through the full thickness of the laminates used and therefore the handheld unit was preferred. The main consideration with using the handheld system was to ensure that the horn is held perpendicular to the laminate surface at all times.

4.1.3.2 The UAZ™ insertion process

The laminate is placed on a smooth metallic surface and a layer of release film is placed over the upper surface to prevent the pick-up of foam debris and fractured z-pin dust which is created during the insertion process. On top of the release film, a layer of non-porous, Teflon coated glass fibre fabric is placed, cut to a size slightly larger than the area to be z-pin reinforced. The Teflon coated fabric is used to provide a low friction surface on which a tool can be used to trim the pins once inserted.

The z-pin preform is positioned on top of the laminate with the high density foam surface facing down, adhesive tape side up. The adhesive tape side is scored into squares so that the z-pins in the preform can be inserted in small sections at a time. The area of the squares scored on the preform should obviously be smaller than the footprint of the ultrasonic horn.

The ultrasonic horn is activated by pulling the trigger on the handheld unit and insertion of the z-pins starts with a little downward pressure from the operator. The author prefers to insert the four corners of the preform first to secure the preform in position. The preform must be held secure; any slippage that occurs under insertion pressure causes the z-pins to buckle.

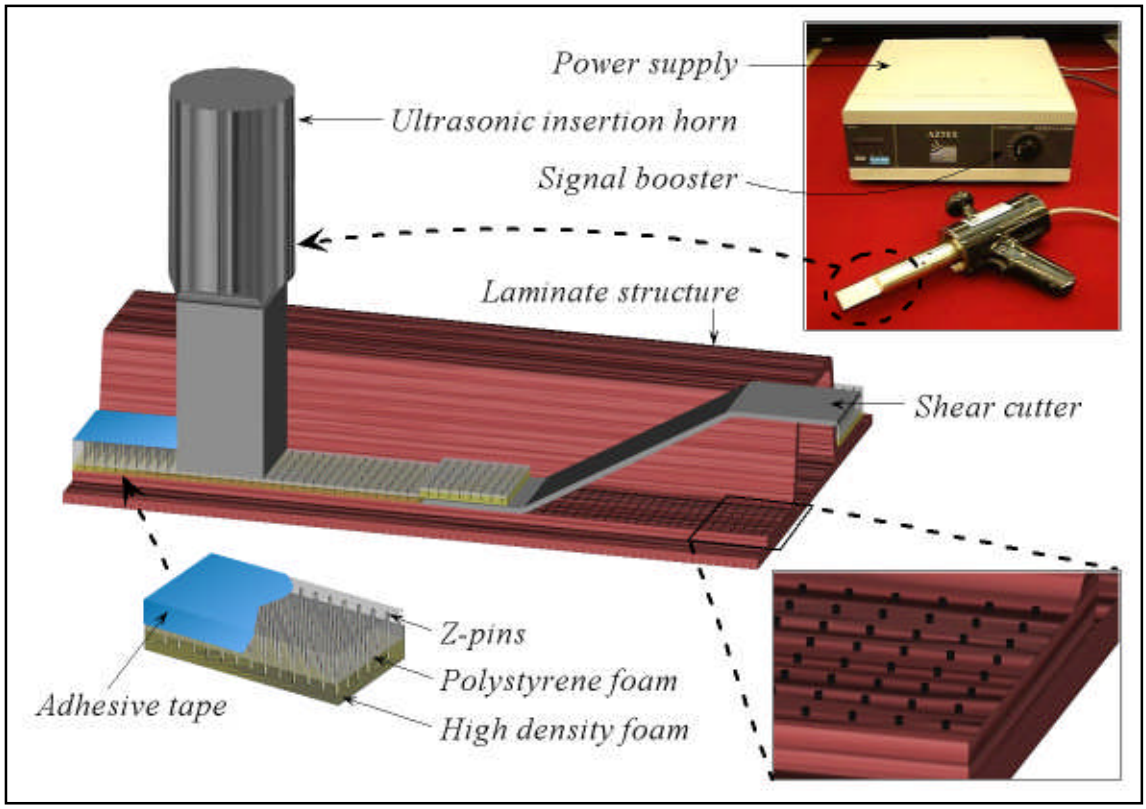

Figure 4.6 – Schematic of the z-pin insertion process (courtesy of D. Cartié)

The combined effect of the ultrasonic excitation and the downward pressure supplied by the operator drives the z-pins into the laminate, crushing the polystyrene support foam in the process. The operator can feel when the z-pins are inserted through the full thickness of the laminate as they hit the metallic plate underneath. Once this happens

any length of z-pin still above the laminate surface on the insertion side is prone to crushing and the operator must take care not to cause undue damage to the z-pins as this can propagate into the inserted length.

Once all z-pins are inserted through the full thickness to the satisfaction of the operator the remaining z-pin length on the insertion side must be trimmed. A blunt shear cutting tool is used to fracture the z-pins flush with the laminated surface; a sharp cutting tool would only catch in the laminate and ruin the surface finish. The Teflon coated fabric and the high density foam of the preform support this process by providing a low friction surface and a stiff foundation support respectively. Care must be taken during the shear cutting process not to misalign the z-pins. If the operator feels that the z-pins are being pushed over and not fracturing as intended then the laminate can be cooled in the freezer so that it stiffens. This is usually required for trimming z-pins inserted into UD laminates.

4.1.4 Operator dependency

Ultimately, operator skill is the major influence behind achieving high quality z-pin insertion. Too much pressure applied during the insertion process causes the z-pins to break by buckling despite the support of the polystyrene foam. Use of lower pressures and lower insertion speed provides enough time for the z-pin to heat up and the laminate to soften due to the ultrasonic excitation; this should allow the z-pins to penetrate with greater ease. Too low a pressure and speed, however, will heat the pins too much without ever inserting them and may burn either the preform or the laminate.

As mentioned previously, z-pins bouncing out of the preform can be minimised through the use of thermo-stable adhesive tape on the preform surface. Sometimes z-pins can bounce out of the boundaries between the small square section being inserted and the remaining bulk of the un-inserted preform because the adhesive tape cannot cover the new sides being formed each time. The most effective way around this is to partially insert all the small square sections first before finishing them off to full insertion in a second pass of the ultrasonic horn. This way each and every z-pin will be anchored in

the laminate ensuring the full quota of z-pin reinforcement. If this is to be done then the second pass of the ultrasonic horn should not be left for too long after the first. In some cases, after the heating under ultrasonic excitation and then the natural cooling down, the z-pins can adhere to the laminate making re-insertion extremely difficult.

The criterion by which the insertion of z-pins is deemed complete is dependent on the operator, there is no standard set. Insertion is considered by some to be complete when the bottom surface of the laminate is marked. Others consider complete insertion to be when the insertion end of the z-pins is seen to be crushed on the underside of the laminate. This is of course dependent on whether the underside of the laminate can be seen which it cannot if the laminate is on a mould tool for example. These two different considerations for complete insertion alone ultimately affect the mechanical performance of z-pin reinforcement.

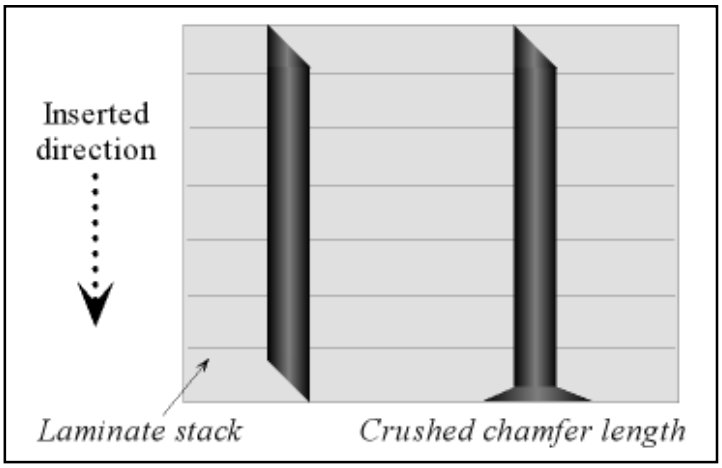

Figure 4.7 – Two types of 'complete' z-pin insertion

If the z-pin is inserted until the chamfer on the insertion end is crushed then the z-pin behaves more like a rivet if the laminate is subjected to an opening mode of loading. Z-pins inserted only until the underside of the laminate becomes marked will provide less resistance to pull-out. This effect was first reported by [3]. For this work the author's criterion for complete insertion was when crushing of the insertion end of the z-pins could be observed on the underside of the laminate.

Whilst the factors described so far are under the control of the operator to some degree there are a few factors affecting insertion which are not. These mainly relate to environmental conditions such as laboratory temperature and air humidity.

4.2 Crash tubes

Hollow carbon fibre / epoxy crash tubes were manufactured to test the effect of z-pins on specific energy absorption. The material used for the crash tubes was Cycom 977-6 / 6K8H / T800 which has a zero-ninety degree weave architecture. The crash tubes were formed by wrapping the pre-preg plies around an aluminium mandrel until the desired tube wall thickness had been achieved. All plies were laid down in the same orientation with the warp yarns aligned with the longitudinal axis of the mandrel to give a $(0/90°)_n$ lay-up.

Firstly, 425 mm long by 145 mm wide plies were cut from the 977-6 woven pre-preg material roll ready to be laid up. The mandrel used was a two-part aluminium mould tool with an external diameter of 42 mm. The mandrel was coated with a thin release film prior to the laying on of plies to assist removal of the mandrel from the final part. The use of a release film was preferred over a liquid release method (such as Chemlease PMR 90 release agent) for coating the mandrel due to the high amount of tool handling required. The release film provides a more robust solution.

The innermost ply of the crash tube was laid onto the mandrel first. The plies were fully defrosted after removal from the freezer but were still cold which allowed them to be removed and re-positioned if laid down incorrectly (the warmer the material the more tacky it becomes and the harder it is to remove and re-position). The mandrel centreline was aligned with the longest edge of the ply and then rolled slowly, with firm downward pressure applied by hand to ensure good contact, until fully wrapped. The major consideration during this process was to ensure as tight a wrap of the material around the mandrel as possible. This was essential to avoid wrinkling of the plies during consolidation (see Figure 4.11). The trailing edge of material was trimmed to give a butt join with the initially aligned edge.

Subsequent plies were laid down in exactly the same manner but offset slightly to ensure that the butt joins never coincided to create weak regions in the finished part. If the tube was to have a total of 12 plies, for example, then the tube was rotated 30° (360 / 12) before laying down each ply.

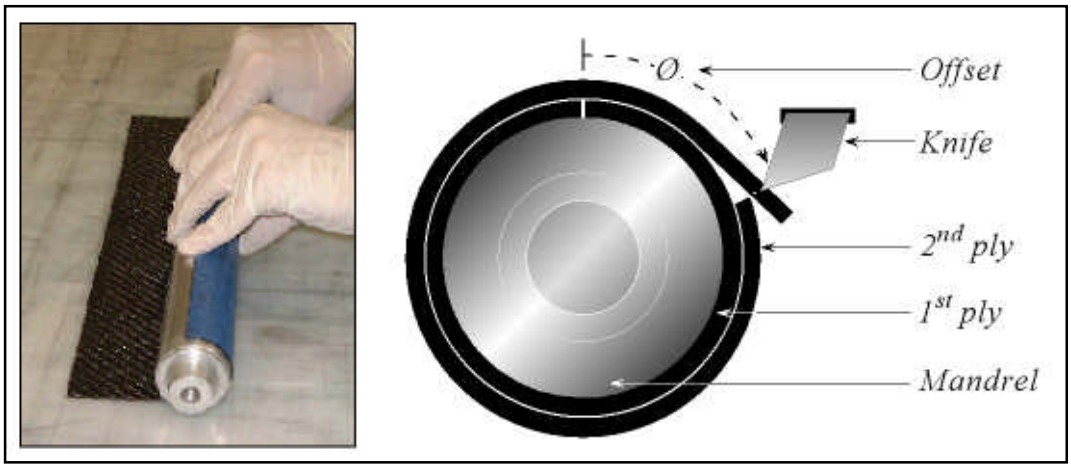

Figure 4.8 – Laying down the first ply (left) and butt joining of plies (right)

After every two or three plies laid down a de-bulking procedure was performed to remove any trapped air from within the plies and to improve compaction. If de-bulking is left until all the plies have been laid down then porosity of the finished tube is higher and the effect of numerous loose plies makes wrinkling a far greater problem. In order to frequently de-bulk the plies, the tube was placed inside a tubular vacuum bag, one end of which was sealed whilst the other was connected to a vacuum pump. The vacuum pump was left to run for 15 minutes after which the tube was removed from the vacuum bag and the next plies were added.

For the specimens to be reinforced with z-pins the insertion was carried out before cure with the tube still on the mandrel. The z-pins were inserted through the full tube wall thickness. Extreme care was taken whilst doing this so as to avoid damaging the aluminium mandrel by pushing too hard for too long with the ultrasonic gun on the z-pins causing them to indent the mandrel. Z-pinning of curved surfaces is not straightforward due to the preform not being flexible. The z-pin preform was cut into several 10 mm wide strips, which were then placed around the tube outer surface. One

zone was reinforced with z-pins per tube, from which two specimens would be cut. Figure 4.9 shows the z-pin reinforcement of the tubes.

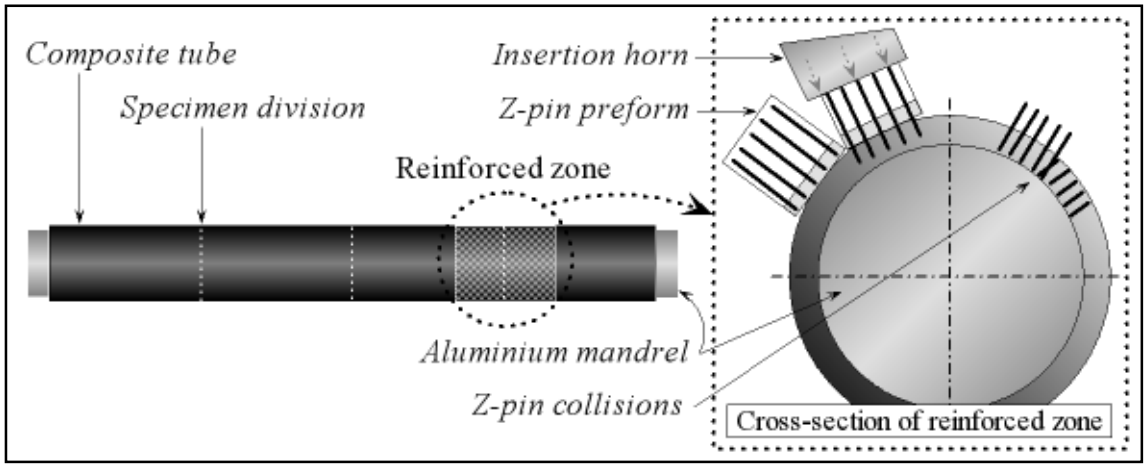

Figure 4.9 – Z-pin insertion of composite tubes on tooling

This method was by far the most convenient for inserting z-pins into the tubular structure. The orientation of the z-pins however is not consistent around the circumference. Individual z-pins will not all point to the centre of the tube and additionally there is likely to be collisions or crossing of z-pins close to the inner surface of the tube.

Figure 4.10 – Shrink tape application for consolidation during oven cure

Once z-pin insertion was complete, the specimen was wrapped in a sheet of release film and wound with heat shrink tape as shown in Figure 4.10. Although pre-preg structures conventionally require an autoclave to provide pressure and temperature when curing, this is not pre-requisite. The use of heat shrink tape, which contracts when heated and

applies the pressure necessary for consolidation, was preferred in this case to avoid the wrinkling effects that an autoclave vacuum bag would produce. Also, a curved, rigid tool would have had to be used around the outside of the tube to protect the vacuum bag from being pierced by the z-pins, this would have been difficult and expensive to accommodate. Furthermore, the tube would have had to be laid flat on its side in the autoclave which is undesirable as this could cause a 'flat spot' when pressure is applied. Two passes of heat shrink tape were wound on in a helical pattern. The doubling up of the heat shrink tape was found to be necessary to control the resin flow during the cure and improve the surface finish.

The prepared tube was placed standing upright in an oven to ensure that all areas were heated evenly. The part was cured according to the material manufacturer's recommended cure cycle as detailed in Chapter 3. Once cured, the heat shrink tape and the release film were removed. The tube, still on the mandrel, was placed in the freezer to cool to -20 °C. At this temperature the aluminium mandrel contracts enough to allow it to be removed with a few gentle taps.

4.2.1 Quality of manufacture

In total, four tubes were manufactured from which individual test specimens were cut. Tubes consisting of 8 plies, 12 plies and 16 plies were manufactured, however, a second 16 ply tube was also made as the quality of the first attempt was not satisfactory. The manufacture steps described previously were fine-tuned during the entire process as the author's experience and skill level increased. The most challenging aspect of the whole process came in trying to prevent ply wrinkling.

Figure 4.11 shows cross-section images taken from each of the four tubes manufactured. The effect of poor manufacture quality was not predicted to have a large effect on impact performance. This is because the main energy absorbing mechanism was expected to be fragmentation of the composite material. The wrinkled areas contain a higher void content and are zones of high stress concentration when loaded. These two factors would be expected to encourage fragmentation. However, the wrinkled cross-

section can be seen to be far from circular and is also non-consistent along the tube length. This makes calculating the material volume extremely difficult and will lead to an inaccurate value for the specific energy absorption of the material. With this in mind the tube quality was ensured to be as high as possible.

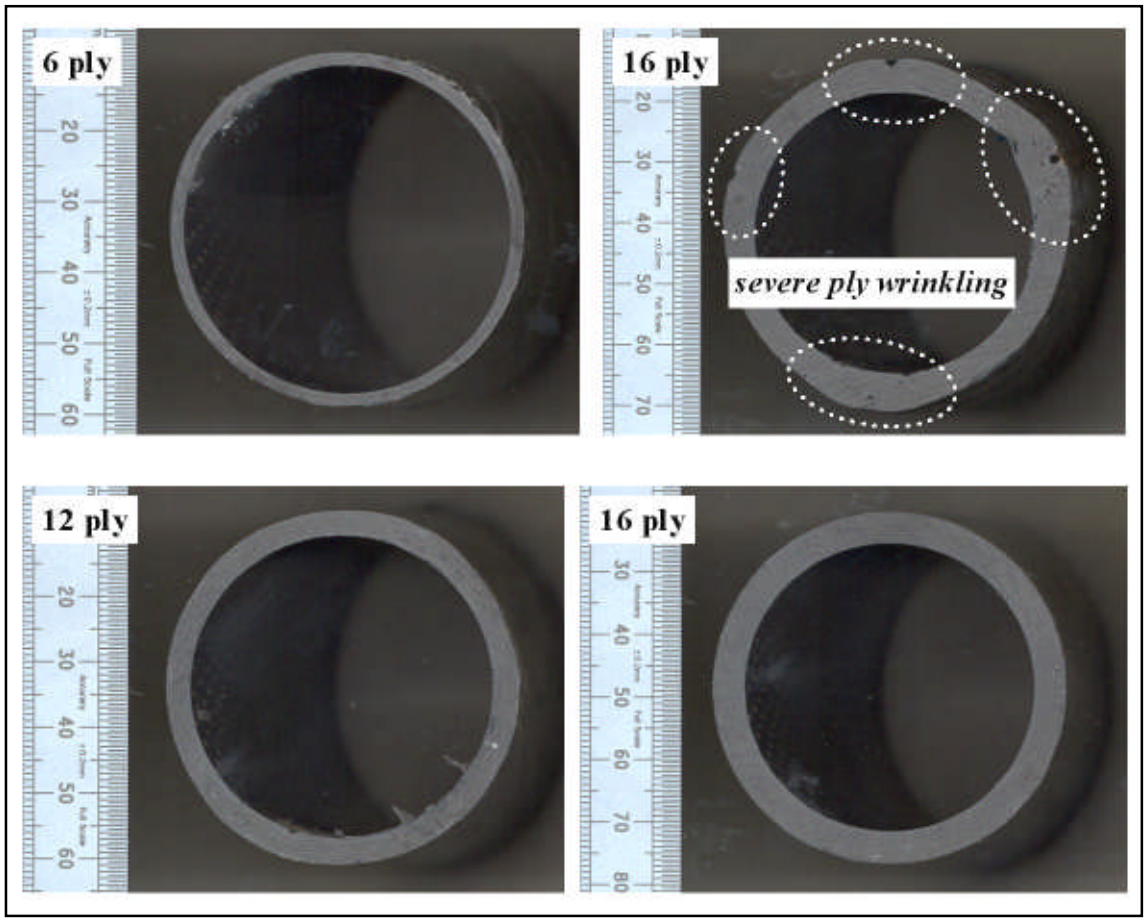

Figure 4.11 – Cross-sections taken from the four manufactured crash tubes

4.2.2 Crash tube test specimen geometry

Each of the four tubes manufactured were cut into four test specimens, two controls and two z-pin reinforced. Figure 4.12 shows the final geometry of the crash tube test specimens. The internal tube diameter was 42 mm as determined by the aluminium mandrel whilst the wall thickness and therefore the external diameter were determined by the number of plies laid down. A 45º chamfer, which acts as a trigger to promote crushing upon impact, was machined on the impact edge of the test specimens.

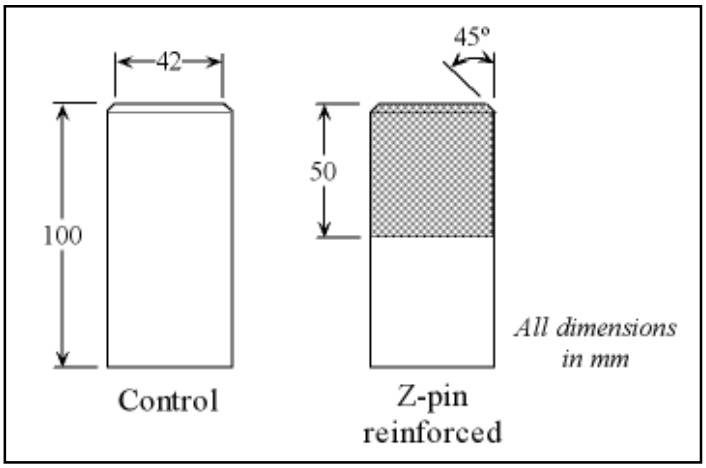

Figure 4.12 – Crash tube test specimen geometry (the shaded region indicates the z-pinned area)

The lay-up for both tube types was $(0/90°)_n$ where *n* signifies the number of plies (either 8, 12 or 16).

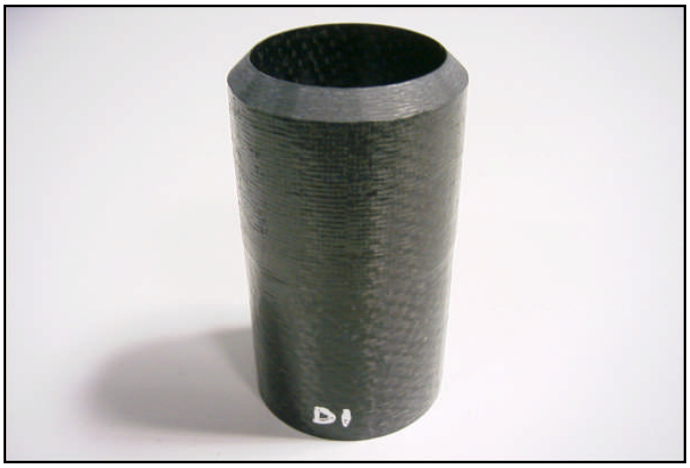

Figure 4.13 – Z-pin reinforced crash tube test specimen ready for testing

4.3 I-sections

The majority of I-section test elements manufactured in this work consisted of two I-sections butt joined and held together by two patches on the outer facing flange surfaces. The remaining test elements, used as controls for comparison, had no join line or patches, just one continuous I-section, with a length equal to the total of the two halves, and similar stacking sequence. An important point to make is that the join line was manufactured into the structure, not machined post cure. All parts of the I-section test element are co-cured. This means that the join line between the two I-section halves is a resin rich connection; however, no reinforcing fibres bridge this line other than those of the patches.

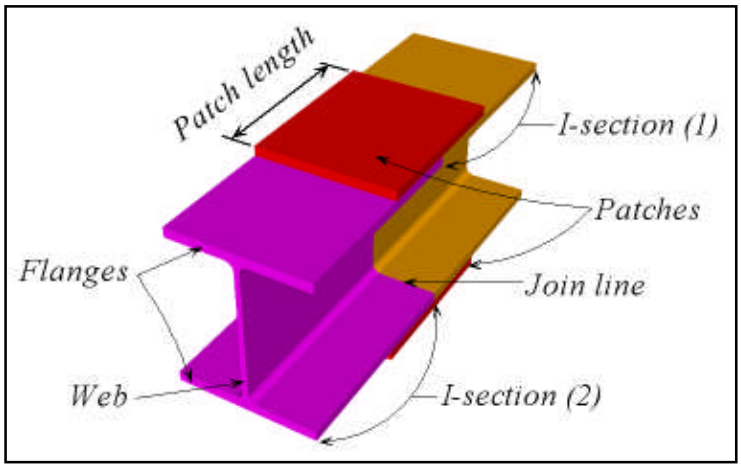

Figure 4.14 – I-section test element terminology

Prior to the bulk of this work, two I-sections were manufactured from off-cuts of woven carbon / epoxy pre-preg (8552 / 986D) to verify a study by [162] which suggested that 2 % areal density of 0.28 mm diameter z-pin reinforcement was the best choice for this type of structural design. For test elements reinforced by z-pinning the z-pins were applied through the patch and into the flange (top and bottom).

In all, three variations of I-section were produced. The first set (Set 1), manufactured from the 914 / 6K5H / T300 material, were mainly used to investigate the effects of patch length on the strength of the joint. The second set (Set 2), also manufactured from the 914 / 6K5H / T300 material with a slightly modified patch design, were used to

investigate the post damage strength. A third and final set (Set 3) were manufactured from the 8552 / 3K8H / HTA material in an attempt to provide additional data on a phenomenon seen in the first two sets, the so called ‘z-pin management of failure mode’ (see Chapter 6).

Quantity	Orientation	Dimensions
4	45° (45/-45)	175 x 105 mm
4	-45° (-45/45)	175 x 105 mm
4	45° (45/-45)	175 x 56 mm
4	-45° (-45/45)	175 x 56 mm
8	90° (90/0)	175 x 56 mm
12	0° (0/90)	Patch length x 56 mm

Table 4-1 – I-section test element material requirement

The I-section test elements were manufactured four at a time. Prior to laying-up all the plies required were cut to size. The material requirement for a single I-section test element is given in Table 4-1. The reference for ply orientation was taken from the longitudinal axes of the test element. The materials used were all contained zero-ninety weave fabrics and the angle stated refers to the warp yarns in all cases.

The I-section test elements were formed on mild steel tooling (tool reference number 45T1085) supplied by Aircelle UK. The tooling was cleaned with acetone ensuring the surfaces were completely smooth before being wrapped tightly in release film. As for the crash tubes, release film was preferred over a liquid chemical release agent due to the high amount of handling the tooling would undergo during the manufacture process.

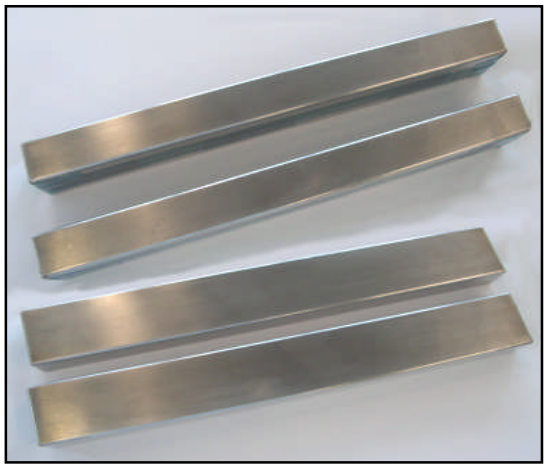

Figure 4.15 – Sets of fully prepared I-section tooling (50.8 x 350.0 x 25.4 mm)

Two C-sections were formed first by wrapping 45° plies (ply 1) around the tooling as shown in Figure 4.16. These were the most quality critical plies and a heated vacuum table was used to make sure the first plies were properly formed over the tooling. Poor forming of the first plies laid down would affect all subsequent plies. -45° plies (ply 2) were laid on next and the C-sections placed back to back. Again the heated vacuum table was used, this time to de-bulk the plies to assist consolidation. Debulking was carried out for 15 minutes at 35 °C.

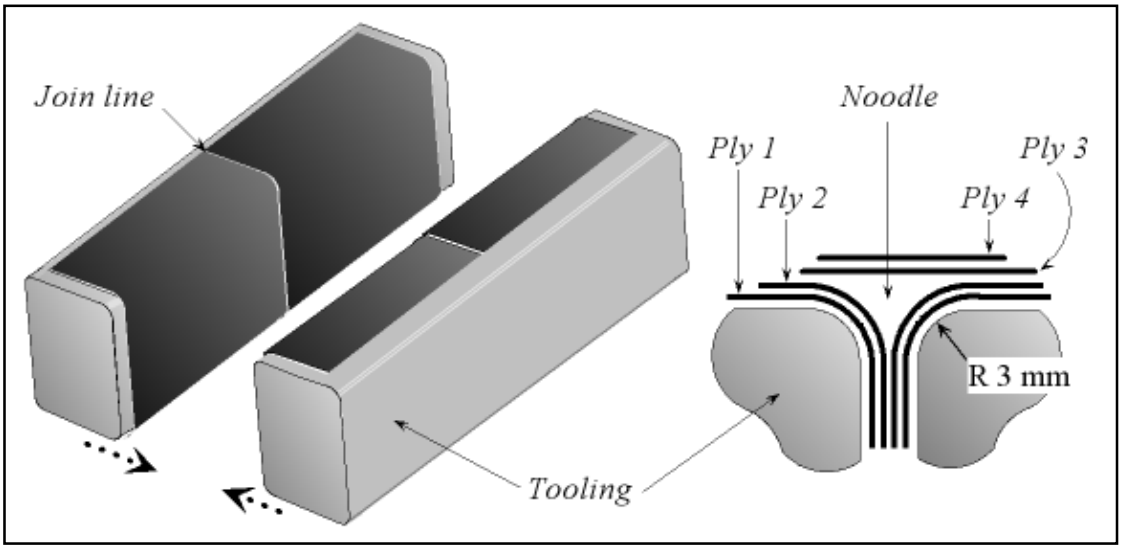

Figure 4.16 – Wrapping plies on I-section tooling and noodle location

When the two C-sections were placed back-to-back two empty regions were formed at the web flange junctions. These regions are known as ‘noodles’. If additional plies are laid straight over the top of an unfilled noodle then consolidation during cure will cause

these plies to sink into the cavity. This is undesirable as it causes fibre misalignment and a poor surface appearance. For I-section test element sets 1 and 2 the noodle was filled with Structil® EA 9685 epoxy filler. The cure parameters of this filler were compatible with the 914 / 6K5H / T300 material. For test element Set 3, six tows of 8552 / 12K / IM7 were twisted together to fill the noodle as these were compatible with the 8552 / 3K8H / HTA material used.

Figure 4.17 – 6 twisted tow bundle in noodle

It would have been preferable to use epoxy filler in both cases as this offers the advantage of being easier to represent in a finite element model. Representing twisted tows of carbon fibre with finite elements is a greater challenge; however, the twisted tow bundle maintains its shape far better than the epoxy and is considered the preferred option from a visual quality perspective. The noodles, epoxy and twisted tow bundle, were moulded by hand at around 35 °C and pressed into the cavity.

Additional -45° and 45° plies (ply 3 and 4 in Figure 4.16) were added to make up the flanges and a further two 90° (ply 5 and 6) plies on top of these. The test element was again de-bulked prior to placing the two 6 ply patches over the join line.

Four patch designs were used in total although they were all fairly similar. Figure 4.18 shows the patch types used. The patches were all geometrically symmetrical and the $(0)_6$ stacking sequence was also common for all types. All patches were positioned with their centreline aligned with the join line. Tapering of plies, as for the Type 3 patch, is

common practice in industry for reducing stress concentrations at laminate edges. This was not done in the majority of cases here as it does not allow for the definition of a single true patch length.

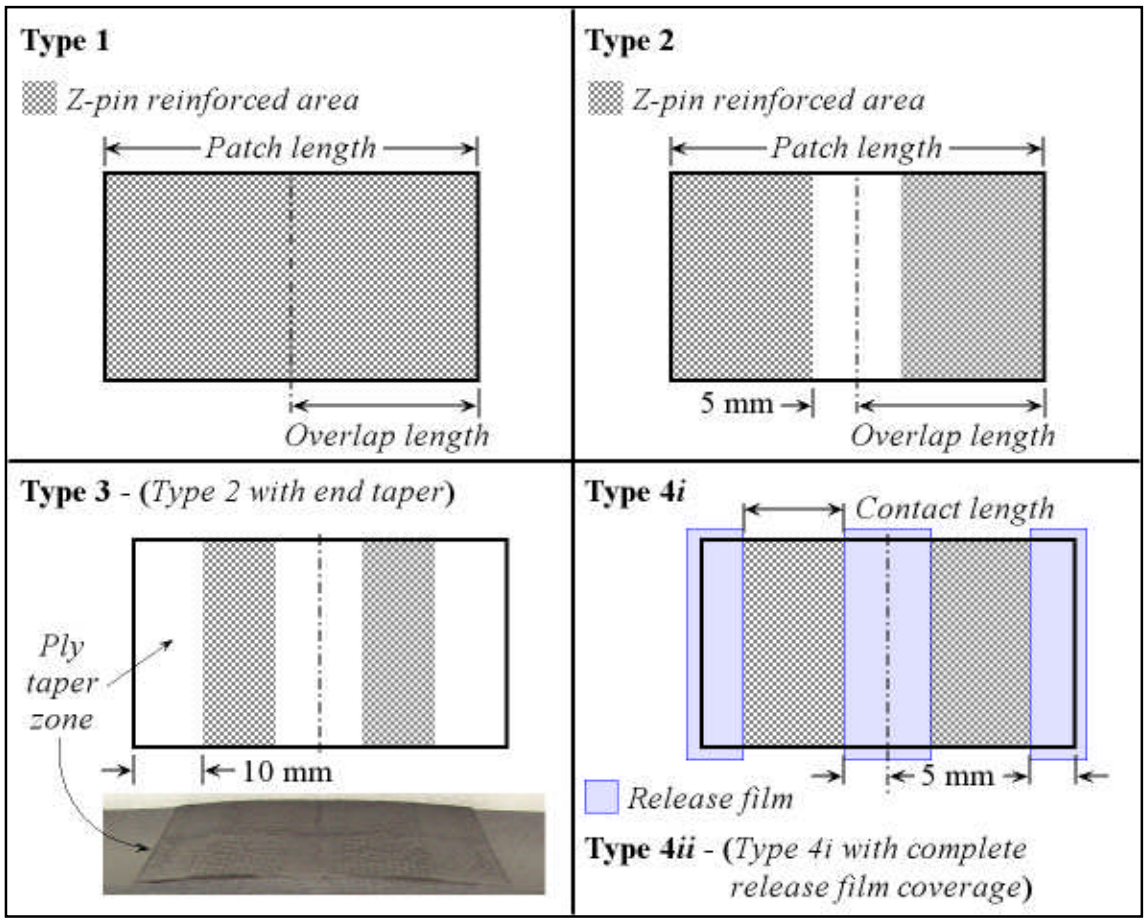

Figure 4.18 – Patch types

The arrangement of z-pin reinforcement was developed continuously. The non z-pinned region shown in Type 2 was intended to allow a delamination to initiate and to grow into the z-pinned region. Type 3 was similar but included tapered edges in an attempt to reduce the stress concentration at those locations. Type 4 was introduced as finite element modelling of the I-section test elements began. Release film was used to make 100 % sure that delamination was present in the patch flange interface. Type 4*ii* allowed the I-section joint to be held together solely by z-pins. Z-pinning through the patches to reinforce the patch-flange interface was carried out in exactly the same way as has been described in Section 4.1.3.2.

Patch	I-section test element	Material system
Type 1	Z-pin verification	8552 / 986D
Type 2	Set 1	914 / 6K5H / T300
Type 3	Set 2	914 / 6K5H / T300
Type 4	Set 3	8552 / 3K8H / HTA

Table 4-2 – Patch types for I-section test element types

Once the manufacture of the I-sections and patches had been completed the I-section test elements were given a final 20 minute debulk at 35 °C to ensure as high a level of consolidation as possible.

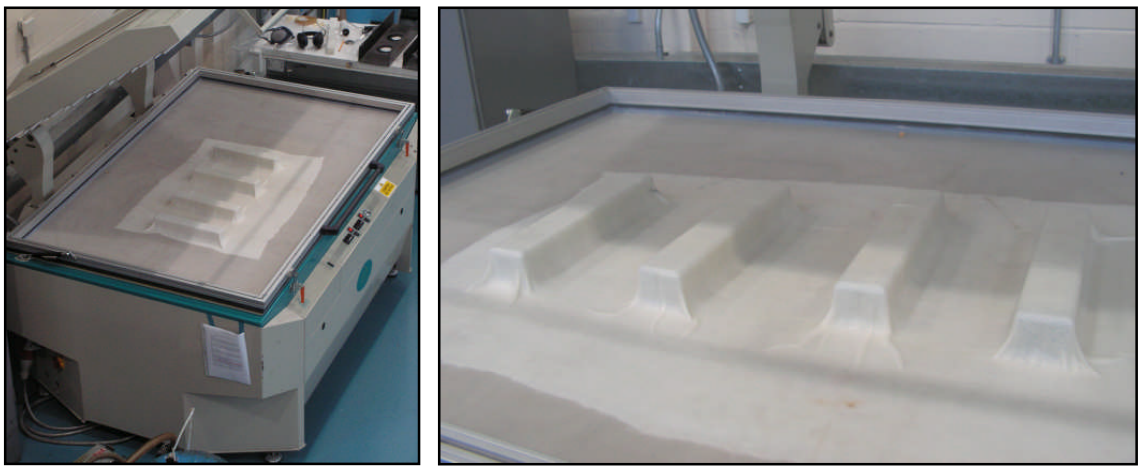

Figure 4.19 – I-section test elements debulking on heated vacuum table

Metallic plates were cut and wrapped in release film to cover the flange surfaces; six plates were required for each section. These plates would act as pressure plates for the autoclave cure process. For the test elements which had z-pin reinforcement of the patch a layer of silicone rubber was placed between the patch laminate surface and the metallic plate. The silicone rubber served to ensure a higher level of consolidation around the laminate around the z-pins; a more detailed reasoning for this is given in Section 4.6.1.2.

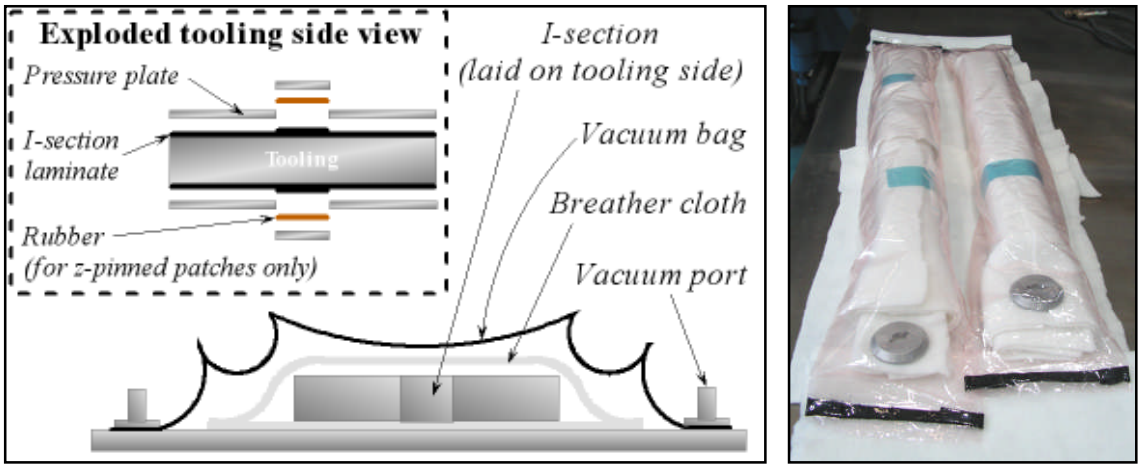

Figure 4.20 – Autoclave over-bag arrangement (right), tubular arrangement (left)

The pressure plates were secured and each test element was individually wrapped with a thick breather cloth. The test elements were vacuum bagged ready for autoclave cure whilst ensuring that each one was placed on its side, not one of the patches, to prevent rocking and to ensure even consolidation. A modified bagging arrangement was made for the Set 3 I-section test elements to save vacuum bagging consumables. Rather than being over-bagged on the autoclave table the test elements were vacuum bagged in a tubular arrangement as shown in Figure 4.20. The cure cycles used for each test element set were exactly as detailed in Chapter 3.

Once cured, and post-cured if required, the test elements were removed from the tooling. Removal of the I-section test elements from the tooling was difficult. The two together had to be cooled to -40 °C in order to shrink the mild steel tooling sufficiently for it to be knocked out. An 8 lb mallet was used to slowly slide the tooling out from the test elements. The tooling was not hit directly. A block of wood was used to prevent damage of the tooling, allowing it to be used repeatedly.

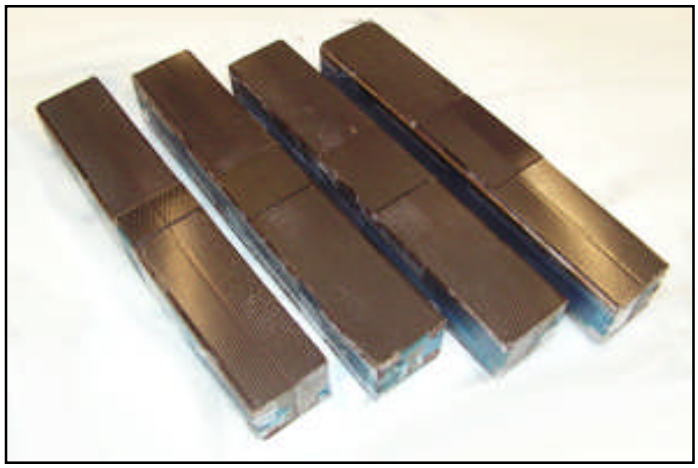

Figure 4.21 – I-section test elements awaiting removal from tooling

4.3.1 I-section test element geometry

Figure 4.22 shows the I-section test element geometry ready for testing along with an exploded detail of the stacking sequence.

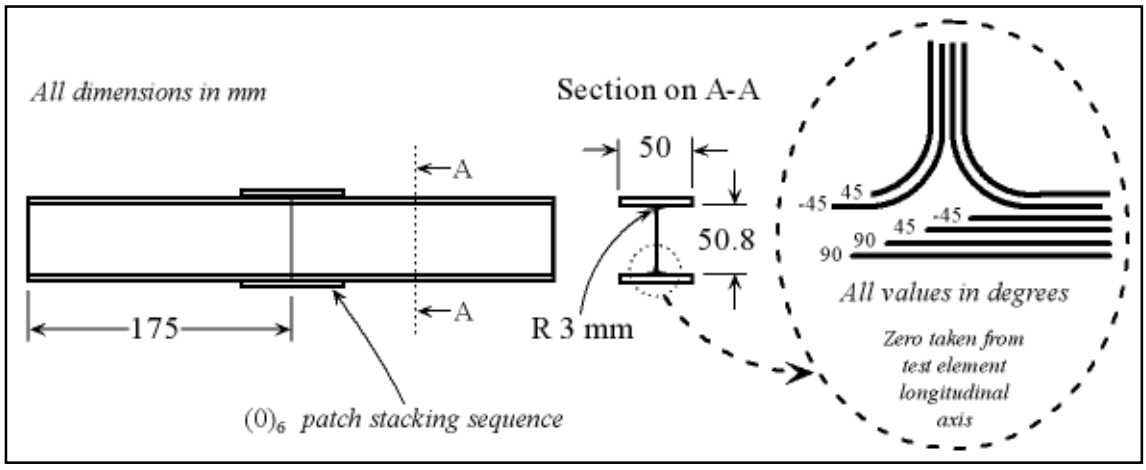

Figure 4.22 – I-section test element geometry

The reader will notice that an undulation in the surface is slightly visible in Figure 4.23 which shows test elements from Set 2. Perhaps the epoxy noodle was not entirely suitable for purpose here and was unable to completely prevent sinking of the upper flange plies. This surface defect was far less pronounced for the Set 4 test elements manufactured with the noodle filled by twisted carbon fibre tows.

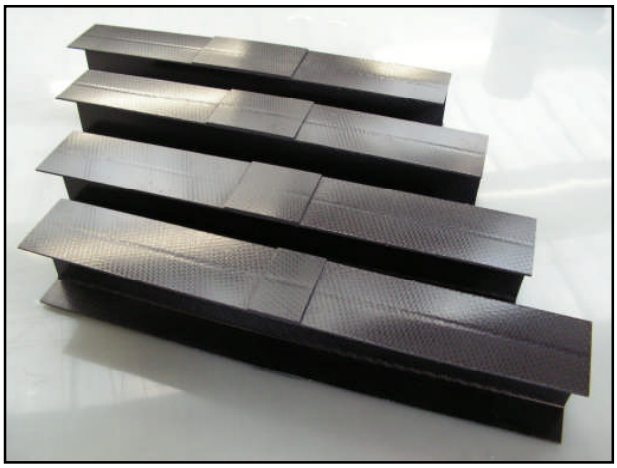

Figure 4.23 – I-section test elements trimmed and ready for testing

4.4 Z-shear specimen manufacture

Shear specimens for testing using Cranfield University's z-shear test jig were manufactured from 913G / UD and 913G / 4H. Three laminates were made in total from which z-pin reinforced specimens would be cut, two with unidirectional glass fibres and one containing the 4H woven fabric. Each specimen was reinforced with 16 z-pins positioned equidistant from each other to assist observation of their deformation under shear loading. Tailor made z-pin preforms were manufactured for this purpose (see Section 4.6.1).

Plies of the UD and woven pre-preg measuring 200 mm x 200 mm were cut and stacked to produce laminates of 8 mm thickness. A release film was included at the mid-plane of each laminate which would become the shear plane for testing. The stacking sequences for each laminate are detailed in Table 4-3. Symmetric stacking sequences were used to prevent warping of the laminates during cure. Debulking was carried out on a vacuum table at room temperature after every five plies were laid. The debulking process was not carried out at an elevated temperature as the 913 resin system was prone to hardening, much more so than any of the other composite pre-preg material systems used in this work.

Material	Plies required for 8 mm thickness	Stacking sequence
913G / UD	60	$(0)30_s$
913G / UD	60	$(90)30_s$
913G / 4H	88	$(0)44_s$

Table 4-3 – Lay-up details for z-shear specimens

Pre-forms containing 0.28 mm and 0.51 mm diameter z-pins were prepared. The 0.51 mm diameter z-pin preform used was modified from a preform supplied previously by Aztex Inc. Individual z-pins were removed from a 2 % areal density to leave the ones remaining at the desired spacing. The 0.28 mm diameter z-pin preform was manufactured solely by the author, the process for which is described in detail in Section 4.6.1. The preforms were made to include an additional row of z-pins in case errors were made in the cutting or polishing processes. If no errors were made the additional pins were discarded in the final trimming process.

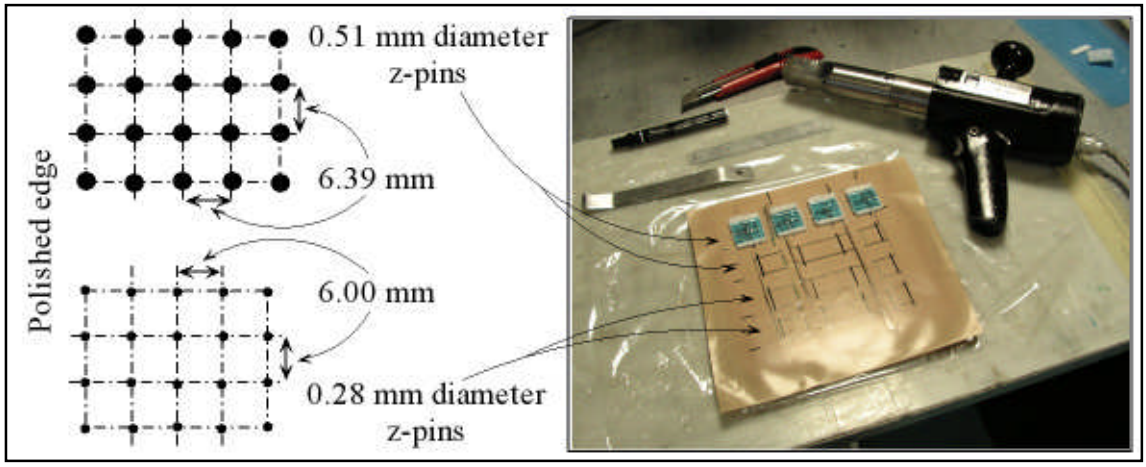

Figure 4.24 – Schematic of tailor-made z-pin preforms and insertion into laminates

The laminates were z-pinned exactly as described in Section 4.1.3.2. For autoclave cure, a rubber membrane was used between the top laminate surface and the pressure plate to improve consolidation around the z-pins. The cure cycle used was as detailed in Chapter 3.

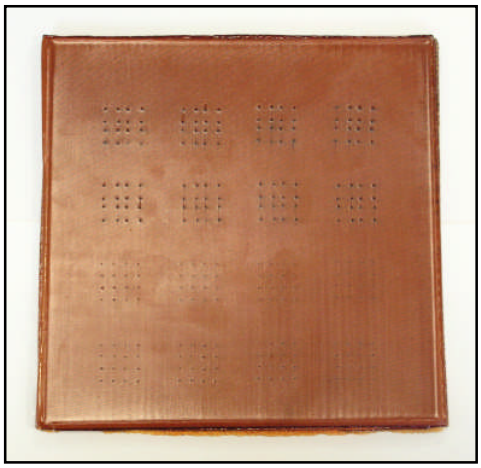

Figure 4.25 – Cured UD laminate containing z-pins for z-shear test specimens (200 x 200 mm)

The z-shear specimens were rough cut from the cured laminates. In order to visualise the z-pins in the laminate, the front edge of the specimen needed to be polished very finely. Wet polishing equipment was used to achieve the surface quality required. Abrasive polishing papers from 120 up to 4000 grit were used to slowly and systematically remove scratches and gradually remove the laminate material to get as close to the leading row of z-pins as possible. The reader will notice (see Figure 4.27) that the z-pin alignment was most often non-perpendicular, adding complexity to the polishing process. All polishing was required to be done by hand rather than using automatic polishing machine cycles. A final polish using a colloidal silica (0.5 μm) solution was completed to give the specimen edges a glass-like finish.

Figure 4.26 – Polishing equipment at Cranfield University

With the polished edge completed the three remaining edges of the specimen were trimmed, taking the polished edge as a reference. The reader will notice from Figure 4.27 the acute angles at which the specimens were polished at in order to find the z-pins. This gives an indication of the misalignment of the z-pins themselves from the desired perpendicular orientation. The reasons for this are discussed in Section 4.6.1.2.

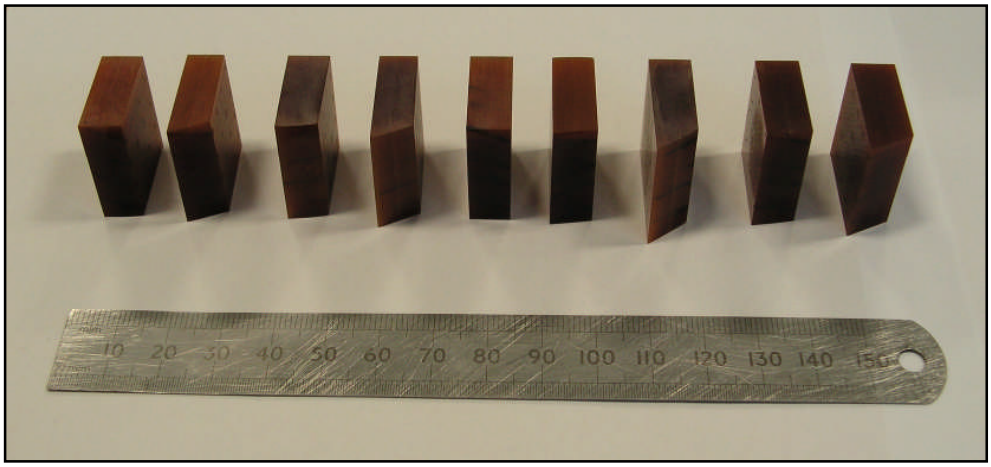

Figure 4.27 – Polished and trimmed z-shear specimens

4.4.1 Z-shear specimen geometry

Figure 4.28 shows the geometry for the z-shear test specimens. Good polishing of the laminate edges makes the z-pins easily visible. Z-pins in the leading row do not always have the same orientation; some disappear back into the specimen as the image shows.

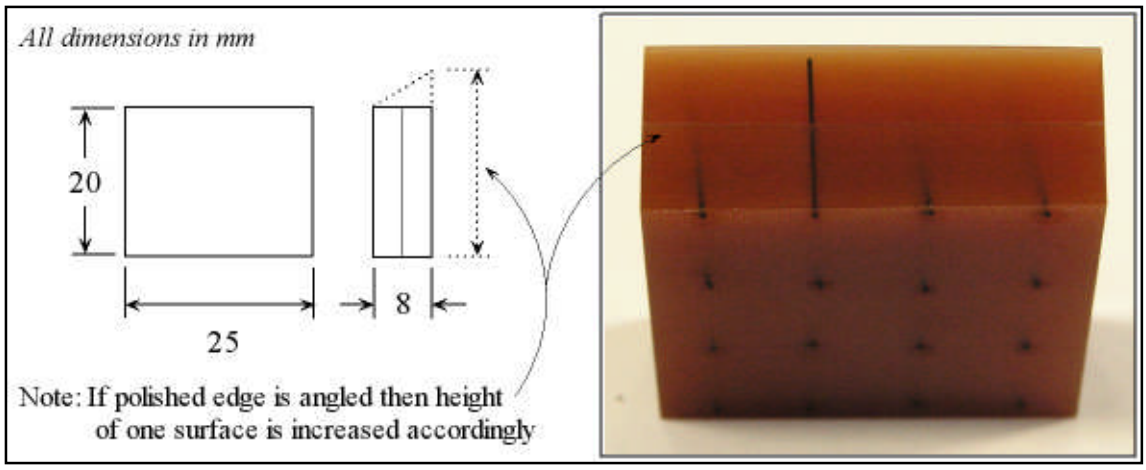

Figure 4.28 – Z-shear test specimen geometry

4.5 ELS coupon manufacture

End loaded split (ELS) test coupons were manufactured from the 914 / 6K5H / T300 and 8552 / 3K8H / HTA material systems. One panel measuring 200 mm x 600 mm was made from each material from which the coupons required were cut. The nominal thickness required for the coupons was 4 mm and, for each material, the corresponding number of plies needed to achieve this thickness were laid down. The number of plies needed was determined by consolidating ten plies together and taking accurate thickness measurements. The panel was made in two halves which were then placed back to back. A thin, 13 μm insert film was laid between the two halves to act as a crack starter at the mid-thickness interface which would be propagated during the ELS test. Debulking was carried out on a heated vacuum table (15 minutes at 35 °C) after every 4 plies were laid down and finally once the stack was complete with insert film (25 minutes at 35 °C).

Material	Plies required for 4 mm thickness	Stacking sequence
914 / 6K5H / T300	14	$(0)7_s$
8552 / 3K8H / HTA	12	$(0)6_s$

Table 4-4 – Lay-up details for ELS coupons

The lay-up was symmetric so as to ensure the panels would not warp during cure. For the stacking sequence given in Table 4-4, the orientation is given for the fabric warp yarns. The stacking sequence used produced an interface with the predominant fibres on each delamination surface aligned at a 90° to the coupon longitudinal axis. This was specifically designed to match the local fibre orientation at the patch-flange interface of the I-section test elements.

A region on each panel was reinforced with z-pins from which the z-pin reinforced coupons would be cut. An areal density of 2 %, 0.28 mm diameter, z-pins at were used for all z-pin reinforced ELS coupons. Figure 4.29 shows the layout of the panels, identical for the two material systems, from which ELS coupons were cut.

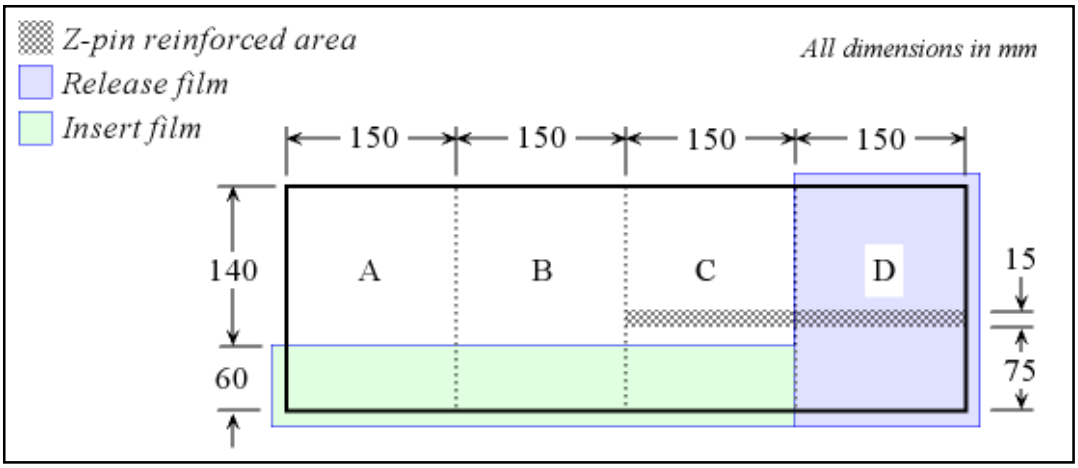

Figure 4.29 – Panel layout for ELS coupon requirements

Zones marked A to D on the panel are for spare, control, z-pin reinforced and z-pin only type ELS coupons respectively.

Due to the presence of z-pins, a layer of rubber was placed between the top of the laminate and the pressure plate to improve consolidation in the vicinity of the z-pin reinforcement during cure (see Section 4.6.1.2). The two panels were cured separately according to the manufacturer's recommended cure cycle for each material, detailed in Chapter 3.

Cured z-pin reinforced coupons still had the z-pin heads protruding from the top surface of the laminate. These were ground down flush with the laminate surface using an abrasive cloth prior to specimen cutting. End tabs, developed specifically for the ELS test, were bonded to the bottom surface of each coupon with Araldite® 420 adhesive at the insert film end.

4.5.1 ELS coupon geometry

The following diagram shows the geometry of the ELS coupons manufactured for testing. Also shown are the designations for measured parameters on which the test method and subsequent analysis rely.

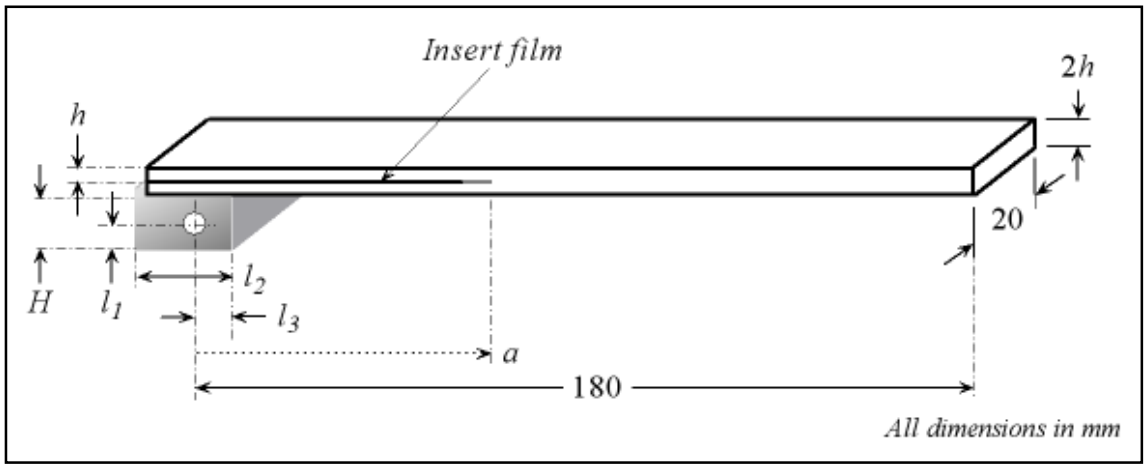

Figure 4.30 – ELS test coupon geometry

4.6 Commissioning of the Cranfield University robot

The acquisition of a six axis robotic arm and supply of a custom built insertion head by Aztex Inc. in 2002 allowed us to manufacture z-pin preform and pin reinforced core constructions, purely for academic research. The robotic arm is a Kawasaki FS020.

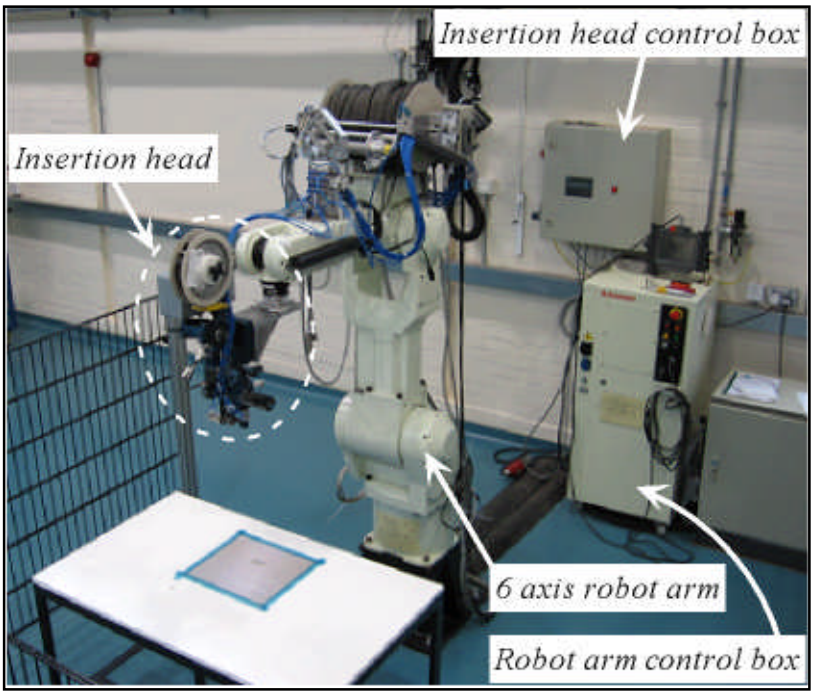

Figure 4.31 – Cranfield University's robotic insertion facility

The author has been responsible for all of the soft programming of this facility and was involved in problem solving regarding the electronic control systems. AS language code was used for programming and this was interfaced through a stand-alone, dedicated desktop PC. The programs were written to allow inexperienced users to quickly set the preform or core parameters and to manufacture them safely. Much of the code therefore includes print commands to give instruction to the operator.

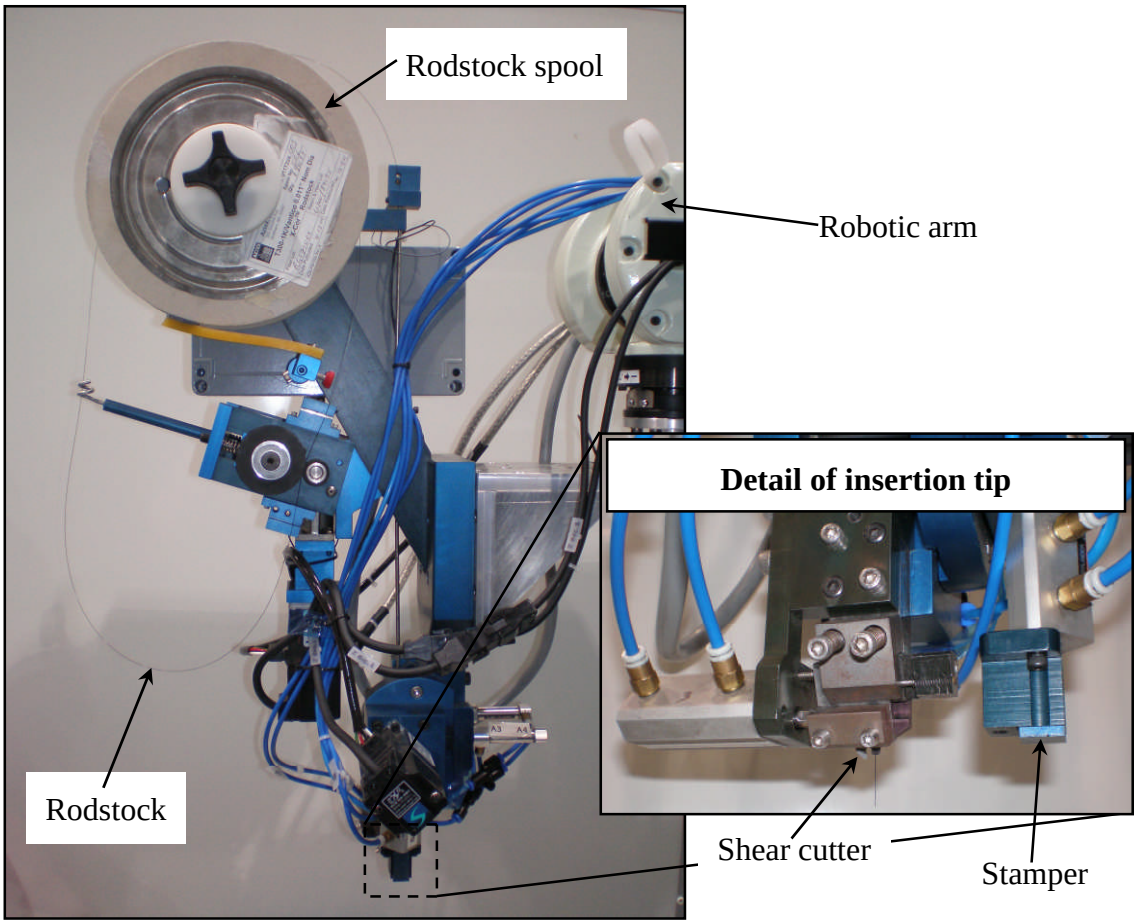

Figure 4.32 – The insertion head in detail

4.6.1 Z-pin preform manufacture

The general manufacture procedure used was identical to the one used by Albany Int. as described in Section 4.1.1. The materials used for the manufacture of z-pin preforms are as detailed in Chapter 3. Foam and rodstock spools were supplied by Albany Int. The z-pin preforms required for the ELS test coupons, z-shear specimens and 80 % of I-section test elements were manufactured using this facility.

This section concentrates on the key development areas of the program code which was used to manufacture z-pin preform using the robotic insertion facility. The program code written for z-pin preform manufacture is included in Appendix A.

The inserted length of rodstock is controlled by the wall mounted insertion head control box. It was possible to store settings for 15 different lengths in the insertion head control box for use at different times during the same manufacture run, if required. For preform manufacture however, only one z-pin length is required and so the program code calls the same setting each time. The length settings required manual input by the operator.

The program code was developed continuously, command functions were refined to improve the efficiency of the instructions given to the control system. Programs were improved to receive feedback from the insertion head as to its current state. This became particularly important as problems with the rodstock quality began to appear (see Section 4.6.3). Frequent breakages led to continuous stopping and re-starting of the manufacture. Feedback on the insertion head state allowed the program to recognise when a problem had occurred. The program would then pause itself automatically and the operator was instructed to rectify the problem prior to re-starting. This eliminated the need for continuous monitoring of the process, saving time.

One important modification to the program which had a significant impact on preform quality was a switch from displacement control command to a coordinate based control method. The displacement control method, used initially, moved the current insertion point to the next by instructing the robot to move a distance specified by the operator. This method was reasonably successful but the major drawback was the issue of compound errors. If the displacement error in moving between adjacent insertion points was 0.2 mm for example then the total error at the end of a row containing 100 z-pins would be 100 times greater. In reality the displacement error between adjacent pins was never as high as this but 2 - 3 mm errors were measured in rows containing around 65 z-pins using this method. The switch to coordinate control removed the compound error problem and opened up the possibility for easier manufacture of preforms with z-pin arrangements other than the standard square array. The program was re-written to continually generate the next insertion coordinate, after the current insertion had been completed, by using the pin to pin spacing, in both the X and Y axes, input by the

operator. The program did only produce square or rectangular z-pin arrays, however, as there was no requirement for an alternative at the time.

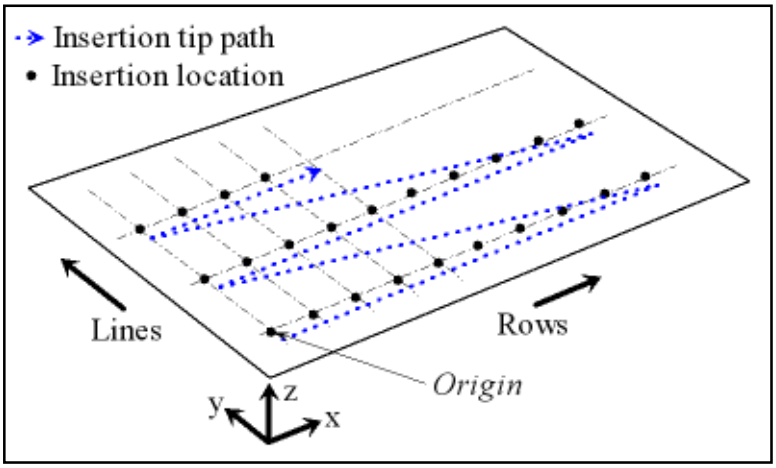

Figure 4.33 – Motion path for z-pin preform manufacture

Figure 4.33 shows the motion path that the program drives the robotic arm to take in order to complete a z-pin preform. The operator is only required to move the robotic arm manually once, in order to set an origin (insertion point for the first z-pin) from which all other z-pin insertion locations are determined. The height of the insertion head (z axis) needs to be set by the operator so that the bottom of the stamper is slightly above the foam surface. If the insertion head is set too low then the stamper hits the foam surface. The compressed air which drives the stamper has sufficient force to push the entire insertion head and robotic arm upwards. Surprisingly, this physical moving of the robotic arm requires less force than is required to locally crush the foam block and therefore positioning errors can occur. There was no way of feeding back the current location coordinates to the program for correction if necessary, so any unwanted adjustment to positioning by external forces affected all subsequent z-pin insertions. The setting of the stamper height was therefore critical to producing good quality preforms. Setting the stamper too high resulted in the z-pins not being pushed down flush with the foam surface once inserted and cut. This was far less of a problem but required the z-pins to be pushed down flush later by hand.

The program was designed to store the origin location in the computer memory, so that it could be recalled if required, and also made use of loop commands to count the

number of rows and lines. When the program needed to be stopped, more often than not due to rodstock breakage, manufacture could be resumed from the last known satisfactory insertion location. This offered far greater benefit than having to reassign a new origin, recalculate the remaining insertion area and, in effect, complete the preform by joining two manufacture runs together. The operator was prompted to input the number of rows and number of lines for the last satisfactory insertion. From this the manufacture could be resumed by calculating the insertion coordinate for manufacture restart using the stored origin coordinate and the x and y pin-to-pin spacings.

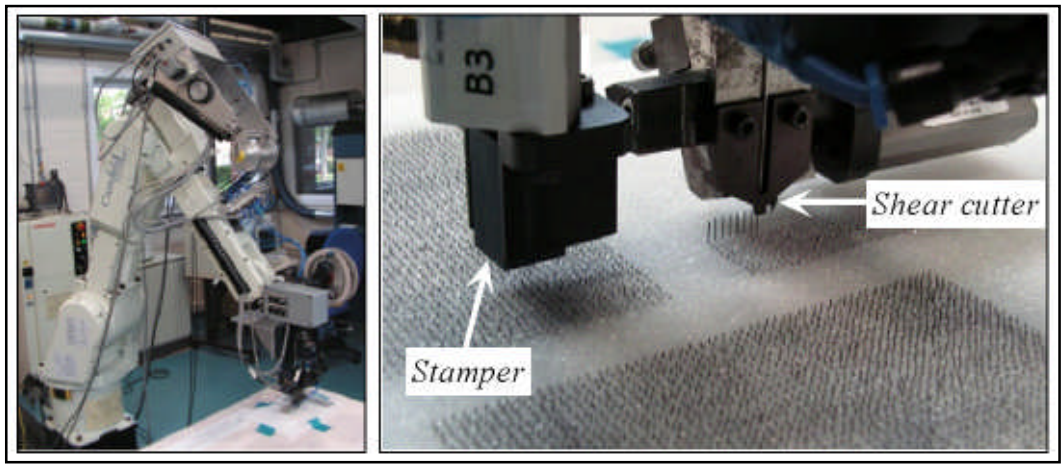

Figure 4.34 – Z-pin preforms being manufactured using Cranfield University's robotic facility

4.6.1.1 Preform quality control

The quality control of the finished z-pin preforms manufactured as part of this work and those manufactured commercially by Albany Int. checks the pin-to-pin spacing, pin length, and pin orientation. A 3° from perpendicular angle is the acceptable limit for z-pins in the finished preform. The pins are also checked using a simple comparison method for their alignment relative to each other.

4.6.1.2 Post cure z-pinning quality and misalignment

Throughout z-pin preform manufacture work and subsequent insertion into laminates the focus was to achieve as near perpendicular insertion of z-pins as possible. The use of a silicone rubber material (Mosite 1495 high strength silicone rubber, 2mm thickness)

between laminate surfaces and pressure plates over z-pinned regions has been mentioned several times in this chapter. The first reason this was done was to improve the consolidation of the laminate around the z-pins. It was impossible to trim the z-pins to a length equal to the final laminate thickness using the method described in Section 4.1.3.2. This meant that, if the z-pins held their orientation during cure, they acted against the laminate consolidation. The silicone rubber was used allowing the z-pin heads to protrude from the laminate surface. The laminate was therefore allowed to consolidate as it should if no z-pins were present.

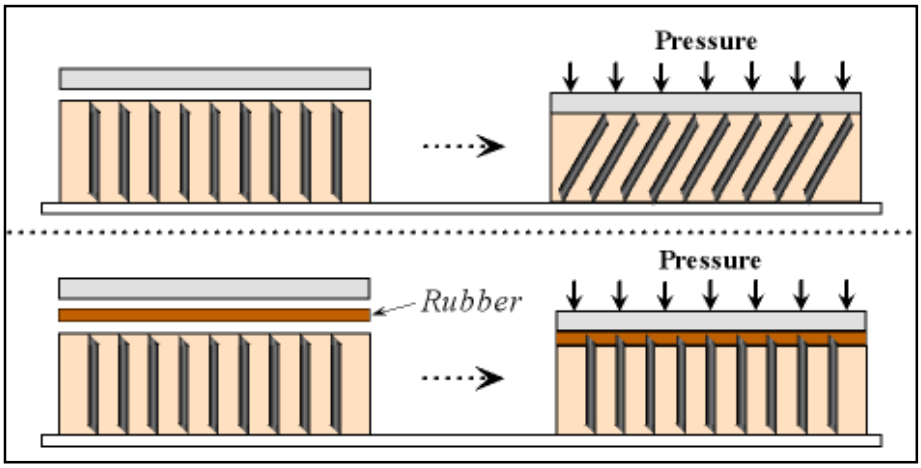

Figure 4.35 – Consolidation of laminate around z-pins

The second function of the silicone rubber was to reduce misalignment of the z-pins themselves. If the pressure plate was left in direct contact with the z-pins during the cure process then the high autoclave pressure, acting to compress the laminate, coupled with the softening of the resin system, as temperature increases, would cause one of two things. Either the z-pins would fail due to buckling or they would be forced to re-orientate by leaning over. In all cases of z-pin misalignment observed by the author the second of these possibilities was the outcome. Figure 4.36 shows z-shear specimens which were polished on one edge close the leading row of z-pins. Looking at this polished edge from the side, the orientation of the pins can be seen. There is a considerable range of orientations even amongst the small number of samples shown here. The author concludes that the single layer of silicone rubber used, whilst useful, was possibly not entirely sufficient.

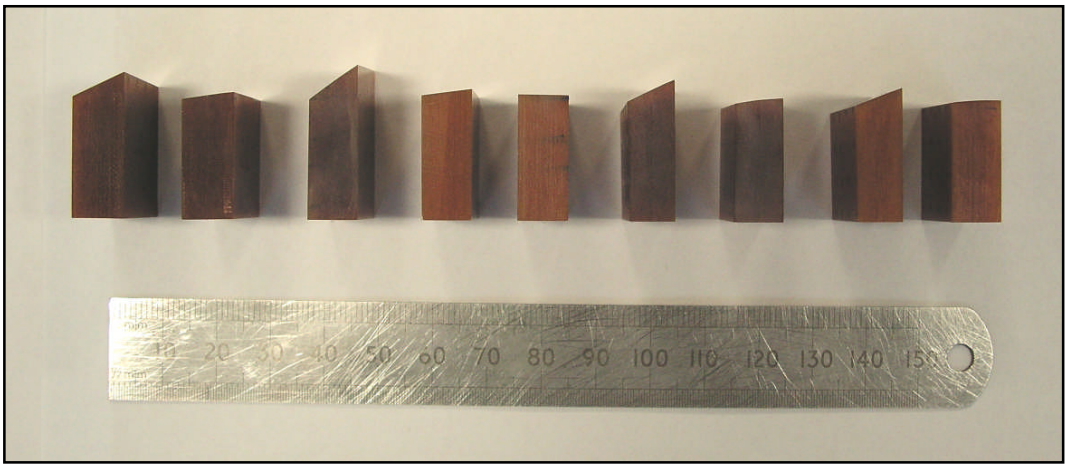

Figure 4.36 – Misalignment of z-pins during cure

Furthermore, the issue of misalignment starts well before use is made of any rubber materials during cure preparation. The z-pins are manufactured with a 45º chamfer angle as first pointed out in Chapter 3. This chamfer angle causes the z-pins to deviate from their desired path during insertion, during both insertion into foam preforms and final insertion into laminate. Effectively, z-pin misalignment starts from the moment the z-pin leaves the insertion head. From the author's own work and experience this 'diving' problem is greater for the smaller diameter z-pins. To prevent this would be quite simple in theory. The z-pin would need to be cut with a pointed, pencil tip like insertion head instead of being shear cut at 45º (see Figure 4.37). Manufacturing wise this is a big challenge. Furthermore, if the point of contact with the insertion horn was in line with the centre axis of the z-pin, instead of being offset to one side, this would increase the likelihood that the pin travels in a direction perpendicular to the laminate. The proposed modification would achieve this.

What Albany Int. has implemented in some instances is to start insertion of the rodstock at a shallower angle than required and utilise the diving effect to leave the pin at the final desired orientation. This is clever but would almost certainly leave the final z-pin not straight and is simply not possible to do with ultrasonic insertion of z-pins into laminates.

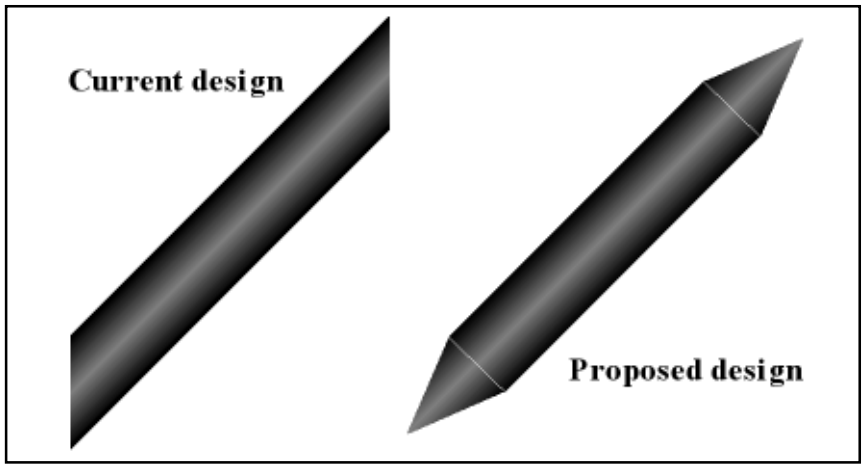

Figure 4.37 – Z-pin modification as a solution for 'diving' problem

The equivalent problem of misalignment also presents itself in the manufacture of pin reinforced cores. The current pin design causes the pins to deviate from the desired path as they are inserted through the foam block in the same way as occurs for z-pin preforms. The result is a marked difference in pin appearance on the non-insertion surface from what is carefully controlled on the insertion side.

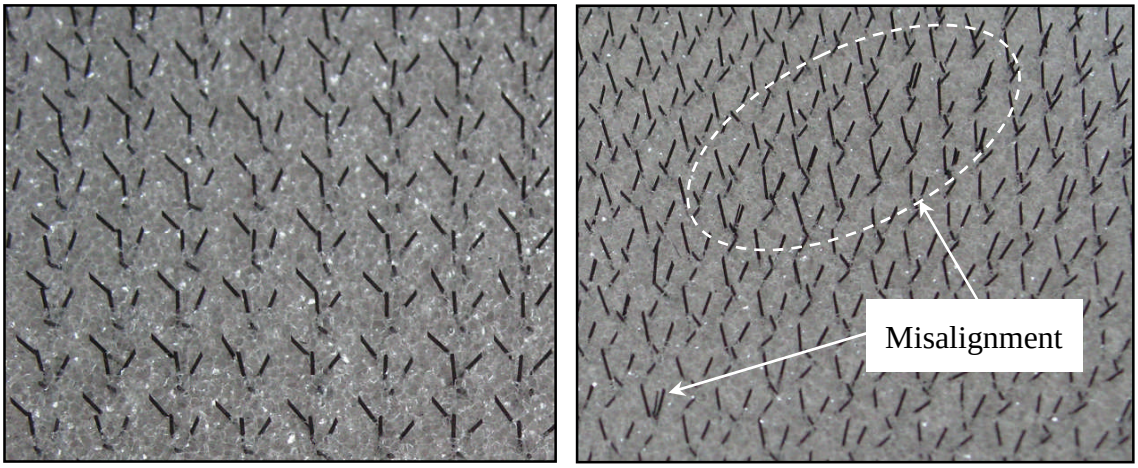

Figure 4.38 – Pin misalignment observed for pin reinforced cores (insertion side left, non insertion side right)

Z-pin misalignment does not always need to have negative effects on mechanical performance. In some cases misaligned z-pins can offer mechanical benefits, such as if the z-pin reinforced laminate is loaded to pull-out or shear against the misalignment angle for example. However, with limited control over final z-pin orientation production

of consistent repeatable test elements to check out such effects experimentally is likely to prove difficult.

4.6.2 Pin reinforced core manufacture

The author is reluctant to refer to these pin reinforced cores as X-Cor™ and K-Cor™. These products are manufactured by Albany Int. to a much higher tolerance than the author has been able to achieve as yet using the robotic facility. Additionally, these products are patented. That being said, the pin reinforced cores produced by the author follow the same manufacture route as is used for X-Cor™ and K-Cor™ and use identical materials. The pin reinforced cores manufactured by the author were not used for any testing in this work. They are detailed here because the experience gained in their manufacture will direct much of the future discussion for further work and development.

Pin reinforced cores for sandwich structures are essentially an extension of z-pin preforms. Their manufacture shares many of the processing steps used for preform manufacture. There are three fundamental differences which separate their manufacture from that of z-pin preform. The first is the type of rodstock used, which is given special discussion in Section 4.6.2.2. Secondly, one single foam piece is used through which rodstock is inserted and trimmed. The foam becomes a structural part of the final sandwich structure and is not discarded before cure. Finally, the angle at which the rodstock is inserted is rarely perpendicular to the foam surface, the complete opposite to z-pin preform, which adds additional complexity to the manufacturing and programming processes.

The foam needed to be mounted slightly differently on the support table to the z-pin preform foam block to allow the rodstock reveal length to exit the lower surface. This was achieved by supporting the foam around the four edges so that the central part of the foam, through which rodstock was inserted, was left suspended. However, the force exerted on this during the rodstock insertion caused the foam to flex. This needed to be monitored closely by the operator as flexing of the foam can result in undesirable pin

misalignment. An alternative approach to this was trialled in which a lower density foam material was used to sit the foam block on to allow the rodstock reveal length to pierce it. However, once insertion was complete, separating the support material from the core foam led to the pins being pulled out.

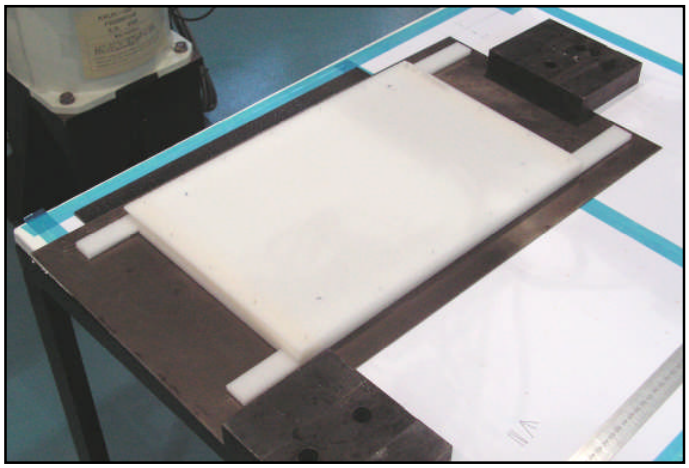

Figure 4.39 – Foam core mounting for pin reinforced core manufacture

The program code written for pin reinforced core manufacture is included in Appendix B.

The coordinate based positioning system was utilised again, as developed for the z-pin preform code. The motion path for the insertion head was also consistent with the approach used for preform manufacture. However, for pin reinforced core manufacture, additional information needed to be given to each insertion coordinate regarding the orientation of the inserted length of rodstock. This information was attached to the insertion coordinates as x, y or z rotations.

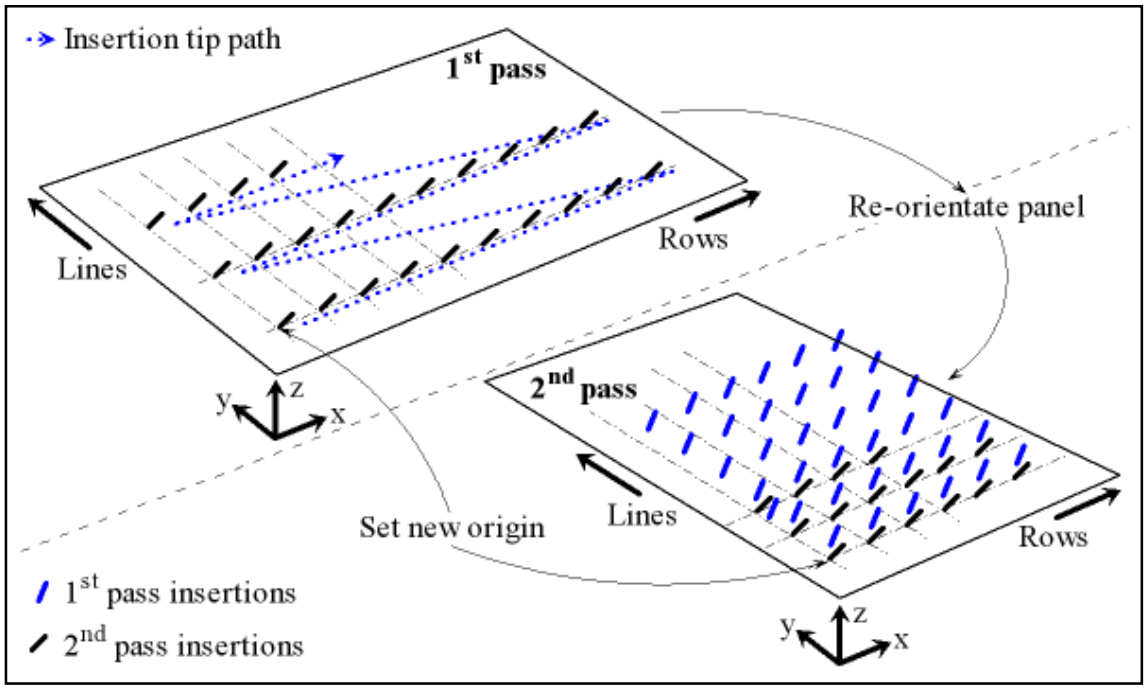

Figure 4.40 – Multiple passes for pin reinforced core manufacture

To build up the different orientations of pins, the core construction was manufactured in passes so that the insertion head had to make the minimum number of orientation adjustments possible. In fact, for the most successful manufacture runs the insertion head simply tilted back to give the desired insertion angle and it was the foam panel which was re-oriented between passes.

The main area of difficulty for pin reinforced core manufacture was ensuring that the insertion tip was able to travel unobstructed above the foam surface once the first pass of insertions had been made. Collision with inserted pin reveal lengths and collision of pins inside the foam thickness were always to be avoided. In the first instance this was managed by careful design of the core construction; experience and practice informed the lower limit of pin-to-pin spacings, changing with insertion angle. Core constructions with a pin-to-pin spacing of 5 mm and an insertion angle of 22° were successfully manufactured by the author. Another adjustment made was to increase the travel on the stamper so that the shear cutter could operate with greater clearance from the already inserted pins. One drawback to this was that the length of rodstock suspended between the insertion tip and the foam surface increased and hence the accuracy of orientation

was reduced. Figure 4.41 shows a core under manufacture using the Cranfield University insertion apparatus and the program developed as part of this work.

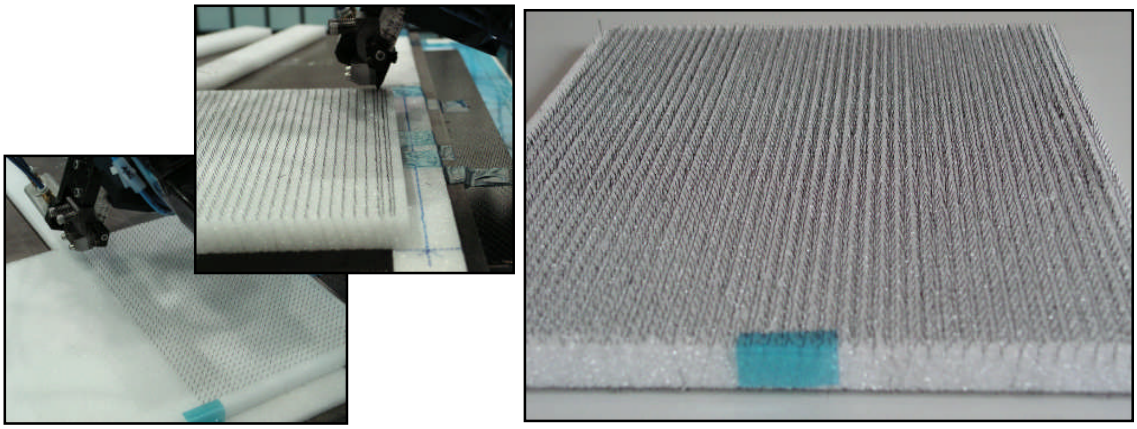

Figure 4.41 – Cranfield University manufactured pin reinforced core (210 x 300 mm panel)

4.6.2.1 Suitability of Cranfield University system for pin reinforced core manufacture

The system as described had a limited range of core parameters which could be successfully manufactured by the author simply due to the design of the insertion head and capabilities of the system. These are summarised hereafter and provide the basis on which the author recognises that the Cranfield University manufactured pin reinforced cores are not of the same quality as X-Cor and K-Cor manufactured by Albany Inc.

Pin angles – were limited initially by the design of the insertion head itself. Rotation was limited on one side by the stamper position. Latterly, the approach of reorienting the foam block was adopted using a workshop machine turntable bed. With no direct link between the insertion head and the turntable, positional accuracy was therefore limited to operator visual measurements.

Pin lengths – were limited by the distance which the insertion tip was required to pass above the foam surface. There is a minimum distance required to avoid collision with existing inserted pins and therefore the inserted length could not be below this distance. This distance, however, is small (~1 mm) and it is unlikely that any core construction would be manufactured on this scale.

Pin spacing – was a very important parameter to be considered and is limited by insertion head design and operator skill. The minimum required pin-to-pin spacing is set by the need to avoid collisions. The sliding travel of the cutter blade further limits the minimum pin-to-pin distance for successful manufacture.

Core densities – the density of the foam core had a direct impact on whether insertion could be achieved at all. If the core foam was too dense then the resistance resulted in the roller systems experiencing difficulty in feeding the rodstock. If the rollers began to slip then the correct length of rodstock was not inserted. The operator could not usually see whether the rodstock has completely inserted through the foam until the manufacture was complete. Foam could not be displaced for constant checking of complete insertion as this disturbed the positional accuracy.

Rodstock – the rodstock itself had a bearing on successful insertion. Apart from it being required to maintain its form and not break (discussed later in this section) is must also not deviate from the desired insertion path. If it does there is a risk that it will collide with already inserted pins. Two pins became misaligned when this occurred and was usually accompanied with rodstock breakage.

Albany Int. has world leading knowledge and experience in dealing with these issues. However, at this time, they do not use robotic arm systems to guide insertion heads, instead they use large gantry machines for the positional accuracy advantage they offer. The robotic arm system comes into its own when the manufacture of curved foam cores are considered, aerofoil sections being a typical example. For these types of cores, pin lengths need to be adjusted to maintain a constant reveal length, a factor which can be controlled with the current set-up of the Cranfield University system through the insertion head control box. The insertion head can be positioned inside otherwise inaccessible areas by the robotic arm.

However, it is the opinion of the author that the system at Cranfield University, in its current form, is not capable of making non-flat core constructions at present. The components required to do this are there in principle but the system is limited in

particular by the control system software capabilities being too basic but also by the motion tolerances of the robotic arm itself. Furthermore, after limited experience and trial time the author believes that a motion driven support table system needs to be used in conjunction with the robotic arm system. This is so that some of the difficult positions the robotic arm has to manoeuvre into in order to complete the more tricky insertions could be shared between the two systems. As mentioned previously, this was trialled briefly by using a hand operated machine turntable. The conclusion from this is that the two positioning systems, robot and turntable, need to be linked and driven by a common program in order to have the required level of positional control and accuracy. The ease with which cores could be manufactured was much greater when using the turntable than having the foam core fixed. Furthermore, the program requirements were reduced as less orientation manoeuvres were needed by the robot arm.

4.6.2.2 Rodstock for pin reinforced cores

The rodstock used for pin reinforced core manufacture is not the same as is used for the manufacture of z-pin preforms. Table 4-5 details the material specifications and differences between the three rodstock types.

Rodstock	Fibre	Resin system	Cure state as supplied	Tg (°C)
Z-pin (UAZ)	T300	Cytec-Fiberite 5250-4	Fully cured	271 from [176]
K-Cor	T300	Huntsman 8615	Partially cured	217 from [177]
X-Cor	T300	Vantico 8606	Fully cured	173 from [178]

Table 4-5 – Comparison of rodstock types

Rodstock for pin reinforced core constructions does not need to undergo the ultrasonic insertion process and therefore the requirements on the resin system used are different. The Tg of the resin system for X-Cor and K-Cor type rodstock does not need to be as high as that for the z-pin type in order to survive the ultrasonic excitation. The K-Cor rodstock is only partially cured and is also able to survive higher temperatures than the

BMI system used for Z-pins. These two factors provide the K-Cor type rodstock with sufficient flexibility and survivability for the process of bending the pin heads flush with the surface of the foam in the heated press. The X-Cor rodstock is fully cured to give the pins sufficient rigidity to pierce the uncured laminate skins during sandwich structure preparation.

4.6.2.3 Pin reinforced cores quality control

Quality control checks were not performed on the cores manufactured by the author as the cores were produced for manufacturing trials only. Nonetheless, visual inspection was sufficient to show that the positional consistency of these cores was not at the same tolerance as the commercial ones.

The inspection process used by Albany Int. for the purposes of quality control of pin reinforced cores focuses on the reveal length and insertion angle. Samples known as tags are manufactured at the edges of the reinforced cores for inspection use. The tolerance on the reveal length for X-Cor and K-Cor is 0.015 mm (0.6 mil). The exact tolerance for insertion angles is not known but it is reasonable to expect that it would be similar to the 3° from perpendicular value used for z-pin preforms.

4.6.3 Rodstock quality

These processes of manufacturing z-pin preforms and pin reinforced core constructions was the author's first experience with z-pin rodstock supplied by Albany Inc. During the course of this manufacturing effort problems were experienced with the rodstock which led to a more in depth look at its quality. During the insertion process the rodstock kept breaking particularly when required to bend through the roller sets on the insertion head or when the rodstock hit the foam surface for insertion. This did not happen all the time; the rodstock contained lengths which processed well followed by long lengths which would break constantly.

It is known that the resin content for each rodstock type is tested by Albany Int. The exact limits for acceptability are unknown however. Albany Int. uses an in-house Wright test to monitor 1 yard lengths of rodstock. The Wright test is a non-standard test and therefore the assumption is that the monitoring of resin content in the rodstock is comparison based only. Furthermore, the continuous pultrusion process used to manufacture the rodstock cannot be paused easily to take 1 yard samples. Samples are most likely to come from the ends of pultrusion runs which can be thousands of yards long.

It is the author's opinion that the problem with frequent rodstock breakage lies in the fact that the wetting out of the carbon fibres in the rodstock with resin is not consistent. With less than sufficient resin coverage, the carbon fibres are exposed causing a more brittle response under bending. The rodstock as a whole is also more prone to splitting as there is insufficient resin binding the fibres together. These two factors would explain the two major problems encountered during processing.

Looking back again at the pultrusion process for rodstock manufacture described in Section 4.1.1 there is no significant consolidation of the rodstock to ensure good resin coverage of the carbon fibre tow. The manufacture relies on the carbon fibre tow picking up enough resin in the pultrusion bath to enable it to withstand all future processing. This along with the small, possibly negligible, amount of consolidation the rodstock receives from passing through the die is not sufficient to ensure resin impregnates to the core of the carbon fibre tow. In the author's opinion, the die only serves to remove a significant proportion of the resin from the surface of the carbon fibre tow.

Attempts to quantify the resin content from bad lengths of rodstock were unsuccessful. The circular cross-section of the rodstock makes clear optical micro-scope imaging difficult. Cross-sectioning the rodstock only causes it to disintegrate due to the lack of resin holding it all together.

However, the issue of rodstock quality does not only affect the foam preform insertion, it also affects the insertion into laminates, and it is here where the issue can be seen. Many examples of z-pinning into carbon fibre composites can be found and in these the individual z-pins are not visible. Manufacture of glass / epoxy laminates which were subsequently z-pinned, cured and polished allowed the individual pins, and the effects of poor rodstock quality, to be visualised.

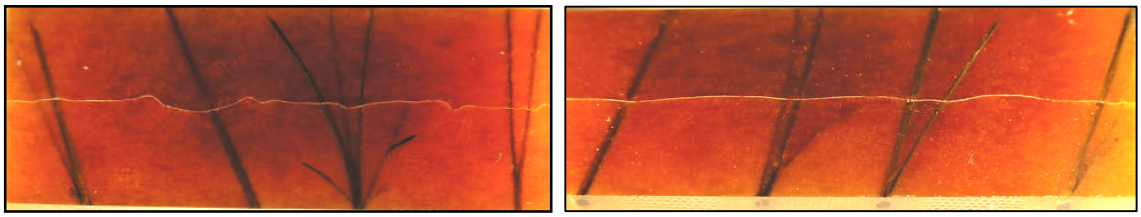

Figure 4.42 – Z-pin splitting in glass / epoxy laminates

The z-pins shown in Figure 4.42 are 0.51 mm diameter, 2 % areal density type supplied to Cranfield University by Aztex Inc.

Chapter 5

Test methods

This chapter details the test methodologies for all experimental work undertaken in this study.

Some of the test methods described in this section follow published international test standards directly and the specifications for these are detailed. For those test methodologies which are non-standard the reader should be aware that protocols for similar, standardised tests were consulted in developing the methods used.

5.1 Tensile testing: I-sections

There is no standardised test method for tensile testing of I-sections; the methodology described here has been developed by the author. The carbon / epoxy I-sections were tested in tension under ambient environmental conditions using a displacement controlled Instron 5500R universal testing machine fitted with a 100 kN load cell. For some of the I-sections manufactured from the 8552 / 3K8H / HTA material system the failure load exceeded this load cell capability requiring the use of an Instron 8800 servo-hydraulic test machine fitted with a 250 kN load cell.

These tests were performed to obtain the ultimate load of the carbon / epoxy I-sections and the associated range of joint geometries by quasi-statically loading them until complete failure. The ultimate stress was calculated from measurements of the I-section geometry. Failure was catastrophic without exception; the total extension at failure was recorded from the test machine crosshead displacement (accurate to ± 0.5%). To negate the effects of load train extension from this measurement the I-sections were pre-loaded to 1 kN. The loading rate was set to 1 mm/min.

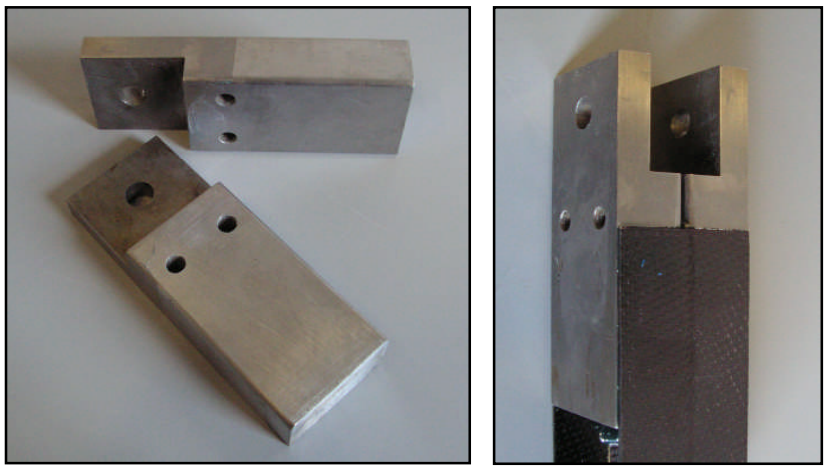

Figure 5.1 – 100 kN rated steel test fixtures used for I-section tensile testing

In order to apply load to the I-sections, without incurring damage to the laminates through the use of over-sized grips, a custom designed loading assembly was employed. Four mild steel fixtures were bonded inside the I-sections, two at each end, and the whole assembly was pin loaded in the test machine. The surfaces to be bonded, on both

the composite I-sections and the steel fixtures, were cleaned thoroughly using acetone prior to application of the adhesive to ensure a secure bond and to prevent failure of the bondline during the test. Figure 5.1 shows these steel test fixtures individually and bonded to one end of an I-section test piece, Figure 5.2 shows a schematic of the whole tensile test arrangement.

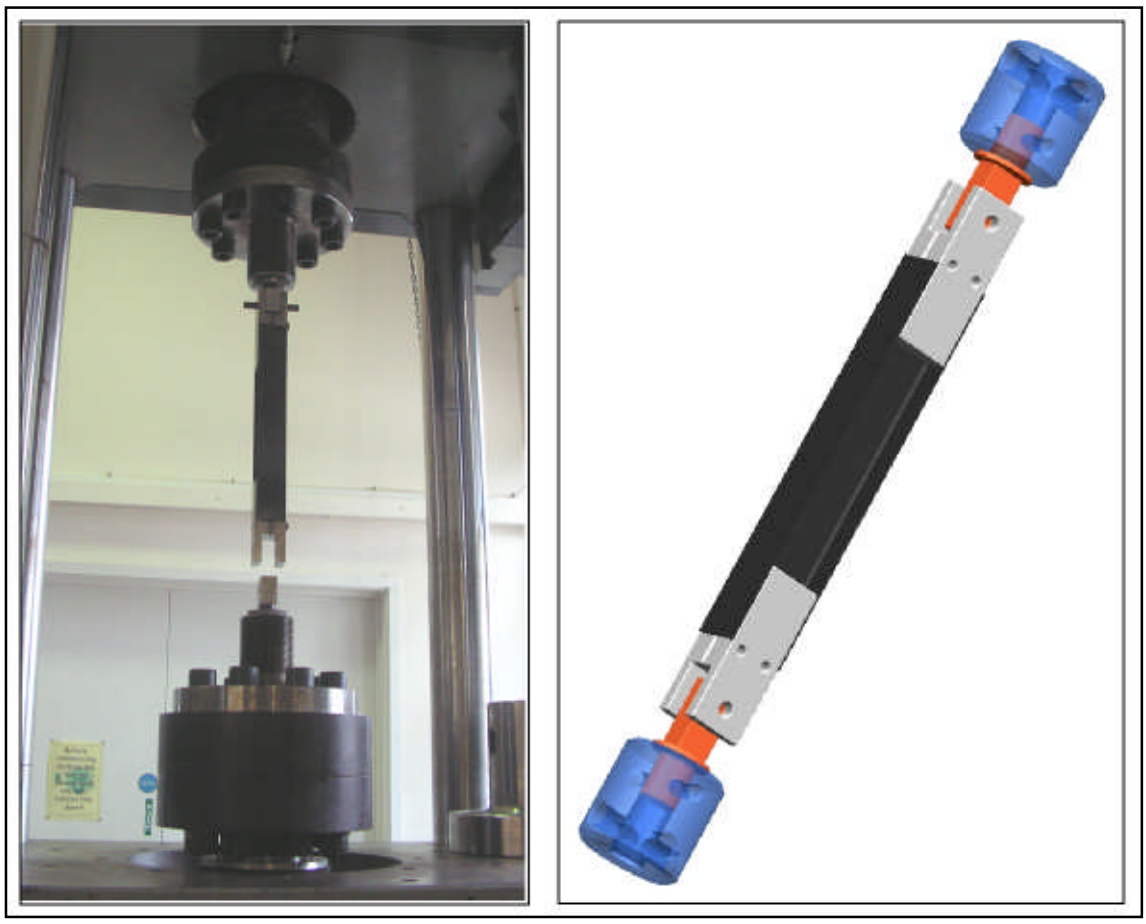

Figure 5.2 – I-section tensile test arrangement

5.2 Tension after impact testing: I-sections

An extension of the I-section study was carried out to investigate the ultimate load capability of the I-section joints after a controlled amount of damage had been introduced by way of an impact event. Again, there is no standard test method for tension after impact testing of I-sections; the methodology described here has been

developed by the author. The tensile testing part of these tests was carried out following exactly the same procedure as described in Section 5.1.

Both patches of each I-section joint were impacted with an energy of 10 J under ambient environmental conditions using a Rosand Instrumented Falling Weight Impact Tester. The impactor tip was hemispherical in shape with a diameter of 16 mm. This type of low energy impact test simulates events that commonly occur to aircraft structures such as dropped maintenance tools or runway debris strikes.

The I-section joints were simply supported and impacted at the intersection of the join line and the web centreline. This position was considered to be the weakest point of the structure and most vulnerable to damage, these impact tests were therefore a worst case scenario for the joints. Considerable care was taken to align the target point with the impactor head; slight misalignment causes large differences in the way the test piece absorbs the impact, twisting or bending of the flanges for example. These were undesirable, damage should be contained within the laminate and the aim was to maintain consistent damage size and quality. Figure 5.3 shows the impact target point on the I-section joint.

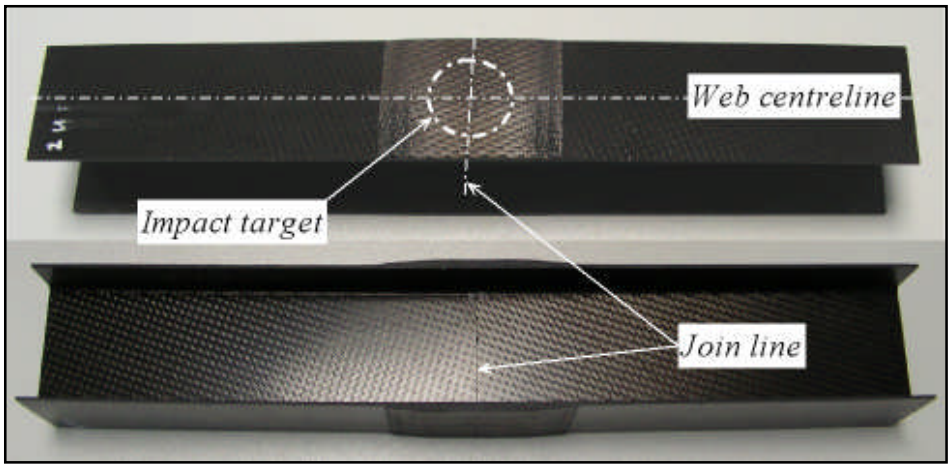

Figure 5.3 – Location of impact on I-section (both sides of the joint were impacted)

Figure 5.4 shows the I-section impact test arrangement simplified for illustration. The impact energy was set by lifting a known mass, attached to the load carriage, to a predetermined height above the target. The energy required and the load carriage mass

selected resulted in an impact speed of 3 m/s. A data recording system was used to measure the dynamic response via a load cell connected to the impactor head. The force versus time responses were used to monitor the quality of the impact event, high peak forces were a good sign that the impactor had hit in the desired location directly on the web centreline. A lower peak force would indicate that the impactor had not hit the target and the energy input would have been damped by bending of the flange.

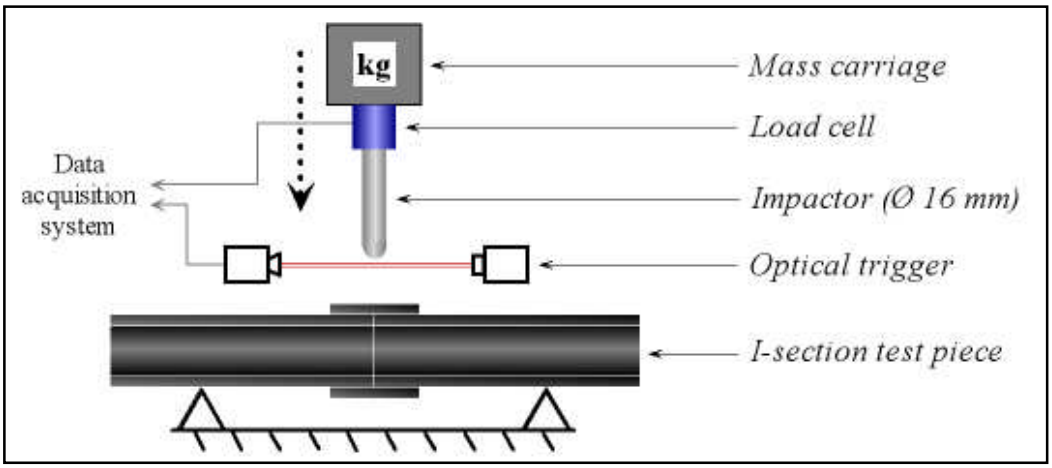

Figure 5.4 – Impact test arrangement for I-sections

5.3 Impact testing: crash tubes

Impact tests were performed on carbon / epoxy crash tubes to assess the effect of z-pins on the specific energy absorption (SEA). The crash tubes were impacted using a Rosand Instrumented Falling Weight Impact Tester, with the maximum mass available, under ambient environmental conditions. This type of high mass test on the crash tubes simulates a side impact crash of a Formula 1 racing car.

The crash tube test pieces were placed free-standing on the test machine base and aligned with the centreline of the falling impactor. The impact velocity was set at 6 m/s to be representative of the Formula 1 scenario and this was achieved by lifting the 100 kg mass to the corresponding height. Figure 5.5 shows the test arrangement, simplified for illustration. The reader will notice that the crash tubes were manufactured with a 45° chamfer on the impact edge; this was done to promote a steady crushing of the tubes.

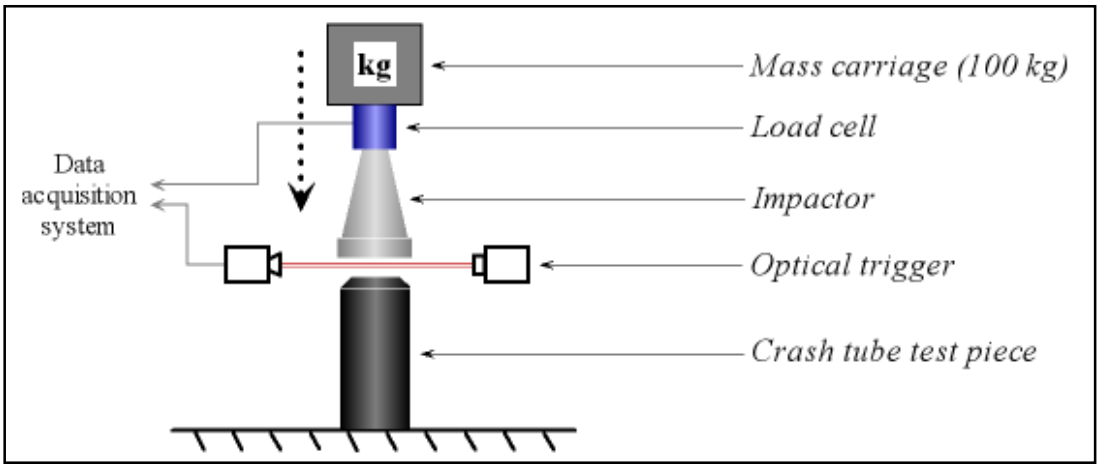

Figure 5.5 – Impact test arrangement for crash tubes

A data recording system was used to measure the dynamic response via a load cell connected to the impactor head. The displacement of the impactor (or crush distance of the tube) is calculated from the second integral of the deceleration, which itself is obtained by dividing the force measured by the load cell by the impactor mass. This is a common method used to obtain displacement for dynamic tests [179]; independent tests have confirmed the accuracy to be within 10 % on the test machine used. In other published work, laser displacement sensors [180] or incremental encoders [181] have been used to provide a more accurate displacement recording; such equipment was not available for this work. The force vs. displacement response from each test was used to calculate the energy absorbed by the test piece. Measuring the weight of the test piece before and after the test allowed the absorbed energy to be expressed specifically. The specific energy absorption for the material system is calculated as follows:

$$SEA = \frac{E}{(m_1 - m_2)} \quad \text{.....(5.1)}$$

where

SEA is the specific energy absorbed expressed in J/g

E is the energy absorbed during the test in J (area under the force vs. time response curve)

m_1 is the mass of the specimen before testing in g

m_2 is the mass of the specimen after the impact test in g

In some cases the impact crush front can pass through the entire z-pin reinforced zone. If this occurs, the crushed mass expression ($m_1 - m_2$) is refined to take account of the mass per unit length difference between the z-pin reinforced and non z-pin reinforced material parts.

In addition, the impact tests were recorded using a high speed video camera. This allowed the author to check that the impactor had hit the crash tubes square on and that a steady propagation of the crash front had been achieved. Figure 5.6 shows a sequence of images recorded for a typical impact test on a crash tube.

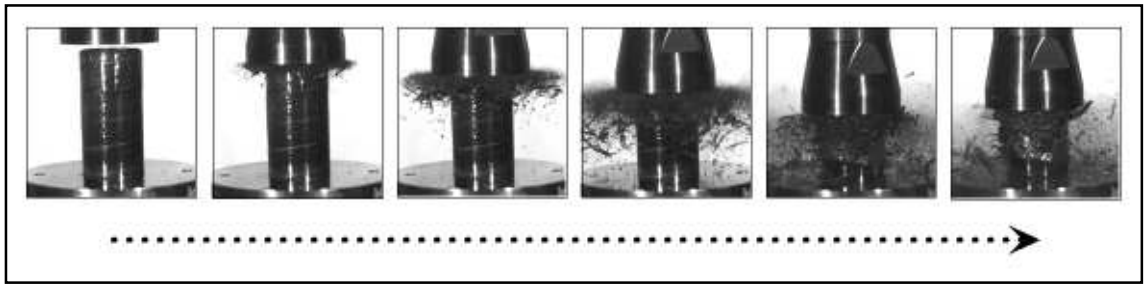

Figure 5.6 – Still images taken from high speed recording of a crash tube impact test

Strips of adhesive tape were also placed around the perimeter of the tube at different radii from the tube centre in order to collect debris for fragment size analysis.

5.4 Flexure testing: 3 point bend

The two carbon / epoxy material samples, 914 / 6K5H / T300 and 8552 / 3K8H / HTA, were subjected to a three point bend test in order to obtain the flexural modulus for FE modelling use and ELS test analysis. Three point bend testing is a standard test for determining flexural properties of fibre-reinforced plastic composites, the test procedure followed here was ISO 14125:1998 [182].

A displacement controlled Instron 5500R universal testing machine equipped with a 5 kN load cell was used to load the 3 point bend specimens at a speed of 0.5 mm/min. The specimens were placed on support rollers set at a span of 80 mm equidistant from a central loading roller. The mid-span deflection was recorded from the test machine

crosshead displacement (accurate to ± 0.5%). Figure 5.7 shows the configuration for the 3 point bend test.

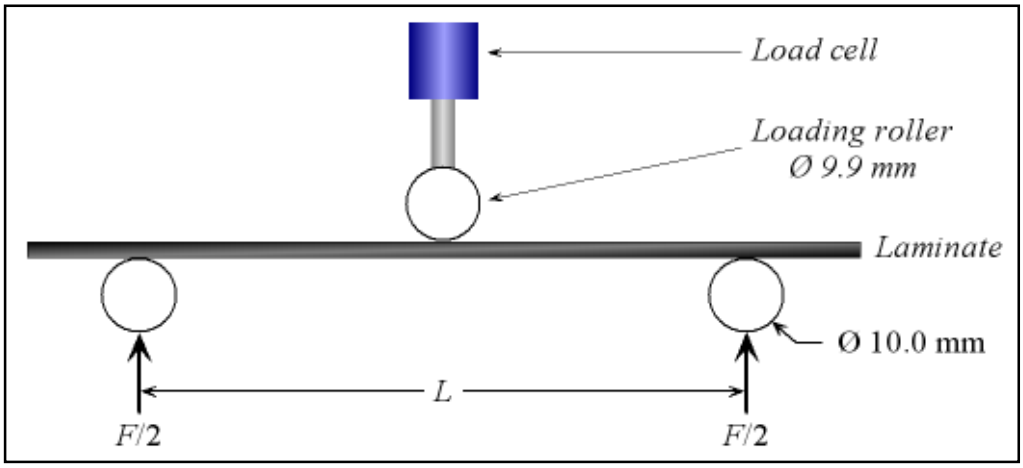

Figure 5.7 – Three point loading arrangement

From the test, a plot of force vs. deflection is obtained. The linear gradient of this plot ($\Delta F/\Delta s$) expressed in N/mm and taken between 5 and 25 % flexural strain, is used to obtain the material flexural modulus.

$$E_f = \frac{L^3}{4bt^3}\left(\frac{\Delta F}{\Delta s}\right) \quad \text{.....(5.2)}$$

where

E_f is the flexural modulus of elasticity expressed in MPa

L is the span in mm

b is the specimen width in mm

t is the specimen thickness in mm

The laminate specimens were not tested until failure, only until sufficient data points were recorded to capture the 25 % flexural strain value.

5.5 Z-pin shear testing (mode II)

These tests were developed and performed to gather information on the mode II behaviour of z-pins. Two investigations were performed; the first looked at the behaviour of z-pins when inserted into composite laminates, the second focused on the behaviour of single un-inserted z-pins (i.e. cut straight from the rodstock). The need for the development of the single z-pin tests came from difficulties discovered in trying to extract individual z-pin data from laminates containing multiple z-pins. These issues are discussed fully in Chapter 7. The shear test methods described here have evolved to provide z-pin mode II data for FE modelling use which is otherwise unavailable solely from one type of test.

Both types of shear test performed here used the same testing apparatus. The ‘z-shear test jig’ is a Cranfield University modification of the Iosipescu test jig which is a standard mode II test apparatus used for the determination of shear properties for fibre-reinforced composites. Figure 5.8 shows the z-shear test jig.

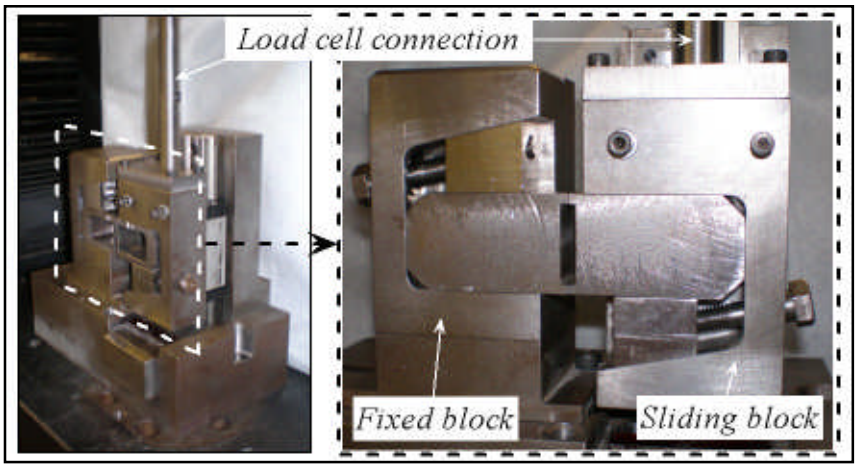

Figure 5.8 – Cranfield University’s z-shear test jig

Development of the z-shear jig was a continuous process and the jig had been used prior to this work to look at mode II z-pin behaviour. The most recent modifications made by the author, mainly focussing on the securing the test specimens in the mounting blocks and preventing opening displacement, have enabled the collection of a more closely controlled data set.

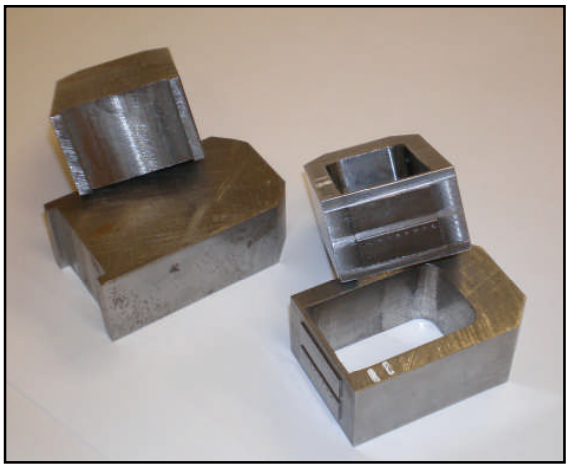

Figure 5.9 – Z-shear mounting blocks for z-pinned laminate (left) and single z-pin tests (right)

A pair of mild steel mounting blocks (20 x 30 x 50 mm) was custom designed and fabricated for each test type as shown in Figure 5.9. Both types of test were carried out using the z-shear jig with the appropriate mounting blocks and an Instron 5500R displacement controlled test machine equipped with a 3 kN load cell. For all tests the load and sliding displacement were recorded. The displacement was measured using the crosshead extension and an LVDT probe fixed to the sliding part of the test jig. This was done to ensure minimal compliance in the test jig itself.

5.5.1 Z-pinned laminate tests

The laminate test specimens were custom designed to include 16 z-pins, at equal pin-to-pin spacing, in a square array. Two sets were made, one set reinforced with 0.28 mm z-pins and the second set reinforced with 0.58 mm z-pins.

The laminate specimens were loaded at a rate of 0.5 mm/min. The specimens were fitted into the mounting blocks and loaded into the test apparatus with the polished surface facing outwards so that the deformation of the z-pins could be observed during the test. No adhesive was required for fixing the specimens in the mounting blocks; the specimens were cut carefully to provide a friction fit. Visualisation of the individual z-pins, once the specimen was mounted in the test jig, was enhanced through the use of miniature spotlights directed on to the specimen edges.

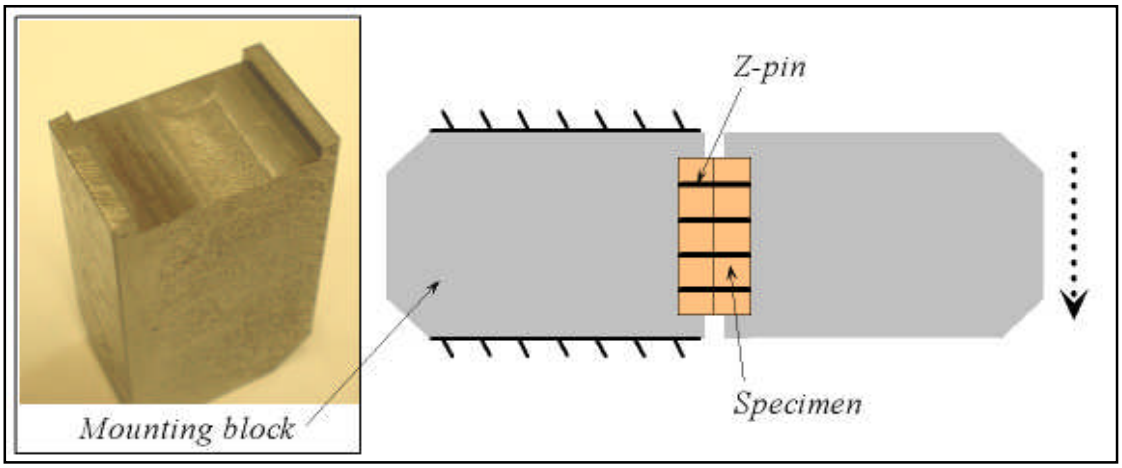

Figure 5.10 – Detailed view of z-pinned laminate specimen in mounting block

5.5.2 Single z-pin tests

The single z-pins were loaded at a rate of 0.1 mm/min. The mounting blocks were designed to allow up to nine z-pins of 0.28 mm and 0.51 mm diameter to be tested simultaneously. Figure 5.11 shows the holes for the two rodstock diameters drilled into a raised surface which was ground to a very high surface smoothness to reduce friction between the two mounting block surfaces.

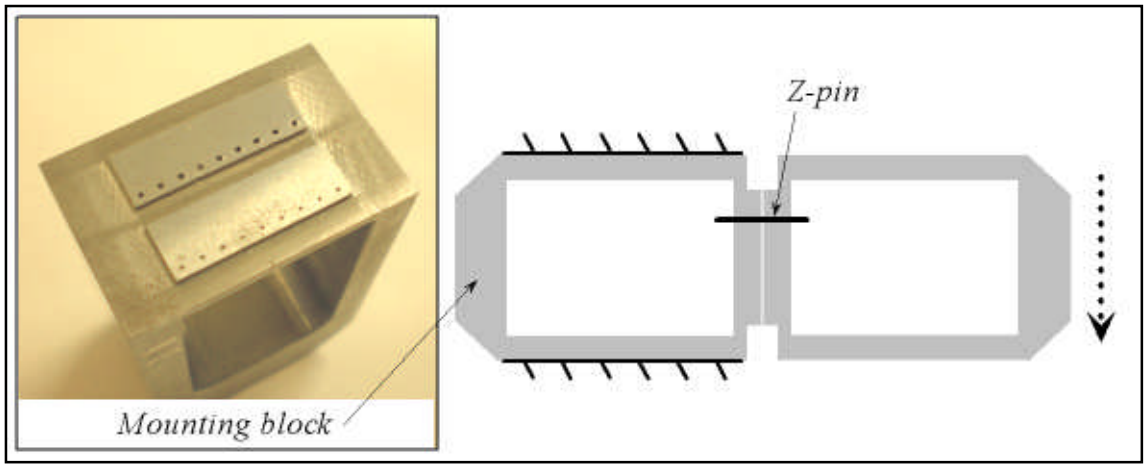

Figure 5.11 – Detailed view of rodstock loaded into mounting block

5.6 Delamination testing: end loaded split (ELS)

As for the 3 point bend tests and z-pin shear tests these mode II ELS delamination tests were carried out to provide the author with material data for FE modelling use. ELS tests were performed on specimens manufactured from the 914 / 6K5H / T300 and 8552 / 3K8H / HTA woven pre-preg systems detailed in Chapter 3. To date, no standard test has been agreed on for mode II testing of fibre-reinforced composites. The ESIS TC4 protocol [183] describes the ELS test method followed here although it has only been developed for unidirectional composites, not woven ones. Nonetheless, the mode II data for these two material systems were important to the development of this work and, with no alternative, the unidirectional composite ELS data analysis approach was adopted.

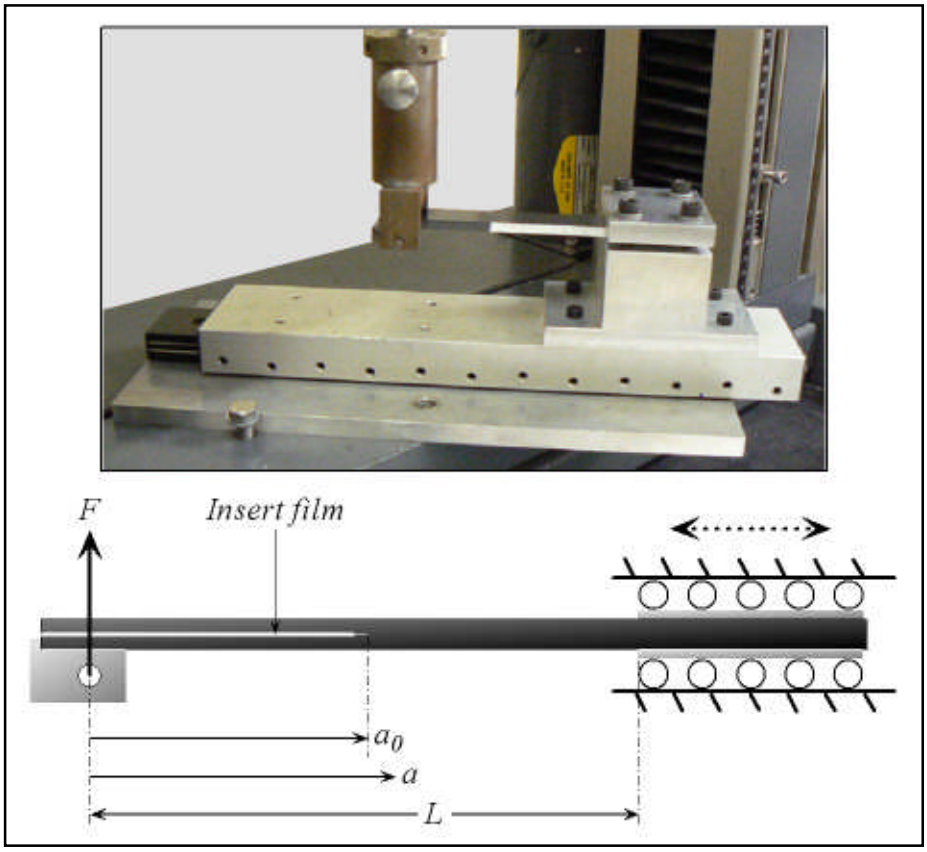

Figure 5.12 – ELS test arrangement

Similar tests were also carried out on specimens manufactured from 977-2 / HTA UD prepreg laminates as a reference against which the analysis steps used for the two woven materials could be compared.

Before testing, the ELS specimens were coated on one side with white correction fluid onto which millimetre increments are drawn. This was done to allow the crack tip position to be monitored. The composite specimens were manufactured to include a thin, 13 μm PTFE insert film to simulate an existing crack in the material. The specimen was opened slightly (in mode I) by hand to advance this manufactured crack tip a few millimetres further into the material. This is an important step to ensure that initiation data gathered upon loading is generated from within the material itself and not from, or a function of, the insert film. The position of the crack tip at this point is designated a_0 [184].

Prior to testing a calibration procedure was performed. This procedure allows the sliding displacement of the ELS fixture to be accounted for in the analysis. The specimen is clamped, with the insert film at the clamp end (opposite to as shown in Figure 5.12), at 10 mm intervals between span lengths of 110 mm and 50 mm. For each of these seven span lengths the specimen is loaded to 250 N and the deflection measured.

The specimen is then clamped at one end as shown in Figure 5.12 so that only horizontal motion is permitted. The opposite end of the specimen is loaded via a pin-loaded load block bonded to the specimen. A Zwick Z010 screw driven, displacement controlled test machine equipped with a 2.5 kN load cell was used to load the ELS test specimens at a speed of 2 mm/min.

The position of the crack tip was particularly difficult to monitor. As the specimen deformed, the position of the crack tip, the load and the loading point deflection were recoded at regular intervals, usually about every 2 mm. The data acquisition system was triggered to plot markers on the load vs. deflection response curve when the crack tip passed the increments drawn on the specimen. An example material response curve is

shown in Figure 5.13. The crack tip positions are noted and related to the corresponding markers on the response curve upon completion of the test.

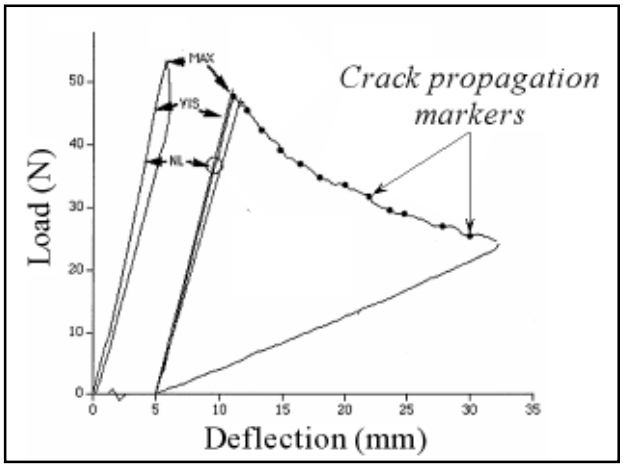

Figure 5.13 – A typical ELS test load vs. deflection curve with crack propagation makers

Data reduction of the load, deflection (measured from the test machine crosshead displacement to ± 2 μm accuracy) and crack length data allows a mode II material resistance curve (or R-curve) to be drawn. A mode II R-curve is a measure of the material's apparent mode II delamination toughness (G_{IIC}) plotted against crack length (a). Four different analyses exist for calculating G_{IIC}, a sign of the development of the ELS test in the recent past [164,167,169,170].

The ELS test analyses include certain corrections. These corrections are detailed fully in Appendix C, and account for the following:

i. Delamination length correction (Δ_{II}) – takes account of crack tip rotation
ii. Large deflection correction (F) – extends beam theory approach to apply for large specimen deflections
iii. Load block correction (N) – takes account of the local stiffening effect of the load block on the specimen
iv. Clamping correction (Δ_{clamp}) – updates the specimen length (L) to take account of the clamping fixture movement

The penultimate analysis, the experimental compliance measurement (ECM) method [169], is given in Equation (5.3). The compliance (C) is determined by dividing the

deflection (δ) by the load (P). This value is plotted against the cube of the crack length (a^3) to obtain the gradient (m).

$$G_{IIC_{ECM}} = \frac{3P^2 m a^2}{2b} \quad \text{.....(5.3)}$$

where

G_{IIC} is the mode II delamination toughness expressed in J/m^2

a is the crack length in mm

P is the load corresponding to each delamination length in N

m is the slope of the C vs. a^3 plot

b is the specimen width in mm

Even experienced ELS test users find visual measurement of the crack length extremely difficult. Equation (5.3) shows that G_{IIC} is related to a^2 and therefore inaccuracy of crack length measurement greatly affects the toughness value. This fact has led to the development of the most recent expression for G_{IIC} which negates the need for crack length measurement altogether by calculating what the crack length should be from the compliance. The corrected beam theory with effective crack length (CBTE) method [170] is expressed as follows:

$$G_{IIC_{CBTE}} = \frac{9P^2 a_c^2}{4E_f b^2 h^3} \quad \text{.....(5.4)}$$

where

E_f is the material flexural modulus expressed in MPa

a_c is the calculated crack length in mm

P is the load for each calculated crack length in N

b is the specimen width in mm

h is the specimen half thickness in mm

Comparison of the ECM and CBTE methods is a good indication of the accuracy of the visually measured crack length.

Chapter 6

Z-pin reinforcement as a technology to manage failure

This chapter details the results obtained from testing of z-pin reinforced automotive crash and aerospace stiffener structures. These tests will show that the z-pinning technology, whilst beneficial in the various scenarios described, could further enhance structural performance if the potential for a design based approach to their use could be harnessed.

6.1 Crash tubes

Crash energy management is one of the primary considerations for composite automotive structures. Early studies showed that composite structures had energy absorption potential comparable or better than traditional metallic structures [185,186]. Metallic and composite structures differ in that the former collapse by plastic buckling whereas the latter collapse by a combination of fracture processes [187]. Design methodologies for traditional metallic structures evolved from a combination of Finite Element analytical methods and extensive experimental testing. Crack propagation in composite structures presents a new set of challenges for these analysis techniques. Using tubular structures subjected to quasi-static or dynamic axial compression as an example, analytical models have been developed more recently to predict the deformation and fracture behaviour when composites are employed [179,181,188]. Experimental work on tubes manufactured from composite [179,181,188-193] and aluminium [180,194,195], the most common metallic choice, has been well covered. Assessment of crash performance and subsequent comparison of materials for this simple structure is made by determination of the Specific Energy Absorption (SEA). Efforts to enhance the energy absorption of commercially available composites has seen the use of toughened resins, through-thickness stitching, thermoplastic resin additives [192] and resin interleaving [192,193].

Carbon / epoxy crash tubes, the manufacture and testing of which have been described in chapters 4 and 5 respectively, were investigated to assess the effects of z-pin reinforcement on the specific energy absorption of impacted composite crash tubes. These crash tubes structures were designed to be similar to the components of the safety structure on the side of a Formula 1 racing car.

Figure 6.1, Figure 6.2 and Figure 6.3 show typical impactor deceleration versus time traces recorded for impact tests on 8, 12 and 16 ply wall thickness crash tubes respectively. For each case, two crash tube test specimens were reinforced, through the wall thickness, with a square array of z-pins (2% areal density, 0.28 mm diameter). Two control specimens in each case were not z-pinned.

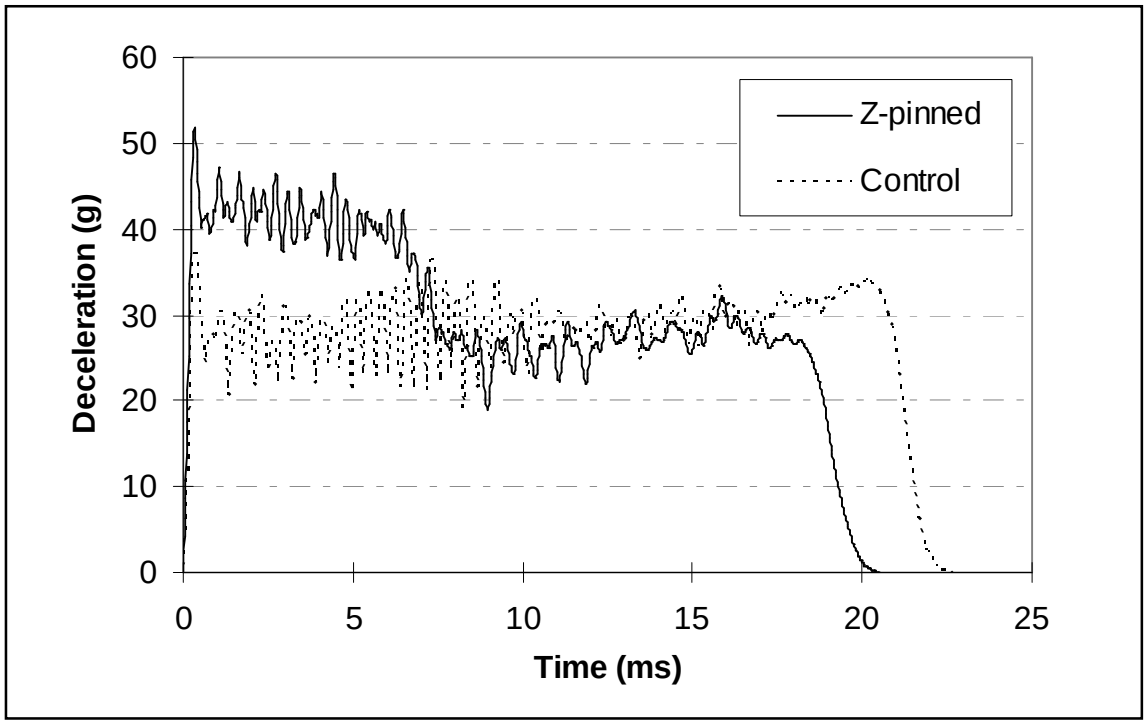

Figure 6.1 – Deceleration versus time plot for 8 ply crash tubes

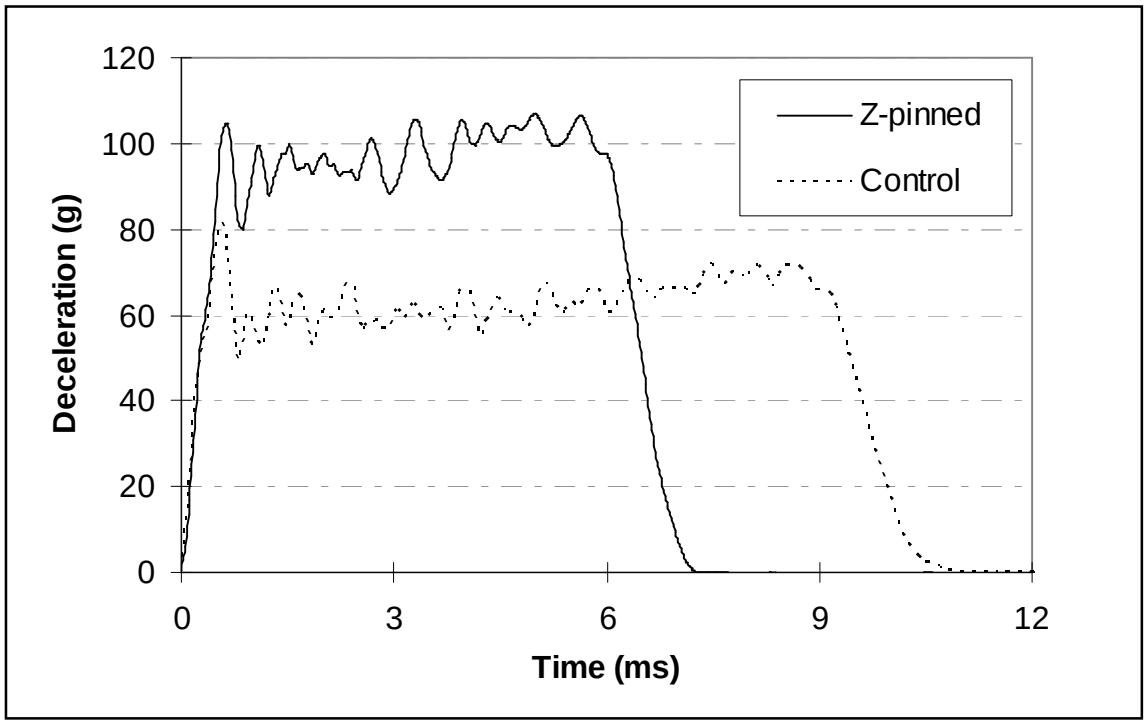

Figure 6.2 – Deceleration versus time plot for 12 ply crash tubes

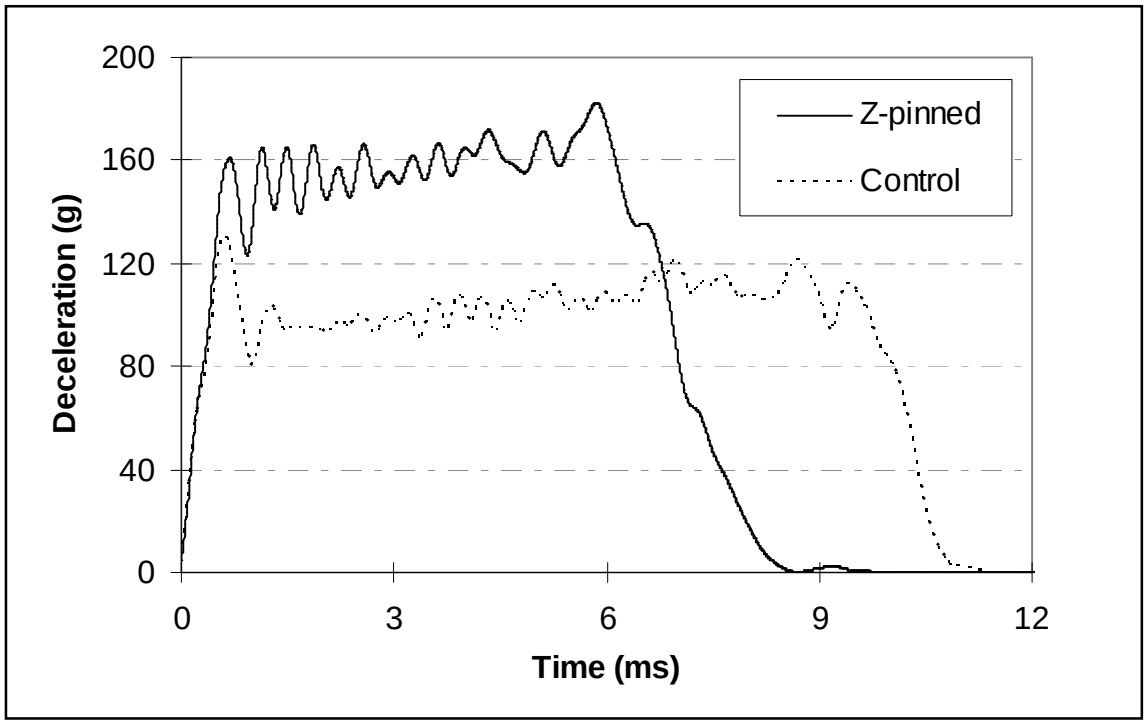

Figure 6.3 – Deceleration versus time plot for 16 ply crash tubes

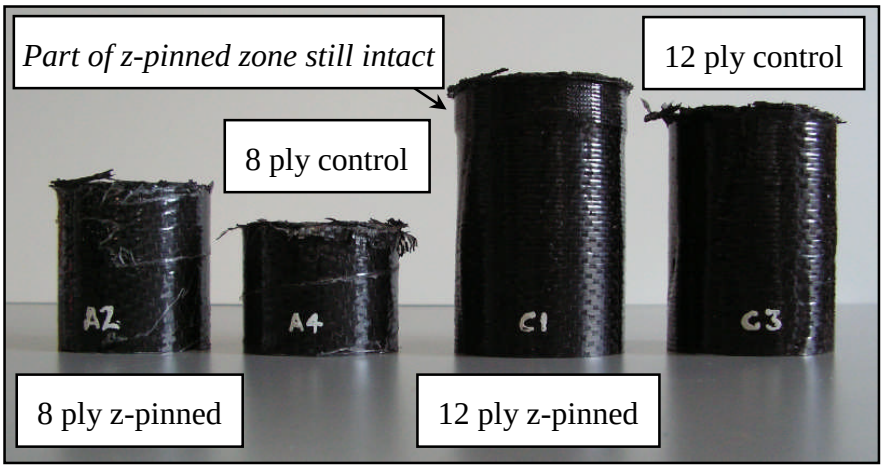

Figure 6.4 – Selection of impacted crash tubes showing crush distances

For the 12 and 16 ply tubes the crush front was contained within the z-pinned region (see Figure 6.4). For the 8 ply tubes, the crush front passed through the entire z-pin reinforced region. The drop in force as this happens can be seen in Figure 6.5. The boundary of the z-pin reinforced region cannot be defined clearly on the plot so a transition region is included instead.

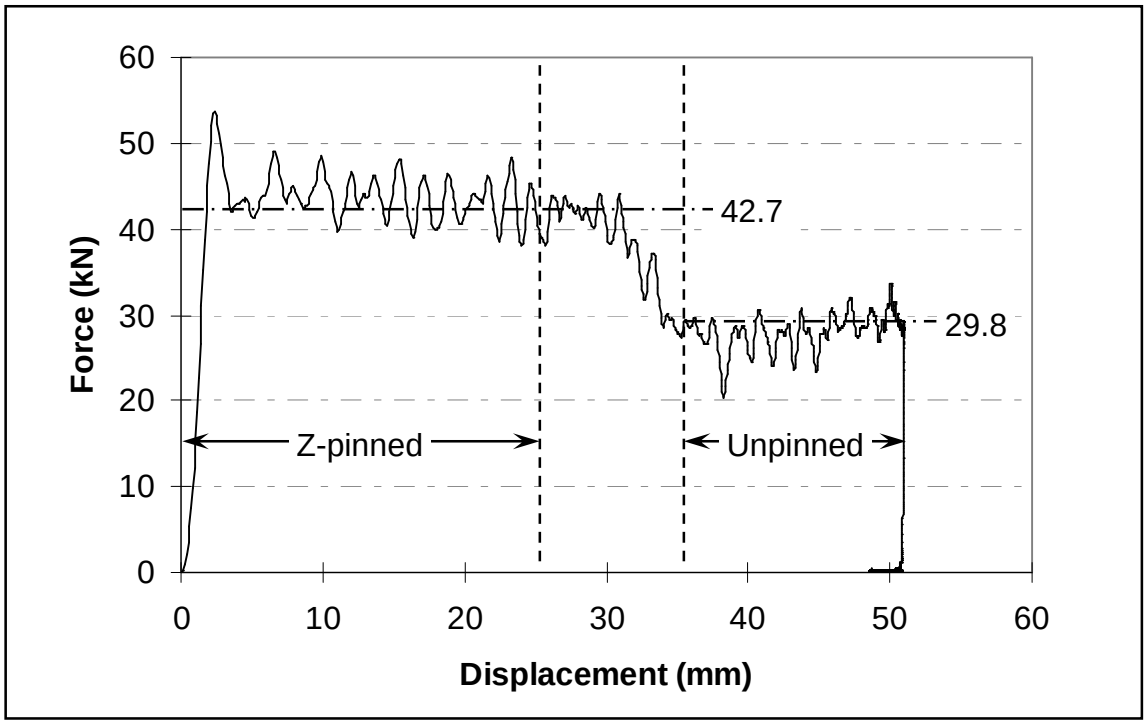

Figure 6.5 – Typical force versus displacement trace of an 8 ply, z-pin reinforced crash tube

Table 6-1 shows the force, separated into the tube regions where applicable, required to crush the tubes.

Tube type	Av. force by region [St. Dev.] (kN)		
	Z-pinned	Unpinned	Combined
8 ply – z-pinned	41.5 [0.6]	30.0 [1.4]	34.5 [0.8]
8 ply – control	-	30.0 [0.3]	30.0 [0.3]
12 ply – z-pinned	95.5 [1.7]	-	95.5 [1.7]
12 ply – control	-	63.0 [0.5]	63.0 [0.5]
16 ply – z-pinned	145.0 [31.1]	-	145.0 [31.1]
16 ply – control	-	85.0 [17.4]	85.0 [17.4]

Table 6-1 – Crushing forces on crash tubes

The test results show that the z-pins have a stiffening effect on the carbon / epoxy material which leads to a greater force required to crush the tubes. The presence of the

z-pins causes a higher deceleration of the impactor. The average deceleration is dependent on the crash tube geometry, rising from ~30 g for the 8 ply control crash tubes to ~60 g for the 12 ply and ~100 g for the 16 ply tubes. The inclusion of z-pin reinforcement increases the deceleration by a further 20 g, 40 g and 60 g for the 8, 12 and 16 ply crash tubes respectively.

The average specific energy absorption (SEA) calculated for the crash tubes tested is given in Figure 6.6. For the 8 ply crash tubes the SEA of the z-pinned region and the unpinned region is 98 J/g and 68 J/g respectively.

The control tubes, and the unpinned region of the 8 ply tubes, give an SEA value of around 70 J/g. The addition of z-pins increases the SEA by 24 % for the 6 ply and 53 % for the 12 ply tubes.

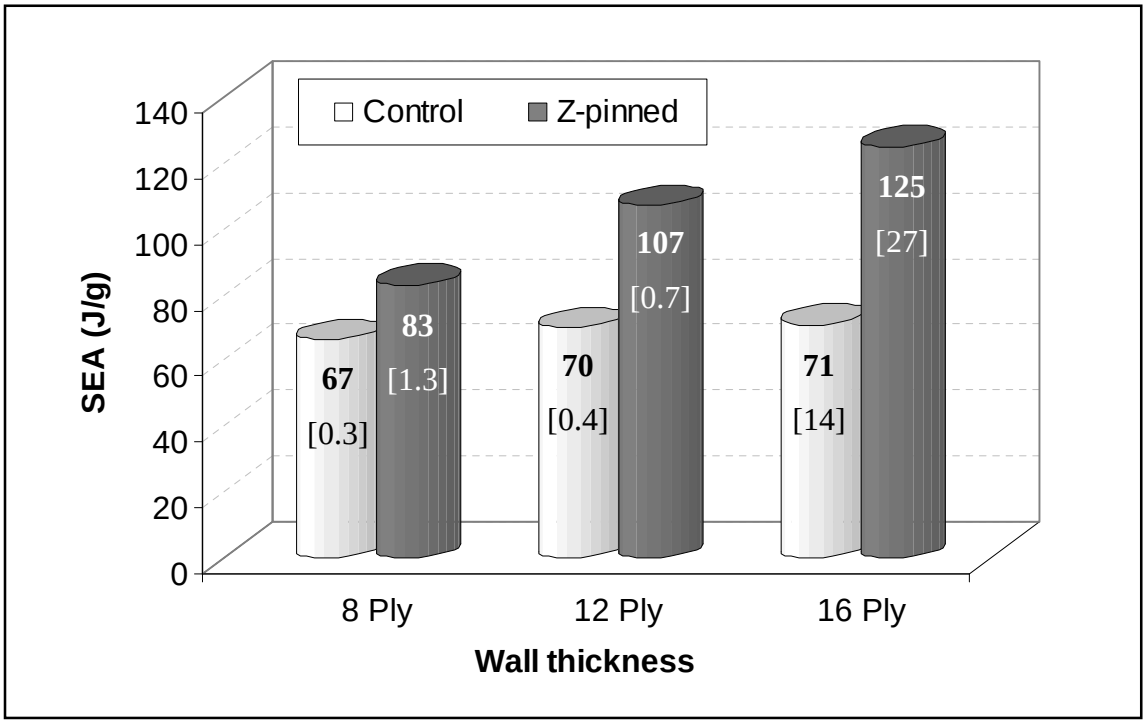

Figure 6.6 – SEA [St. Dev.] versus crash tube wall thickness

Published SEA values for carbon-fibre composite tubes are typically lower than those determined through this work. The range of tube dimensions and fibre architectures used make a direct comparison difficult. Furthermore, care must be taken to distinguish

between values recorded from dynamic and quasi-static tests. Figure 6.7 shows typical SEA values for a small selection of engineering materials.

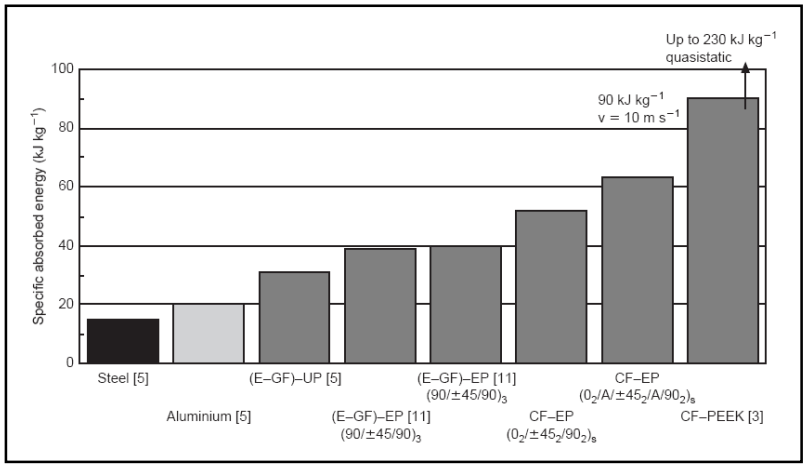

Figure 6.7 – Typical SEA values for a selection of engineering materials (modified from [193])

Similar work has shown that SEA of carbon-fibre composite material systems can be improved through modifying matrix formulations [192]. Resin interleaving in composite crash tubes has been shown to improve SEA by 19 - 22 % depending on the fibre architecture used [193]. More interestingly, due to the structural similarity to z-pinning, through-stitching of Non-Crimped Fabric (NCF) tubes was found to improve SEA by 18 % for low stitching density and 23 % for high density [192]. It is not known if these improvements would be greater for increased wall thicknesses as in the case of z-pinning. Nonetheless this is a useful improvement for composite structures manufactured by resin infusion techniques, using dry fabric materials which are unsuitable for z-pin reinforcement.

It is the author's belief that the presence of the z-pins promotes fragmentation of the composite. Cranfield University is currently involved in the development of nano-scale image and particle analysis techniques, as part of a European research effort, which would be able to provide confirmation of this. Microscopy has shown localised porosity around the z-pins from which damage would initiate. The increase in total fracture surface area from increased fragmentation would explain why the z-pinned tubes absorb more impact energy. The percentage increase in SEA as the wall thickness increases indicates that the z-pin effect is laminate geometry dependent. The mechanical

performance of z-pins has been shown to be length and / or laminate thickness dependent previously [1,2].

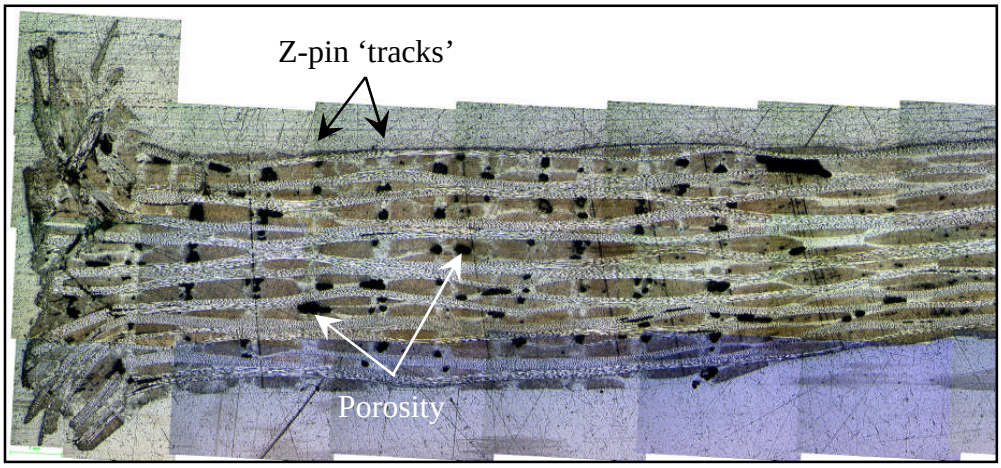

Figure 6.8 – Localised porosity around 0.28 mm diameter z-pin reinforcement in crash tubes

These results show that the use of z-pins in a composite crash tube structure provides a valuable increase in energy absorption performance. However, for Formula 1 requirements the deceleration levels recorded for these crash tubes are too high. To ensure the survival of the driver the Formula 1 technical regulations [196] require that the average deceleration experienced by the crash tubes does not exceed 20 g and that the force does not exceed 80 kN for more than a cumulative 3 ms. In order to meet such requirements, using the same materials, these tubes would have to be redesigned, most likely using a wall thickness less than 6 plies, using the same material system.

The study of these crash tubes provides the first example in which the z-pinning arrangement could be optimised better for the structure. The Formula 1 deceleration requirement could be achieved by altering the positioning of the z-pins and tailoring the crushing process to meet the structural performance need. The arrangement used in these tests was a block of equally spaced rows of z-pins, set by the standard preform provided by Aztex Inc., covering the entire tube circumference. Increasing the spacing between the z-pin rows could conceivably reduce the deceleration levels by allowing the crush front to travel further. The same might be true if the block of z-pins was replaced by thinner bands of pins providing zones of high energy absorption through which the crush front would have to travel.

There are many design permutations for the z-pinning arrangement in a structure such as this to make the best use of the energy absorption performance z-pinning offers. What is required is a means by which these alternative design solutions can be assessed. The traditional route of conducting an extensive experimental programme would not be suited to this due to the difficulty in producing consistent z-pinning quality, as has been discussed in Chapter 4, and the time required.

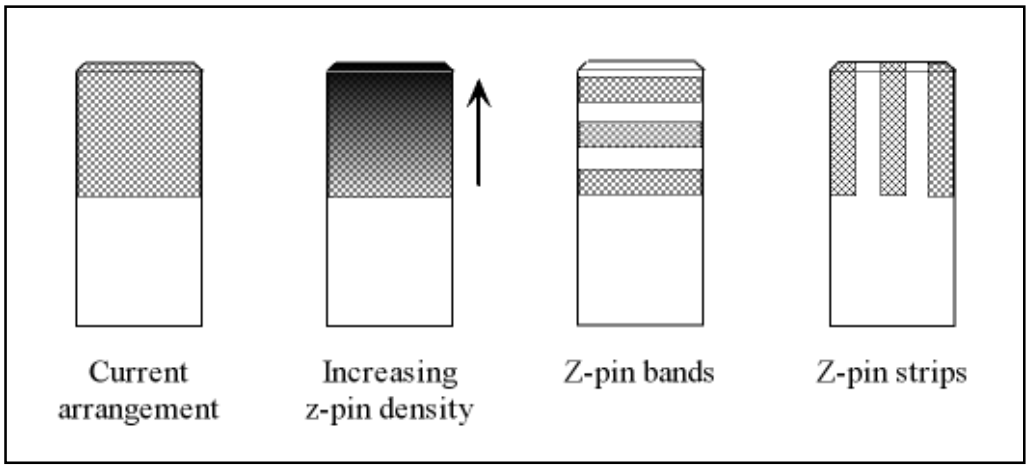

Figure 6.9 – Alternative crash tube z-pin reinforcement arrangements

6.2 I-sections

The geometry of the I-section test elements and the loading type were derived from a need to join stiffened panels of a composite aircraft nacelle structure. The use of I-sections to stiffen panels is commonly used to counteract bending loads; typically one flange of the I-section experiences a tensile load and the other a compressive load. In this case, the nacelle structure had a curved surface geometry and was pressurised from within. The positioning of the I-section stiffeners on this curved nacelle panel was such that both flanges experienced a tensile load, albeit not of equal magnitude.

This large nacelle structure was simplified to a small, flat test panel on which joining methods could be trialled. Figure 6.10 shows a schematic of the test panel incorporating the I-section stiffeners which need to be joined. The particular stiffeners on each of the three pieces of this panel, including the cross junction, are manufactured by folding a single sheet of composite pre-preg. At certain locations these folded pre-preg stiffeners

need to be joined to the adjacent piece. The purpose of the I-section experimental work, detailed hereafter, was to investigate the effects of reinforcing the patch joints, between the I-section stiffeners, with z-pins. All previous joining attempts had resulted in a delamination between the patch and the I-section stiffeners upon loading.

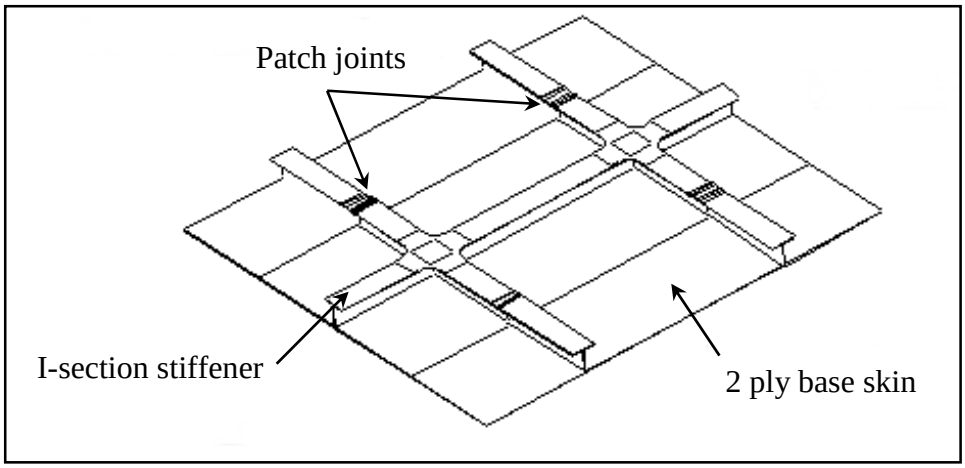

Figure 6.10 – Schematic of an I-section stiffened test panel

The I-sections manufactured in this work are tested in tension to mimic the in-service condition. In all tests carried out, the I-section test elements were loaded until ultimate failure. The ultimate load carrying capability of the various joint configurations used was hence obtained. These loads have not been converted to strengths (stress) as it was found that the mode of failure was not consistent for all the cases tested. For the three test sets detailed hereafter, the material used and patch designs are as described in Chapter 3 and Chapter 4 respectively. The testing method used is as described in Chapter 5.

For the patches to be reinforced with z-pins an initial study verified earlier findings by [162] that a 2 % areal density of 0.28 mm z-pins was best suited to this type of shear loaded joint structure. Figure 6.11 shows the load versus displacement responses for a 100 mm long patch reinforced with 2 % and 4 % z-pins of 0.28 mm diameter. Both tests failed by delamination of the patch from the I-section flanges, however, the 2 % z-pin areal density test produced an increase in both ultimate load and in the elongation limit. The higher failure load of the 2 % case is likely to be due to the lesser disruption to the load carrying laminate fibres.

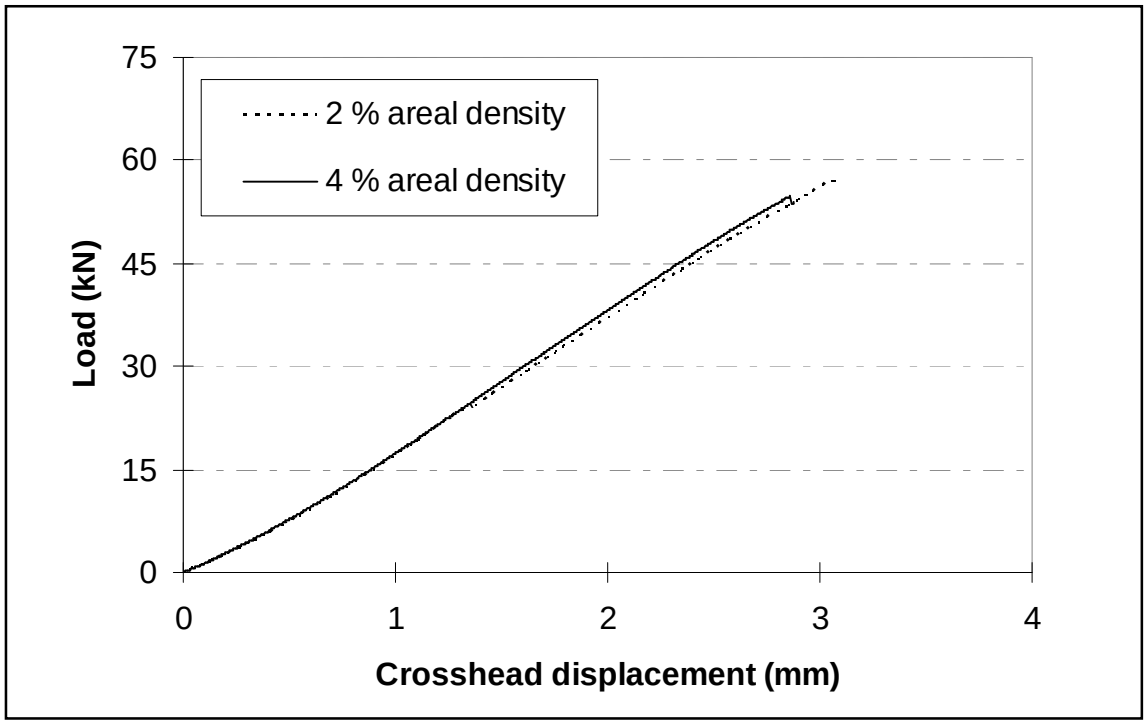

Figure 6.11 – Z-pinning areal density comparison

The test elements, shown in Figure 6.12, failed by fracture of the patch laminate at the position of the join line. Because the join line is the known weakness in these structures, and was observed to fracture prior to final failure of the joint, final failure was encouraged away from this zone. The z-pin arrangement was modified for subsequent tests to allow delamination to propagate away from this join line by leaving a 5 mm zone either side of the join line which was not reinforced with z-pins.

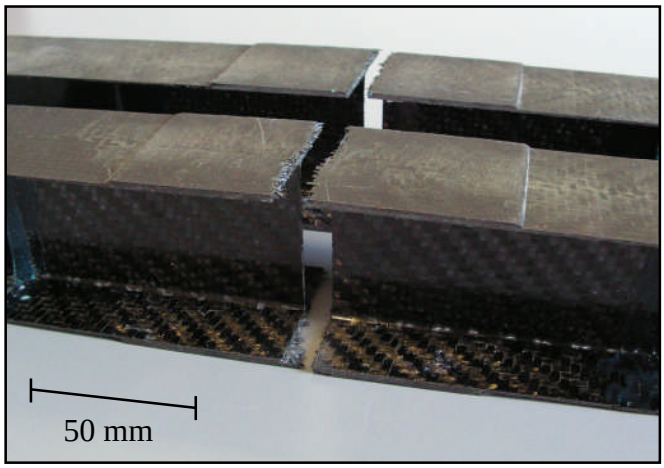

Figure 6.12 – Failed I-section test elements from preliminary areal density checks

6.2.1 Set 1 – Patch overlap length vs. ultimate load

The first set of tests looked at the effect of patch size on the strength of the joint. The joint width and thickness were fixed; the design variable was therefore the patch length. Results are presented as a function of overlap length which is half of the total patch length, or the amount by which the patch overlaps each half I-section. The ultimate loads obtained for the z-pin reinforced and control joints are summarised in Table 6-2.

Test type	Overlap length (mm)	Ultimate load [St. Dev.] (kN)	Extension at ultimate load [St. Dev.] (mm)	Failure energy [St. Dev.] (J)
Controls	15 mm	27.8	1.9	22.8
	25 mm	34.7	2.2	36.1
	35 mm	42.7	2.4	48.4
	45 mm	53.9	3.0	78.3
Z-pinned	10 mm	20.4	1.3	12.5
	15 mm	29.1	1.8	24.4
	25 mm	37.4	2.2	40.9
	35 mm	39.0	2.2	41.1
Pristine	n/a	61.4 [2.4]	3.7 [0.1]	110.7 [8.7]
Z-pinned pristine	n/a	55.8	3.3	88.7
No patch	n/a	5.3 [0.3]	0.4 [0.0]	1.0 [0.1]

Table 6-2 – Ultimate tensile loads recorded for 914 / 6K5H / T300 I-sections

Also detailed in Table 6-2 are a number of additional tests which were performed to complete a failure envelope for the structure. These tests are referred to as follows:

Pristine – an I-section test element with no join line and no patch. These tests represent the absolute maximum load capability any joint design of this geometry could have.

Z-pinned pristine – as above with a 20 mm wide band of z-pins inserted through each flange offset by 5 mm either side of the join line. It is well documented [99] that the use of z-pins results in a reduction of in-plane laminate properties. For UD laminates, a typical tensile strength knock-down of 27% has been recorded [98]. A lesser reduction is expected for the woven fabric laminates used in this work. This test quantified the load capability knock-down due to the use of z-pins in these structures. For the z-pinned joints this test replaces the pristine result as the absolute maximum joint load capability.

No patch – the two half I-sections held together with just the resin rich connection of the join line. These tests represent the absolute minimum load capability of the joint design for both the z-pinned and control joints.

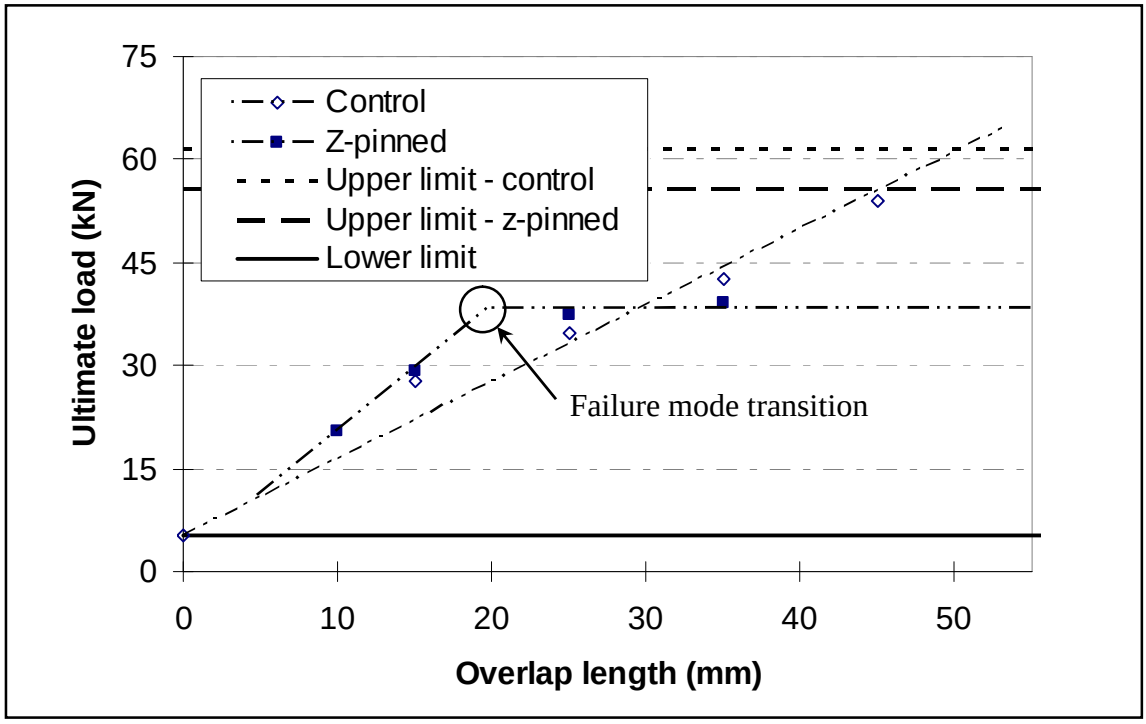

Figure 6.13 – Failure envelope for 914 / 6K5H / T300 I-section joints (inc. Type 2 patch design)

From the ultimate load values obtained, a failure envelope was drawn for the joints and is shown in Figure 6.13. Firstly the knock down in load capability of the *pristine* I-section due to the use of z-pin reinforcement is 20 % (or 22 kN). Both the *pristine* and

z-pinned pristine tests failed by catastrophic laminate fracture. For the *z-pinned pristine* test the laminate fracture initiated at the edge of the z-pinned zone. For the *pristine* I-sections laminate fracture initiated in the length between the bonded test fixtures. The *no patch* tests failed by fracture of the join line.

The ultimate load for the control joints increases linearly with increasing patch overlap length. The tests on the control joints all failed by delamination of the patch from the I-sections. The linear rise in load is expected as the joint failure is dominated by the resin strength and contact area of the patch / I-section interface. The control results have been extrapolated to the intersection with the upper load limit. The patch overlap length that would initiate laminate failure of the I-sections is predicted to be 52 mm.

The ultimate load of the z-pinned joints increases with increasing patch overlap length initially as the z-pins reinforce the weak patch / I-section interface and act to retard delamination. After a z-pinned overlap length of approximately 25 mm the ultimate load reaches a plateau of 38 kN. This plateau is 68 % of the upper limit load for the z-pinned I-section. Up to patch overlap lengths of 30 mm the use of z-pinning provides additional ultimate load capability to the joints, beyond 30 mm the use of z-pinning is detrimental.

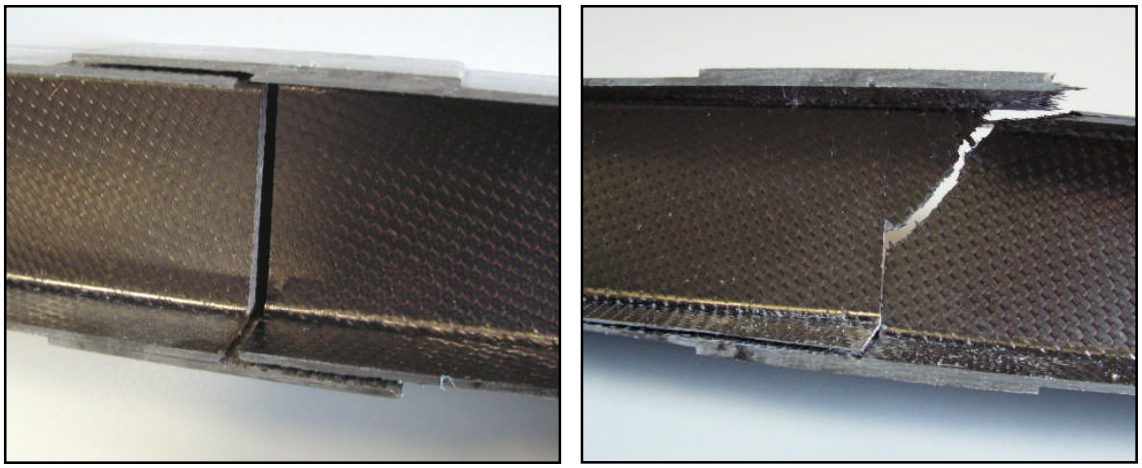

Figure 6.14 – Failure mode switch for z-pin reinforced patch joints; patch delamination (left) and laminate fracture (right)

The most significant observation of the z-pinned joint tests was that, between z-pinned patch overlap lengths of 15 and 25 mm, a change in the mode of failure occurs. Up to

the point of failure mode transition, patch delamination from the I-section occurs. Beyond, the joints fail by catastrophic laminate fracture (see Figure 6.14).

For the z-pinned specimens which failed by patch delamination evidence of mode I loading on the z-pins is observed despite the global mode II shear loading condition on the joint. The mode I loading occurs due to the unbalanced laminate stacking sequence of the I-sections. Figure 6.15a shows an array of four z-pins, remaining embedded in the patch, having pulled out from the I-section flange. The points to be noted from the SEM images are that there are no obvious large resin pockets associated with the z-pins and that the fibre fracture does not occur in line with a row of Z-pins, or even in one plane. The magnified image in Figure 6.15b shows detail of the z-pin chamfer introduced during the manufacture of the Z-pin preform. There is evidence of damage within the pin itself but the image indicates a good interface between the z-pin and the laminate.

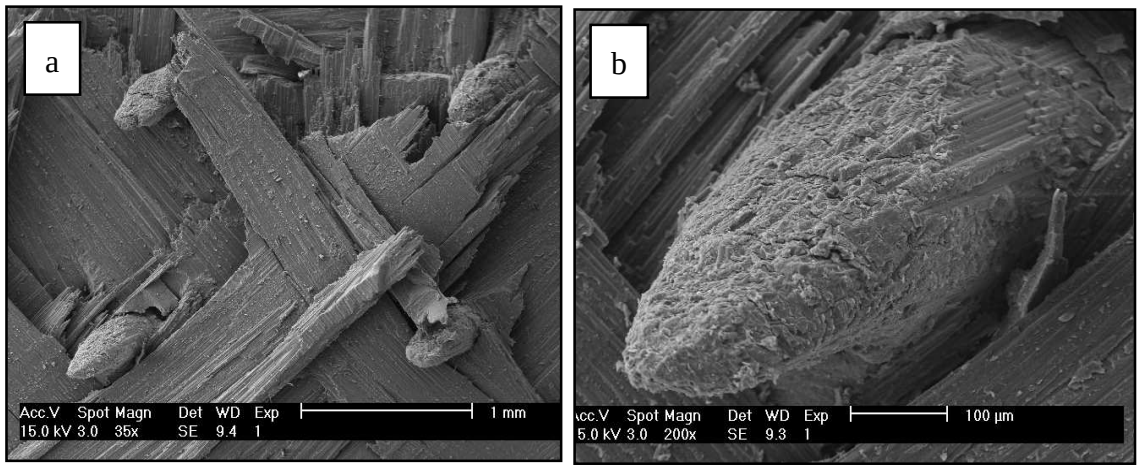

Figure 6.15 – SEM micrographs showing Z-pins in failed I-section laminate surface

Given the presence of the pull-out mode, the effect of the z-pin block on delamination propagation can be expected to be highly dependent upon the thickness of the 'patch plus flange' laminate. This dependence has been evaluated in previous study in the author's group [2] and is illustrated in Figure 6.16.

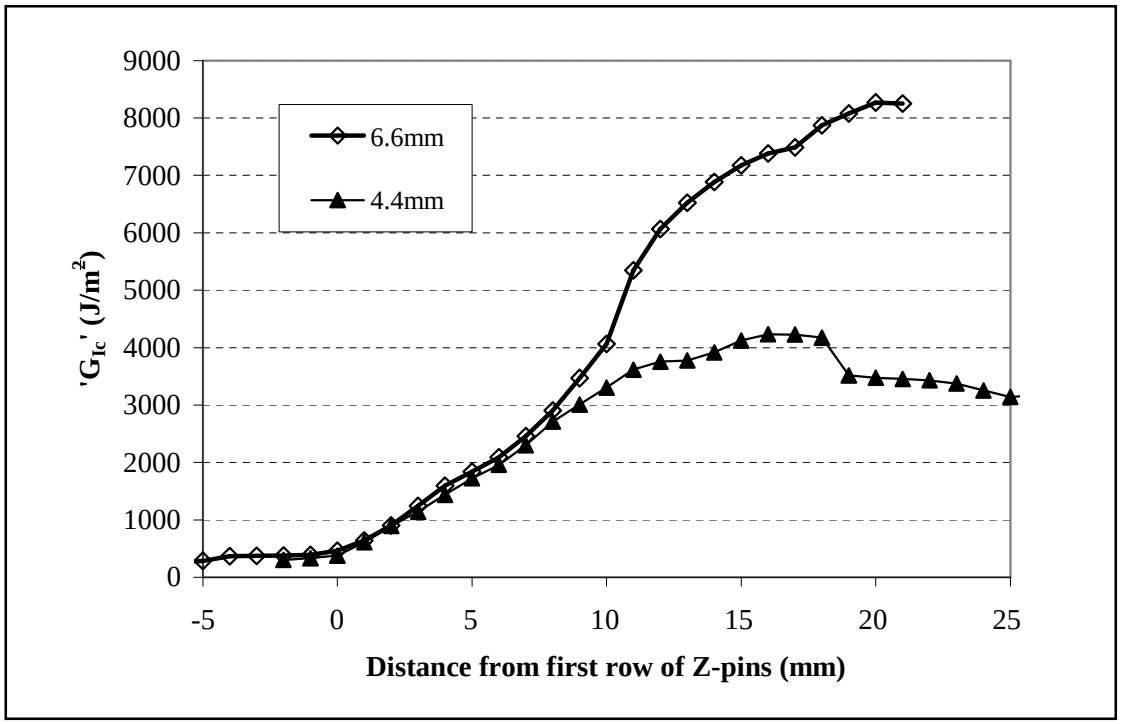

Figure 6.16 – Effect of laminate thickness on the apparent toughness in a G986/M21 carbon fabric/epoxy laminate (0.5 mm diameter Z-pins, 2% areal density, insertion depth 4.4 mm) from [2]

The occurrence of laminate fracture past the failure mode transition point explains why an ultimate load plateau is reached for the z-pinned joints. There is a reduction of 18 kN in ultimate load capability from the upper limit for a z-pinned I-section to the z-pinned patch joint plateau. The reasons for this difference cannot be explained fully from the information obtained from these tests results. Possible causes are that this is either a joint design effect, possibly due to the stress raising square edged patch design, or an interaction between the z-pins and the laminate material on a meso / micro-mechanical scale.

These results suggest that the trigger for the failure mode switch is the quantity of z-pin reinforcement used and that at a critical quantity of z-pins premature fracture of the joint laminate can occur. The z-pinning arrangement used is the standard 2 % square array supplied by Albany Int. It is entirely feasible that these z-pinned joints could benefit from a more tailored z-pinning arrangement. The purpose of this would be to maintain the ultimate load benefit but optimise the arrangement of the critical number of z-pins before the failure mode shifts. In regions of high stress concentration, particularly at the square patch edge where there is a sharp drop in stiffness to the I-section flange, this

could provide great benefit. Some simple suggestions to demonstrate a more optimised arrangement are given in Figure 6.17.

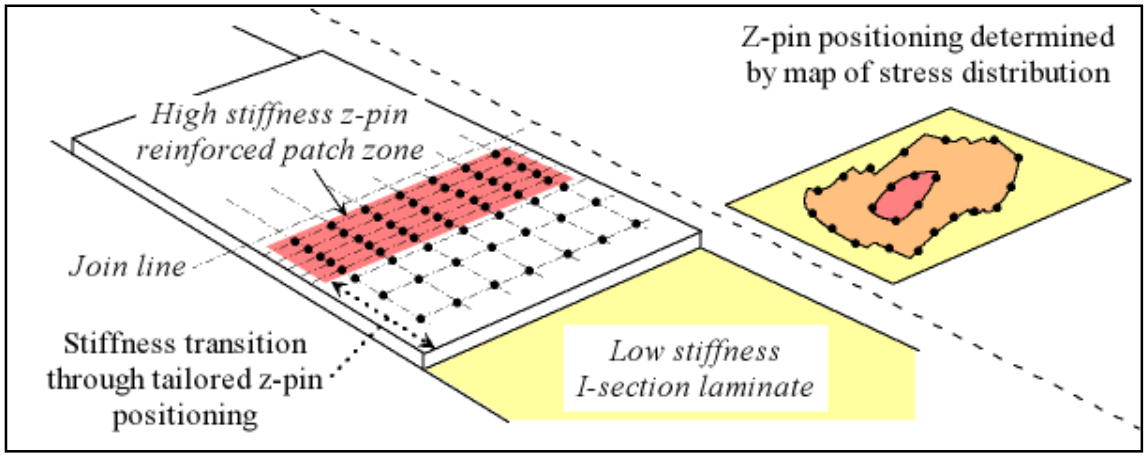

Figure 6.17 – Revised z-pin layout possibilities for patch joints

6.2.2 Set 2 – Damage tolerance assessment

This set of tests, completed by the author and Profeta [197], looked at the ultimate load capability of the I-section joints after a controlled impact of 10 J. The damage was introduced to the two patches directly above the join line, the weakest part of the structure, to represent a worst case scenario. A single joint geometry was used for this study in which the patch design was modified to include a tapered edge which gradually reduced the patch thickness down to the I-section flange surface. This modification was made to address some of the stress concentration observations highlighted in the previous set of tests. The z-pin reinforced joint data are compared against controls in Table 6-3.

The control specimens all failed by delamination of the patch from the I-sections, the z-pinned specimens all failed by I-section laminate fracture initiating at the z-pin block. Having replaced the square edged patch with a tapered edge design, the ultimate load recorded for the both the z-pinned and control tests is still 26 % below the upper z-pinned limit for these joints as determined in the Set 1 tests. The failure mode transition and the difference between the upper z-pinned I-section limit and the z-pinned patch joint plateau can therefore be attributed to the presence of z-pins.

Test type	Av. ultimate load [St. Dev.] (kN)	Av. extension at ultimate load [St. Dev.] (mm)	Av. failure energy [St. Dev.] (J)
Z-pinned	41.6 [4.4]	2.4 [0.2]	51.6 [11.8]
Control	41.2 [2.0]	2.3 [0.1]	48.4 [5.0]

Table 6-3 – Impacted I-section joints results summary (inc. Type 3 patch design)

The polished surfaces shown in Figure 6.18 were obtained by sectioning the 'patch plus flange' laminate at the row of z-pins nearest to the join line, and at an equivalent location for the control joints.

Comparison of microscope images of the sections shows that the presence of the z-pin block limits the sideways extent of the impact induced delamination. The result of this constraint is to transfer the failure into the web of the joint. Similar effects have been noted by other researchers in the testing of T-joints [88].

The results from this set of tests again show the failure mode change due to the use of z-pins. The z-pinned joints show an increased damage tolerance compared to the controls. The ultimate load for the z-pinned joints remains the same as the controls but the energy to failure increases by 7 %. The 20 % ultimate load knock-down, which was measured for the z-pinned joints in the previous set of tests, is not visible in the results obtained here. This can be attributed to the limitation of impact damage provided by the z-pins due to the fact that they have now been subjected, through impact, to the mode I loading for which they are best suited. This is not a stand-alone observation, similar effects have been seen in compression after impact tests [137]. These findings suggest that a well designed joint containing z-pin reinforcement will automatically be damage tolerant.

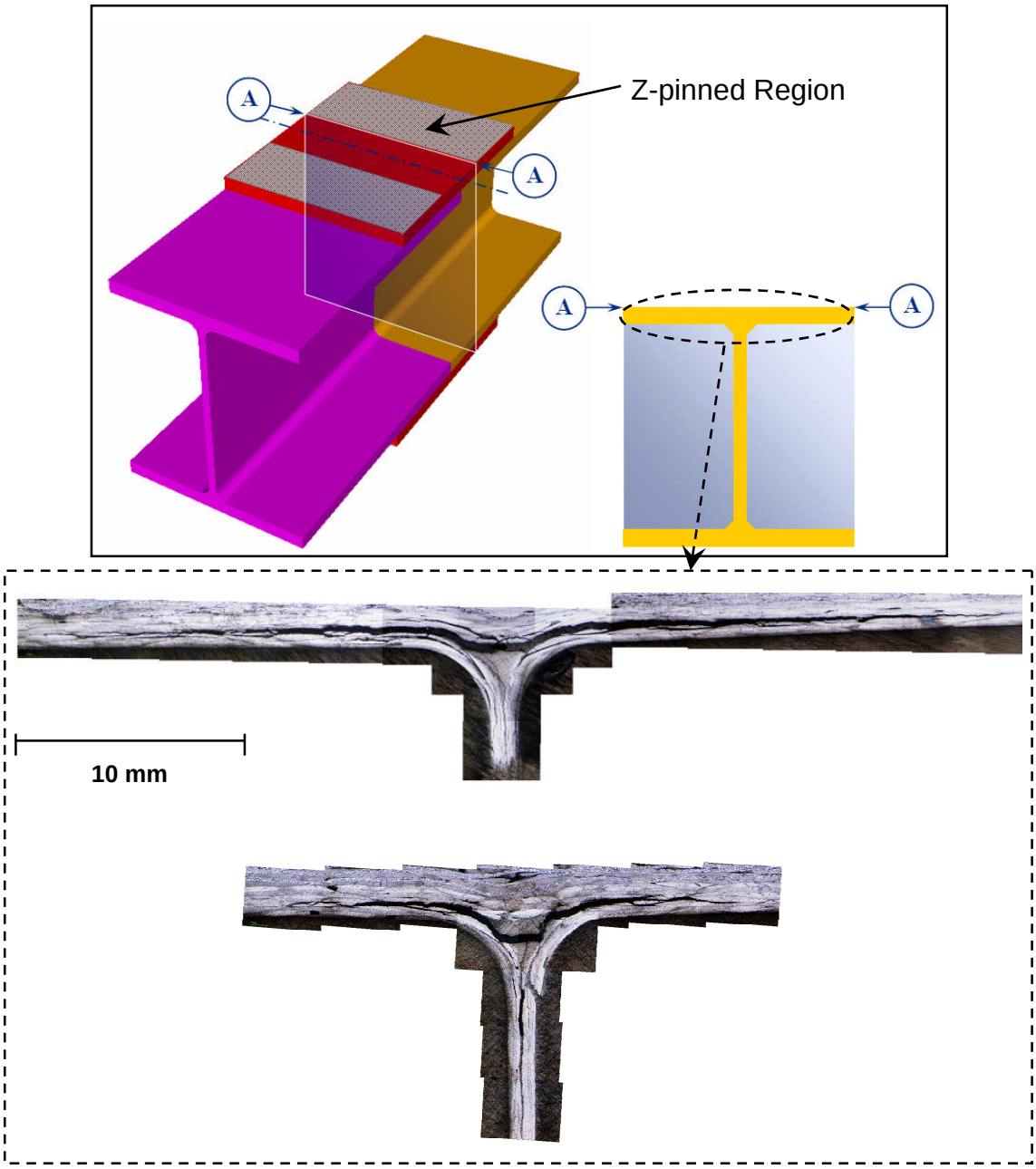

Figure 6.18 – Polished cross-sections around the I-section 'noodle' region (web-flange junction) showing extent of impact induced delamination for failed damage tolerance I-section test elements, control (top) and z-pinned (bottom). The I-section schematic (above) shows the location from which the polished cross-sections (below) were taken.

6.2.3 Set 3 – Re-assessment of failure mode transition

This final set of I-section joint tests was undertaken with Kalchman [198] in an attempt to reinforce the findings regarding the failure mode transition through the use of z-pins with a larger data set. The material system used for this set of tests was 8552 / 3K8H / HTA. A similar approach to that used for the Set 1 tests was adopted for joint strength assessment. The overall patch design and z-pin reinforcement layout were as described in Section 4.3.

This study was extended further to test joints held together solely by z-pins also. To achieve this, a release film was placed between the patch and the I-sections; z-pins were inserted through the interface as normal leaving no material laminate connection. With the Set 1 tests highlighting a need for analytical tools to assist the design of z-pinned structures, these tests were included to isolate the performance of the z-pins in the joint. Table 6-4 details the results obtained for the 8552 / 3K8H / HTA I-section joints tests, Figure 6.19 plots these results as a failure envelope.

Test type	Overlap length (mm)	Ultimate load [St. Dev.] (kN)	Extension at ultimate load [St. Dev.] (mm)	Failure energy [St. Dev.] (J)
Controls (resin only)	10 mm	26.5	1.6	19.9
	20 mm	37.3	1.9	33.3
	25 mm	46.3	2.3	51.1
	30 mm	53.0	2.7	69.4
	40 mm	64.5	3.1	97.7
	50 mm	73.0	2.4	87.8
Z-pins (z-pins only)	10 mm	15.1	1.0	7.4
	20 mm	18.2	1.0	8.7
	30 mm	26.3	1.5	18.5
	40 mm	25.1	1.6	18.5
	50 mm	29.6	1.1	17.5
Z-pinned (resin + z-pins)	10 mm	33.5	1.9	29.4
	20 mm	44.3	2.3	46.7
	30 mm	62.8	3.0	88.0
	40 mm	54.7	1.7	45.4
	50 mm	96.7	3.0	151.7
Pristine	n/a	104.2 [2.8]	4.0 [0.5]	227.9 [49.9]
Z-pinned pristine	n/a	105.5 [3.5]	4.0 [0.1]	216.7 [9.0]
No patch	n/a	16.7 [0.9]	1.0 [0.1]	8.0 [1.1]

Table 6-4 – 8552 / 3K8H / HTA I-section joints test results summary

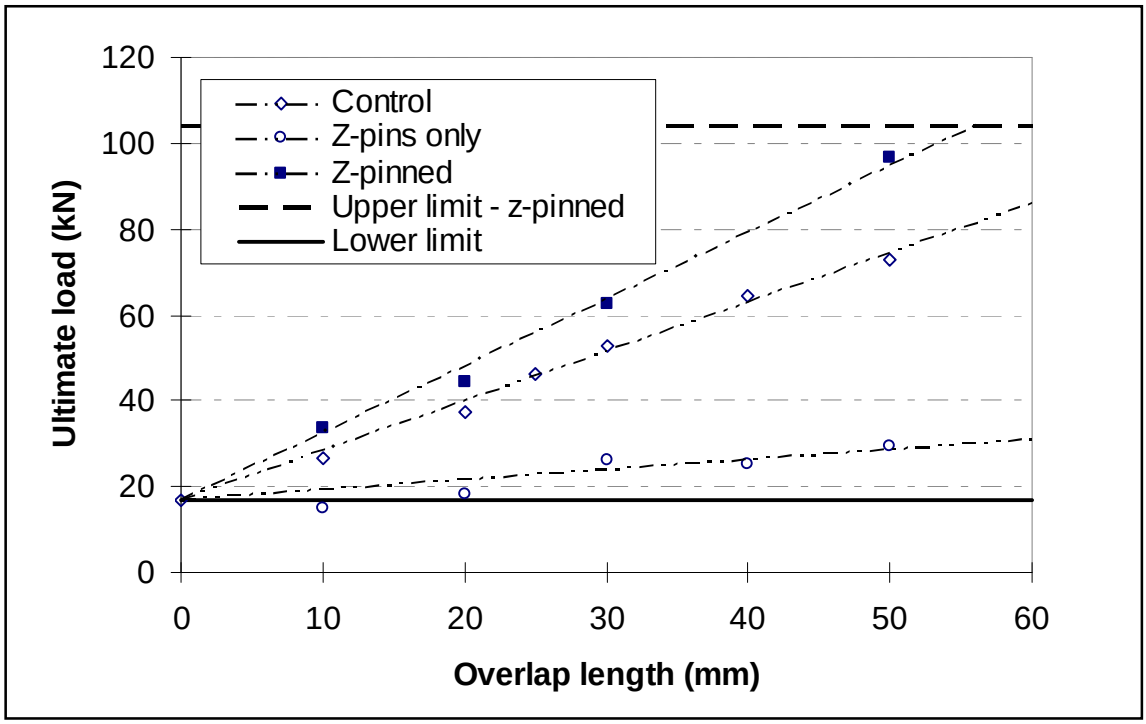

Figure 6.19 – Failure envelope for 8552 / 3K8H / HTA I-section joints (inc. Type 4 patch design)

The *pristine* and *z-pinned pristine* tests failed by catastrophic laminate fracture. The fracture for the *pristine* tests initiated from the bonded test fixtures and therefore does not represent the true upper limit for the I-sections. Failure of the *z-pinned pristine* tests initiated at the edge of the z-pin block. Failure for both of these test types occurred at the same load and hence the knock-down due to the presence of z-pins cannot be seen.

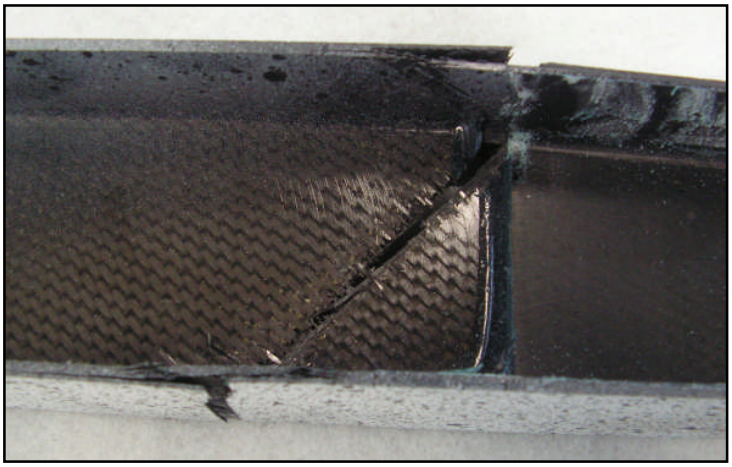

Figure 6.20 – Laminate fracture initiating from the test fixture

The *no patch* tests failed by fracture of the join line as was observed for the Set 1 tests. The tests performed on the *control*, *z-pins only* and *z-pinned* joints all failed by delamination of the patch from the I-sections. For the joints manufactured from the 8552 / 3K8H / HTA material there was no transition of failure mode.

The ultimate load for the control joints again increases linearly with increasing patch overlap length, as expected, due to the resin strength and contact area of the patch dominating the delamination failure mode. The control results have been extrapolated to the intersection with the upper load limit. The patch overlap length that would initiate laminate failure of the I-sections is predicted to be 75 mm. The z-pinned joints show a linear trend also with ultimate joint load rising with increasing patch overlap length. The length at which the z-pinned joint load intersects with the upper limit is estimated to be 55 mm.

Whilst noting that the design of the patch is similar but not identical for the Set 1(patch type 2) and these Set 3 (patch type 4) tests, the ultimate loads obtained show that the 8552 / 3K8H / HTA material system is stronger compared to that used in the Set 1 tests. This material system, in the range tested, shows no susceptibility to z-pin induced failure effects and this allows z-pinning to have a beneficial effect on the ultimate load capability of the joint. There is a suggestion in the results that the load capability of the *z-pinned* joint is equal to the summation of the *control* and *z-pins only* joint loads.

The absence of failure mode transition in this case is an important observation. Comparison with the Set 1 tests show that the effects of z-pinning are different for the two material systems tested. The loads at which the various modes of failure occur for these I-sections are dependent on both the material type and the presence of z-pins. In general, the use of z-pins may or may not affect the interaction of the failure modes depending on the laminate geometry and material properties. In some instances, simply reinforcing a structure with z-pins may provide the desired effect, in others it can lead to unexpected results. This unpredictability is unsatisfactory for aerospace and automotive composite applications. These results reinforce the need for greater ability to analyse the effects of z-pinning on structures at the design stage.

6.3 Observing z-pin reinforcement in a high performance crash structure

The change in failure mode through the use of z-pins has been observed outside of the experimental tests carried out as part of this work. The following examples show impact safety qualification tests on the rear crash structure (RCS) of a Formula 1 racing car. Two of these structures are compared, a control manufactured from carbon / epoxy composite and a similar structure reinforced with z-pins. The reason for z-pin use was to provide improved energy absorption for the composite structure, as has been found in testing of the crash tubes in this work.

The sequence of images in Figure 6.21, taken from a high speed video recording of the test, shows the impact on the control RCS. The RCS crushes progressively, absorbing the energy of the moving impactor in the process. The energy is absorbed through fracture of the composite; the debris can be seen flying off. The impactor is stopped within the length of the structure and recoils.

The sequence of high speed video images, shown in Figure 6.22, is from the impact test on the z-pinned RCS. If the trends observed from the crash tubes testing are directly transported to this structure then higher energy absorption can reasonably be expected. This would translate, in visual terms, to the impactor being stopped within a shorter distance of the z-pinned RCS compared to the control. In fact this does not happen. What is observed is a severe change of failure mode; from initial crushing of the composite structure to a global buckling failure and a section of the structure flying off completely. Furthermore, the buckling failure occurs at the edge of the z-pin reinforced zone. The change in the expected failure behaviour of the z-pinned RCS caused it to underperform. The z-pinned RCS did not absorb the impactor energy and the impactor travelled right through and hit the mounting wall.

The cost involved in manufacturing and testing structures such as these does not make multiple tests on differing z-pin reinforcement arrangements a viable option.

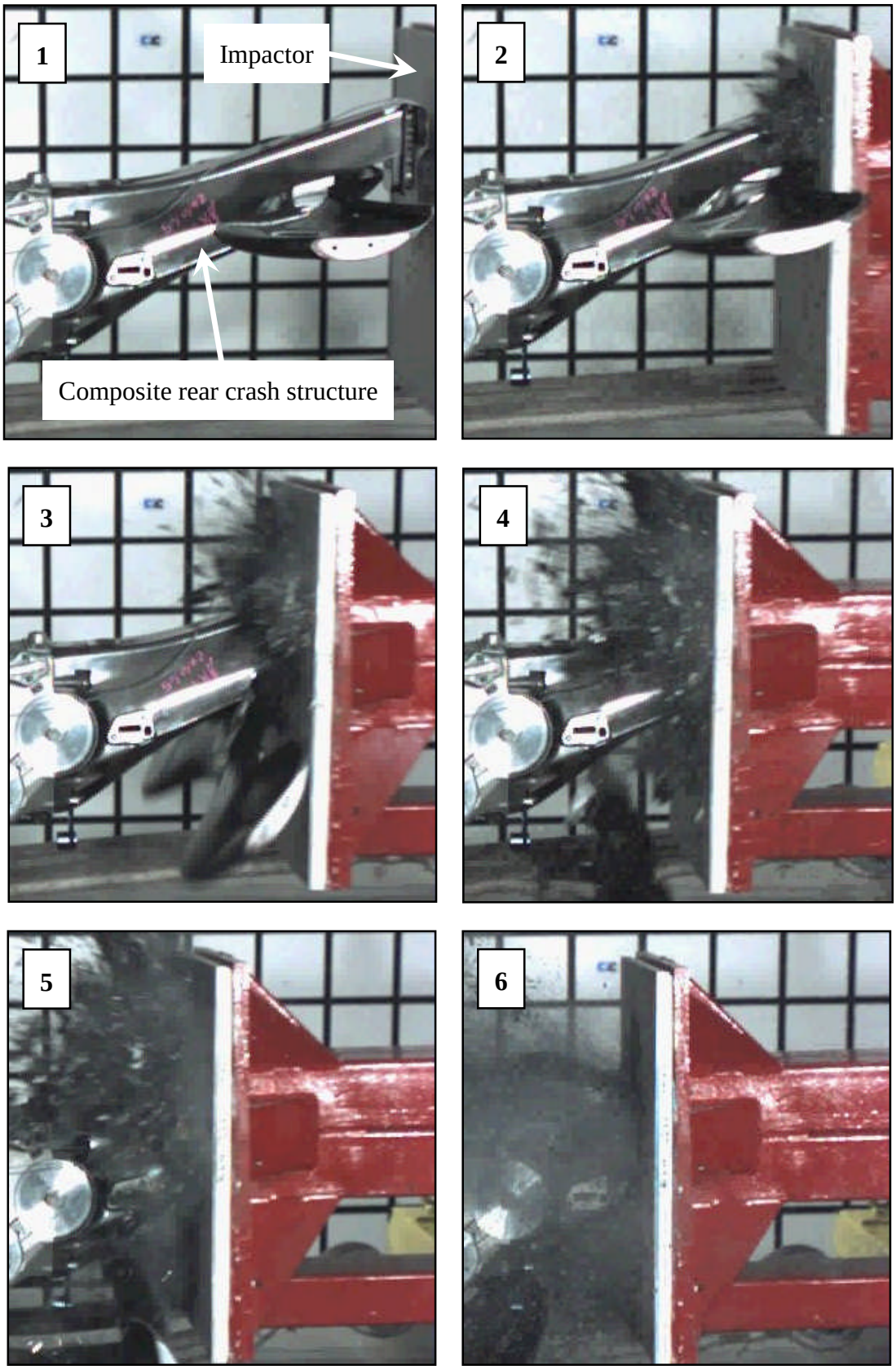

Figure 6.21 – High speed photography stills of impact qualification test on a Formula 1 rear crash structure

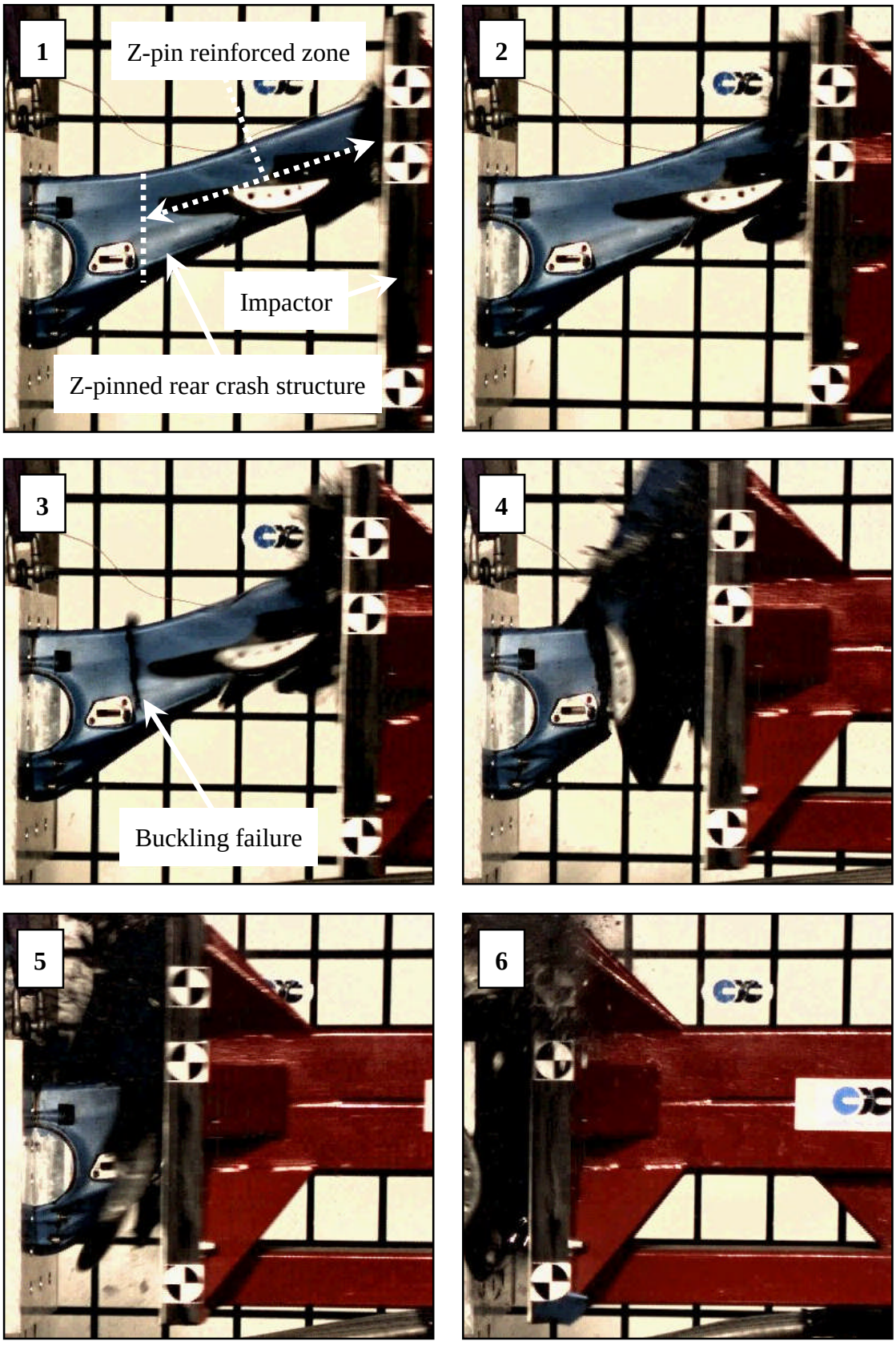

Figure 6.22 – High speed photography stills of impact qualification test on a z-pin reinforced Formula 1 rear crash structure

6.4 Failure management of z-pinned structures

Structural design in general is an iterative process. The areas of a structure which are most likely to fail are monitored closely during the design process and redesigned if necessary. Improving the strength of the weakest area of a structure sufficiently will move the failure location to the next weakest part. In this case, the failure mode may change also.

The I-section tests in Set 1 highlight an important development which needs to be made to the way in which a designer uses z-pin reinforcement. The use of z-pinning to improve delamination resistance is proven and documented but there are no examples in published literature of the consequences this has on a structural component. In simple terms, designers at present do not appear to show consideration for the knock-on effects that retarding delamination by z-pinning (or indeed stitching or tufting) has on a structure; the next point at which failure is likely to occur is never considered. The reason why further consideration is not made is almost certainly due to a suitable means of assessment being unavailable.

The Set 1 I-section tests have shown that the use of z-pins to reinforce the original weakness of the structure (the patch / flange interface delamination) was sufficient to shift the failure to the next weakest part. This happens to be in the same location but is of a different failure type (laminate fracture). However, the load required to fail the structure for the new failure type is actually lower than was required originally. The z-pinned Formula 1 rear crash structure is another example where this is the case.

These effects produced by z-pinning are most definitely structure specific. They will be prevalent in certain materials and not in others (e.g. not seen in the Set 3 I-sections) and be dependent on the loading conditions on the structure. Modes of failure in which the in-plane properties of the material are important will be most susceptible.

Z-pinning of composite structures has been shown to alter the mode and location of failure. In some cases the alteration is favourable, in others not. In cases where z-pins

have been used failure is often due to the z-pins and has occurred on or near the edge of the z-pin reinforced zone. These crash tube, I-section and rear crash structure examples would have benefited from a more structurally tailored use of z-pins. It is evident that the use of z-pins needs to be considered at the design stage rather than as a simple fix for delamination in an existing structural design. Users of z-pin reinforcement should be encouraged to view z-pinning as an integral structural component rather than a ‘repair kit’. In order for this to happen, tools capable of accurately predicting the performance of z-pins, in all modes of failure, need to be developed and made available. The total management of structural failure and design optimisation which is possible through the use of z-pins is a big incentive. Cases of unexpected structural under-performance due to z-pin use can be reduced. Without a design oriented approach, expensive trial and error experimental testing remains the only option.

Chapter 7

Developing a design tool for intelligent local reinforcement

This chapter begins by detailing the construction of a finite element model of the I-section test elements from which the performance of alternative arrangements of z-pin reinforcement could be assessed. This modelling approach targets the use of a new element which facilitates the simulation of mode II z-pin behaviour at a structural interface.

The interface elements used require a traction response to be described so as to represent the interface properties correctly. The z-pinned interface is subsequently separated into the laminate material response and the response of the z-pins. The mode II experimental testing and analysis undertaken to develop the separate traction responses is described. The traction responses developed are assessed separately using finite element models of the mode II ELS test.

7.1 Application of FE modelling

Adoption of a Finite Element Analysis (FEA) approach enables z-pin reinforcement modifications to be trialled virtually rather than by an extensive experimental testing approach. Many factors affected the decision to use FEA for this purpose; economy of time was one considerable advantage. However, the main reason was that throughout the work detailed up to this point, it had become increasingly apparent that the manufacturing inconsistency creates uncertainty in the performance results and would become a particular problem when trying to place z-pins in very defined, specific locations.

7.1.1 MSC.Marc software overview

Finite element analysis (FEA) is a critical part of the virtual design process. Many of the FEA programs available are ‘linear’, meaning that they can only study parts that deform a small amount and do not exceed the linear elastic range of the materials. When dealing with structures such as those detailed in the previous chapter and loading them until failure, FEA tools capable of non-linear analysis are required. MSC.Marc is a non-linear FEA program and was the selected software for developing a design methodology intended to enable selection of z-pin placement.

MSC.Marc enables assessment of the structural integrity and performance of parts undergoing large permanent deformations as a result of thermal or structural load. The types of behaviour the software can address include geometric nonlinearities such as bending and material nonlinearities such as yielding and damage. MSC.Marc can also simulate deformable, part-to-part or part-to-self contact under varying conditions that include the effects of friction.

MSC.Marc can be driven through aerospace industry standard pre-processors (e.g. Patran), however, the processor used for this work was Marc Mentat. MSC.Marc offers an extensive library of material models, along with a library of 175 elements for

structural, thermal, and fluid analysis. One particular element on offer, the type 188 interface element, was a key reason for the selection of the MSC.Marc package.

Interface elements, as defined by Harper et al [199] are specialised finite elements used to simulate crack initiation and propagation in numerical models. The use of interface elements has increased recently for modelling composites, particularly in relation to delamination [200-207] and failure of adhesive bond-lines [208-211]. The previous modelling technique of choice, the Virtual Crack Closure Technique (VCCT) is limited to the tracking of a single crack path. Interface elements offer the advantage of including both crack initiation and propagation and the ability to model multiple crack paths. In this respect, computationally expensive crack-path following algorithms are no longer needed. A further advantage of using interface elements over the VCCT technique is that the direction of crack propagation does not need to be known in advance. Cracks therefore have the potential to propagate along any path where interface elements are placed which is more representative of real propagation in composites. The use of interface elements is often referred to as 'cohesive-zone' modelling. Cohesive-zone modelling is typically used when the conditions of small-scale crack bridging or linear elasticity of the interface are violated [210].

7.1.2 Type 188 interface element

The interface element available in MSC.Marc is a recent addition to the package and is of particular interest to this work because of its ease of implementation. Alternative methods for interface modelling require the use of multiple spring elements which are far more intricate to build into a model [144].

The exact interface element used within the MSC. Marc FE software was element 188 described as an 'eight-node three dimensional interface element'. This can be used to simulate the onset and progress of delamination. Figure 7.1 shows the connectivity of the 188 interface element which is typically used to model the interface between different materials, where nodes 1, 2, 3 and 4 correspond to one side (the bottom) of the interface and nodes 5, 6, 7 and 8 to the other (the top).

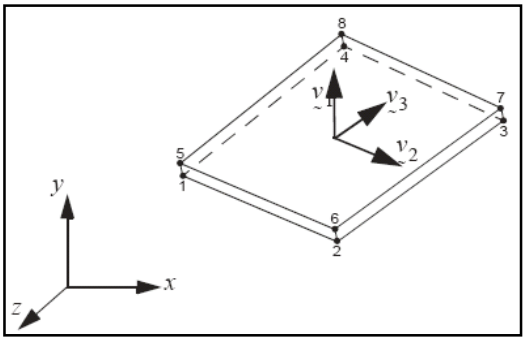

Figure 7.1 – Connectivity of element type 188 from [212]

The stress components of the element are one normal traction and two shear tractions, which are expressed with respect to the local coordinate system (v_1, v_2, v_3). The corresponding deformations are the relative displacements between the top and bottom face of the element. The element is allowed to be infinitely thin, in which case the faces 1-2-3-4 and 5-6-7-8 coincide.

Within MSC.Marc the constitutive behaviour of the 188 interface element is defined via the 'COHESIVE' model definition option. The traction response of the 188 element can be described by the user in two ways, either through the MSC.Marc options available 'on screen' (as shown in Figure 7.2) or by using a user subroutine which the software accesses separately during analysis. Inputting the required traction response on screen limits the user to very basic interface response representations by allowing only the cohesive energy plus the critical and maximum opening displacements of the traction law to be set. These limit the responses to linear or exponential representations. The use of user subroutines enables the user to describe more complex material responses but requires the use of FORTRAN programming language.

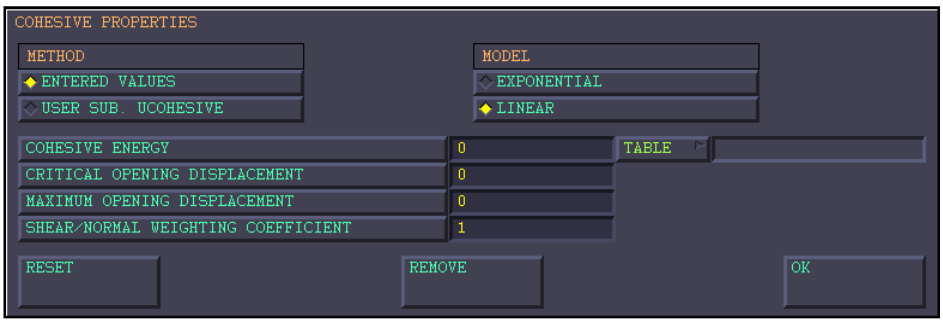

Figure 7.2 – Cohesive element properties panel in MSC.Marc

There is no documentation provided with the MSC.Marc software for assistance in FORTRAN programming and therefore use of subroutines requires separate development and verification to ensure the correct cohesive interface response is achieved. Figure 7.3 shows representation examples of cohesive interface responses using the MSC.Marc on screen options and a customised user subroutine. Clearly, for more complex cohesive interface responses, limiting the response to critical and maximum opening displacements only is not sufficient.

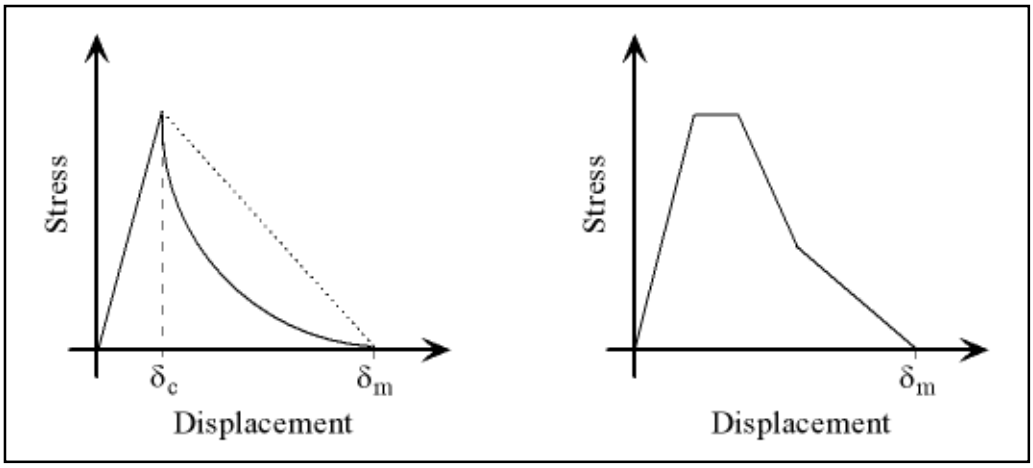

Figure 7.3 – Simple interface response (left) and interface response profile made possible by using a FORTRAN user subroutine (right)

7.1.3 Target study identification and FE modelling aims

As the previous chapter has shown there is a real need for understanding the effects of z-pin use on failure modes and furthermore, a means by which z-pin positioning can be altered to provide the desired structural response. The issues discussed in Chapter 4 concerning rodstock quality and processing repeatability have shifted the focus away from an experimental testing approach to an FE modelling one. The MSC.Marc software package provides the basis on which attempts to represent the behaviour of a z-pinned structure can be made virtually.

The experimental work described in the previous chapter posed the question as to whether there was a superior z-pin arrangement for reinforcing the specific structures tested. There appears to be a critical amount of pins which resulted in a change of the

failure mode in the I-sections, but was the z-pin arrangement used optimised? The I-section test elements were selected as the structure to take forward as an FE modelling study. The tensile loading of the I-sections produces a predominantly mode II shear loading component on the z-pinned patch-flange interface providing an opportunity to investigate this mode of failure in detail. Furthermore, the quasi-static loading of these structures negates the need for collection of dynamic material data as would be needed for modelling the crash tubes. Lastly, the thin wall geometry of the I-sections lends itself to FE representation using shell elements which assists in keeping the FE processing requirements low.

The aim of the modelling work was to build a tool which would allow the position of z-pins reinforcing a mode II delamination interface to be altered and the effects on mechanical performance to be assessed. The second aim was to use this capability to offer an alternative arrangement pattern for z-pin reinforcement of the patch.

The six major developmental steps for building the FE model / design tool are detailed below.

i. Accurate representation of I-section geometry (detailed in Chapter 8)
ii. Generation of reliable mode II response data for z-pins
iii. Generation of mode II data for laminate materials
iv. Representation of laminate material mode II response using type 188 interface element
v. Representation of z-pin mode II response using type 188 interface element
vi. Implementation of the combined response in the I-section model

7.2 Generating mode II data for woven pre-preg laminate materials

7.2.1 Selection of test method

End Loaded Split (ELS) tests were performed to obtain the mode II interfacial fracture energy and, ultimately, the sliding displacements of the two woven pre-preg material systems. Three other test methods exist from which this mode II data could have been obtained; the End Notched Flexure (ENF), the Stabilised End Notched Flexure (SENF) and the 4 Point End Notched Flexure (4ENF).

A good account of the alternative test methods is given by Troulis [2], however, since then much development has been made to the ELS test configuration by the ESIS TC4 group and the ELS configuration has become the preferred mode II test configuration. The analysis for all of these tests, including the ELS configuration, has been developed for UD materials only. Little published work exists on mode II testing of woven materials as a result [2,126]. None of the mode II tests have been accepted as standards, the data analysis exists in the form of test protocols at the present time.

It is important to clarify these points here as the data required for the interface element traction responses have been obtained using a non-standard test method on a material type for which the analysis has not been developed.

In practice, when testing woven materials rather than UD materials using the ELS test, propagation of the mode II crack is more difficult. The stiffness of ELS test specimens manufactured from these woven materials is less than a typical UD carbon-fibre specimen of similar thickness. This reduction in stiffness requires greater deflection of the test specimen in order to achieve propagation of the crack. Specimen deflections that become too large can inhibit propagation. Furthermore, the fractured surfaces of woven test specimens are much rougher compared to UD specimens. Increased loading

therefore needs to be applied to the woven test specimen to overcome the additional friction induced and achieve crack propagation.

7.2.2 Mode II experimental data collection

As the ELS test procedure has been developed for UD materials the results gathered for the two woven materials using this method are presented alongside those for a 977-2 UD material for comparison.

ELS test coupons were manufactured to the specification described in Section 4.5.1 and prepared for testing as described in Section 5.6. Calibration checks were performed on the test apparatus using a single specimen of each material type. It was found that careful execution of the ELS calibration was critical to achieving good correlation between the ELS test results obtained experimentally and subsequent ELS FE modelling work.

Before presenting mode II data obtained for the two woven laminate materials used the reader should be aware that four analysis methods exist for the calculation of mode II toughness, as first detailed in Chapter 5. The two most recent methods of analysis, ECM and CBTE, are discussed here for the calculation of mode II fracture toughness (G_{IIc}). The ECM analysis method precedes the CBTE method and, whilst both of these methods produce similar values for unidirectional composite materials, it was learned that they do not produce similar G_{IIc} values for woven materials as used here. There are two reasons why the values could differ. Firstly, some difference in the values calculated for G_{IIc} comes from the difficulty in measuring crack lengths accurately for woven materials. Differences between measured crack lengths as used for the ECM method and calculated crack lengths used by the CBTE method were as much as 14 mm in the specimens tested. Secondly, the way in which compliance is determined is different between the two methods. The ECM method updates the load line compliance using a regression analysis of the plot of load line compliance against the cube of crack length.

$$C = C_0 + ma^3 \quad \text{.....(7.1)}$$

where

C_0 is the load line compliance in mm/N

a is the crack length in mm

m is the slope of the C vs. a^3 plot

The gradient of this plot (m) is used in the final calculation of G_{IIc} (see Equation 5.3). The use of Equation 7.1 is based on the assumption that the fracture surface area increases consistently with each increment of crack length. Although the plots of C vs. a^3 for the woven materials tested are similar to those for the 977-2 UD material (see Figure 7.4) the disagreement of mode II fracture toughness values calculated for the two methods (see Figure 7.5) suggests, understandably, that this assumption does not hold for woven materials.

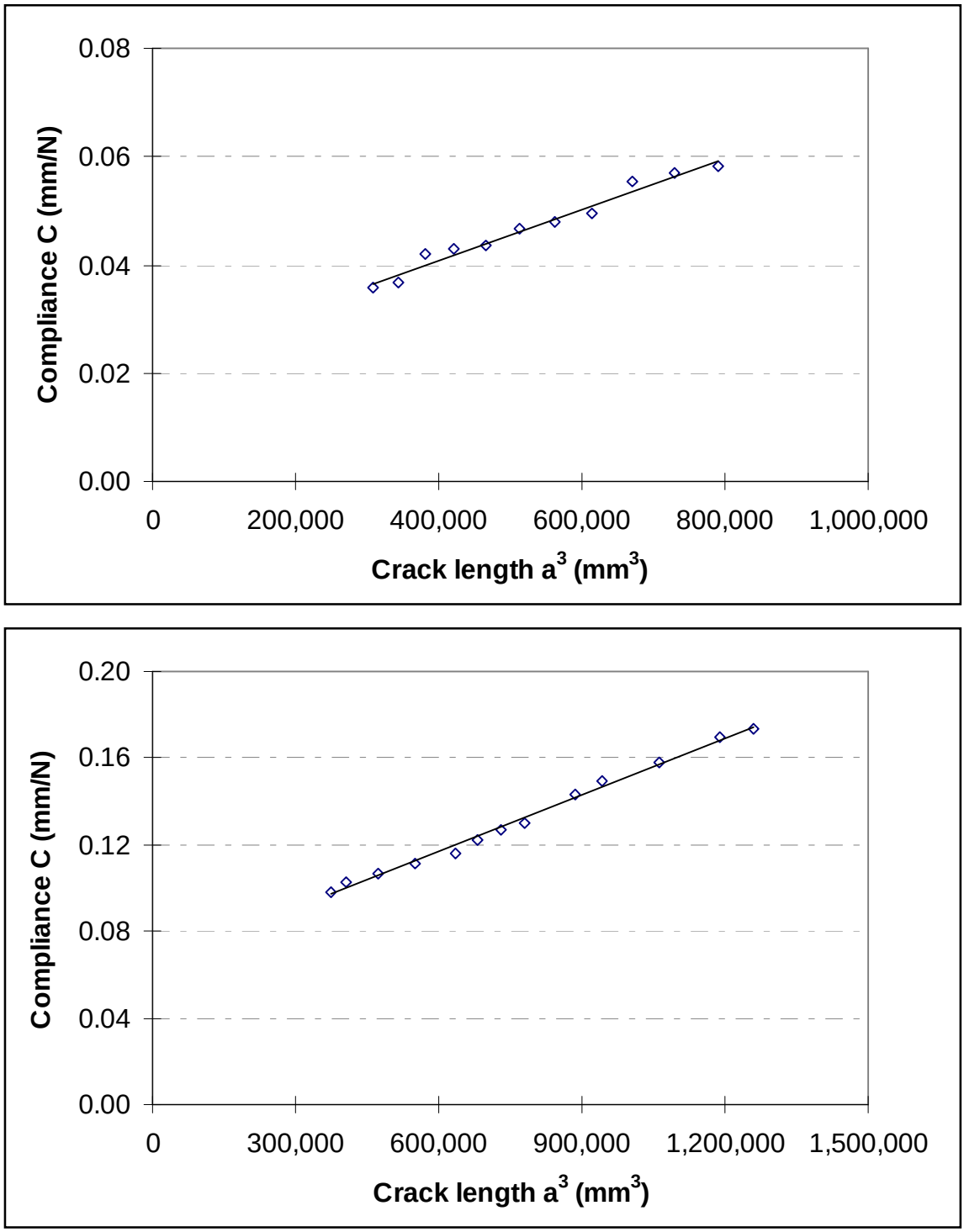

Figure 7.4 – Typical compliance vs. a^3 plots for 977-2 UD (top) and typical woven pre-preg material (bottom)

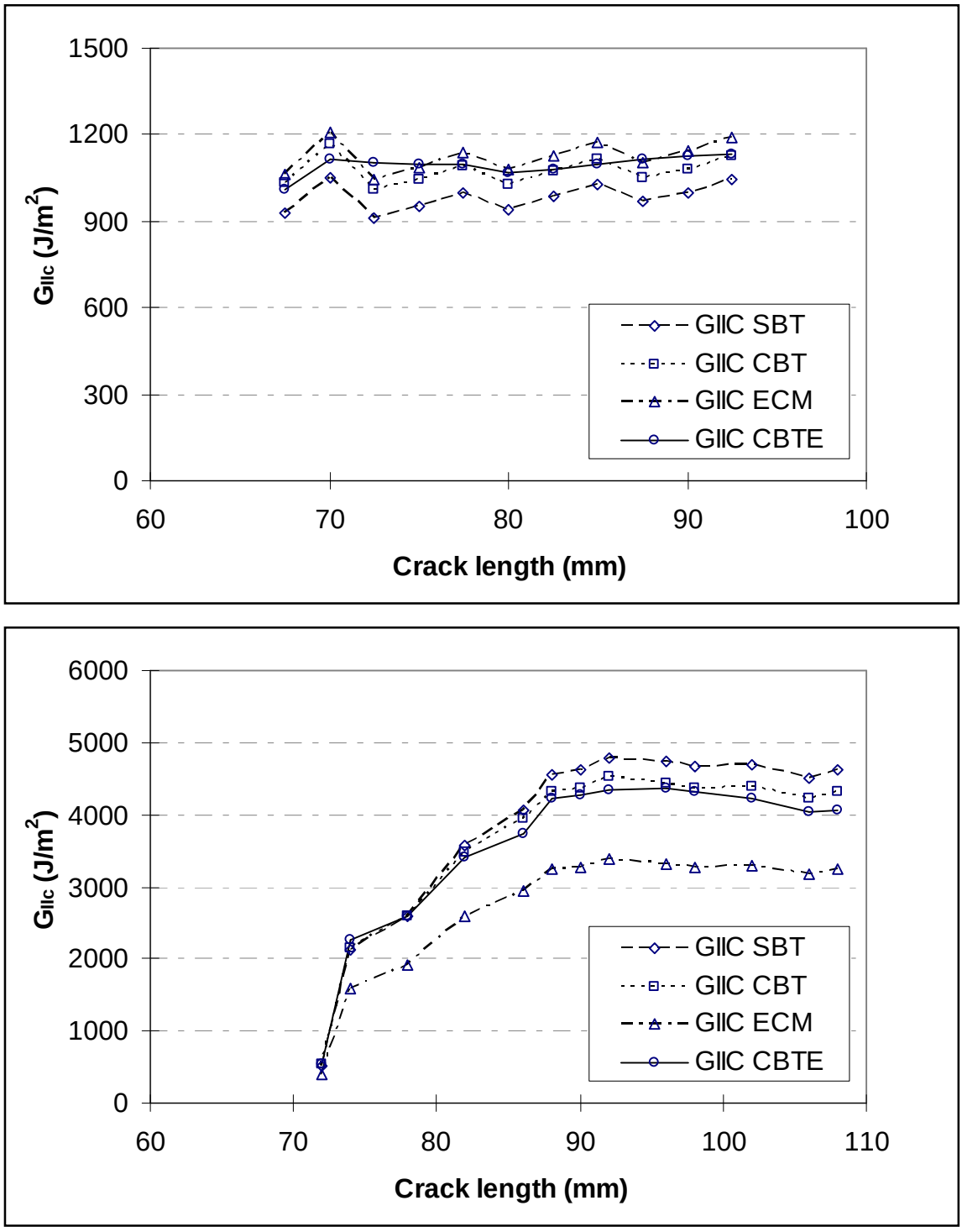

Figure 7.5 – R-curve comparison of mode II fracture toughness calculation methods for 977-2 UD (top) and typical woven pre-preg material (bottom)

What is interesting in the R-curves in Figure 7.5 is that the Simple Beam Theory (SBT), Corrected Beam Theory (CBT) and CBTE results maintain a close agreement with each other whilst the ECM result switches from giving the highest value for the 977-2 UD

material to the lowest for the woven materials. This is true for both woven materials tested. Greater understanding of the reasons for this is required. Based on this, only results from the CBTE analysis method will be presented hereafter.

Table 7-1 shows flexural modulus values for the two woven pre-preg materials measured experimentally using the 3 Point Bend (3PB) test configuration. These are in excellent agreement, as expected, with the tensile modulus values generated using the Component Design Analysis (CoDA) laminate analysis software (see Table 8-3). These flexural modulus values were required for the CBTE analysis method.

Material	Average flexural modulus [St. Dev.] (GPa)
914 / 6K5H / T300	53.0 [2.9]
8552 / 3K8H / HTA	57.3 [4.9]

Table 7-1 – Flexural modulus values measured from 3 Point Bend test

Figure 7.6 and Figure 7.7 show the mode II R-curves obtained for the 914 / 6K5H / T300 and 8552 / 3K8H / HTA woven pre-preg materials respectively. Initiation values have been omitted from these curves so the values shown are for mode II crack propagation only.

The reader will notice that the R-curves for these woven materials exhibit a rising trend. The main reason for the rising R-curves is friction as the two rough surfaces either side of the crack wake are forced over each other. This is accounted for in subsequent representation of these tests in Section 7.3.2.2. Inspection of the failed test specimens also showed a very small amount of crack bridging in approximately one third of the specimens tested. Due to the nature of these woven materials, it is also likely that multi-cracking will have occurred during the test. Inspection of the failed test specimens confirmed that no inter-ply cracking was present other than along the desired interface. However, small cracks propagating away from the crack tip, into fibre tows or resin rich pockets for example, could not be discounted. The presence of multi-cracking in particular is undesirable in ELS test specimens as it invalidates assumptions regarding

the crack surface area in the subsequent analysis. However, crack propagation in woven materials cannot occur without out-of-plane crack propagation, that these tests have confined the crack propagation within one ply thickness is good and the standard ELS analysis can be used to get an indicative fracture toughness value in the absence of alternative, suitable mode II tests.

In all cases tested the G_{IIc} value rises initially as the crack length increases. At a certain point the R-curves level off as a steady propagation G_{IIc} value is reached. In two specimens tested for the 914 / 6K5H / T300 material and three specimens for the 8552 / 3K8H / HTA material, levelling off to a steady propagation state was not observed. However, in the majority of specimens tested a steady mode II propagation state was reached.

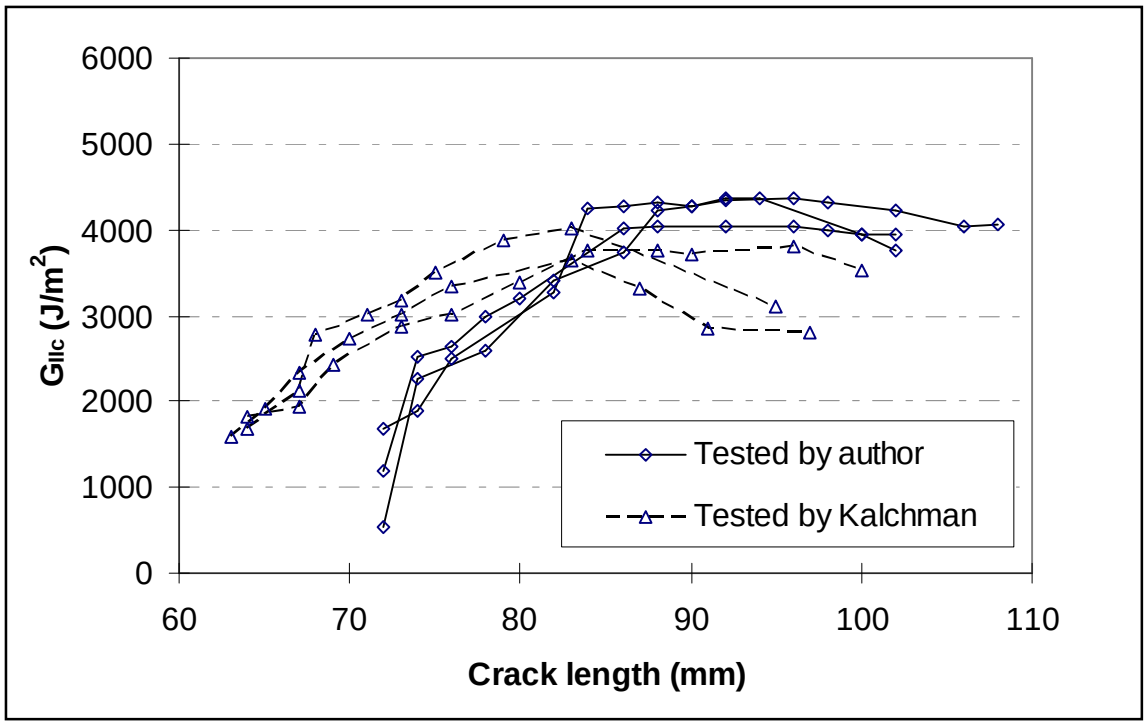

Figure 7.6 – Propagation R-curves from ELS tests on 914 / 6K5H / T300

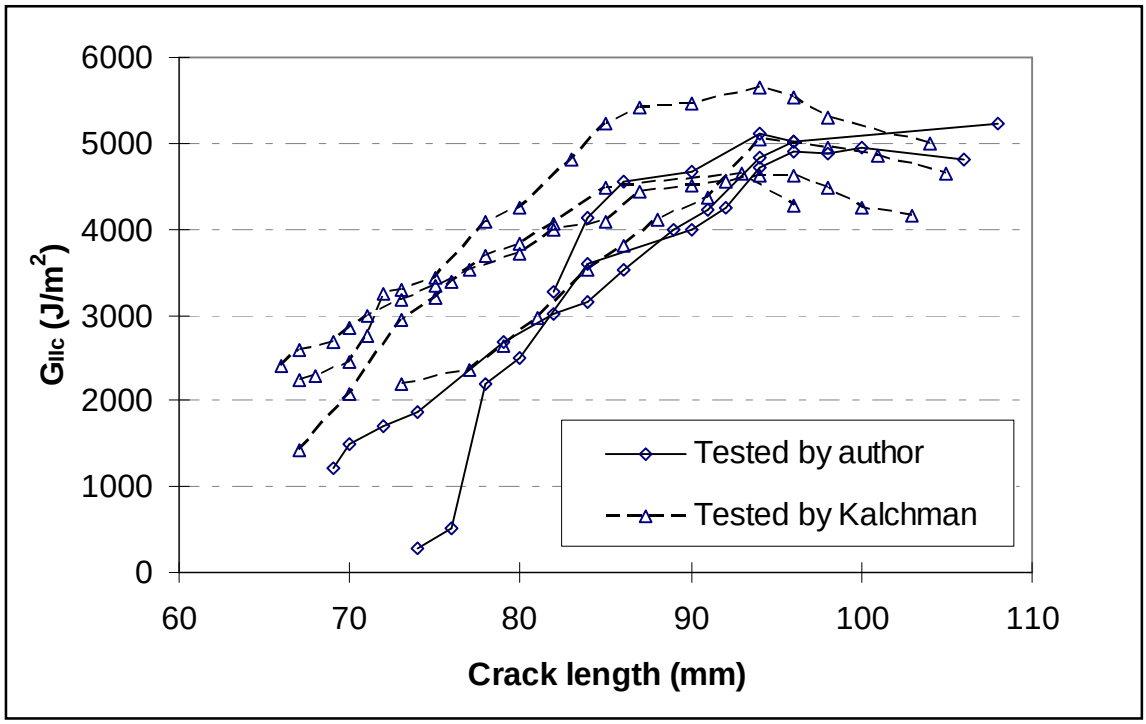

Figure 7.7 – Propagation R-curves from ELS tests on 8552 / 3K8H / HTA

When ELS testing materials which need to settle to a steady propagation state, the length of specimen from which data can be recorded is shortened. In an attempt to overcome this problem a trial specimen of each material was clamped at 150 mm, a distance greater than recommended in the protocol. Ultimately this proved unsuccessful as the increased length meant that the crack growth could not be initiated without very large load line deflection. This is an effect of using the ELS test for woven materials which needs further investigation.

Testing of these woven materials was sensitive to the initial crack length. The R-curve gradients recorded for 914 / 6K5H / T300 specimens (shown in Figure 7.6) are not similar due to the crack length at the start of the tests, carried out by the author and Kalchman [198], being different by approximately 7 mm. The initial R-curve gradient for the 8552 / 3K8H / HTA specimens shows much closer agreement as the initial crack lengths were almost identical. The initial crack length used does not appear to affect the steady propagation G_{IIc} value.

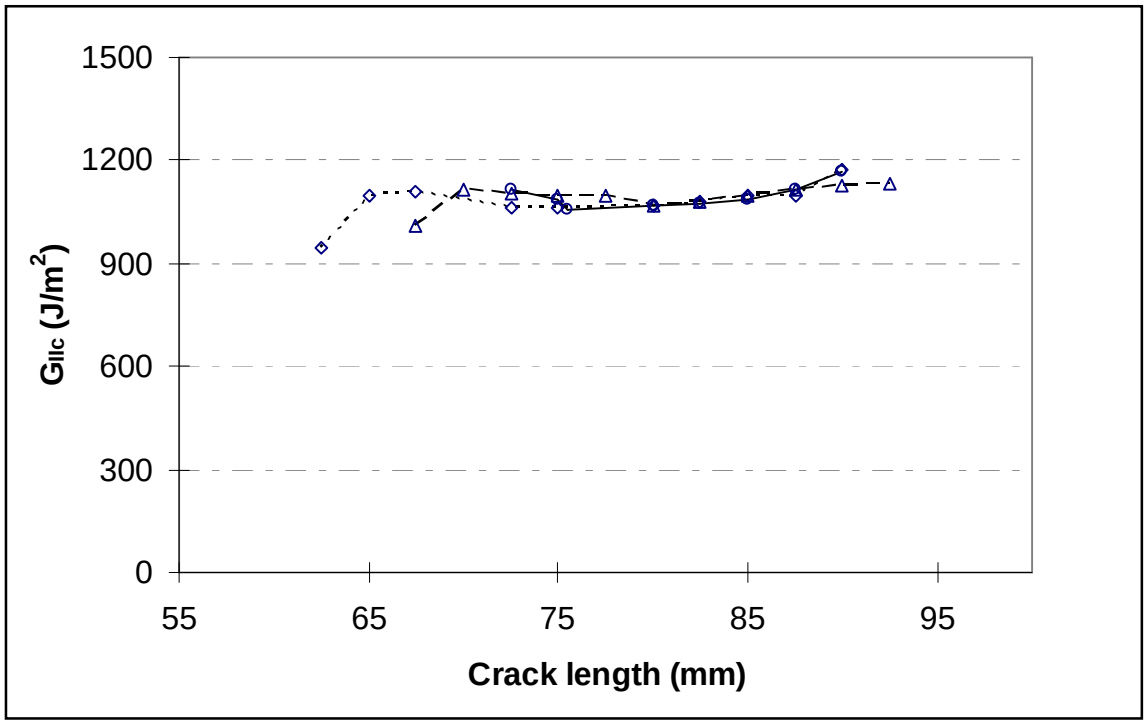

Figure 7.8 – Low R-curve scatter for comparative 977-2 UD material

Simple observation of the individual R-curves recorded for the woven materials shows that the scatter for the woven materials is much greater than for typical UD material as shown in Figure 7.8. This is to be expected as the plane of crack propagation for UD specimens is clean and resin rich whereas for woven materials the propagating crack must negotiate a path past nestled fibre reinforcement tows (see Figure 7.9).

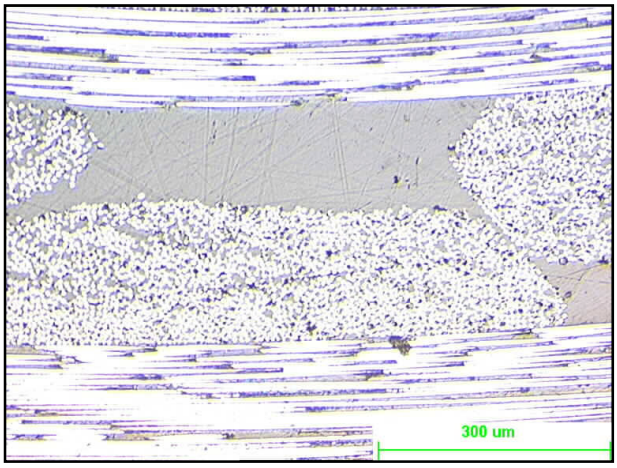

Figure 7.9 – ELS mode II crack plane example for woven materials

The R-curves for the two woven materials which did not display a steady crack propagation state were not considered for further analysis. The remaining R-curves were used to determine the average G_{IIc} value for steady crack propagation. This average is determined from the plateau region in the R-curve generated from each ELS test. These values, calculated for the two woven materials, are given in Table 7-2.

Material	Average G_{IIc} [St. Dev.] (J/m^2)
914 / 6K5H / T300	4113 [247]
8552 / 3K8H / HTA	4850 [421]

Table 7-2 – Average G_{IIc} values deduced for steady crack propagation in woven materials

These average G_{IIc} values are required by the type 188 interface elements in order to represent the woven laminate mode II response. The G_{IIc} values determined here describe the total energy required to fail each interface element under mode II loading conditions.

7.3 Representation of woven pre-preg laminate response using MSC.Marc interface element

This section details the methodology used to produce a traction response for the type 188 interface to give the same mode II behaviour as was measured experimentally by ELS test. Again the work in this section for the woven materials will be compared against the 977-2 UD material.

The first task in producing the traction response is to convert the load line deflection recorded during the ELS test to the sliding displacements required by the traction response. The sliding displacements required need to be relative to the initial crack length (the a_0 position). In order to do this a new analysis was created to convert load line deflection recorded during the ELS test to sliding displacement relative to a_0.

7.3.1 New analysis to convert ELS test load line deflection to a_0 relative sliding displacement

The analysis described hereafter, developed to calculate sliding displacement from load line deflection recorded during the ELS test, is based on Simple Beam Theory (SBT). SBT can be applied to beams in bending for small deflections. The ELS test analysis has used SBT for calculating mode II fracture toughness and its applicability has been extended to larger deflections by using correction factors. This analysis is required because the sliding displacement relative to the original crack position (a_0) cannot be measured during the ELS test. As a final step, a simple FE model is used to monitor the accuracy of the analysis developed.

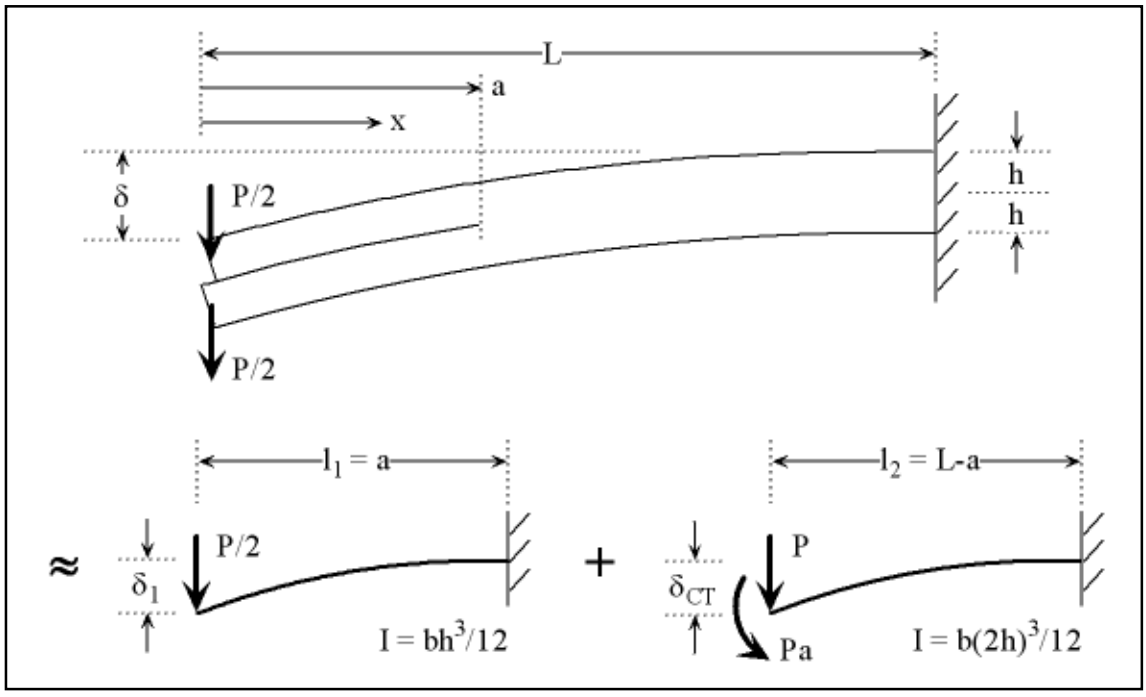

Figure 7.10 – SBT representation of ELS test specimen

The ELS test specimen can be split into two parts for easier analysis as shown in Figure 7.10. This methodology is developed by [213]. The total load line deflection of the beam can be calculated by summing the deflections of the two parts and from this we get to the compliance expression for the ELS test:

$$\delta = \delta_1 + \delta_2 \quad \text{.....(7.2)}$$

For the ELS specimen geometry:

$$\delta_1 = \frac{2Pa^3}{E_f bh^3} \quad \text{.....(7.3)}$$

From SBT, δ_2 equals the sum of the displacement at the crack tip (δ_{CT}) and the additional displacement at the end of the full beam due to the rotation at the crack tip (θ_{CT}):

$$\delta_2 = \delta_{CT} + \theta_{CT} l_1 \quad \text{.....(7.4)}$$

For the ELS specimen geometry:

$$\delta_{CT} = \frac{2P\left(L-a\right)^3 + 3Pa\left(L-a\right)^2}{4E_f bh^3} \quad \text{.....(7.5)}$$

$$\theta_{CT} = \frac{3P\left(L-a\right)^2 + 6Pa\left(L-a\right)}{4E_f bh^3} \quad \text{.....(7.6)}$$

$$\delta_2 = \frac{2P\left(L-a\right)^3 + 6Pa\left(L-a\right)^2 + 6Pa^2\left(L-a\right)}{4E_f bh^3} \quad \text{.....(7.7)}$$

$$\delta = \frac{3Pa^3 + PL^3}{2E_f bh^3} \quad \text{.....(7.8)}$$

The compliance for the ELS test is written as:

$$C = \frac{\delta}{P} = \frac{3a^3 + L^3}{2E_f bh^3} \quad \text{.....(7.9)}$$

The displacement at any point x along the length (L) of a simple, non-cracked beam can be determined as follows:

$$\delta_x = \frac{PL^3}{E_f bh^3}\left(2 - 3\frac{x}{L} + \frac{x^3}{L^3}\right) \quad \text{.....(7.10)}$$

The total displacement at any point x in the cracked region of the ELS specimen includes the displacements of the non-cracked region and is expressed as follows:

$$\delta_x = \delta_{CT} + \theta_{CT}(a - x) + \frac{Pa^3}{E_f bh^3}\left(2 - 3\frac{x}{a} + \frac{x^3}{a^3}\right) \quad \text{.....(7.11)}$$

In order to calculate the sliding displacement, the total rotation at any point *x* along the crack length (θ_x) must be known. This is found by summing the rotation at the crack tip and the rotation at any point x along the cracked region (obtained by differentiating Equation 7.10 with respect to *x*), and is expressed as follows:

$$\theta_x = \theta_{CT} + \frac{Pa^3}{E_f bh^3}\left(3\frac{x^2}{a^3} - \frac{3}{a}\right) \quad \text{.....(7.12)}$$

The total rotation at any point along the crack length can be related to the load line deflection by substituting the compliance (Equation 7.9) for *P*:

$$\theta_x = \theta_{CT} + \frac{2\delta a^3}{3a^3 + L^3}\left(3\frac{x^2}{a^3} - \frac{3}{a}\right) \quad \text{.....(7.13)}$$

The ability to calculate the rotation at the load line, for any given crack length, allows a trigonometric estimation of the sliding displacement to be made.

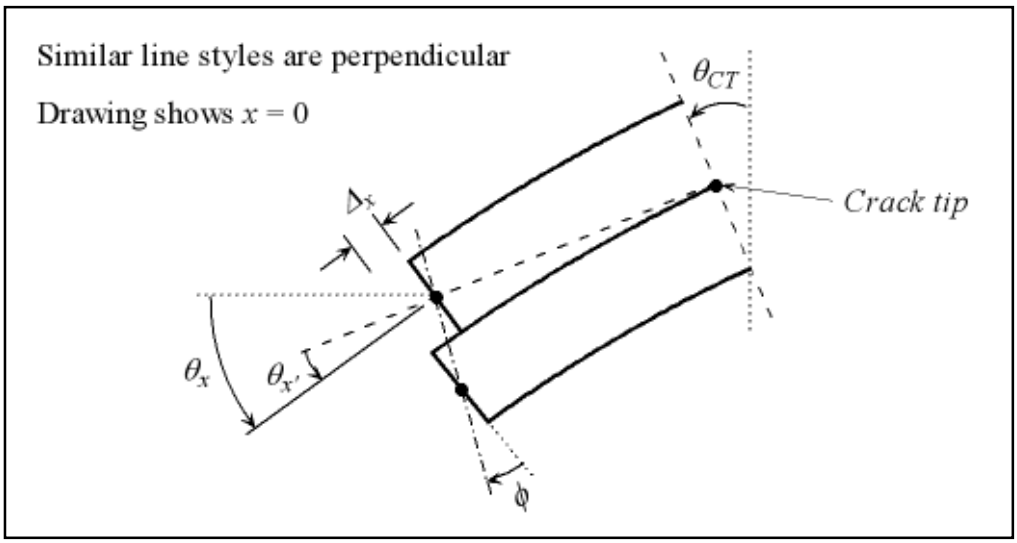

Figure 7.11 – Rotational terminology assigned to cracked region of ELS specimen

The following analysis assumes that the sliding displacement at any point in the crack wake x is due to the rotation difference between x and the crack tip a. The sliding displacement at the crack tip, and ahead of the tip, is zero.

$$\theta_{x'} = \theta_x - \theta_{CT} = -\tan\phi \quad \text{.....(7.14)}$$

$$\tan\phi = -\frac{2\delta a^3}{3a^3 + L^3}\left(3\frac{x^2}{a^3} - \frac{3}{a}\right) \quad \text{.....(7.15)}$$

Sliding displacement Δ_x is given as:

$$\Delta_x = \tan\phi.h \quad \text{.....(7.16)}$$

At the crack tip, where $x = a$, this expression gives $\Delta_x = 0$.
At the load line, where $x = 0$, $\theta_x = \theta_{CT}$.

By substituting the original crack position a_0 for x the sliding displacement Δ_{a0}, relative to the original crack position, can be expressed for any given crack length. The equation for ELS test sliding displacement is as follows:

$$\Delta_{a_0} = -\frac{2\delta a^3 h}{3a^3 + L^3}\left(3\frac{{a_0}^2}{a^3} - \frac{3}{a}\right) \quad \text{.....(7.17)}$$

The values obtained for Δ_{ao} using Equation 7.17 were compared against a non-linear FE solution (FEΔ_{a0}) as a means to assess accuracy. FEΔ_{a0} is the sliding displacement at the starting crack position (a_0) determined directly from the FE model. The ELS test specimen FE model used to create this plot had E_f = 50 GPa, L = 110 mm and h = 2 mm. This 2D model was constructed from eight-noded quad elements with height 1 mm and length 2.5 mm. Frictionless contact was assigned between the two arms of the FE model to be consistent with the SBT solution. Figure 7.12 shows a plot of Δ_{a0} / FEΔ_{a0} versus crack length for a range of load line displacements.

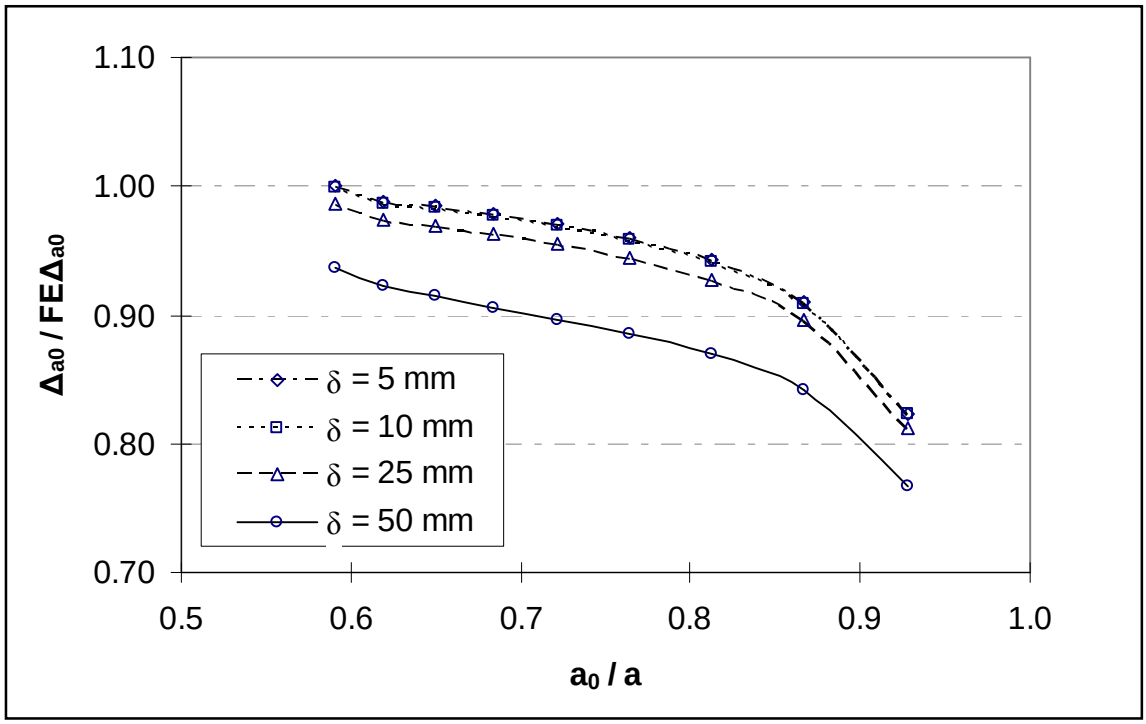

Figure 7.12 – Accuracy assessment of sliding displacement at a_0

In general, the expression developed to quantify the sliding displacement relative to the crack start position corresponds well to the values taken from the FE simulation of the ELS test. Figure 7.12 shows that the sliding displacement relative to the crack start position taken directly from the FE model is always larger than the calculated value. However, for large load line displacements, up to 50 mm, this calculated value is never more than 25% lower than the FE value.

The solutions appear to agree less well as a_0 / a approaches unity. This effect is not as severe as the graph suggests and is exaggerated by the fact that the simple mesh used in the FE model limits the accuracy of the solution close to the crack tip. As with all finite element models the results obtained are mesh dependent. With sufficient time being available, refinement of the model to include a finer mesh arrangement around the crack tip would be advisable as it is expected that this would lead to better agreement with the calculated value in the region approaching crack tip. However, this relatively simple FE model gives sufficient agreement with the calculated value to be confident in using the calculated analysis for further work.

Large beam deflections cause the calculated solution to lose accuracy due to the beam theory approach being applicable to small deflections. Equation 7.16 would benefit from development of a large deflection correction factor, as was done for the ELS test analysis, to extend the applicability of the beam theory approach used and hence improve the accuracy of the calculated result.

7.3.2 Generating a traction response to simulate experimentally measured mode II behaviour

7.3.2.1 Re-plotting R-curves to describe steady propagation for the woven materials

Having developed a method to obtain the sliding displacement at the crack start position the R-curves measured for the two woven materials (Figure 7.6, Figure 7.7 and Figure 7.8) can be re-plotted against this value. Figure 7.13 and Figure 7.14 show the re-drawn R-curves for the 914 / 6K5H / T300 and 8552 / 3K8H / HTA materials. These plots were used to determine an average sliding displacement value for the onset of steady crack propagation (*steady* Δ_{a0}). These *steady* Δ_{a0} values are shown on the respective graphs and detailed in Table 7-3. Also indicated on the graphs are the average G_{IIc} values determined for the respective materials. These Δ_{a0} and G_{IIc} values are key data from which a traction response for these materials can be developed.

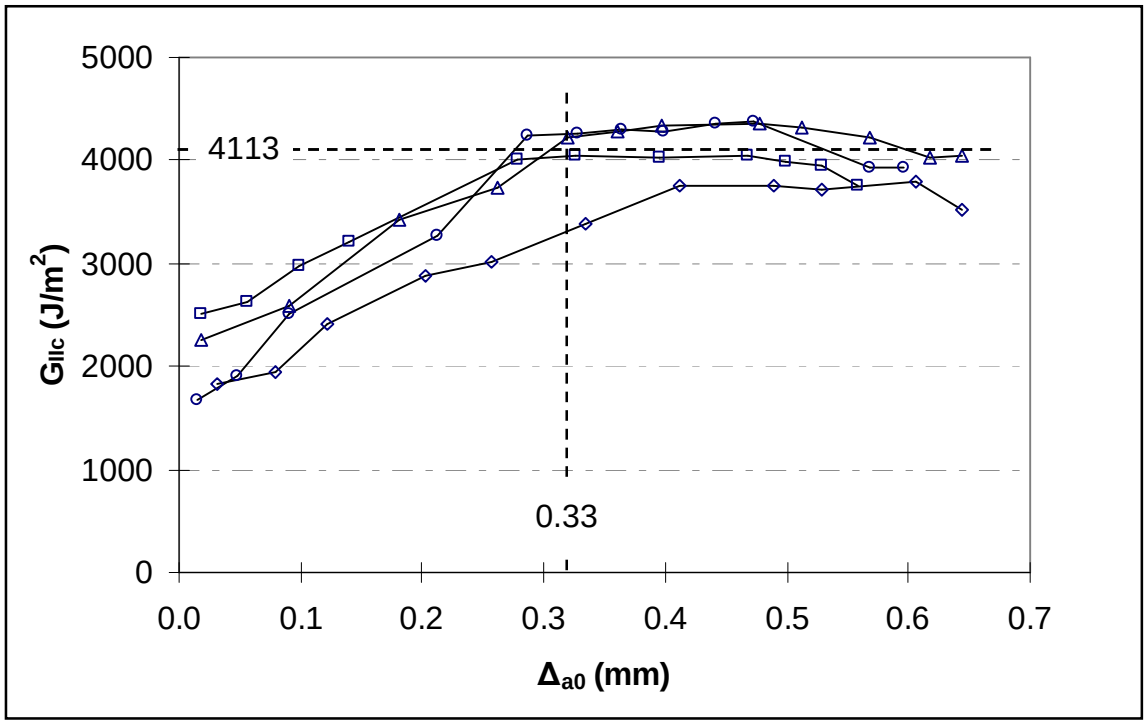

Figure 7.13 – Plot of mode II fracture toughness (propagation only) versus sliding displacement relative to a_0 for 914 / 6K5H / T300

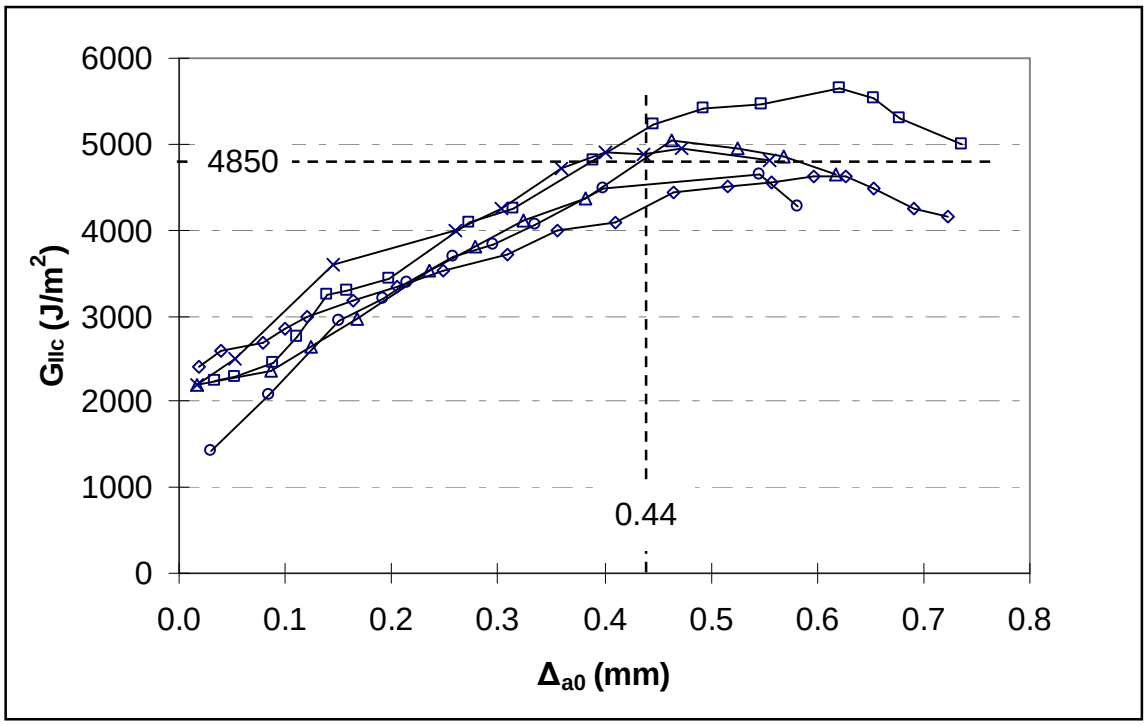

Figure 7.14 – Plot of mode II fracture toughness (propagation only) versus sliding displacement relative to a_0 for 8552 / 3K8H / HTA

Material	*steady* Δ_{a0} (mm)
914 / 6K5H / T300	0.33
8552 / 3K8H / HTA	0.44

Table 7-3 – *steady* Δ_{a0} values for woven pre-preg materials

The values shown in Table 7-3 mirror the physical nature of these woven materials. The more coarse 3K tow, 8 harness architecture of the 8552 / 3K8H / HTA material is expected to require a larger sliding displacement to reach a steady propagation state than the 6K tow, 5 harness architecture of the 914 / 6K5H / T300 material. Figure 7.15 shows the mode II fracture toughness versus sliding displacement relative to a_0 plot for the comparative 977-2 UD material. Whilst flat R-curves are generally desirable from ELS testing estimation of *steady* Δ_{a0} from a curve such as this is impossible. The very small amount of bridging of the UD material requires less load line displacement for crack propagation. This in turn means that the sliding displacements determined for the UD material are much lower than for the woven materials.

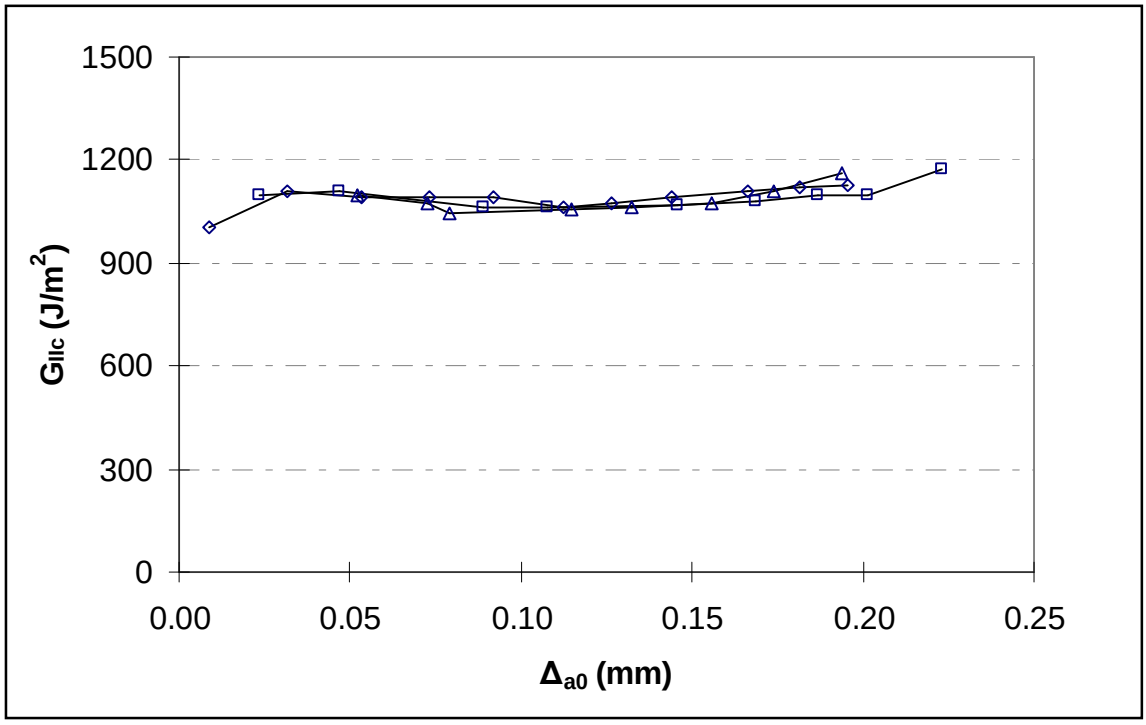

Figure 7.15 – Plot of mode II fracture toughness (propagation only) versus sliding displacement relative to a_0 for 977-2 UD

7.3.2.2 Designing a traction response to fit experimental data

The first task in creating a traction response to give the same material interface response as measured by the ELS test was to consider the nature of the crack path itself. For UD materials the interface can be considered as a pure resin layer through which crack propagation occurs. The crack is bound inside the resin layer by the UD fibres above and below. For woven materials, the interface is not as simple (see Figure 7.9). The propagating crack in ELS tests on woven materials must negotiate a path through the nestled tows of reinforcing fibres and resin rich regions.

For woven material interfaces, there is no way to be certain whether, for example, a propagating crack passes through the fibre tows or negotiates a path around them through the neat resin only. To deal with this uncertainty the interface for woven materials was analysed twice; the first, as a pure resin pathway and secondly as a composite one.

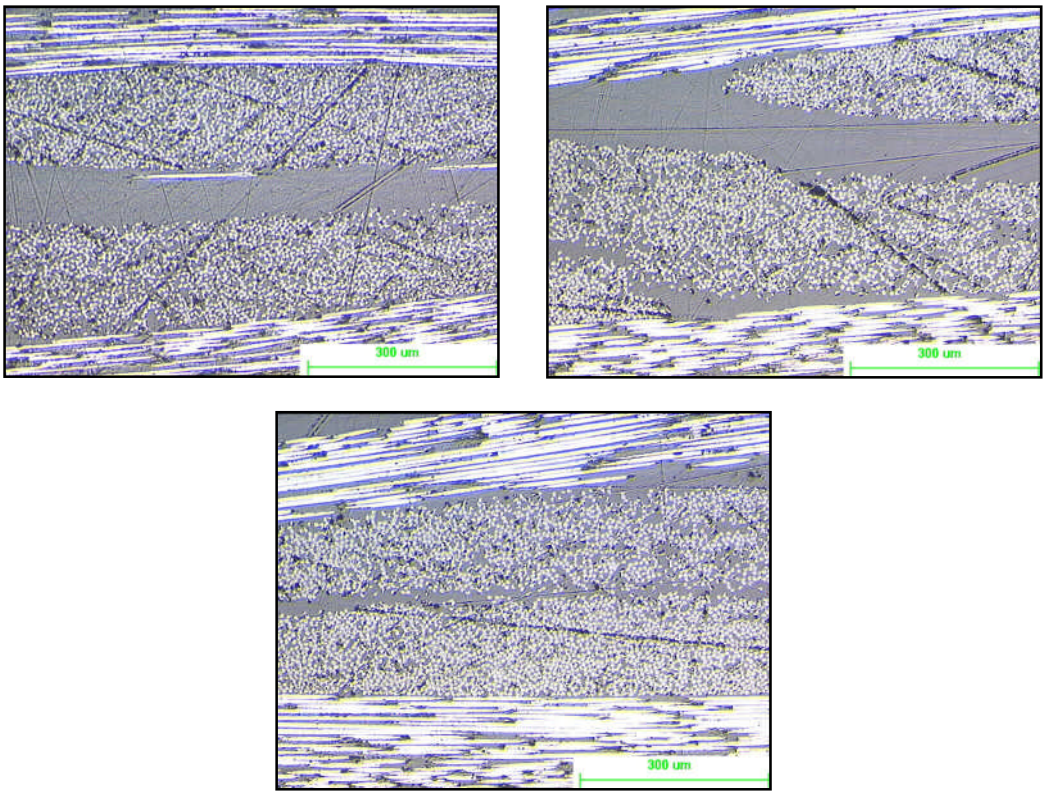

Figure 7.16 – Sample microscopy images of woven interface for interface thickness measurement

The interface (crack path) thickness is important to the generation of traction responses for these materials. Microscopy images of the woven material interfaces (see Figure 7.16) were analysed for the woven materials to obtain the average resin layer thickness. For the 977-2 UD material a typical interface thickness value was provided by [214] obtained from resin film interleaving work. The interface values used for the three materials under consideration are detailed in Table 7-4. When the interface was considered as a composite, for the woven materials, the interface thickness used was taken to be the mid-ply separation of the two plies either side of the interface. This value is equal to the cured ply thickness of the material.

Material	Av. resin interface thickness [St. Dev.] (μm)	Composite interface thickness (μm)
914 / 6K5H / T300	64 [35]	337
8552 / 3K8H / HTA	80 [51]	387
977-2 UD	1.5	-

Table 7-4 – Material interface thicknesses

The remaining information required for the traction responses was the resin and composite shear moduli and shear strengths. Young's modulus values for the resin systems were obtained from the material supplier (as detailed in Chapter 3) and converted to shear modulus using the following equation:

$$G = \frac{E_{bulk}}{2(1+\nu)} \quad \text{.....(7.18)}$$

where

G is the shear modulus expressed in GPa

E_{bulk} is the bulk Young's modulus in GPa

ν is the Poisson's ratio

However, shear strength data for neat resins are not readily available. Extensive searches of published literature provided the neat resin shear strength for the Hexcel 914 epoxy resin only; 80 MPa from [215]. To overcome this lack of data, upper and lower bound neat resin shear strength values (80 MPa and 150 MPa respectively) were used for the 8552 / 3K8H / HTA and 977-2 UD materials. A separate traction response was created for the upper and lower bound values. In addition, a shear strength value based on the von Mises yield criterion was generated. The von Mises yield criterion, considers a material to start yielding when its von Mises stress reaches a critical yield strength value. The von Mises stress is used to predict yielding of materials under any loading condition from results of simple uniaxial tensile tests. A separate traction response was created for the von Mises approach also. For the cases where the woven material interface is considered as a composite, shear modulus and shear strength values were generated for a 90/90 lay-up using the CoDA analysis software.

The traction responses for the woven materials are simplified to the OABCD curve shown in Figure 7.17. The general shape of these traction responses was developed to provide a match to the profile of the experimentally measured R-curves which, in the case of the two woven material systems, display an initial rising R-curve feature (see Figure 7.13 and Figure 7.14). The B-C-D plateau region of these traction responses was the key design inclusion and provides a representation of the rising R-curve region (see Figure 7.21 and Figure 7.22) in the traction response fit.

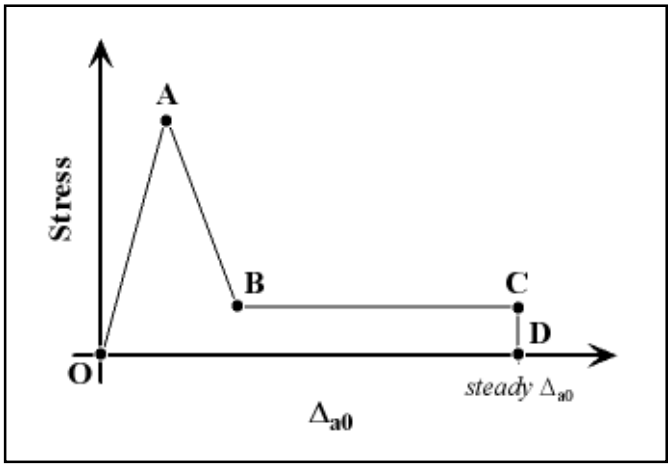

Figure 7.17 – Simplified traction response curve for woven materials

In all cases, the initial part of the response (O-A) is taken to be linear and is determined by the shear strength and shear modulus values. The sliding displacement value corresponding to point A is deduced from the corresponding shear strain and knowledge of the interface thickness. Point D is set by the *steady* Δ_{a0} value which defines the limit of the traction response. The area under the OABCD curve, and hence the total energy of the traction response, is equal to the G_{IIc} values measured from the ELS tests. The stress value of the plateau (B-C) is approximately equal to the differential of mode II fracture toughness divided by a_0 relative sliding displacement (dG_{IIc} / $d\Delta_{a0}$) in the steady propagation region. The only part of the traction responses which is 'fitted' is the position of point B. This point is positioned to give the correct total energy of the traction response.

The traction response for the 977-2 UD material was handled slightly differently. Steady crack propagation is achieved almost instantly during the ELS test and therefore there is no way to assess the sliding displacement limit. The OA region was determined in the same manner as for the woven materials. After point A the traction response was simply given the correct total energy by positioning point B along the zero stress line. Points C, D and E are therefore omitted. The following figures show the fit of the traction responses for the various material interfaces against the experimental G_{IIc} versus Δ_{a0} curves. The traction responses developed for the 977-2 UD, 914 / 6K5H / T300 and 8552 / 3K8H / HTA materials are shown in the following figures.

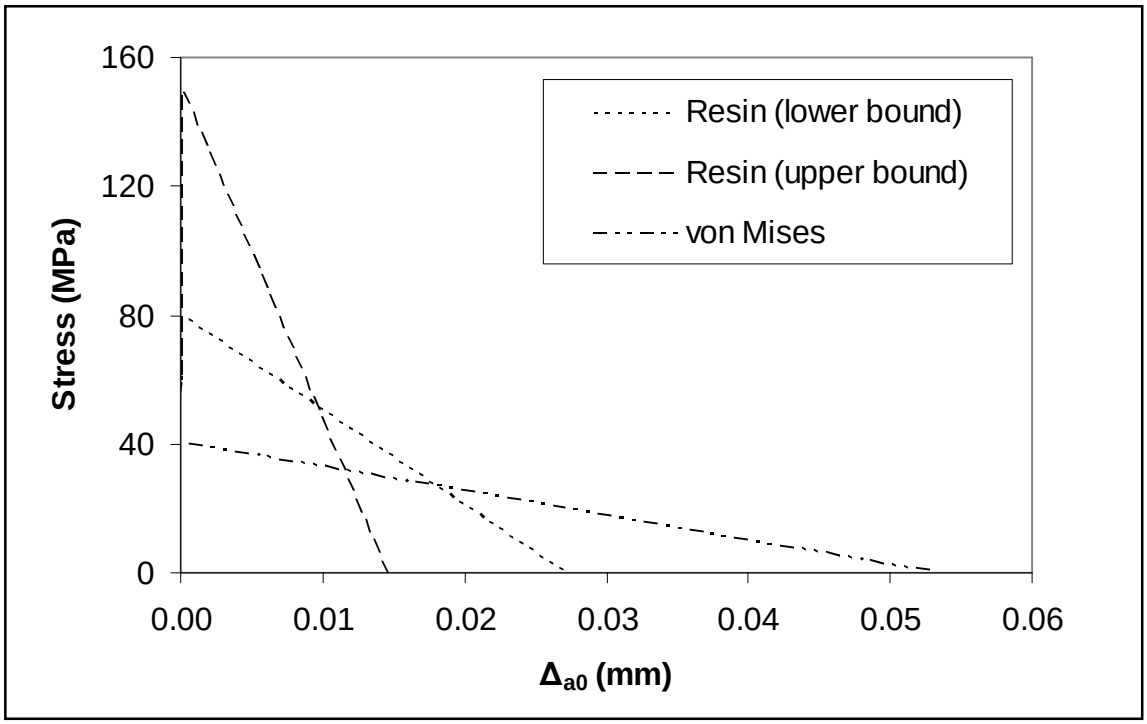

Figure 7.18 – Traction responses for 977-2 UD material interface

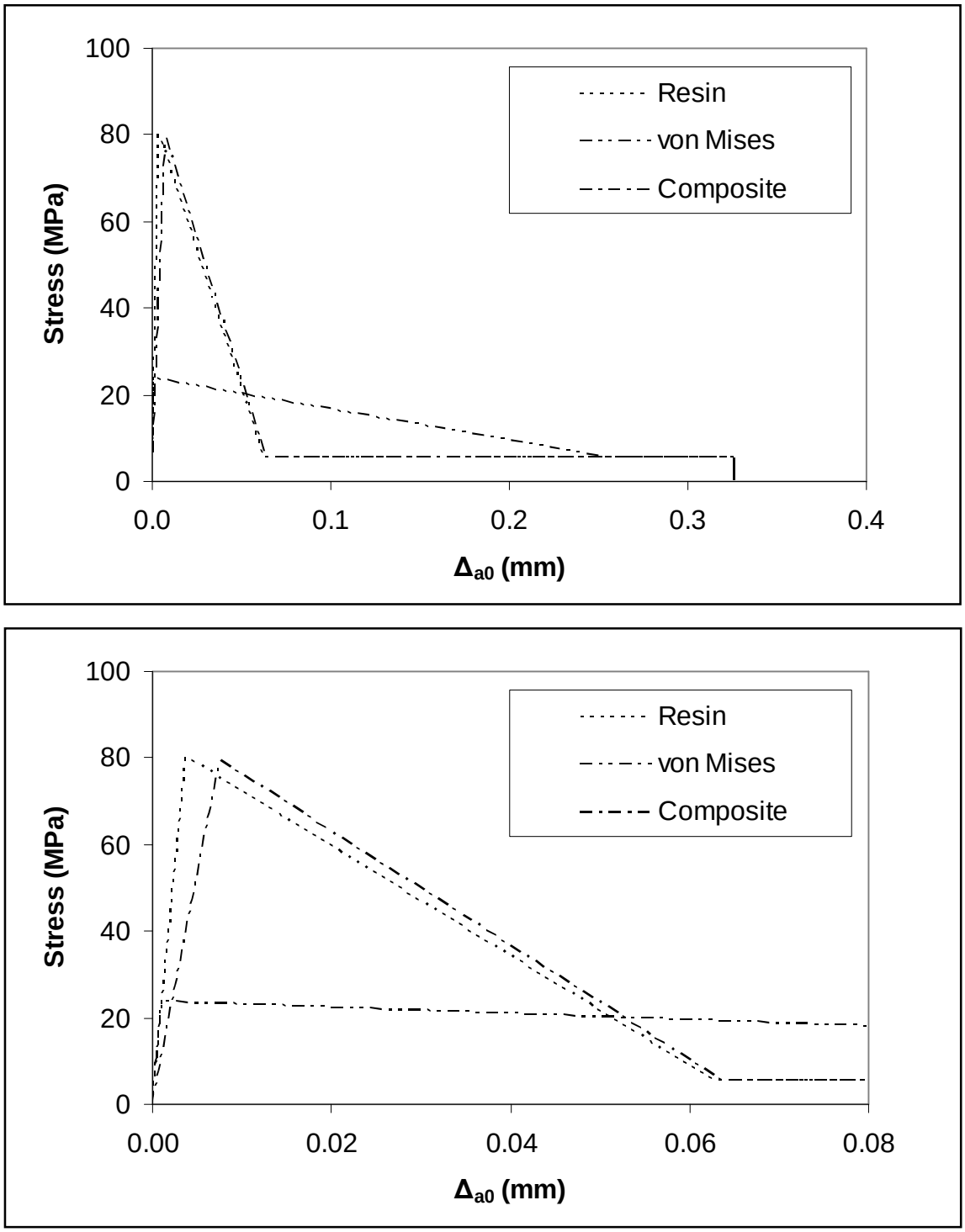

Figure 7.19 – Traction responses for 914 / 6K5H / T300 material interface; full response (top), initial response detail (bottom)

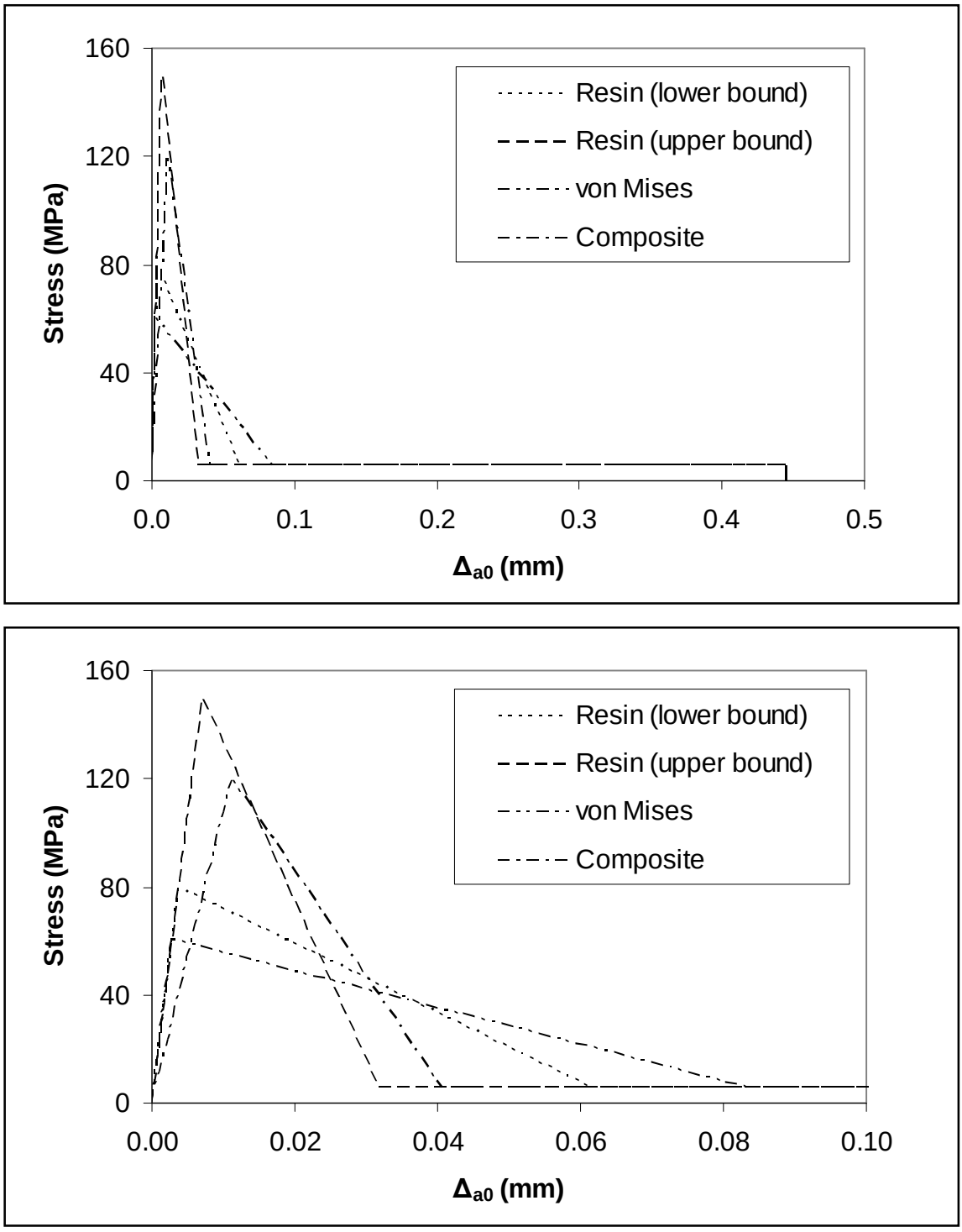

Figure 7.20 – Traction responses for 8552 / 3K8H / HTA material interface; full response (top), initial response detail (bottom)

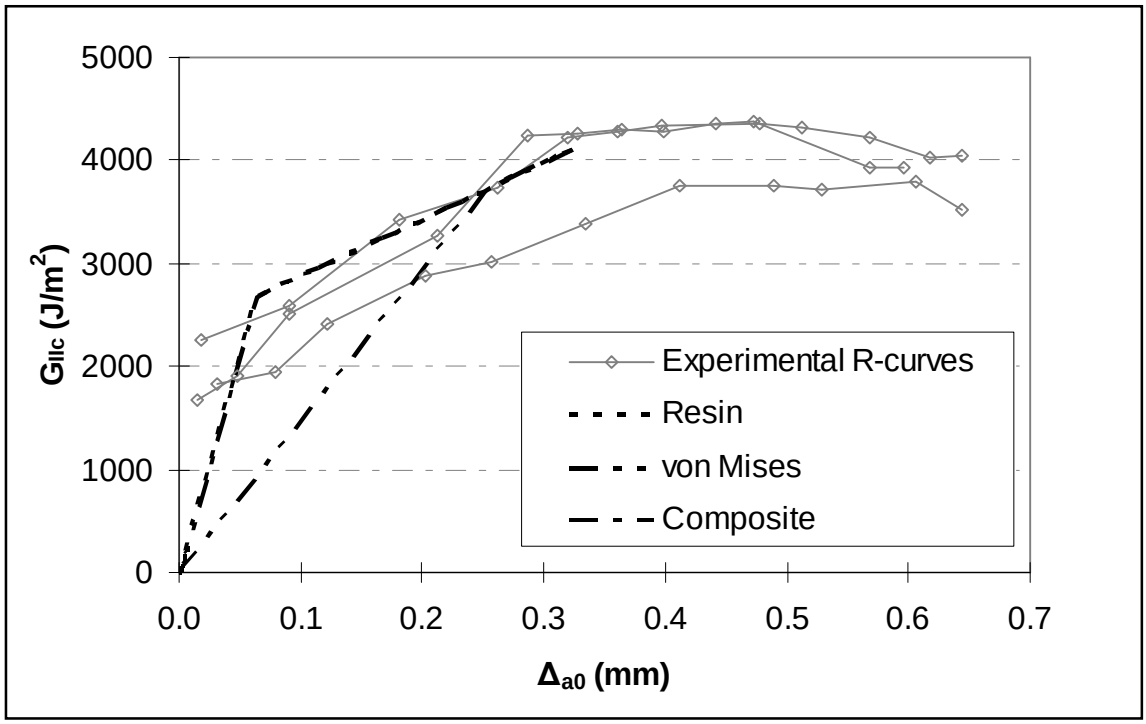

Figure 7.21 – 914 / 6K5H / T300 traction response fit to experimental G_{IIc} measurement

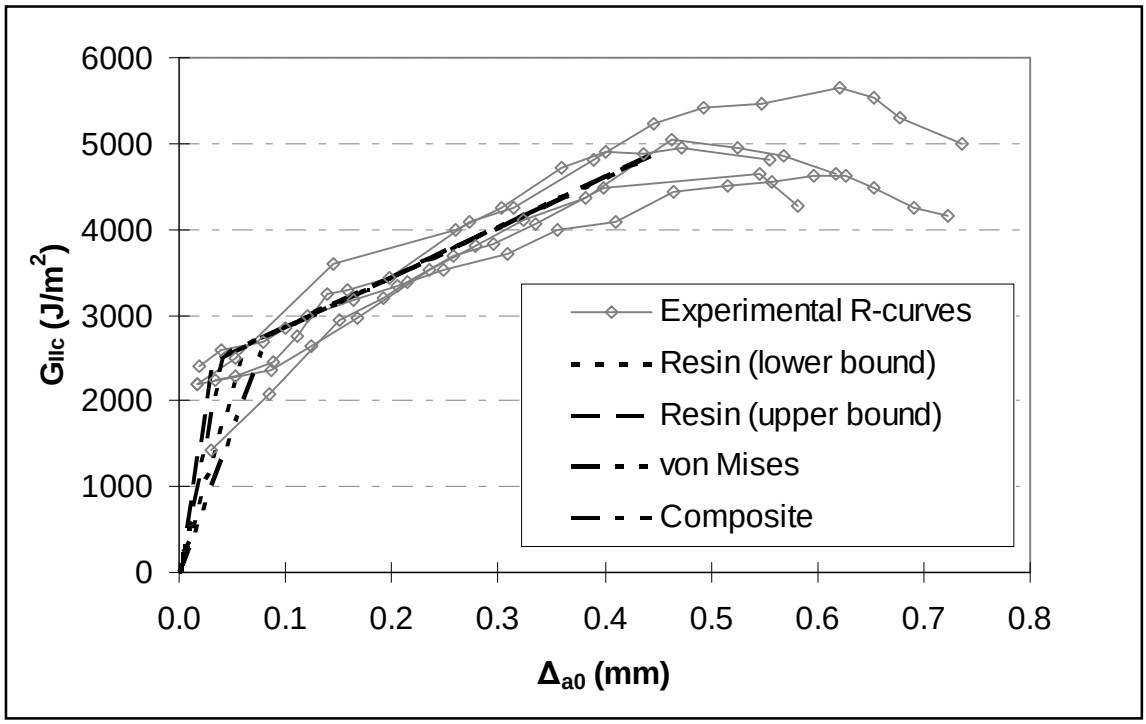

Figure 7.22 – 8552 / 3K8H / HTA traction response fit to experimental G_{IIc} measurement

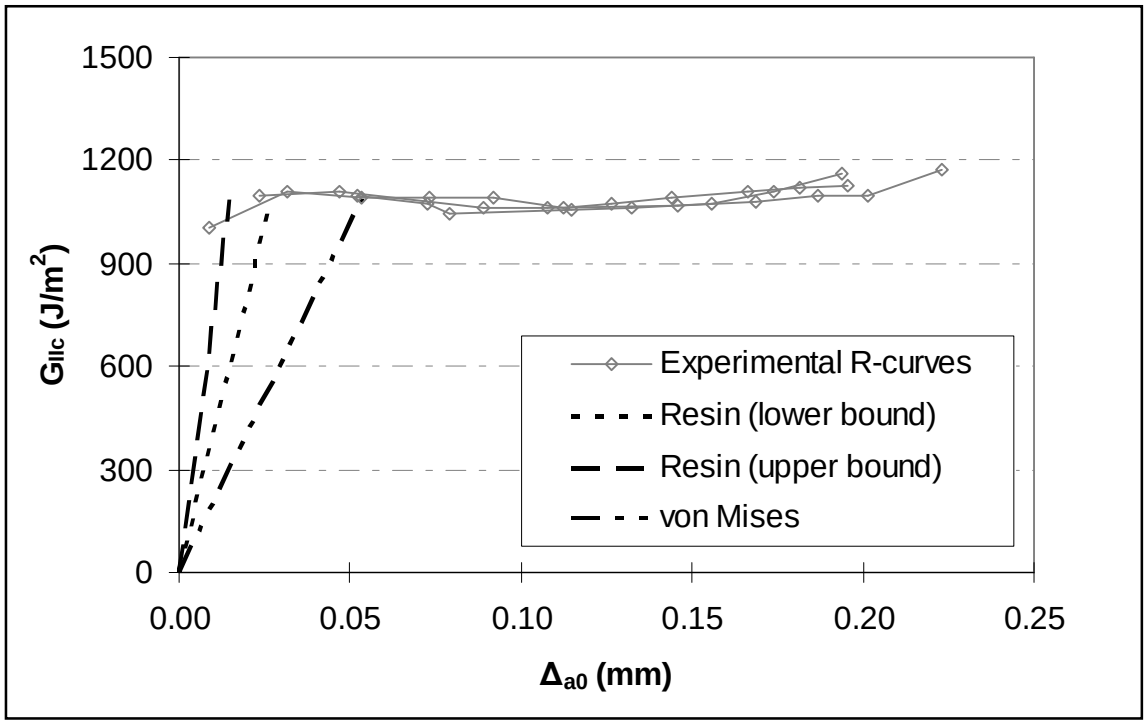

Figure 7.23 – 977-2 UD traction response fit to experimental G_{IIc} measurement

Implementation of these traction responses into the MSC.Marc analysis required user subroutines to be written in FORTRAN code. The complete set of FORTRAN user subroutines, developed by the author, is included in Appendix D.

What is apparent from the traction responses when compared with the experimental data is that the initial part of the response is not well described. The true mechanics behind crack initiation remain unknown. The ELS test itself is not designed to provide data for this region and crack measurements made by eye are not accurate enough to provide these data. For the woven materials the first recorded crack propagation values from the ELS test give a Δ_{a0} value which is up to 20 times outside the OA range. For the UD material this first corresponding Δ_{a0} value is 550 times outside the OA range. To better understand the interface mode II fracture initiation response a new test would need to be developed on a scale which could be monitored directly in an SEM microscope for example.

7.3.3 ELS model verification

The traction responses were tested in a 2D FE model of the ELS test specimen. This FE model included the type 188 interface elements at the mid-plane interface. The interface elements were collapsed to have zero thickness. Contact was simulated between the two specimen halves also. The free end of the specimen was displacement controlled. All degrees of freedom at the clamped end, except displacement in the x-axis, were set to zero.

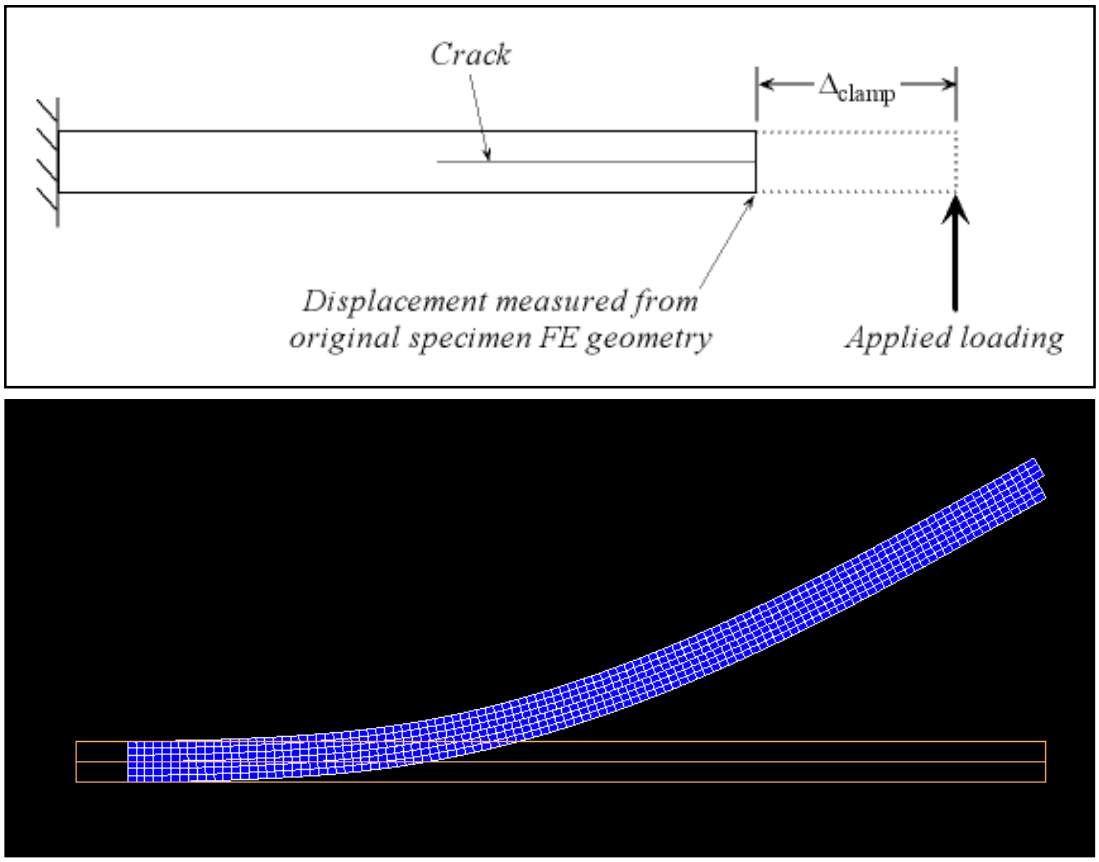

Figure 7.24 – Dealing with Δ_{clamp} correction (top) and deformed mesh of the ELS test FE model geometry (bottom)

One important modification was made to these models to account for the Δ_{clamp} correction, which comes from the ELS test calibration procedure and is used in the CBTE ELS test analysis, correctly. The Δ_{clamp} correction accounts for the 'softness' of the clamp on the test jig, not for the sliding displacement of the clamp as it may appear at first. The clamping of ELS test specimens is not perfect. The Cranfield University ELS test jig is manufactured from aluminium and is therefore relatively compliant. This

has a measurable effect on the specimen compliance. The ELS models were modified to represent this accurately. In simple terms, the non perfect clamping arrangement causes the ELS specimen to act as if it is slightly longer than it is in reality and this is how the Δ_{clamp} correction is incorporated into the model. The free length (L) of the specimen is increased by the Δ_{clamp} distance and the displacement control loading applied at the extended end node. However, the deflections measured are still relative to the uncorrected geometry and deflection values output from the model are hence taken from the original geometry. The extended section of the specimen has the same material properties as the rest of the test specimen.

The Δ_{clamp} values obtained from the calibration procedure for the materials tested are listed in Table 7-5. These values indicate that as the specimen stiffness increases the higher the value of the Δ_{clamp} correction becomes.

Material	Δ_{clamp} (mm)
914 / 6K5H / T300	2.35
8552 / 3K8H / HTA	5.46
977-2 UD	15.77

Table 7-5 – Δ_{clamp} correction values

The following figures show the load versus load line deflection responses measured for the ELS test specimens and the responses obtained from the ELS models for the three materials.

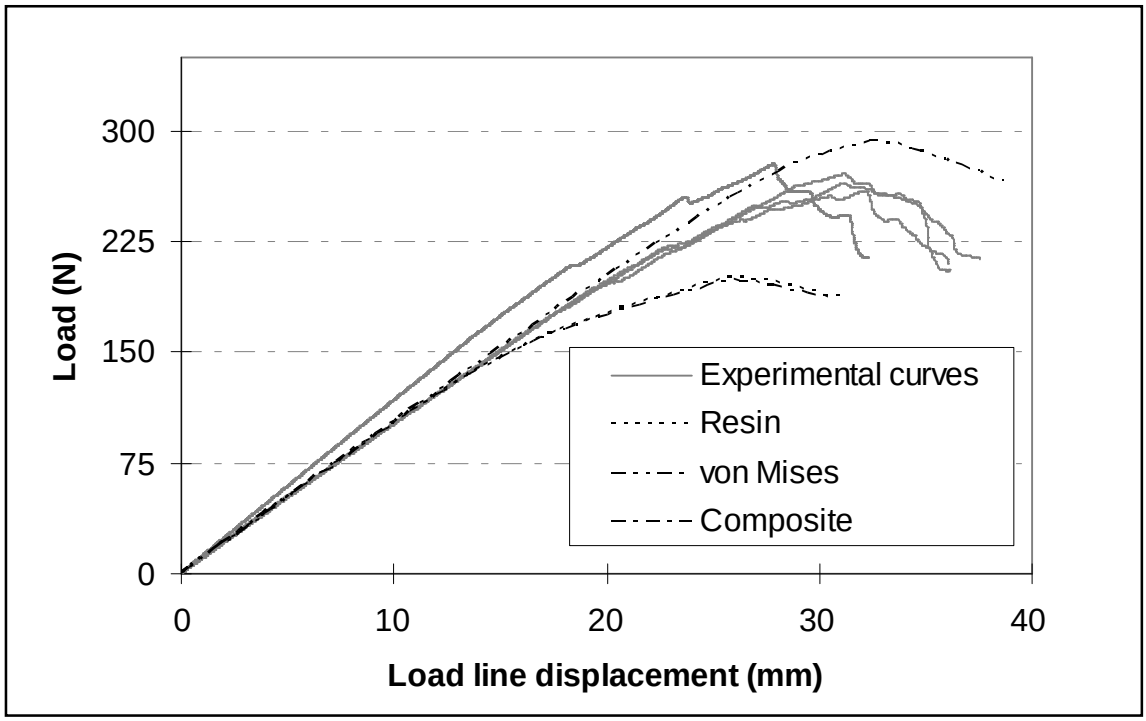

Figure 7.25 – Load vs. load line displacement response for 914 / 6K5H / T300

The closest agreement between the model and experimental responses is found for the 914 / 6K5H / T300 material as shown in Figure 7.25. The 914 / 6K5H / T300 material ELS FE model had the following material and geometric properties: E_f = 53 GPa, a_0 = 72 mm, L = 112.35 mm. For this case the experimental response falls between the models analysed using the von Mises and Resin traction responses. The model correctly replicates the initial stiffness, within the experimental scatter. For the models analysed using the resin and composite traction responses, failure of the interface (taken to be at the point of non-linearity) occurs at a lower load than the experimental tests. For the von Mises case the interfacial failure occurs at a higher load. The load line deflections (crosshead displacement) follow a similar trend with complete failure of the specimen interface for the resin and composite cases failing at a lower deflection than the experimental tests and the von Mises model slightly higher.

The 8552 / 3K8H / HTA ELS FE model had the following material and geometric properties: E_f = 53 GPa, a_0 = 72 mm, L = 105.46 mm. The traction responses developed for the 8552 / 3K8H / HTA material, included in the corresponding FE model do not find good agreement with the load versus crosshead displacement curves measured from

the experimental ELS tests. Figure 7.26 shows that the interface in the FE model starts to fail at a much lower load than the experimental tests. Failure of the interface is taken to be at the point where the load versus crosshead displacement response becomes non-linear. As mentioned previously, the methods described until now to develop the traction responses do not provide sufficient information for the initiation part of the interface traction response and the poor initial fit for the 8552 / 3K8H / HTA material is as a result of this. However, in the crack propagation region (the non-linear region) the FE model response correlates much closer to the experimental ELS test curves.

The 977-2 UD ELS FE model had the following material and geometric properties: E_f = 147 GPa, a_0 = 67 mm, L = 115.77 mm. For the 977-2 UD material the fit of the FE model with the experimental ELS test load versus crosshead displacement curves is satisfactory, particularly considering the limited information which could be deduced from the original flat ELS test R-curves (Figure 7.23). Again, failure of the FE model interface occurs before the experimental tests as a result of limited knowledge regarding failure initiation of the interface.

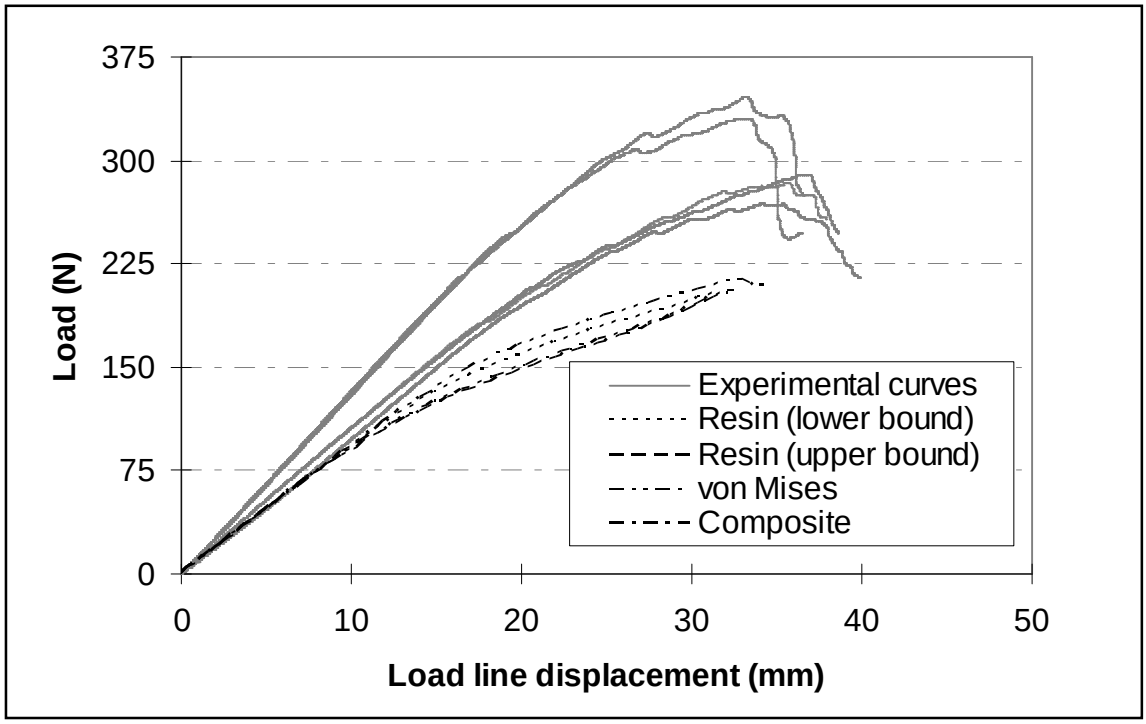

Figure 7.26 – Load vs. deflection response for 8552 / 3K8H / HTA

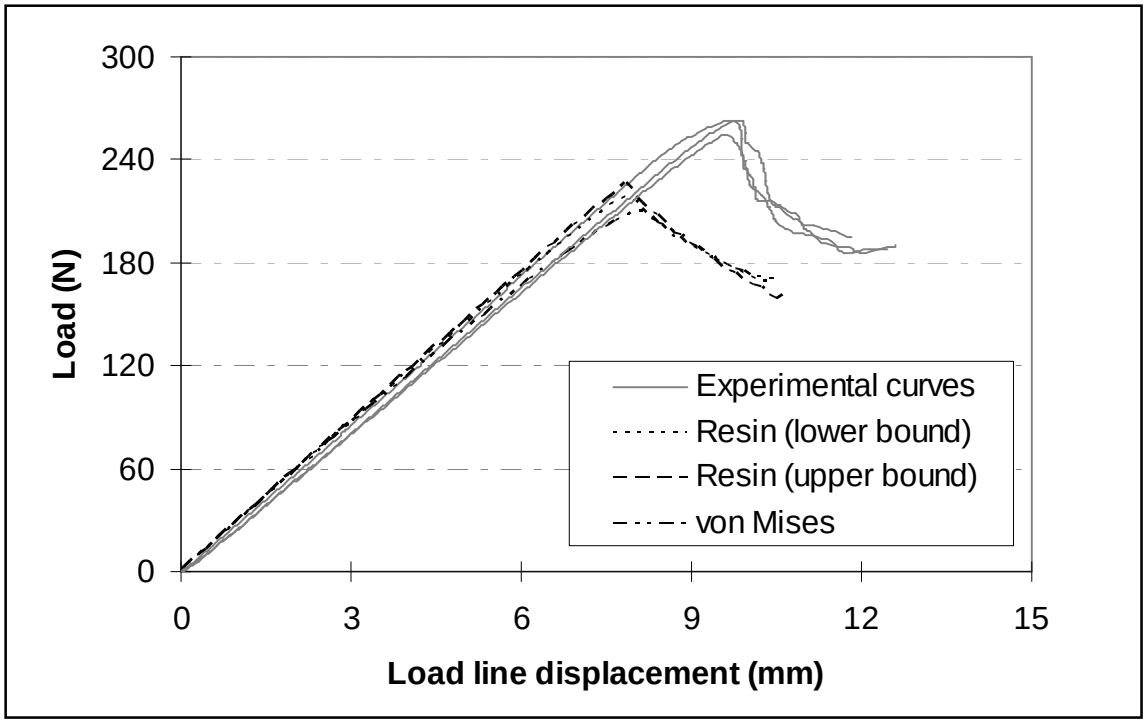

Figure 7.27 – Load vs. deflection response for 977-2 UD

It would be possible to fit the FE model responses to the experimental curves almost perfectly through trial and error based movement of the points on the OABCD traction responses. This was not done as it masks the areas which have been highlighted as requiring further consideration. The work described in this section is based on measured properties and sound assumptions; fitting of the curves would undermine this effort and provide no further insight regarding the mechanics of the mode II interfacial response of these materials.

The R-curves for the three materials tested are presented in Figure 7.28, Figure 7.29 and Figure 7.30. In each case the R-curves have been developed from the von Mises traction responses which gave the best fit to the experimental load versus load line displacement curves. Furthermore, two FE generated R-curves are presented in each case for which a different method for obtaining the crack length was used. The compliance calculated crack length curve was generated by back-calculating the crack length, from the FE generated load and displacement values, using the ELS compliance equation (Equation 7.9). The interface element crack length was obtained using a purpose built FORTRAN program which outputs the number of failed interface elements. Knowledge of the

interface element length, which was constant, allows a simple measurement of crack length to be made. The FORTRAN code developed for this purpose is included in Appendix E.

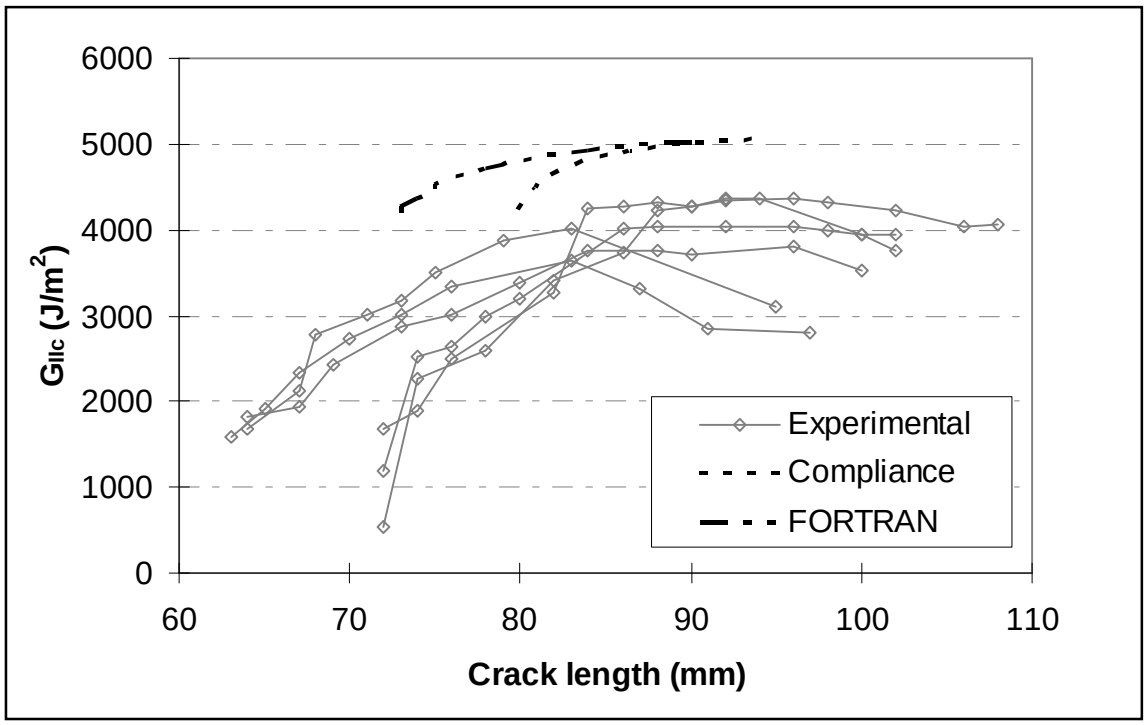

Figure 7.28 – FE generated R-curves 914 / 6K5H / T300

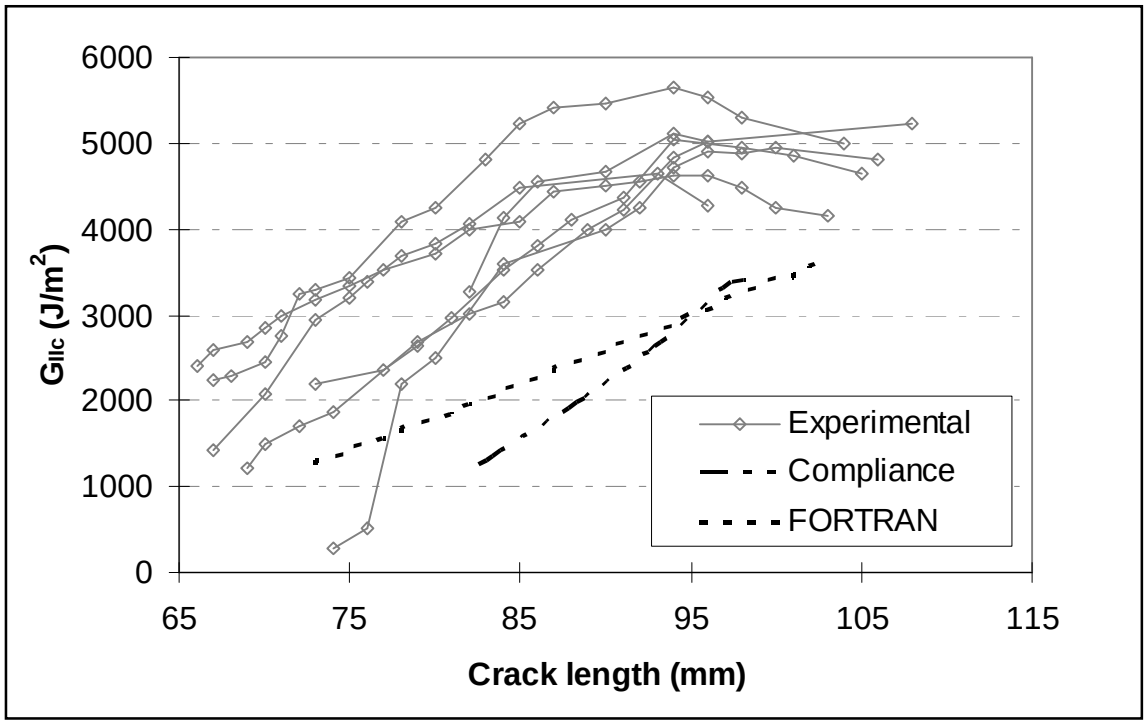

Figure 7.29 – FE generated R-curves for 8552 / 3K8H / HTA

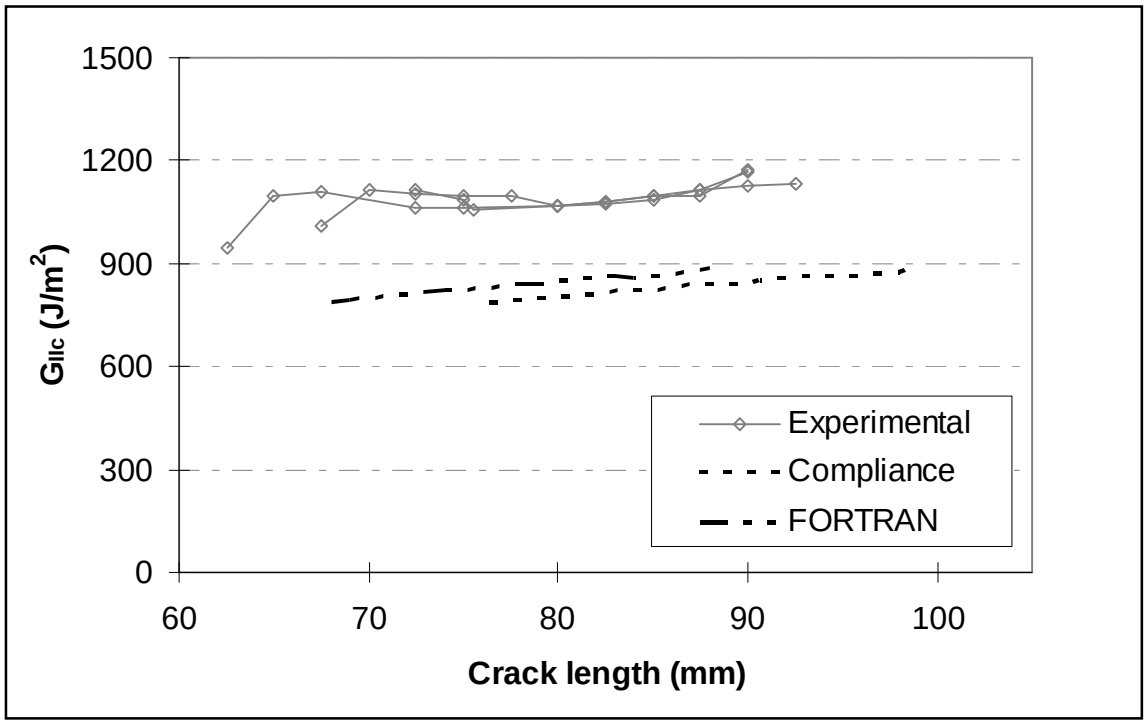

Figure 7.30 – FE generated R-curves for 977-2 UD

The FE generated G_{IIc} values, with the exception of the 8552 / 3K8H / HTA case, are in excellent agreement with each other but disagree with the R-curves obtained from experimental tests. The reason for this traces back to the lack of information available from which to describe the original traction responses. As for the load versus load line displacement curves, these R-curves could be fitted to give the same responses as those measured experimentally but would give no further understanding of the interfacial fracture behaviour. The positioning of the FE generated R-curves relative to the experimental R-curves is consistent with the fitting of the load versus load line displacement plots. The 914 / 6K5H / T300 case over-predicts G_{IIc} whilst the 8552 / 3K8H / HTA and 977-2 UD values are under-predicted.

The R-curves show that the compliance calculated crack lengths are consistently shorter than those obtained from interface element fracture measurement. The point at which the interface elements were considered to be fractured in the FORTRAN code was at a sliding displacement value corresponding to point B of the OABCD traction response. As discussed previously, this value is somewhat arbitrary. To be comparable with the experimental tests it should correspond to what is possible to measure visually on the side of the ELS test specimen. The value used affects the crack length generated and will shift the R-curve left or right. There is no standard distance that can be used for this fracture. Further investigation on this point is required.

7.4 Generating mode II data for z-pins

Two sets of mode II shear tests were carried out as part of this work, using the modified Z-shear test jig (see Chapter 5), to obtain a traction response for z-pins which could be used with the type 188 interface element in MSC.Marc. The first set of tests was carried out on glass fibre / epoxy laminates reinforced with 16 z-pins to show that a pure mode II z-pin failure occurred in a brittle manner when opening displacement is constrained to be negligible. The glass fibre laminates used allowed the inserted length of z-pin to be monitored, for bending under the applied load, during the test. Work by Cox in particular describes predominant z-pin flexure under mode II loading [124]. An understanding of the mode II behaviour of inserted z-pins was required to validate the

modelling approach used. The second set of tests was carried out on the raw z-pin rodstock material. The need for these tests came from the large scatter of data from the first set of tests. Furthermore, the single z-pin or rodstock samples could be aligned perpendicular to the loading axis, eliminating the insertion angle variability from the analysis.

7.4.1 16 z-pin tests

Z-shear shear tests were performed on glass laminate specimens containing 16 z-pins each. Three laminate types were tested; UD 0°, UD 90° and a 0/90 woven fabric. The 0° fibre orientation reference was parallel to the direction of the applied load (see Figure 5.10). Two diameters of z-pin were tested for the three laminate types; 0.28 mm and 0.51 mm. The following figures show the load displacement responses for these test configurations.

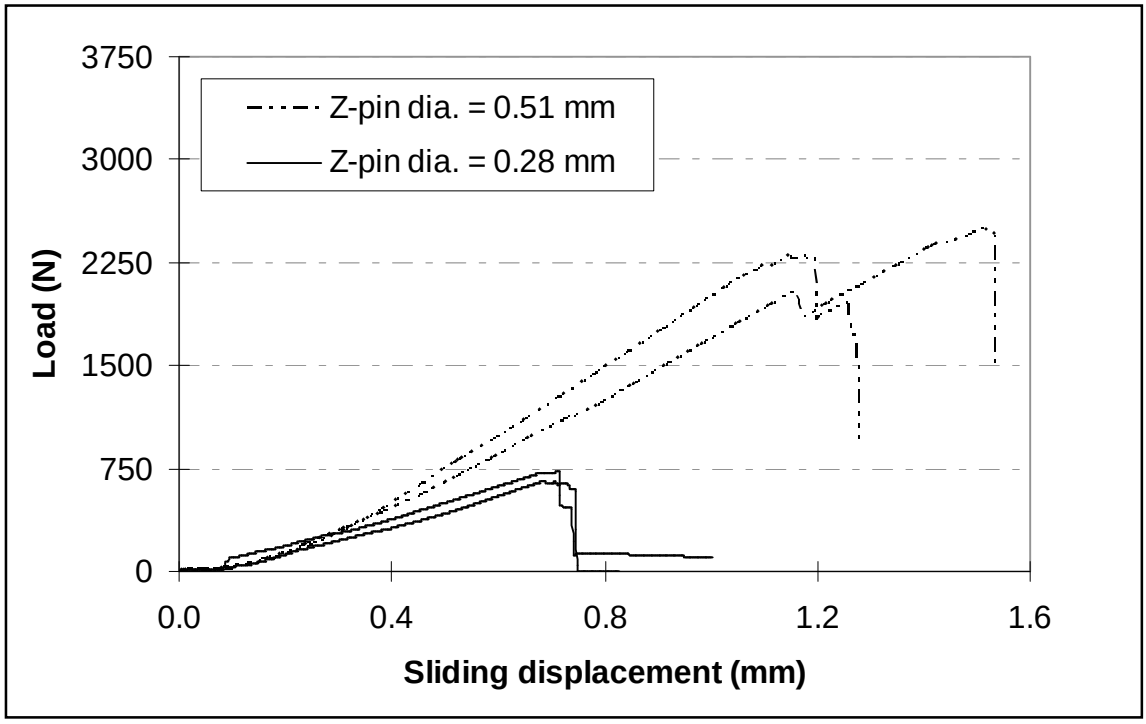

Figure 7.31 – Load vs. displacement curves for 16 z-pins in 0° UD glass / epoxy laminate

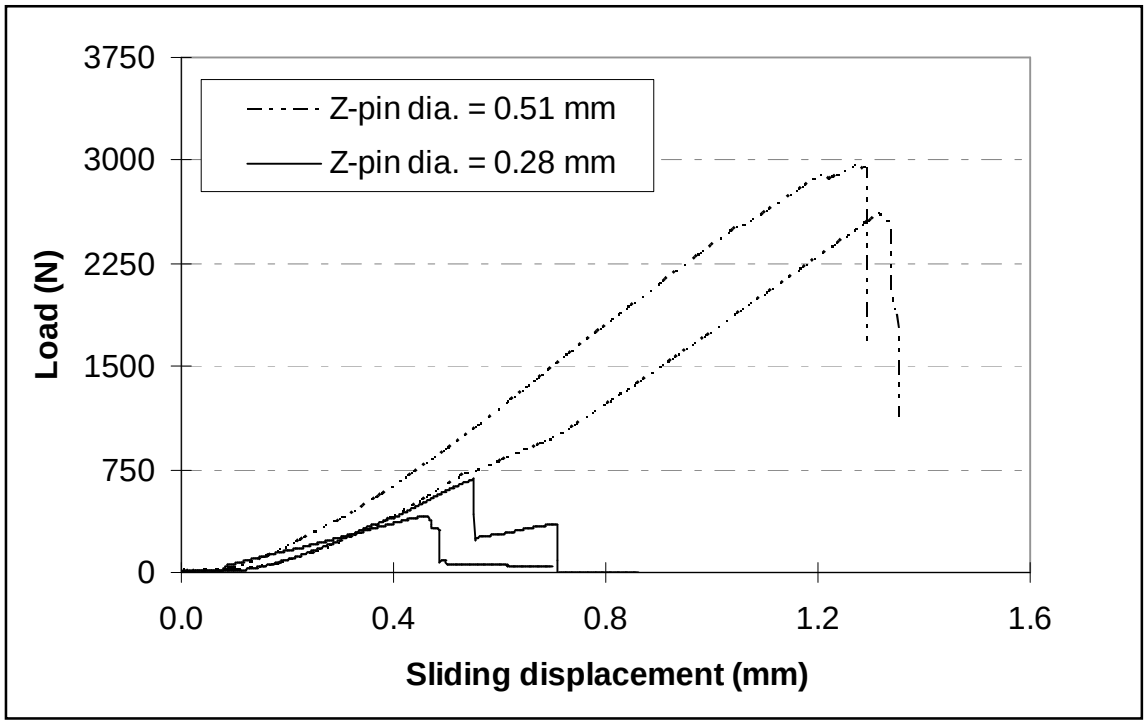

Figure 7.32 – Load vs. displacement curves for 16 z-pins in 90° UD glass / epoxy laminate

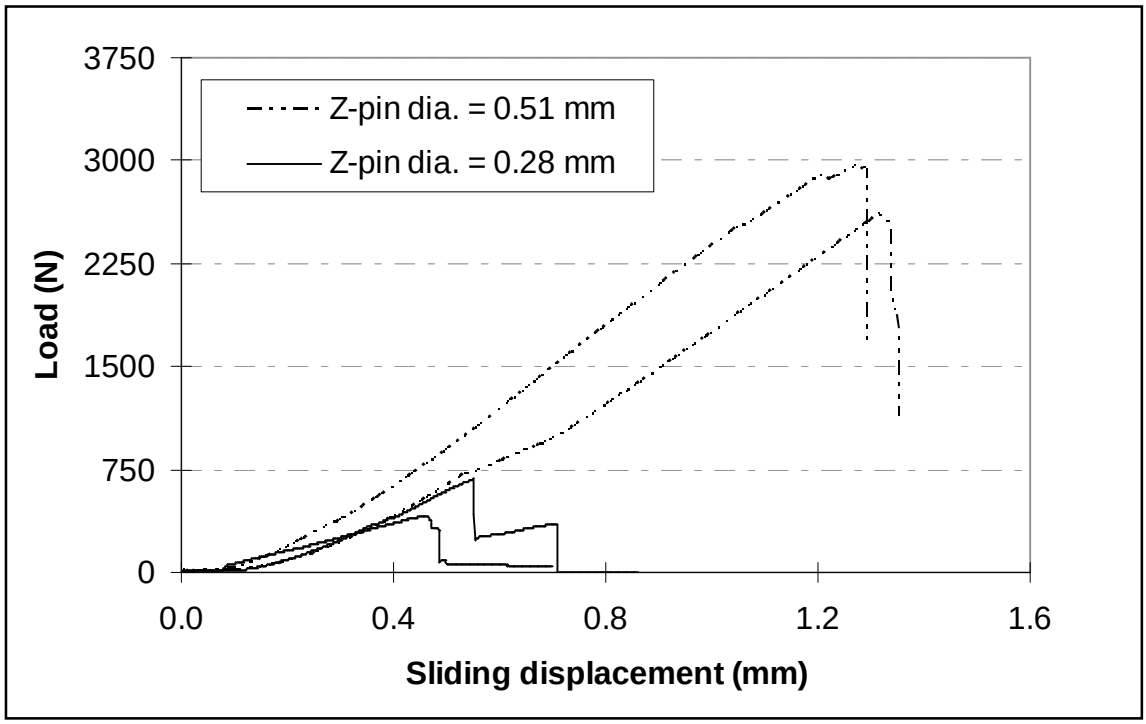

Figure 7.33 – Load vs. displacement curves for 16 z-pins in 0/90 woven glass / epoxy laminate

The insertion angle and pin quality variability observed in these specimens was high, the reasons for which have been discussed in Chapter 4. From the load versus displacement plots it can be seen that the traces do not rise linearly from the plot origin, taking around 0.4 mm to settle down. This is caused by frictional forces between the two laminate surfaces. This effect hides the true initial z-pin response. Furthermore, opening displacement was not successfully constrained for the 90° UD laminate. Settling of the UD fibres during manufacture left a non-flat shear plane which forced itself open upon loading and would have increased the friction between the two laminate surfaces considerably. For the 0° UD laminate specimens this effect did not force the shear plane open and for the 0/90 woven laminates the shear plane manufactured flat as intended.

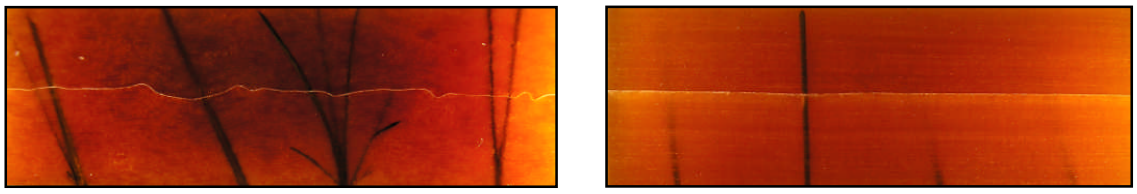

Figure 7.34 – Shear plane in UD (left) and 0/90 woven (right) laminate shear specimens containing 0.51 mm diameter z-pins

The average energy absorbed per z-pin until failure was estimated by dividing the area under the load versus displacement response by the number of z-pins observed to have bridged the shear plane; not always 16 due to some z-pins failing during insertion. These results are presented in Figure 7.35.

The failure stress per z-pin was also calculated for the two diameters and the three laminate types and is presented in Figure 7.36. The foundation has an effect on the shear stress, the 0/90 woven laminate values lie between the separate UD laminate cases suggesting an averaging effect of the foundation support. The failure stress per z-pin is similar for the two z-pin diameters tested. For the same rodstock type, the failure loads of other z-pin diameters can therefore be estimated.

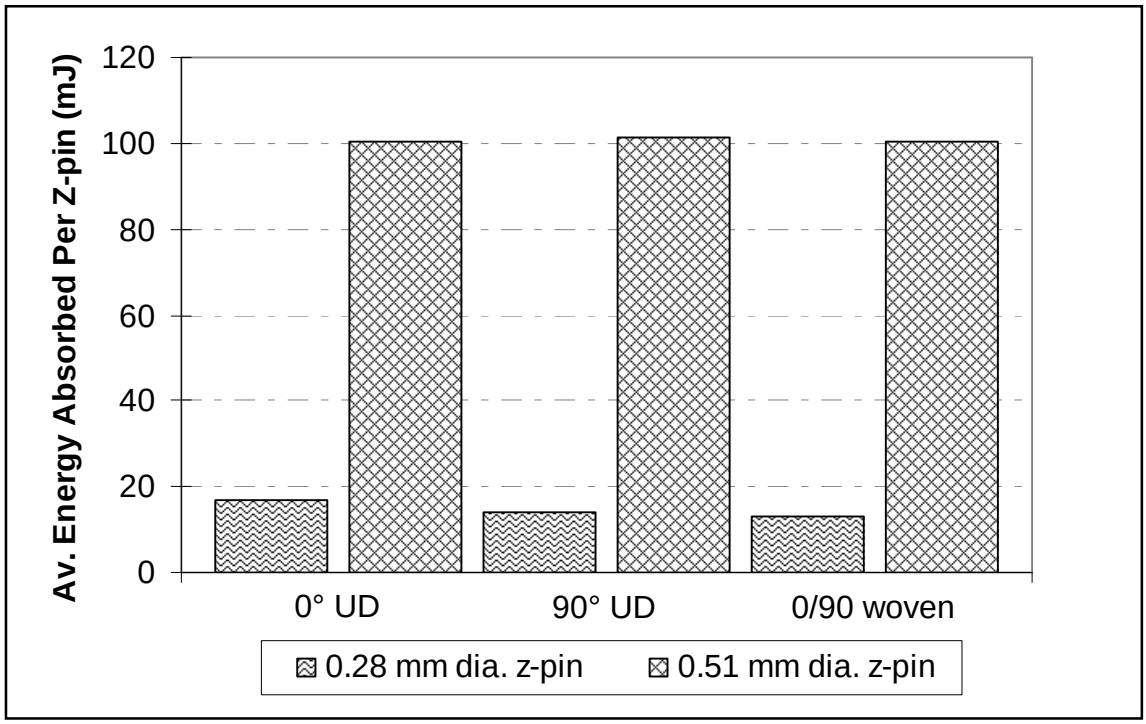

Figure 7.35 – Average energy absorbed per z-pin for two z-pin diameters tested in three laminate types

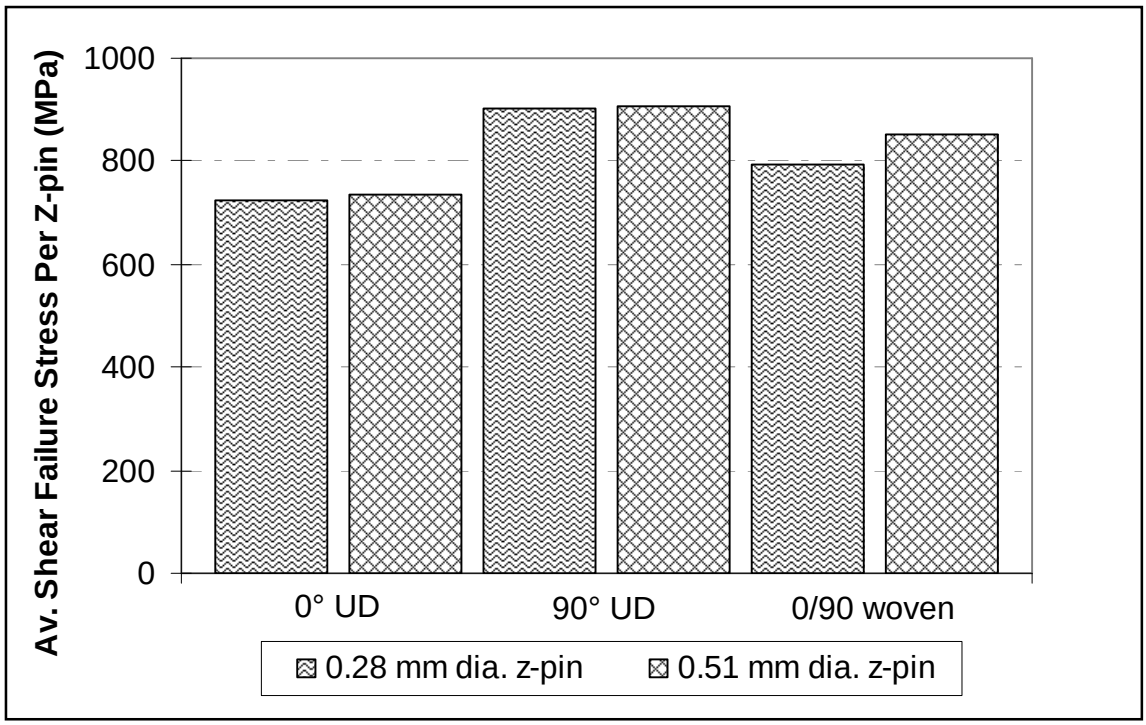

Figure 7.36 – Average shear failure stress per z-pin for two z-pin diameters tested in three laminate types

The digital video recordings taken of these shear tests did not show any deformation of the inserted z-pin length. If the opening displacement can be constrained and the laminate foundation is tough enough to prevent z-pins ploughing through the laminate, then the z-pins will predominantly fail in a brittle manner under mode II loading conditions. Ploughing of the z-pins through the laminate was prevalent in the 0° UD specimens tested but not seen in the 90° UD or 0/90 woven specimens. Brittle fracture is characterised by the steep load drops displayed in the 90° UD and 0/90 woven load versus crosshead displacement responses. The Z-shear test jig used can successfully produce this brittle mode II failure of z-pins and has been verified by SEM micrographs of the failed specimens.

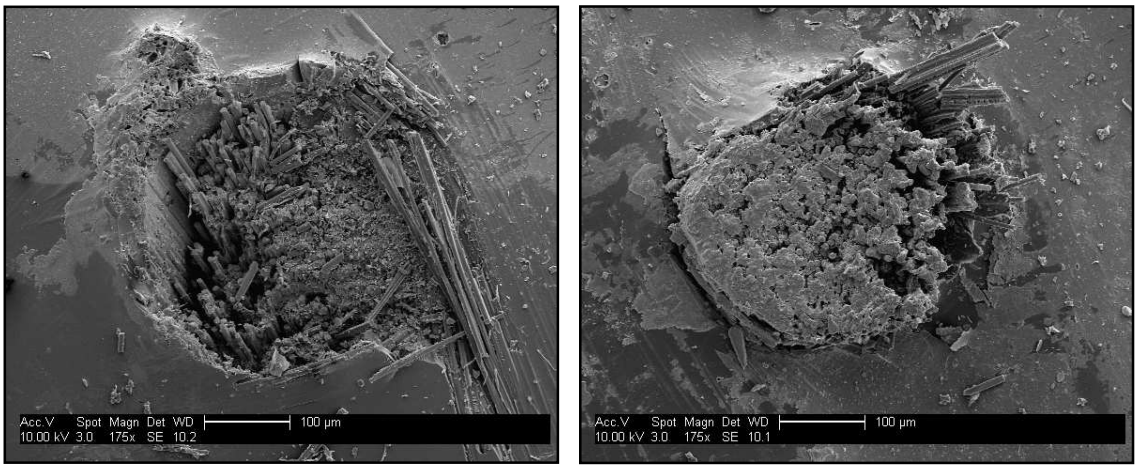

Figure 7.37 – SEM micrographs of mode II z-pin failure (0.28 mm diameter z-pin in 0/90 woven glass laminate).

However, it was realised that these tests on specimens containing multiple z-pins masked the effects of poor z-pin insertion quality. The variability of insertion angle and z-pin quality following insertion, present in all these test specimens, is averaged out by the large number of z-pins present. This is not satisfactory when trying to use this data to create accurate traction responses to be used in FE models to represent z-pin behaviour. From the failed specimens in which we can see brittle mode II fracture surfaces under the SEM, evidence of mode I pull-out was also present. This occurred when opening displacement was not perfectly constrained as for the 90° UD specimens and for z-pins which were not orientated perpendicular to the shear plane in a soft foundation as for the 0° UD specimens. As has been shown previously [1] the extent of pull-out is related to the z-pin orientation and its presence introduces an opening

component on the shear plane. It was clear from this work that mode II testing of specimens containing multiple z-pins did not provide suitable data from which a traction response for z-pins could be determined.

Ideally, mode II tests on a perfectly aligned, undamaged, single z-pin in a strong foundation were needed to generate data for the pure mode II traction response required. The failure effects seen raised the question as to whether a single pure mode II traction response would be adequate for modelling a wider range of composite materials.

7.4.2 Single z-pin tests

To answer the need for a more closely controlled data set the Z-shear test was modified for single pin testing (described fully in Section 5.5.2). Single lengths of 0.51 mm diameter raw material rodstock were held perpendicular to the loading direction in the low friction, steel mounting blocks. The load versus sliding displacement responses from these tests are presented in Figure 7.38. The curves shown have been treated to remove the small friction effect on the recorded load; measured to be a constant 18.6 N across the sliding displacement range.

The failure load and subsequent load drop displayed in Figure 7.38 is slightly less sharp than expected due to a small lag in the LVDT instrument used to measure the sliding displacement. The double gradient in the initial loading part of the curves is due to the z-pin sample settling in the mounting block hole. It was impossible to achieve a perfect fit of the z-pin in the mounting block and a small bearing deformation of the mounting block holes was observed after the test. Each mounting block hole was therefore used once only. The data obtained from the single z-pin tests produced a more consistent data set than was obtained previously from the laminate specimens containing 16 z-pins. These single pin tests were only carried out with the 0.51 mm diameter rodstock. The 0.28 mm rodstock could not be mounted in the test fixture without causing damage and no experimental results are presented. However, the z-pinned laminate shear tests showed that the failure stresses are similar for the two rodstock diameters and hence the

failure load for the 0.28 mm diameter z-pins can be deduced by scaling down the 0.51 mm diameter data set.

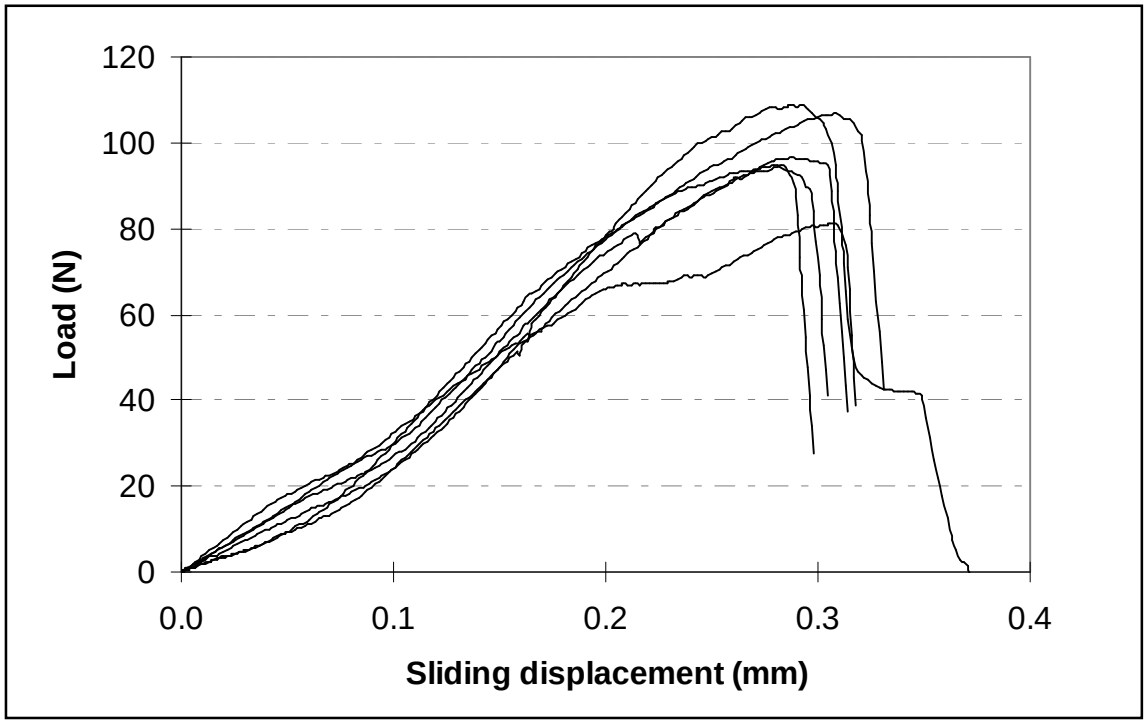

Figure 7.38 – Load vs. sliding displacement plot from single 0.51 mm diameter z-pin mode II testing

The z-pin mode II failure energy was calculated for each test from the area under the load versus sliding displacement response. The average energy determined for these 0.51 mm diameter tests is 16.5 mJ.

7.5 Representation of z-pin mode II response using MSC.Marc interface element

The equidistant spacing of z-pins, to provide the desired areal density, requires the traction response to be treated before being used in the FE model. The generation of a z-pin traction response is made easier, however, by the fact that the Z-shear test measures the sliding displacement directly rather than having to be calculated after the test as for the ELS tests.

7.5.1 Generating a fit to experimentally measured z-pin mode II behaviour

The load versus sliding displacement responses measured experimentally for the 0.51 mm diameter z-pins are presented as pin shear stress versus sliding displacement in Figure 7.39 based on the assumption that the z-pin cross-section at the shear plane is perfectly circular. The plot shows an approximated fit to the data which is the first step towards producing a representative z-pin traction response for FE use. The average mode II fracture energy measured for a single 0.51 mm diameter z-pin is 16.5 mJ. The approximated fit is made based on the pin failure energy and is has a total energy equal to 16.5 mJ.

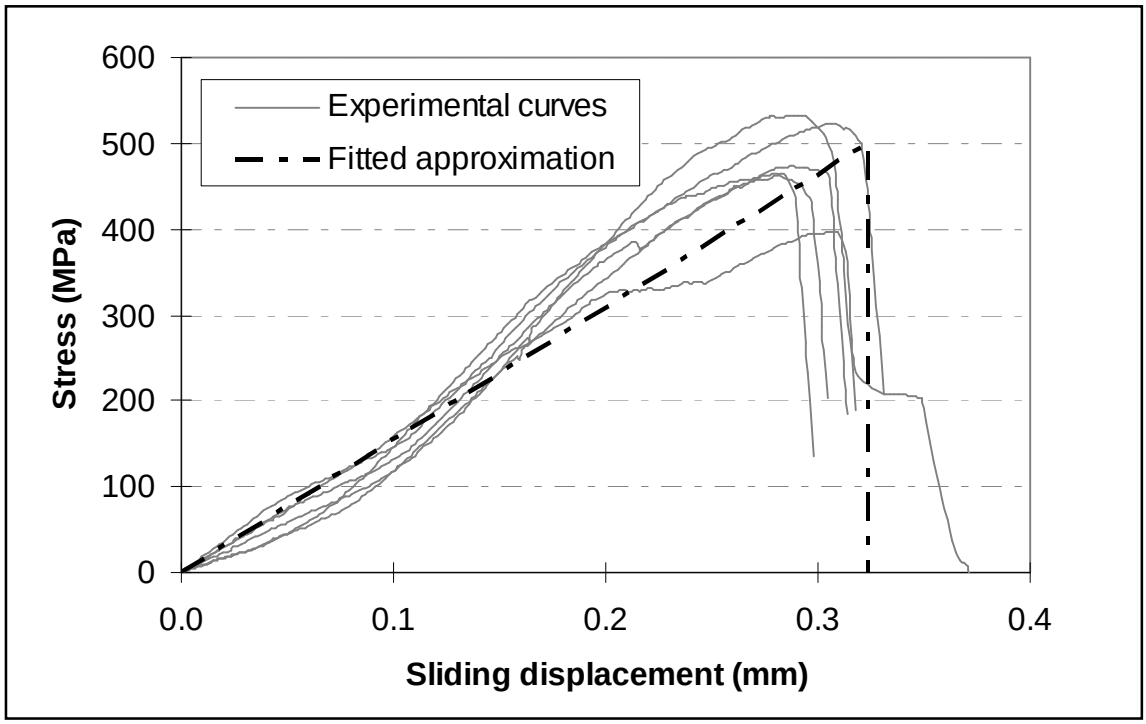

Figure 7.39 – 0.51 mm diameter z-pin shear stress vs. sliding displacement

For the 0.28 mm diameter z-pins, in the absence of experimental data from the single pin Z-shear test, the traction response is deduced from the 0.51 mm diameter results. The shear failure stress is kept constant as the material types are similar. The critical sliding displacement is obtained by applying the same critical sliding displacement to diameter ratio, as measured for the 0.51 mm z-pins, to the 0.28 mm diameter z-pin case. Again, this is based on the assumption that the z-pins have a perfectly circular cross-

section at the shear plane. Work conducted by Troulis [2] supports this critical displacement assumption. The mode II fracture energy of the 0.28 mm single z-pin is 2.8 mJ.

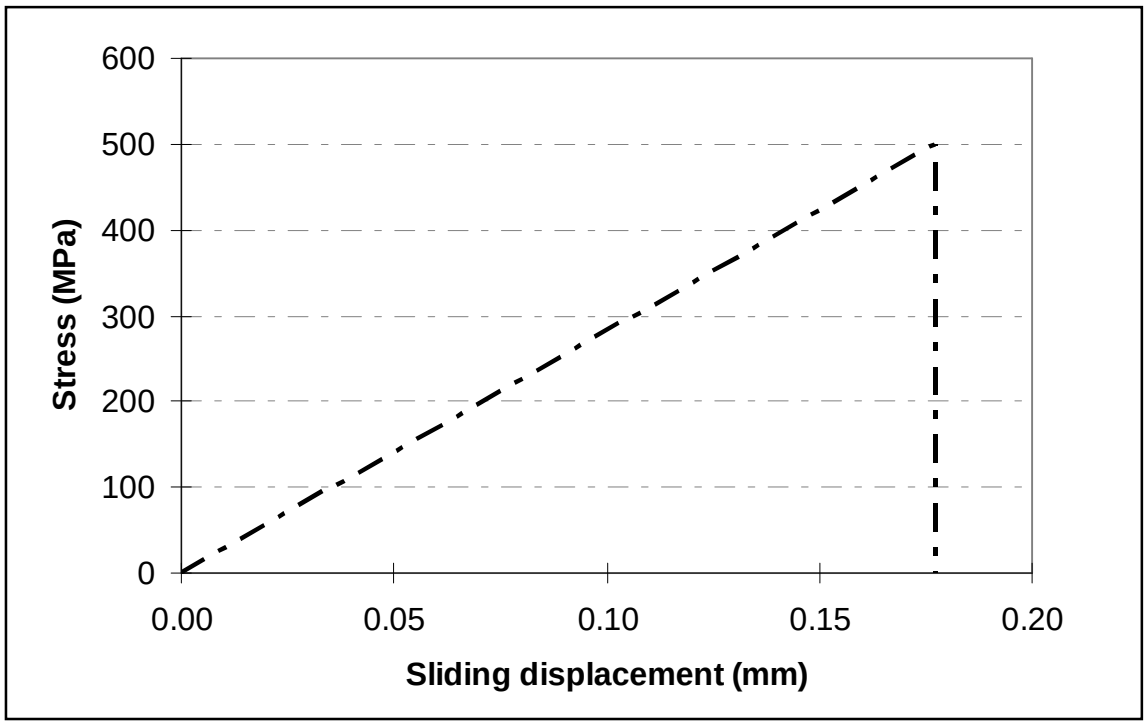

Figure 7.40 – 0.28 mm diameter z-pin shear stress vs. sliding displacement approximation

7.5.2 Treating the mode II z-pin response to account for areal density in the final traction response

Firstly, for the FE models developed in this work, z-pins are not modelled individually using the type 188 interface element. The reason for this is that the mesh size used in the z-pin reinforced regions of the FE models does not allow for this. In order to model individual z-pins the mesh size would have to be extremely fine which is both expensive and unnecessary in computational terms.

The plots for the 0.51 mm and 0.28 mm z-pins shown in Figure 7.39 and Figure 7.40 do not account for the areal density of the z-pin reinforcement. To accurately represent a block of z-pins, the areal density needs to be accounted for in the traction response for the FE model. Instead of converting the mode II z-pin loads (Figure 7.38) to z-pin stress

(Figure 7.39 and Figure 7.40) the measured loads need to be converted to stress which is relative to the areal density. For a z-pinning areal density of 2 % using 0.28 mm z-pins, the single pin response acts over a surface area of 3.06 mm^2 (1.75 x 1.75 mm). This area is used to obtain the traction response stress not the cross-sectional area of the single z-pin. Figure 7.41 shows the traction response used in the FE models which represents a square, 0.28 mm, 2 % areal density z-pinning arrangement. The responses for other common areal densities, 0.5 % and 4 %, are also shown for comparison.

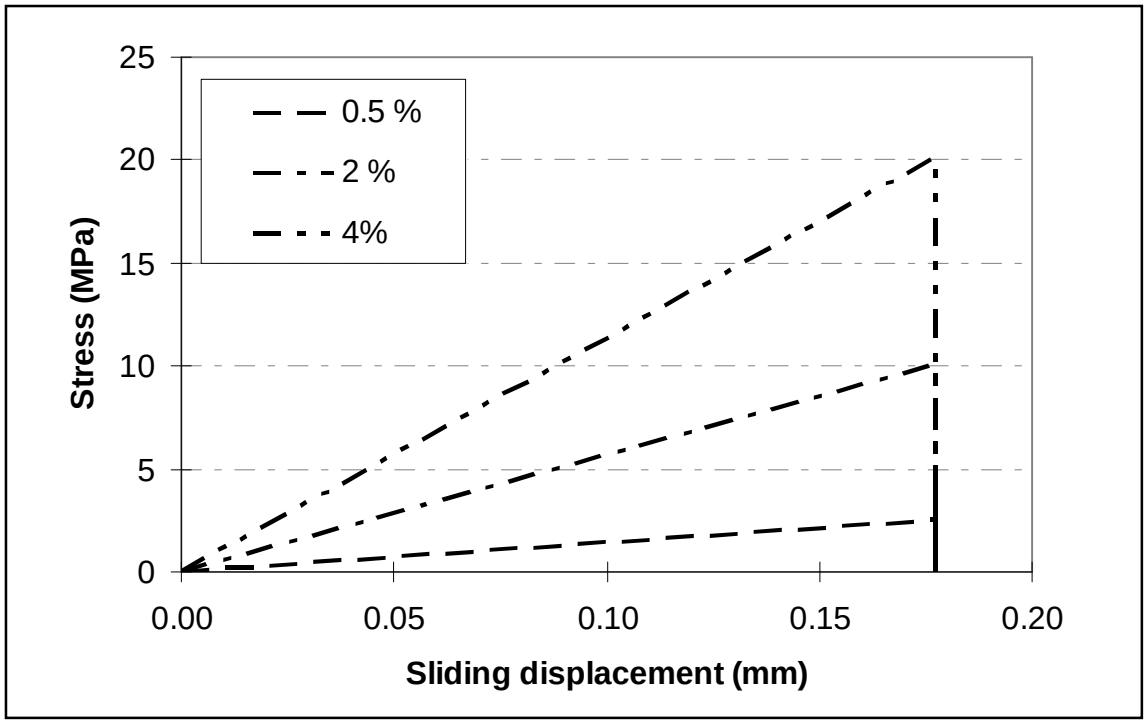

Figure 7.41 – 0.28 mm diameter, 0.5 to 4 % areal density traction responses for FE interface element implementation

7.6 Implementation of combined responses in I-section FE model

Implementing the traction responses for the material and the z-pins on the same interface can be done in three ways. Firstly, the MSC.Marc FE software only allows one response to be described through the 'on screen' module so at least one user subroutine is required. If one of the traction responses is simple enough to be described by the on screen module then the most straightforward way to implement the combined z-pin and

material response is to use the on screen module plus one user subroutine. Secondly, if both the z-pin and material traction responses are too complex to be described using the simple on screen module then two user subroutines can be used. This has an impact on processing requirements as there are more external information sources which are called during the analysis. Finally, the z-pin and material traction responses can be combined to produce a single unified response. In doing this, however, it is much more difficult for the user to re-position the z-pin response and to investigate the effects of different z-pin arrangements on the structure.

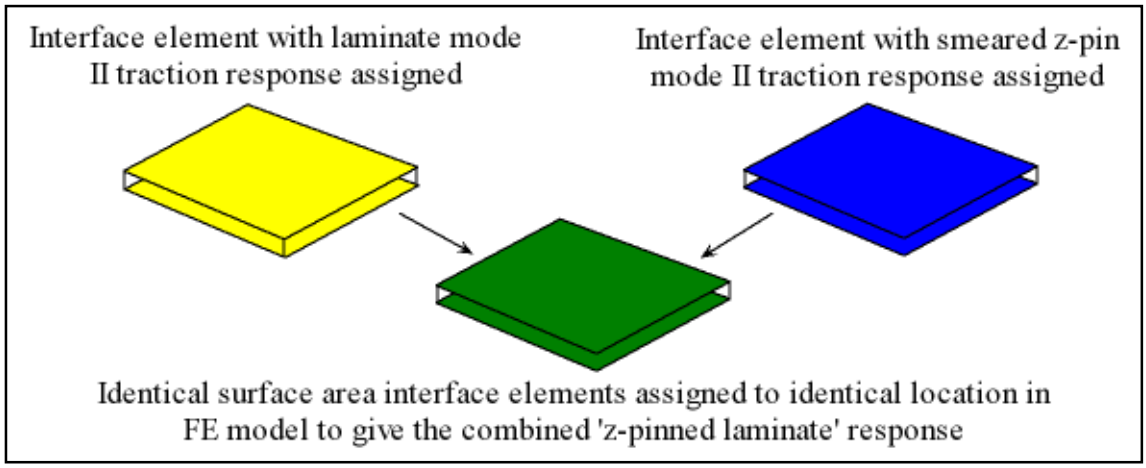

Figure 7.42 – Overlaying interface elements

For this work the overlaying of interfacial elements was used to model the z-pin reinforced material interface. The simple z-pin traction response profile was input via the on-screen interface element module, the more complex material interface traction response was input via a separate user sub-routine.

Chapter 8

Using predictive tools to optimise z-pin reinforced structures

This chapter describes the development of MSC.Marc FE models to represent the 914 / 6K5H / T300 woven pre-preg I-section specimen geometries, the experimental test results from which were detailed in Chapter 6. The beginning of this chapter details the construction of these FE models, incorporating the interface elements and mode II traction responses developed in Chapter 7. Finally, the results obtained from the FE models are reported and compared against results from the experimental tests.

For modelling the z-pins, the von Mises type traction response is used as this provides the closest match to the ELS test load versus load line displacement curves (see Figure 7.25) for the 914 / 6K5H / T300 material system. The traction responses generated for the z-pin mode II response assumes that the z-pins are perfectly aligned and are not subjected to any opening displacement or local foundation (laminate) yielding.

8.1 FE model representation of the base-line I-section geometry

The I-section test elements have three lines of symmetry and therefore, for computational economy, only one eighth of the test element was modelled. Figure 8.1 shows the cross-sectional geometry of the I-section test element and the 1/8th finite element model representation.

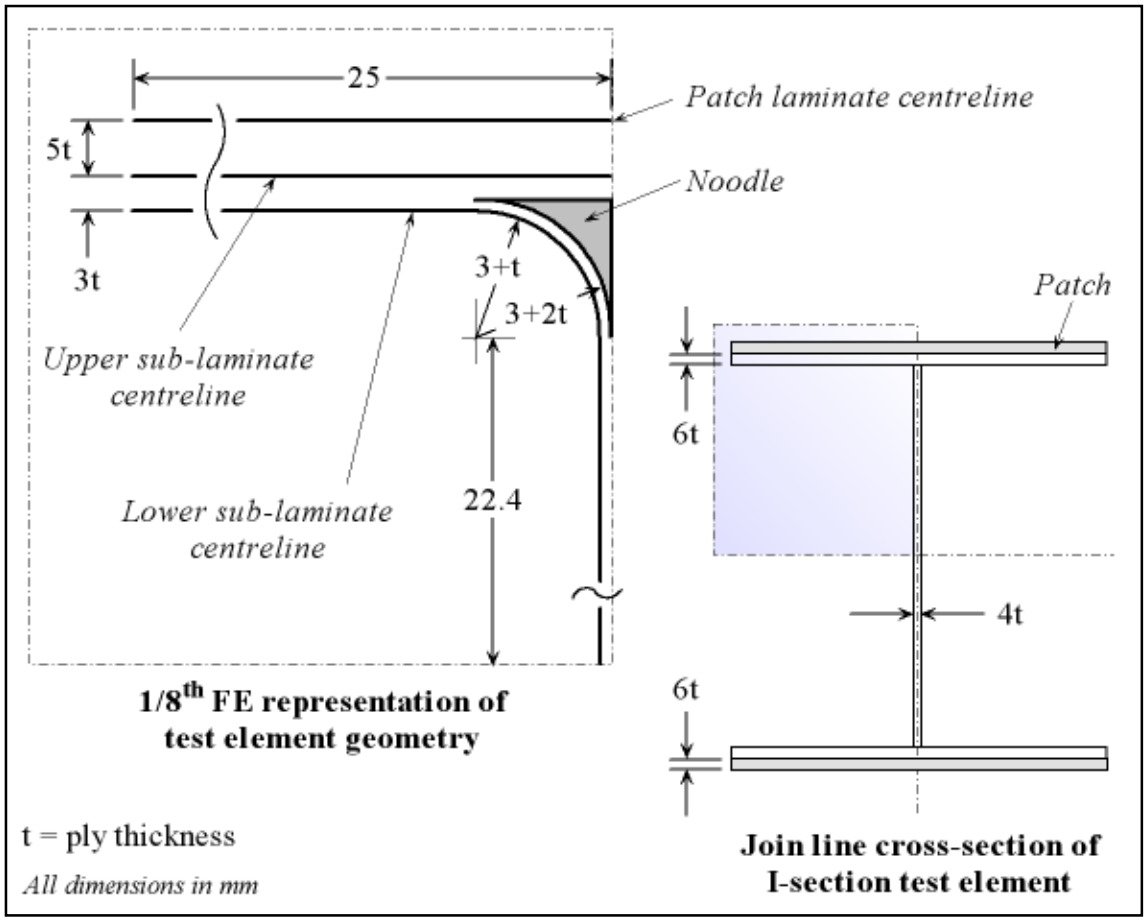

Figure 8.1 – I-section test element cross-sectional geometry and 1/8th FE representation

Splitting the I-section laminate into two equivalent sub-laminates, as shown in Figure 8.1, was the only successful way to re-produce the correct geometry and incorporate the noodle detail. Offsetting the sub-laminate mid-planes from the geometry surfaces was attempted but proved unsuccessful. However, linking these two layers of shell elements together so that they behaved as one single laminate was not straightforward. Multi Point Constraint (MPC) definitions were trialled without success, as were rigid links.

Ultimately, the only way in which the correct deformation response could be achieved was through the use of elastic beam elements. The elastic beams were assigned a Young's modulus of 5 x10^6 MPa so as not to deform themselves and thus correctly simulate the laminate deformation upon loading. Elongation of the elastic beams would represent an opening between the sub-laminates (delamination), contraction would be equivalent to the laminate crushing, both of which were not the case during testing and were therefore undesirable in the model. Figure 8.2 identifies the elastic beam connections between the shell element nodes on the sub-laminate mid-planes and noodle surfaces. The noodle region, made up of solid elements, was coated on the connected surfaces with thin shell elements. This gave the nodes the correct number of degrees of freedom to allow them to be connected to the laminate shell elements.

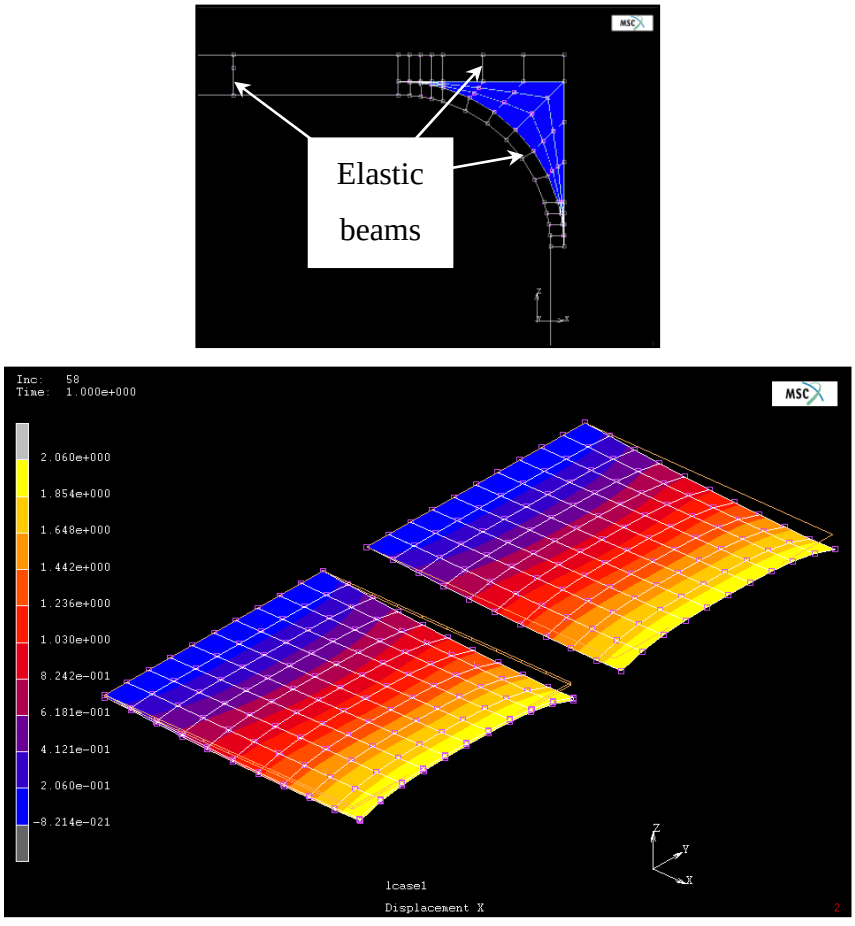

Figure 8.2 – Use of elastic links to connect sub-laminates in I-section model (top) and in verification model (bottom)

Figure 8.2 also shows a verification test on a loaded laminate modelled as two shell element surfaces linked with elastic beams (left) and as a single shell element surface (right). The laminate lay-up was specifically set to be unbalanced to check that the warping effect is consistent between the two methods. This model validates that the elastic beam links give the necessary connectivity and provide the correct deformation response.

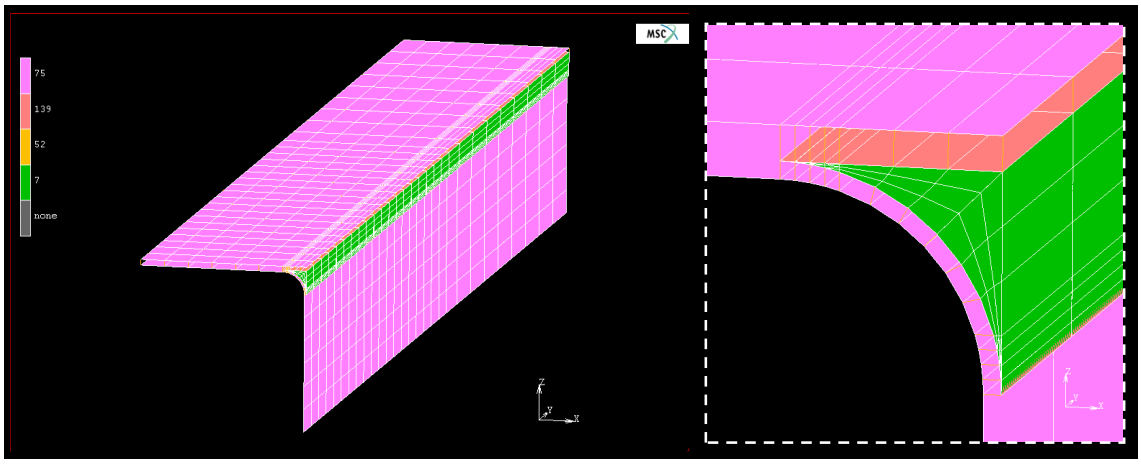

Figure 8.3 – Extruded cross-section and element identification

Figure 8.4 – Sub-laminate definition for shell elements

The 1/8th cross-section geometry was extruded 175 mm to form one half of the total I-section test element length (see Figure 8.3). The individual ply orientations which make up the sub-laminate thicknesses were input via the material properties module and assigned to the corresponding shell elements (see Figure 8.4).

8.1.1 Mechanical property input values

The 914 / 6K5H / T300 laminate material properties for the I-section, required by the FE model, were not measured experimentally. Instead, they were generated using laminate analysis and knowledge of the raw material mechanical properties gathered through manufacturer's data and published literature. To assist with micromechanics calculations the Component Design Analysis (CoDA) software was used, a tool specifically designed to produce laminate mechanical property approximations in this way.

Table 8-1 and Table 8-2 detail the resin and fibre properties input into CoDA for generation of the ply properties used in the MSC.Marc I-section FE model. To obtain an estimation of the mechanical properties, the woven ply was treated as four layers of UD composite stacked $(90/0)_2$. The total thickness of this four layer stack was equal to the cured ply thickness of the woven prepreg material. The reason for using a four ply stack instead of a simple (90/0) representation was that the effect of warp fibre bias is more closely matched to physical reality. Table 8-3 details the mechanical properties calculated by CoDA.

	Hexcel 914 epoxy resin	Source
Density (kg/m^3)	1290	[216]
Modulus (GPa)	3.9	[216]
Poisson's Ratio	0.41	[216]
$Strength_T$ (MPa)	47.7	[216]
$Strength_C$ (MPa)	180	[216]
$Strength_S$ (MPa)	80	[215]
G_{12} (MPa)	unknown	-
ε_{max} (%)	unknown	-

Table 8-1 – Resin properties required for CoDA analysis

	T300 carbon fibre	Source
Density (kg/m^3)	1760	[217]
E_{11} (GPa)	230	[217]
E_{22} (GPa)	15	[218]
Poisson's Ratio	0.2	[218]
$Strength_T$ (MPa)	3530	[217]
G_{12} (MPa)	15	[218]
Diameter (μm)	7	[217]

Table 8-2 – Fibre properties required for CoDA analysis

	914 / 6K5H / T300
E_{XX} (GPa)	55.1
E_{YY} (GPa)	55.4
G_{XY} (GPa)	3.5
ν_{XY}	0.04
ν_{YX}	0.04
Density (g/cm^3)	1.55

Table 8-3 – CoDA estimation of 914 / 6K5H / T300 woven pre-preg properties

For the Structil EA9 epoxy noodle standard isotropic epoxy properties were given to the solid noodle elements in the absence of any manufacturer's data (Young's Modulus = 2.8 GPa, Poisson's Ratio = 0.4). The thin shell elements used to coat the noodle solid elements were assigned identical properties to the epoxy type noodle.

8.1.2 Boundary conditions

Four boundary conditions were applied to the I-section FE model. The first boundary condition accounted for the steel test fixture, bonded at the end, through which the I-sections were loaded during the experimental tests, the final three were required to correctly account for the three symmetry lines of the 1/8th geometry model. Figure 8.5 to Figure 8.8 show the various boundary conditions (indicated by the red arrows) on the I-section FE model and details of the degrees of freedom constrained. The images shown are from a geometry which includes a patch joint to show the additional assignments made in this case.

Displacement X	0
Displacement Y	-
Displacement Z	0
Rotation X	0
Rotation Y	0
Rotation Z	0

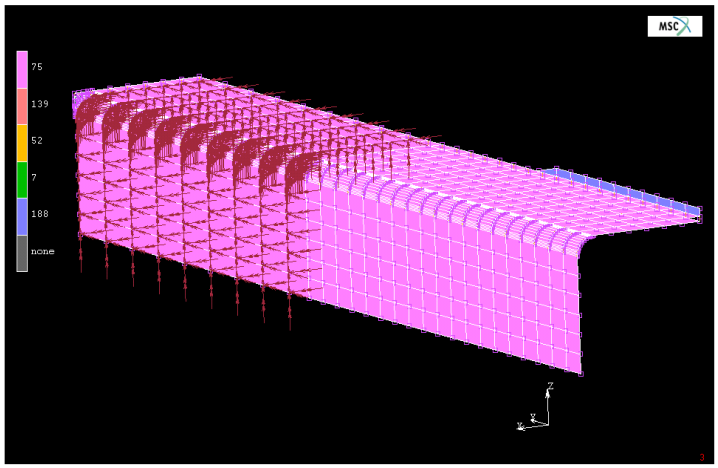

Figure 8.5 – Test fixture boundary constraints

Displacement X	-
Displacement Y	-
Displacement Z	-
Rotation X	0
Rotation Y	0
Rotation Z	0

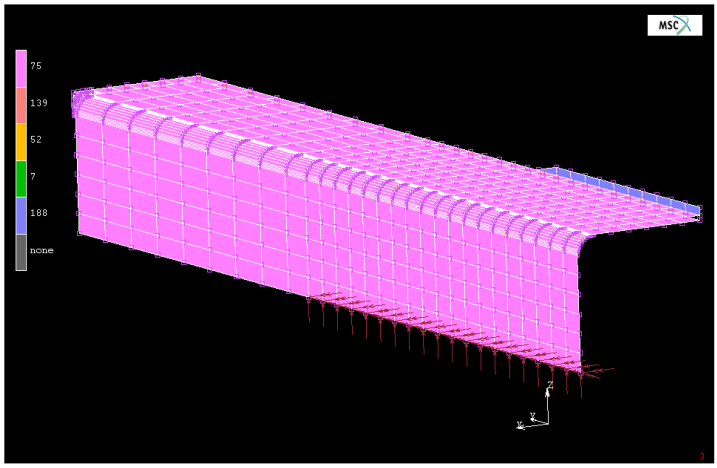

Figure 8.6 – I-section height symmetry line boundary condition

Displacement X	0
Displacement Y	-
Displacement Z	-
Rotation X	-
Rotation Y	0
Rotation Z	0

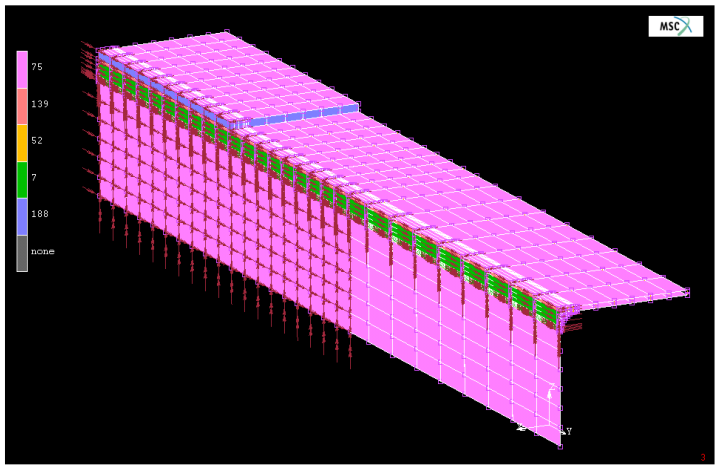

Figure 8.7 – I-section width symmetry line boundary condition

The areas in Figure 8.6 and Figure 8.7 in which application of the boundary condition seems to be missing are deliberate. It was found that if more than one boundary constraint was set on the same node then the analysis would not run. In this case, the test fixture and symmetry line boundary conditions are applied to similar nodes; the symmetry line condition was therefore removed.

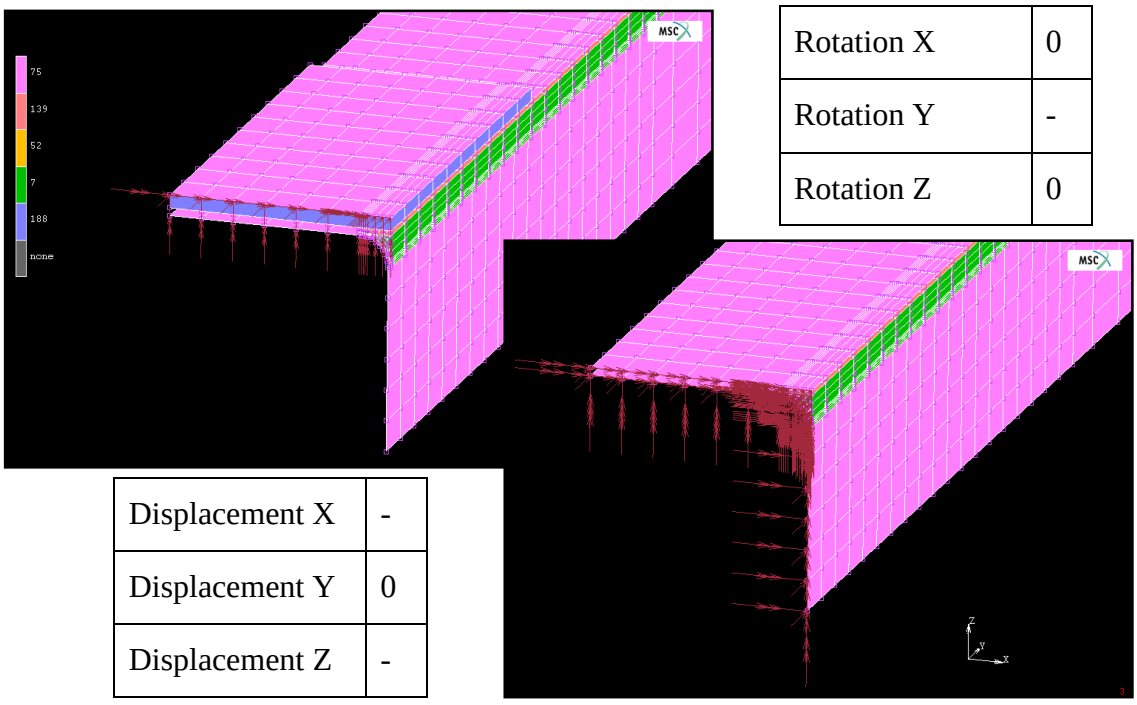

Rotation X	0
Rotation Y	-
Rotation Z	0

Displacement X	-
Displacement Y	0
Displacement Z	-

Figure 8.8 – Join line boundary conditions for I-section model with patch (left) and without patch (right)

8.1.3 Loading conditions

One key detail learned from the elastic beam links verification model (shown in Figure 8.2) was that, when using these to link two layers of shell elements, additional nodes were required on which to apply loading forces or displacements. If forces or displacements are applied on edge nodes of either shell layer then the layers will skew. In the region corresponding to the bonded steel test fixture, additional nodes were placed between the two linked shell layers. These nodes were positioned corresponding to the full laminate mid-plane. Including these extra loading nodes required a corresponding number of extra elastic beam links to be included.

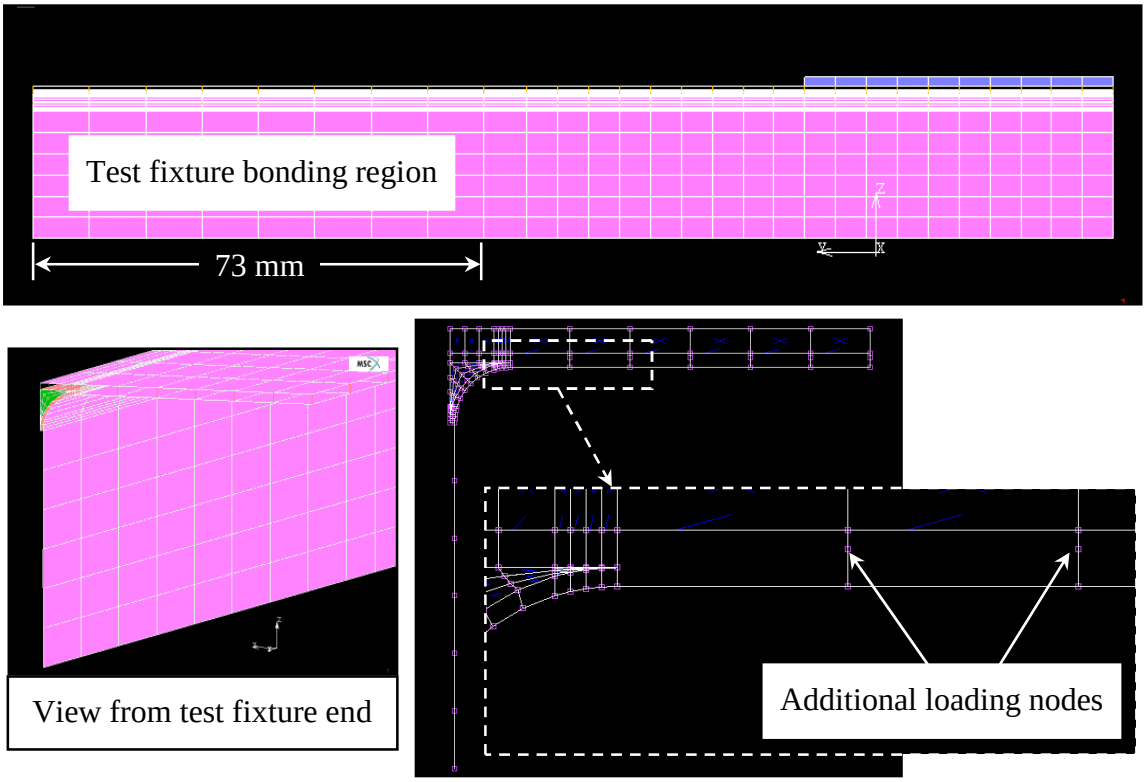

Figure 8.9 – Nodes for loading between linked surfaces

The nodes in the test fixture bonding region were all connected to a single node using kinematic constraints to assist in applying loading conditions. This single, outlying node corresponded to the loading pin position in the mechanical testing set-up. The kinematic constraints were set up so that the longitudinal displacements (+y displacement for this model) of the nodes in the bonded region were to be equal to the displacements of the single node. Only this one degree of freedom was linked. In physical terms, this means

that there is no extension of the laminate in the bonded region. This assumption is sound as there was no failure of the bond-line during the experimental tests.

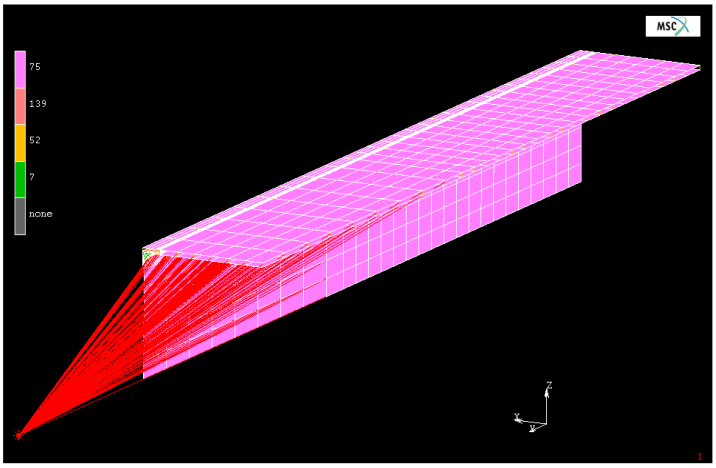

Figure 8.10 – RBE2 type kinematic links for load application

The use of the single loaded node assisted in data retrieval and analysis. The total reaction force of the I-section could be obtained from this one node rather than having to sum the reactions of all the nodes in the bonded region. Displacement driven loading of the model was preferred over force application. A displacement of 5 mm in the longitudinal (y) direction was applied incrementally to the single loading node; all other degrees of freedom were set to zero.

8.2 Addition of the patch joint

Shell elements were again used to represent the patch laminate. The separation between the patch mid-plane and the uppermost shell layer of the I-section was a function of the material ply thickness. Extension or reduction of the patch length was a simple case of adding or removing patch shell elements. Material properties and ply orientations were assigned to the patch shell elements in the same manner as for the I-section sub-laminates.

The physical link between the I-section and patch shell elements was provided by the interface elements which would ultimately be assigned with the relevant interfacial traction response(s).

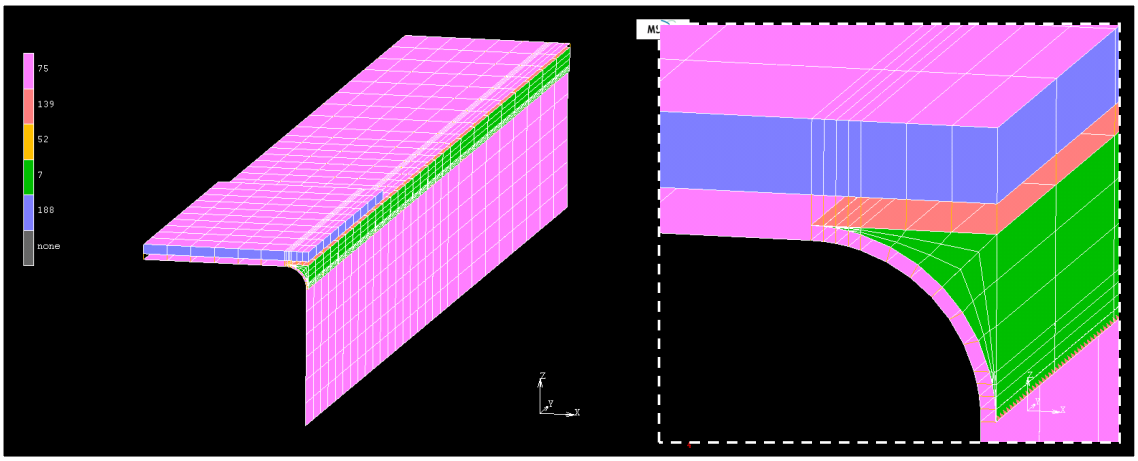

Figure 8.11 – Addition of patch to the I-section model and inclusion of type 188 interface elements

8.3 Mesh size

The meshing arrangement is less than ideal in the noodle region (see Figure 8.12). At the tips of the noodle the aspect ratio of the elements used is not desirable but is ultimately limited by the noodle geometry. Positioning of the nodes for the laminate elements directly above and along the corner radius was made so as to achieve vertical and radial alignment of the connecting elastic beam elements. Any modifications to the mesh arrangement in the noodle therefore had a direct affect on the mesh design in the rest of the structural model.

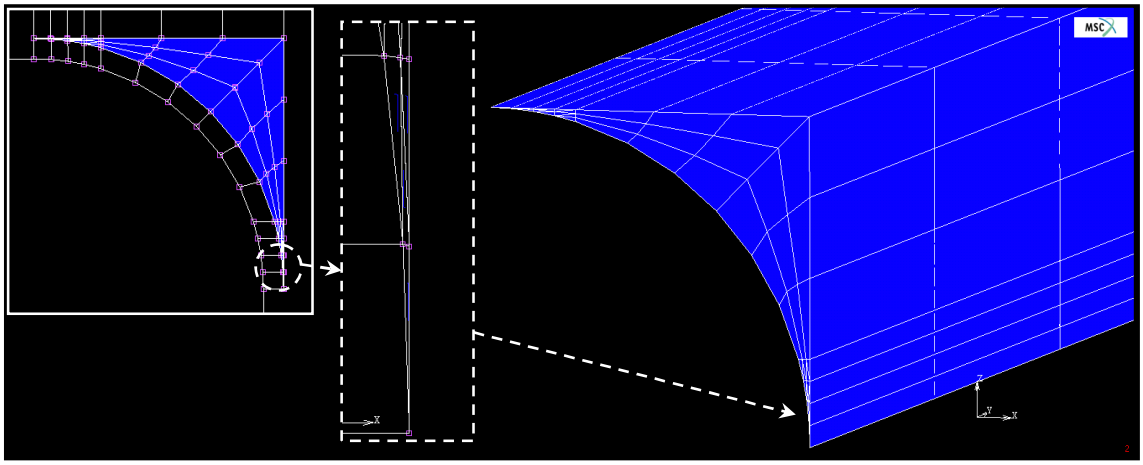

Figure 8.12 – Non-ideal noodle mesh arrangement

Very fine meshing in the tips of the noodle region was not implemented because, on the laminate surfaces, this would create the need to connect small elements to large elements which is not recommended without some intermediate grading of element sizes. Furthermore the increase to the processing time incurred outweighed the perceived benefit. This noodle region is not critical to the structural performance of the structure however.

The length of the shell elements on the patch surface was determined for ease of representation of the patch geometry. This dimension affected the sizing of the interface elements in this region also. The mesh arrangement in the rest of the model was implemented based on experience, with a consideration for computational processing time.

Ideally, despite the time involved, all modelling work would include a mesh sensitivity study whereby the mesh size would be altered, usually reduced, to assess any change in the computed solution. For this work, such an optimisation check would have required a complete overhaul of the model each time in order to alter the mesh size and was therefore not viable. Two areas where a finer mesh would be most useful in this model are discussed hereafter.

A fine mesh is always desirable at the delamination front where high stresses occur. However, delamination in this structure is not static and therefore the finely meshed region would have to be dynamic within the model in order to track the propagation front. Dynamic meshing was avoided as the complex meshing algorithms required are computationally expensive. The sizing of the interface elements remains important however, and this is discussed further in Section 8.6. The region at the end of the patch could also have been meshed finer to pick up stress concentrations in the composite laminate.

8.4 Modelling the z-pin reinforcement and laminate failure

It is important to state that in this model the z-pin geometry is not represented; interface elements are used to represent the z-pin mode II response. There are two areas in which the z-pins affect the structure in this model. Firstly, the interface between the patch and the I-section flange and secondly the I-section and patch laminate in-plane mechanical properties.

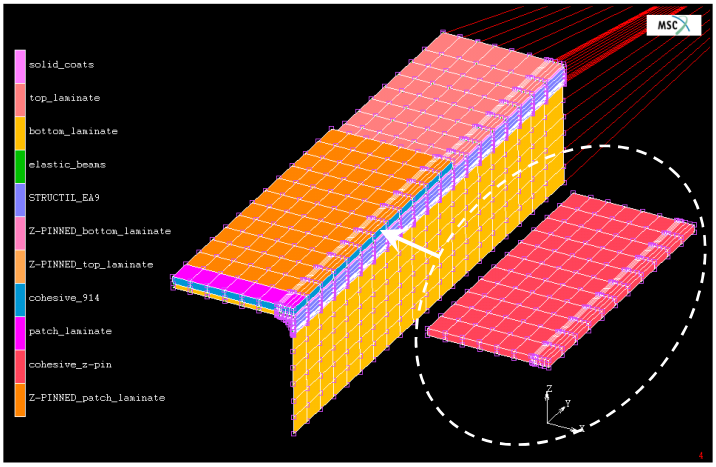

Figure 8.13 – Assigning z-pinned laminate properties and overlaying interface elements

Figure 8.13 shows the interface elements, which represent the z-pin mode II response, ready to be overlaid onto the laminate response interface elements which are already in position. The colour coding refers to the material properties assigned to each region of the model. The ply properties assigned to the elements corresponding to the z-pinned laminate regions are listed with the non-z-pinned ply properties in Table 8-4.

The in-plane moduli for the 914 / 6K5H / T300 ply were reduced by 8%, based on experimental findings reported in [99], for the z-pinned ply. The normal modulus (E_{33}) was increased by 26% based on information from the same source. The presence of z-pins in the laminate will also affect the Poisson's ratios and shear modulus values. This information was not available but is not critical to the loading case in this model and is therefore left unchanged.

	914 / 6K5H / T300	Z-pinned 914 / 6K5H / T300
E_{11} (GPa)	55.1	50.6
E_{22} (GPa)	55.1	50.6
E_{33} (GPa)	9.8	12.3
v_{12}	0.04	0.04
v_{23}	0.4	0.4
v_{31}	0.04	0.04
G_{12} (GPa)	3.5	3.5
G_{23} (GPa)	3.3	3.3
G_{31} (GPa)	3.3	3.3

Table 8-4 – Input 914 / 6K5H / T300 and z-pinned 914 / 6K5H / T300 ply properties

In order to predict the ultimate load capabilities for the various I-section joint designs using this model, maximum allowable ply strength data for the unpinned and z-pinned laminates are required. For this model the tensile strengths are the most critical, the input values used are detailed in Table 8-5.

The CoDA analysis software was used to predict the 914 / 6K5H / T300 ply failure strengths. These values were modified using the Chang et al model [95] which predicts the tensile strength of z-pinned laminates using an empirical constant derived from experimental test data. This relationship is given in Equation 8.1.

$$\sigma_p = \sigma_o \left(1 - \alpha D c_r\right) \quad \text{.....(8.1)}$$

where

σ_p is the z-pinned laminate tensile strength (MPa)

σ_o is the unpinned laminate tensile strength (MPa)

α is the z-pinning area fraction (areal density)

D is the z-pin diameter expressed in mm

c_r is an empirical constant

A value of 29 mm^{-1} was used for c_r in this model obtained from Freitas et al [92].

	914 / 6K5H / T300	Z-pinned 914 / 6K5H / T300
Max. tensile stress X (MPa)	673	564
Max. tensile stress Y (MPa)	673	564

Table 8-5 – Maximum allowable ply failure stresses for laminate failure monitoring

The Hoffman failure criterion was used to implement these strength data in the FE model. This criterion monitors the element stresses against maximum allowable input values. In-plane and out-of-plane tension, compression and shear values can be assigned

8.5 FE simulation results

Initial execution of the I-section FE model analysis showed that the laminate stacking sequence induced a more significant than expected mode I component on the patch / I-section flange interface.

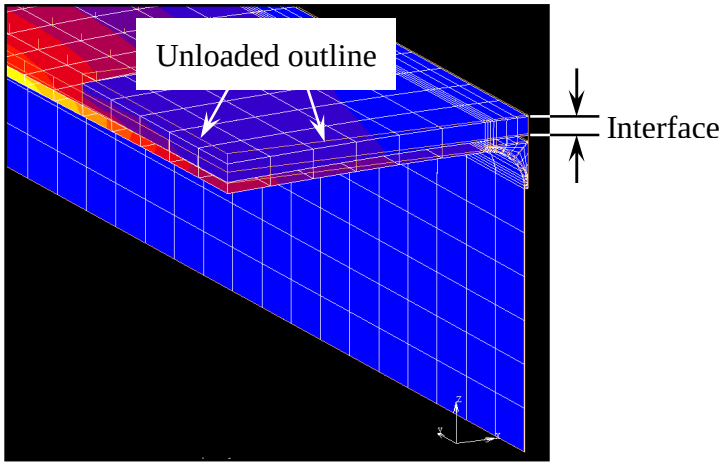

Figure 8.14 – Deformation exaggerated view of mode I component on the patch / I-section flange interface under predominant mode II shear loading

For the 914 / 6K5H / T300 material, a mode I fracture toughness (G_{IC}) value of 786 J/m^2 was obtained from Double Cantilever Beam (DCB) tests. The DCB data enabled a shear / normal weighting coefficient (ratio of mode II to mode I fracture toughness, equal to 5.2) to be incorporated into the 914 / 6K5H / T300 von Mises traction response sub-routine. The addition of this weighting coefficient enabled the failure of each interface element to take account of local mode I components in addition to the predominant mode II deformation.

It should be noted that the incorporation of the shear / normal weighting was limited by the capability of the FE software which did not allow for a separate mode I traction response to be assigned. Whilst the total mode I failure energy could be defined, the profile of the response had to be identical to the response developed for mode II (see Figure 7.17) when, in fact, it is unlikely to be similar. The interface elements which represent the z-pins were not modified to include a mode I response as test data for z-pins in this material system was unavailable.

Table 8-6 shows the ultimate tensile loads and modes of failure obtained from the FE models compared against identical I-section geometries tested experimentally. The FE model is able to show the mode of failure as well as the ultimate load capability. The two modes of failure for these I-section structures are delamination of the patch from the I-section, in the cases where a patch joint is included, and fracture of the I-section laminate. These two failure modes are identified by the labels A and B respectively and for the FE model they were deduced from the load versus displacement curves.

Patch overlap length	Experimental test		FE model	
	Ultimate load (kN)	Failure mode	Ultimate load (kN)	Failure mode
Pristine	61.4	B	61.7	B
Z-pinned pristine	55.8	B	54.7	B
10 mm	-	-	30.6	A
15 mm	27.8	A	43.0	A
20 mm	-	-	50.5	A
25 mm	34.7	A	54.8	A
30 mm	-	-	55.4	A
35 mm	42.7	A	56.0	A
40 mm	-	-	56.6	A
45 mm	53.9	A	57.0	A
50 mm	-	-	57.3	A
10 mm z-pinned	20.4	A	31.9	A
15 mm z-pinned	29.1	A	44.9	A
20 mm z-pinned	-	-	54.0	A
25 mm z-pinned	37.4	B	58.4	B
30 mm z-pinned	-	-	58.8	B
35 mm z-pinned	39.0	B	56.6	B
40 mm z-pinned	-	-	60.0	B

Key: A – Patch delamination B – I-section laminate fracture

Table 8-6 – Comparison of FE model results with experimental tests

The most successful outcome of this modelling effort is the prediction that the failure mode changes, from delamination of the patch to fracture of the I-section laminate, for the 20 mm patch overlap length. This result is consistent with the experimental tests. Furthermore, all modes of failure obtained using the FE model, for the range of joint geometries simulated, agree with the experimental test findings. The FE simulated ultimate failure loads of the pristine and z-pinned pristine geometries are in excellent agreement with the experimental test results.

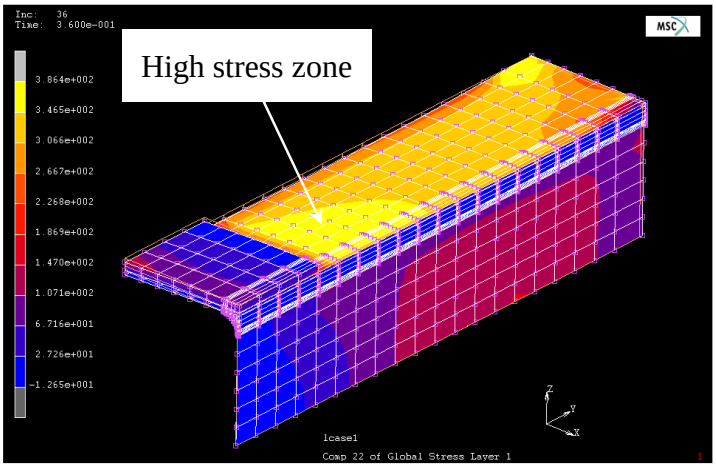

Figure 8.15 – Stress contours in the 20 mm z-pinned FE model

The first I-section laminate element to fail in the FE model cannot be identified at present but the stress contour image in Figure 8.15 suggests strongly that fracture occurs at the edge of the patch. The stress concentration is highest in this region. If failure of the FE model at the edge of the patch can be confirmed then this would be consistent with the location of failure in the experimental tests.

However, the ultimate loads obtained from the FE model simulations of the patch joints are consistently higher than those obtained from the experimental tests. The ultimate load plateau seen in the experimental results for the z-pinned joints is not replicated by the FE simulations either. Lastly, the linear relationship between ultimate load and patch overlap length for the control joints, observed in the experimental tests, is not seen in the FE simulations (see Figure 8.16).

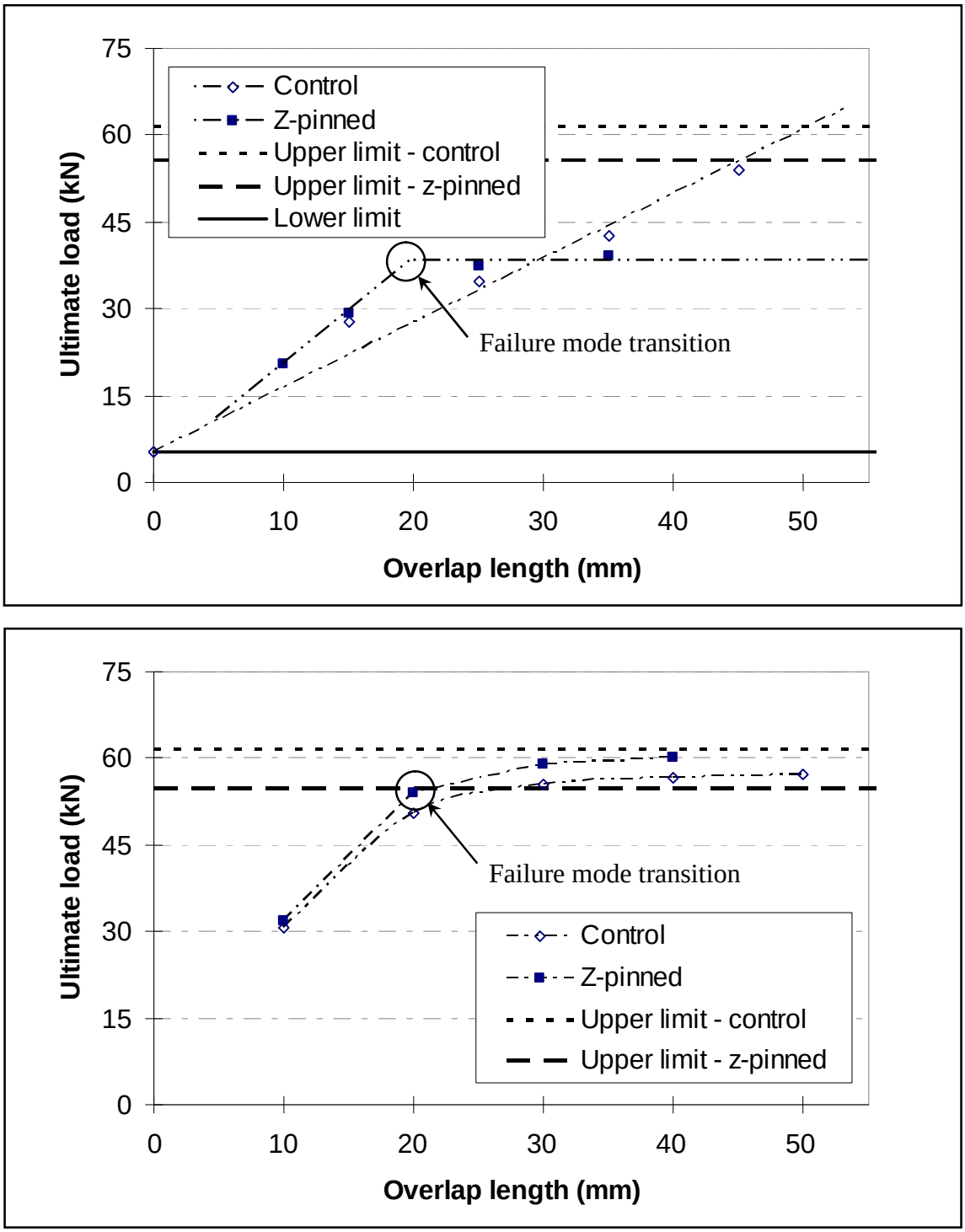

Figure 8.16 – Comparison of failure envelopes plotted from experimental test results (top) and FE model results (bottom)

8.6 Sensitivity assessment

The over-prediction of ultimate failure load by the FE model was investigated by modifying the 914 / 6K5H / T300 traction response. As a test, the traction response was redrawn, still using the general OABCD profile, to produce the best fit to the ELS load versus load-line displacement curves detailed in Chapter 7 (see Figure 7.25). The best fit was found using a resin shear strength value of 35 MPa. The modified traction response was constructed to have the same cohesive energy as the original von Mises traction response. The modified traction response was used to re-analyse two FE model geometries, the 10 mm and 20 mm z-pinned patch overlap length models.

For the 10 mm patch overlap length model, using the modified traction response gave an ultimate load of 27.3 kN, a reduction of 3.3 kN compared to the result generated using the von Mises traction response. For the 20 mm z-pinned patch overlap length model an ultimate load of 49.6 kN was obtained using the modified traction response, a reduction of 4.4 kN compared to the von Mises result.

It is clear from this initial assessment that the ultimate load obtained from the model is sensitive to the profile of the traction response. The reduction in load obtained using the modified response is still less than required to find agreement with the experimental results but it may be possible to find agreement between the two sets of results if fitting of the traction response were to be continued. The difference between the ultimate failure load values of the FE model and the experimental test, and the sensitivity of the model to the specifics of the traction response, possibly suggest that the traction response profiles used are not accurate representations of the true material response. This would further endorse the need for a new test to observe the mode II material behaviour at much higher magnification, such as the SEM instrumented test proposed in Chapter 7.

Very recent work [199,219,220] has identified a link between a characteristic distance ahead of the crack tip, the cohesive zone length, and the traction response profile used. Within this cohesive zone length, the number of interface elements to be used is advised

and is correlated to the maximum displacement of the traction response. All of the work in this area has been carried out using bi-linear traction responses and unidirectional composite materials which both differ from this work. However, Harper et al [199] state that for a standard 3 point ENF test model, for which the numerical cohesive zone length is given as 4.1 mm, the interface element length should be in the order of 1.5 mm. This provides at least two interface elements in the cohesive zone which gives an optimised solution. Any less than 2 interface elements and their solution begins to oscillate as the model fails to capture the point of propagation.

Further investigation would be needed to look at these effects with this I-section model as this is a possible cause for the over-estimation by the model of the failure load. Firstly, an assessment should be made of the cohesive zone length specific to this I-section structure manufactured from the woven composite material. Parameters not always included in current formulae for predicting cohesive zone length, such as specimen depth, longitudinal modulus and shear modulus are shown by Harper et al [199] to have a significant influence. These will have important implications in mesh design methods, which rely on an accurate prediction of cohesive zone length to minimise computational expense, whilst preserving the accuracy of numerical analyses. Most certainly, an interface element length of 1.5 mm in a structure as large as these I-sections would result in a hugely computationally expensive model, the length currently used is 5 mm.

8.7 Design optimisation

The model has been used to determine the quantity of z-pin reinforcement required to promote laminate fracture. If a hypothetical design brief is imposed here, requiring the joint to be designed for maximum load capability whilst avoiding laminate fracture, then the critical quantity of z-pins is the primary design parameter. Development of the design solution then becomes a case of making the best use of these pins.

The FE model analysis showed that there is a mode I loading component on the patch / I-section interface which is caused by bending deformation of the unbalanced and

unsymmetrical laminate lay-up. This occurs despite the tensile loading of the joint producing predominantly mode II, shear loading of the interface.

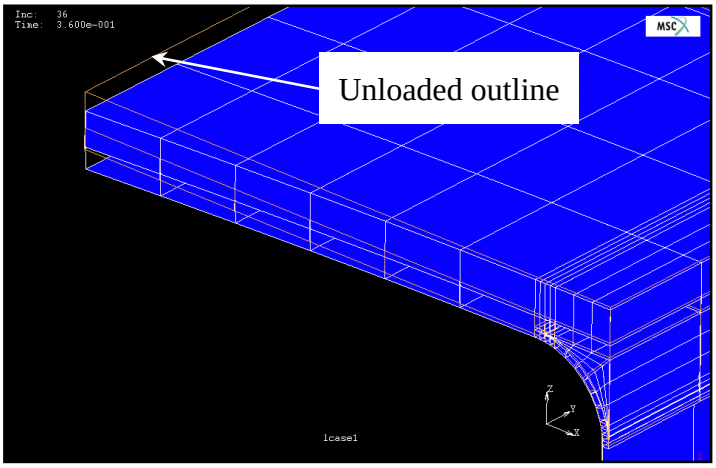

Figure 8.17 – I-section deformation under tensile loading

Concentrating z-pin reinforcement in the most highly loaded or highly strained regions is likely to provide the greatest load carrying capability. However, this needs to be tempered by the effect of the z-pins on the laminate properties. Too many z-pins in a particular area (or a very high areal density) will have a large knock-down effect on the laminate in-plane strengths. An iterative design process, where strength parameters are modified with each pin z-pin placement solution will eventually produce an optimal z-pinning arrangement which is tailored for the structure.

Chapter 9

Overall discussion

This chapter draws together all the points of discussion raised during this work. Suggestions for improving the z-pinning process in order to achieve greater control over the final z-pin orientation in the laminate are made. These will assist in the future testing of z-pins and the continued development of the z-pinning database.

Attention is given to refining the shear test methods used in this work, as the FE modelling work has shown particular sensitivity to the data obtained from these. Finally, improvements which can further enhance the modelling methodology adopted in this study are discussed.

9.1 Improving materials and manufacture

The issues regarding the raw rodstock material were introduced in Chapter 4. This is primarily a tendency to fracture during processing, suspected to be a result of insufficient wetting of the carbon fibres during the pultrusion process. The rodstock spools used contained lengths which would process well, followed by lengths which would break readily. At the time of writing, the only evidence to support the suspicion of poor wetting was provided by the images of fractured z-pins once inserted and the unique opportunity to manufacture the author's own z-pin preform and pin reinforced cores. It was not possible to state for definite whether the occurrence of split pins was due to raw rodstock issues or the ultrasonic insertion process. In the author's opinion there was most likely a contribution from both. Whilst a selection of z-pin preform produced by Albany Int. is subject to a quality checking process [221] subsequent UAZ processing can still cause pin splitting.

Recently, further investigation of the rodstock conducted by Treiber [222] has provided additional experimental and microscopy data which supports the author's claims that the wetting out of the rodstock is insufficient. Table 9-1 shows the results of 3 point bend tests on the rodstock from which the flexural stiffness was obtained. These tests were selected as the resin plays a significant part in the mechanical response and therefore any variance in the quantity of resin in the rodstock would be expected to be seen.

Sample set	Stiffness (GPa)	Standard deviation (%)
1	117.99	11
2	136.67	4
3	115.06	6
4	143.25	7

Table 9-1 – Flexural test data for carbon / epoxy rodstock (courtesy of Treiber [222])

Treiber has also supplemented this data set with microscopy images which show the poor wetting of the fibres with resin. Large resin-free and/or fibre-free pockets can be

seen in the rodstock cross-sections. With rodstock microstructures such as these it is a natural progression to observe pin splitting upon insertion, as was found during this work.

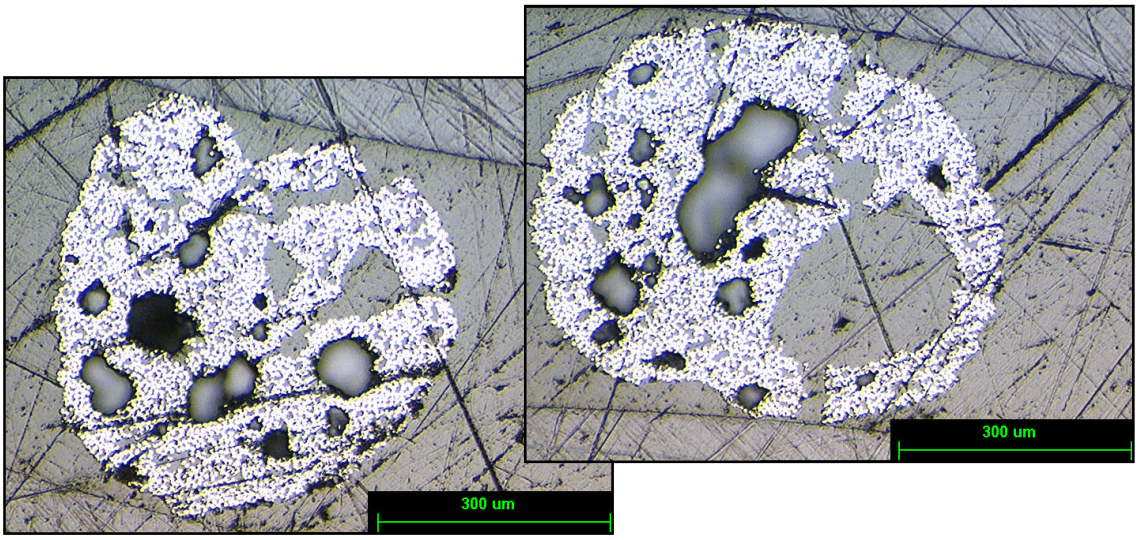

Figure 9.1 – Porosity in 0.51mm diameter z-pinning rodstock samples (courtesy of Treiber [222])

To conclude the rodstock discussion, it is interesting to not have seen this issue raised or discussed in published literature before. It is not the author's intention to speculate on the reasons why, however, the economic costs of using z-pinning technology and pre-preg composite material systems mean that z-pins are usually used with carbon fibre / epoxy composites. The z-pinning of glass fibre / epoxy laminates as part of this work was unusual and allowed the splitting of the pins to be observed. Careful cross-sectioning and polishing must be completed in order to see the z-pins in carbon fibre / epoxy laminates and therefore defects such as those shown here might not be immediately obvious.

The control over z-pin orientation during the various stages of the manufacturing process is limited. The orientation of the z-pins in the cured laminate does affect the mechanical response but is generally accepted as being a nuance of the z-pinning technology and is never corrected. In the author's opinion, the additional manufacturing complexity required to modify the current 45º chamfer design to a conical one as proposed in Chapter 4 is not cost effective. This would still not correct the large contributions to pin misalignment made by the shear cutting process and cure of the laminate, as has been shown in Chapter 2.

Misalignment is a particular problem, however, when attempting to obtain z-pin properties to feed numerical simulations. It is important to have close control over orientation angles to obtain data for the z-pin traction laws, particularly in the case of single pin testing. During this work, the author found that the use of rubber layers which prevented contact between the z-pins and rigid tooling during the cure process produced the best quality z-pin laminates. The following diagrams propose an improved z-pinned laminate manufacture process. One important effect of using the rubber layers was that the z-pins could be 'anchored' in the laminate.

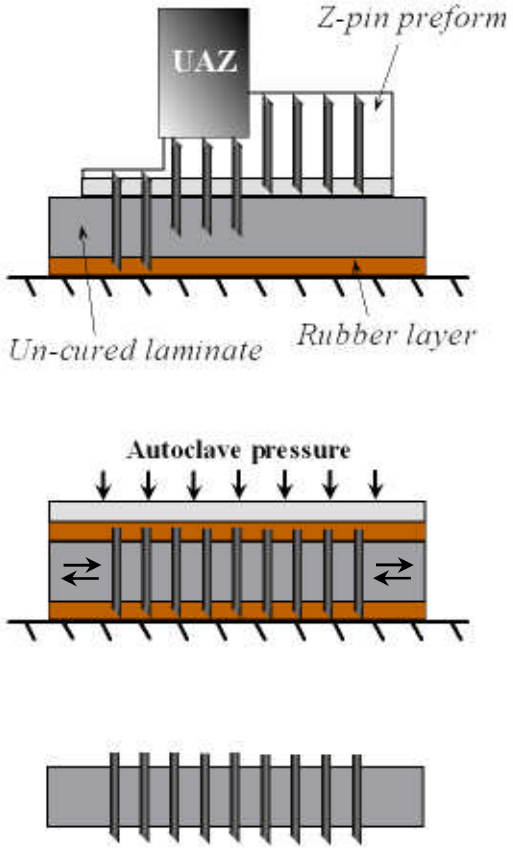

Z-pins are inserted through the full laminate thickness into the rubber layer. Any crushing of the pin tips occurs outside the uncured laminate stack.

A second rubber layer is positioned on top of the z-pinned laminate. Consolidation of the laminate during the early stages of the cure cycle is enough to allow the z-pins to penetrate the top layer of rubber. The z-pins are anchored, top and bottom, to reduce misalignment due to laminate shear.

The pin tips need to be removed for a flat surface finish but the z-pin orientation, position and insertion quality can be visually inspected

Figure 9.2 – New proposal for manufacture of full thickness z-pinned laminates with greater perpendicular z-pin alignment

This proposal has not been trialled as yet but the author believes that a greater control over z-pin orientation could be achieved using this method. It is also unknown whether such an approach would be suitable for large scale components; for small, flat laminates this approach is feasible.

A secondary benefit to this newly proposed manufacture methodology is that it has the potential to remove the variance due to pin end crushing. Crushing of the z-pin tips during insertion was discussed in Chapter 4 and affects mechanical performance; measurements vary on otherwise identical z-pinned laminates where the z-pinning has been carried out by different operators. Inserting through the full laminate thickness into a rubber layer can remove this variance.

9.2 Refinement of test methods

Chapter 5 introduced the test methods adopted during this work. Of particular relevance was the End Loaded Split (ELS) test for measurement of mode II fracture toughness. Over recent years the ESIS TC4 group in particular have been responsible for the development of a standard mode II test protocol, which at present does not exist. Progress on this is moving forward and a protocol for the mode II testing of adhesives has been submitted to the British Standards Institute (BSI) for publication as a full standard. The TC4 group plan to submit a protocol for composites in due course following the completion of a round-robin testing programme to obtain a larger supporting test database. However, these protocols are still for UD materials only; the mode II testing and analysis of woven materials remains unresolved.

The ELS test was selected to provide mode II fracture toughness which in turn was used to produce traction responses for interface elements in the FE model. Chapter 7 described the methodology used for this and raised the issues regarding the mismatch of scales between the experimental test and the initiation region of the generated traction responses.

Taking the 914 / 6K5H / T300 material system as an example, the sliding failure corresponding to the ‘assumed’ shear fracture strength of the resin interface was estimated to be several micrometers. This distance is well outside (up to 20 times) the distance at which the first crack propagation value is recorded from visual observation of the experimental test. The suitability of the ELS test to describe any interface behaviour in the initiation region therefore is questionable. What is required in order to

gather more accurate information is the development of a shear test, for either neat resin or a composite interface, which can be observed at much higher magnification. A test apparatus capable of being placed inside an SEM microscope would be an obvious first thought.

The development of the traction responses has also required knowledge of the shear strength of the resin system for the various materials used in this work. Such determination is usually unsuccessful for all but the most toughened resins. The problem arises from the fact that resin samples fracture readily and this fracture cannot be encouraged to occur in a single shear plane. Accurate shear strength values therefore cannot be obtained which forced the adoption of broadly spaced upper and lower bound estimates for this work. FE simulation of the ELS tests showed that the sensitivity of the load versus load line displacement results to the resin shear strength used is relatively low. The variation in the simulated results using various resin shear strengths is approximately equal to experimentally measured scatter.

The FE simulated ELS responses appear to be more sensitive to the intermediate and maximum sliding displacements of the bridging responses proposed. The maximum value was deduced from the ELS experimental tests, based on the assumption that when the rising mode II R-curves had reached a plateau, this represented the end of the bridging response. This was the only way to estimate the bridging limit, but this method cannot be considered as providing an accurate value. The intermediate sliding displacement values of the traction responses were positioned to provide the correct fracture energy. Once again, this cannot be considered to represent the true interfacial response accurately. This has been highlighted as the only part of this modelling effort that has been fitted and was necessary to complete this study. However, all other opportunities to fit the traction responses to match the FE simulated results to those measured experimentally have been rejected, the reason being that nothing is learned about the real interface behaviour of these materials. The sensitivity to the traction response displacements again shows the need for a more accurate, smaller scale, higher magnification study of the interfacial response.

An SEM compatible and instrumented shear test would be helpful in achieving better understanding of the mechanics of crack growth along a woven material interface. The ELS test was developed for UD materials on the basis that the crack is strictly bound between the upper and lower specimen arms and that the fracture area increases proportionally with crack growth. The ELS test is not necessarily valid for woven materials because these two assumptions cannot be guaranteed. For woven materials the crack negotiates a path past the nestled fibre bundles and must therefore travel perpendicular to the measured propagation direction in order to do so. The 5 harness fibre architecture of the 914 / 6K5H / T300 material system used in this work has produced similar agreement between the simulated and experimentally measured mode II response as was obtained for the comparative 977-2 UD material. This suggests that the crack growth in this woven material is similar to the UD case; the 5 harness architecture has sufficiently little fibre crimp to be suitable for the UD based ELS methodology. However, the 8552 / 3K8H / HTA material system, from which similar compatibility to the UD ELS test methodology could be expected due to the even lower fibre crimp of the 8 harness architecture, produces very poor agreement between the simulated and experimentally measured mode II responses. The load versus load line displacement comparison of the FE simulation and the experimental tests show that the simulation fails prematurely in all cases trialled. This is indicative of the traction response not being described correctly.

One of the earliest users of the Z-shear test jig was Troulis [2] who also investigated the mode II behaviour of z-pins. Troulis produced a full assessment of the various z-pin parameters (diameter, density, orientation and insertion depth) on the mode II response. The single pin load versus displacement plots that Troulis produced were obtained from multi-pin test specimens but are shown here against the single pin responses obtained in this study for comparison.

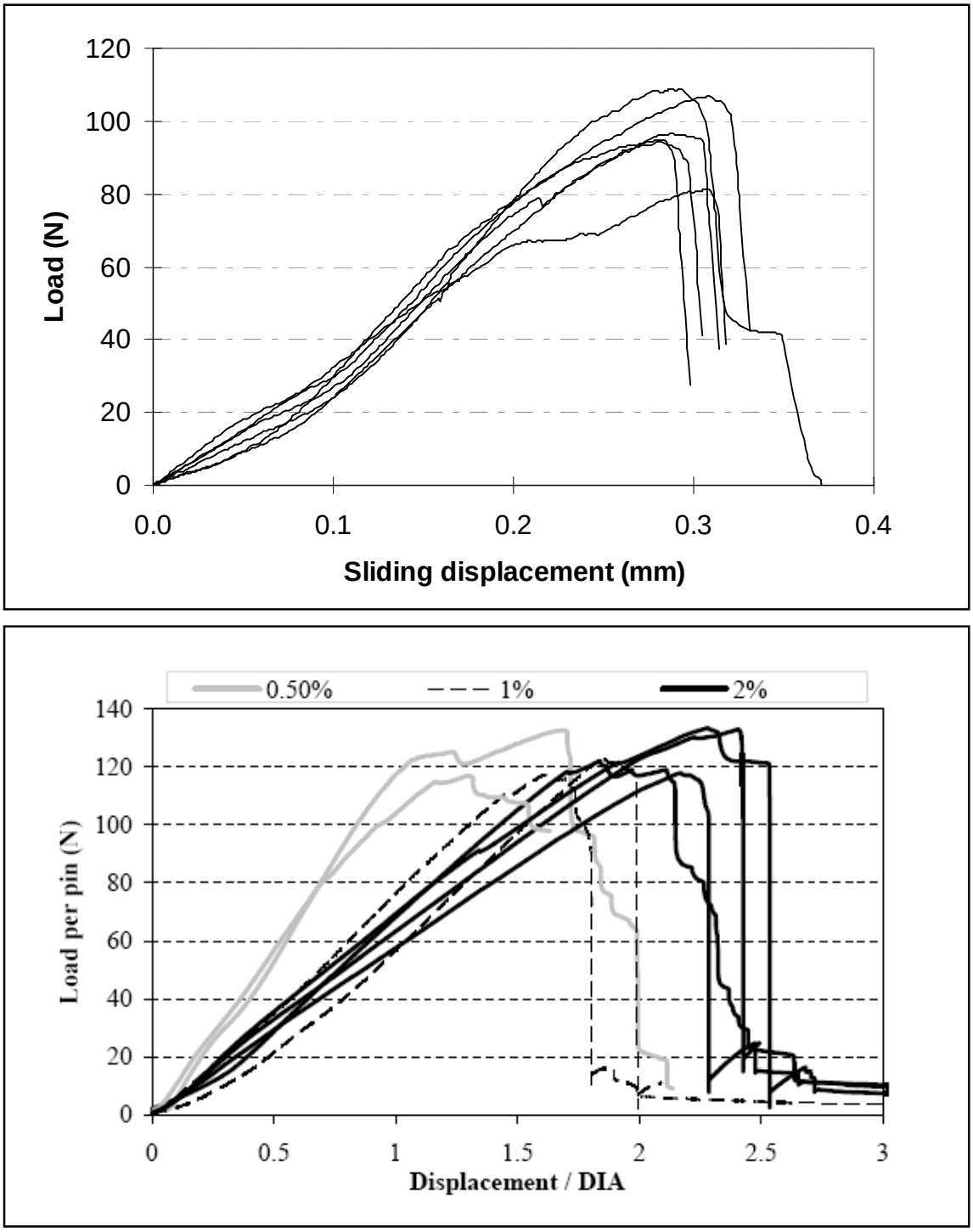

Figure 9.3 – 0.51 mm diameter z-pin shear load vs. sliding displacement with zero opening displacement (top) and load vs. normalised displacement for 0.51 mm diameter z-pins for a range of areal densities from [2] (bottom)

These two responses differ in that the tests produced for this work successfully constrained the opening displacement. Turning attention to similar data obtained for the 0.28 mm diameter z-pins, Troulis' measured the opening displacement for his tests to

reach a maximum of approximately 0.17 mm. When the shear faces are allowed to open there is clearly a large difference in pin fracture energy. This work calculated a mode II fracture energy of 2.8 mJ whereas Troulis' data give approximately 9.3 mJ for a fully inserted, 0.28 mm diameter z-pin. This is a 330 % difference. It is known that the energy absorbed by a z-pin in a pull-out mode, which is facilitated by crack opening, is greater than the energy absorbed in shear fracture but the difference between these two sets of tests is large for such a small amount of opening. The flexibility of the z-pins appears much increased if opening displacement is allowed, 4 times the pin diameter according to Troulis, against half the diameter measured here. That the z-pin can be this flexible does not agree with the authors' own experience with the normally brittle z-pin rodstock. The integrity of the z-pin must be completely lost in order for such flexibility to occur; a possibility if poor resin wetting facilitates the pin splintering into smaller fibre bundles.

The FE modelling work carried out here showed a higher than expected mode I opening component in areas of the z-pinned interface of the I-section joints. The z-pin responses used are still valid but the model should be extended to include the mode I z-pin response. Interface elements containing the mode I z-pin response could simply be overlaid on the two existing interfacial responses. This would produce a combined mixed mode z-pinning response closer to Troulis' mode II plots.

This work towards creating a design tool for z-pin use shows the need for a 'database of bridging laws' so that the full range of laminate materials can be assessed accurately. Existing analytical models would reduce the amount of experimental testing required to create such a database if a way of measuring some of the more obscure foundation properties could be found. The laminate foundation has a large effect on the z-pin responses in both mode I and mode II loading conditions. Another option could be available through the use of interface elements as used in this work. If the mixed mode output from combined mode I and mode II interface elements could be verified against mixed mode experimental test data then the overlaying of mode I and mode II z-pin responses to produce a mixed mode response has great advantages. The mode II testing is simplified to the fully constrained opening case achieved successfully in this work.

The pull-off test has already been used to successfully produce mode I bridging laws [1] and is currently being refined further.

For future z-pin mode II testing, the author would recommend a redesign of the mounting blocks for the Z-shear jig. The mounting blocks used for testing in this work required precision drilling of the 0.51 and 0.28 mm holes. This was particularly difficult and as a result incurred a high cost. Furthermore, it has been realised that fabricating a pre-drilled hole into which the z-pin is inserted is not ideal. What this method did manage to achieve was a low friction, perfectly flat shear plane which removed all opening displacement from the test. The perpendicular alignment of the z-pin was also ensured. However, due to the z-pin not being perfectly round, the fit of the pin in the hole was not perfect and bearing deformation of the hole was observed after the test.

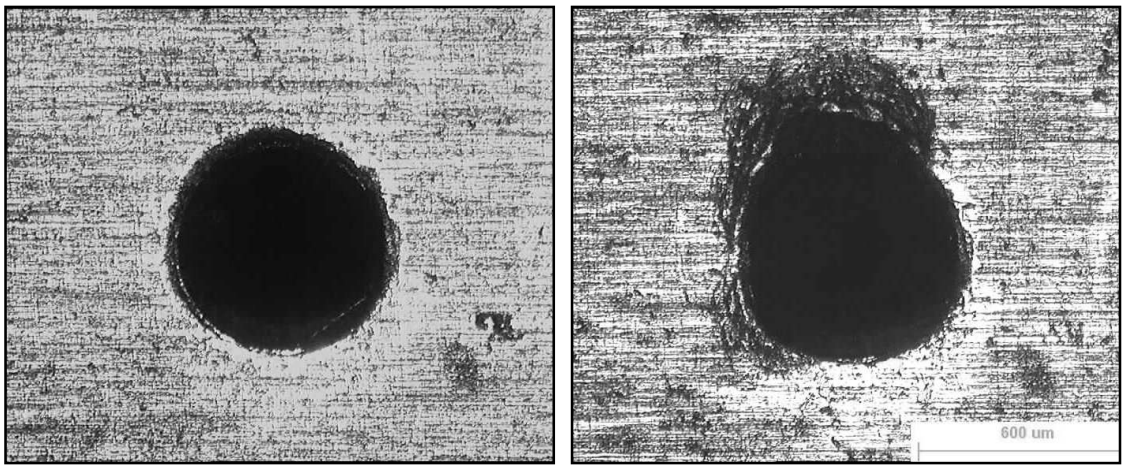

Figure 9.4 – Bearing deformation of 0.51 mm diameter holes in steel Z-shear mounting block (right) seen against the as new hole (left)

What is required for future testing of this kind is for the mounting blocks to be moulded around the z-pin, thus creating a perfect fit which is the true representation of the pin in the laminate. The z-pin should be aligned as desired and the mounting blocks created by pouring a casting compound into a shaped mould. The shear plane should be created by including a release film between the two moulded blocks. Additional laminate samples could be included close to the shear plane on either side to simulate the required foundation also. A schematic of this proposed solution is shown in Figure 9.5.

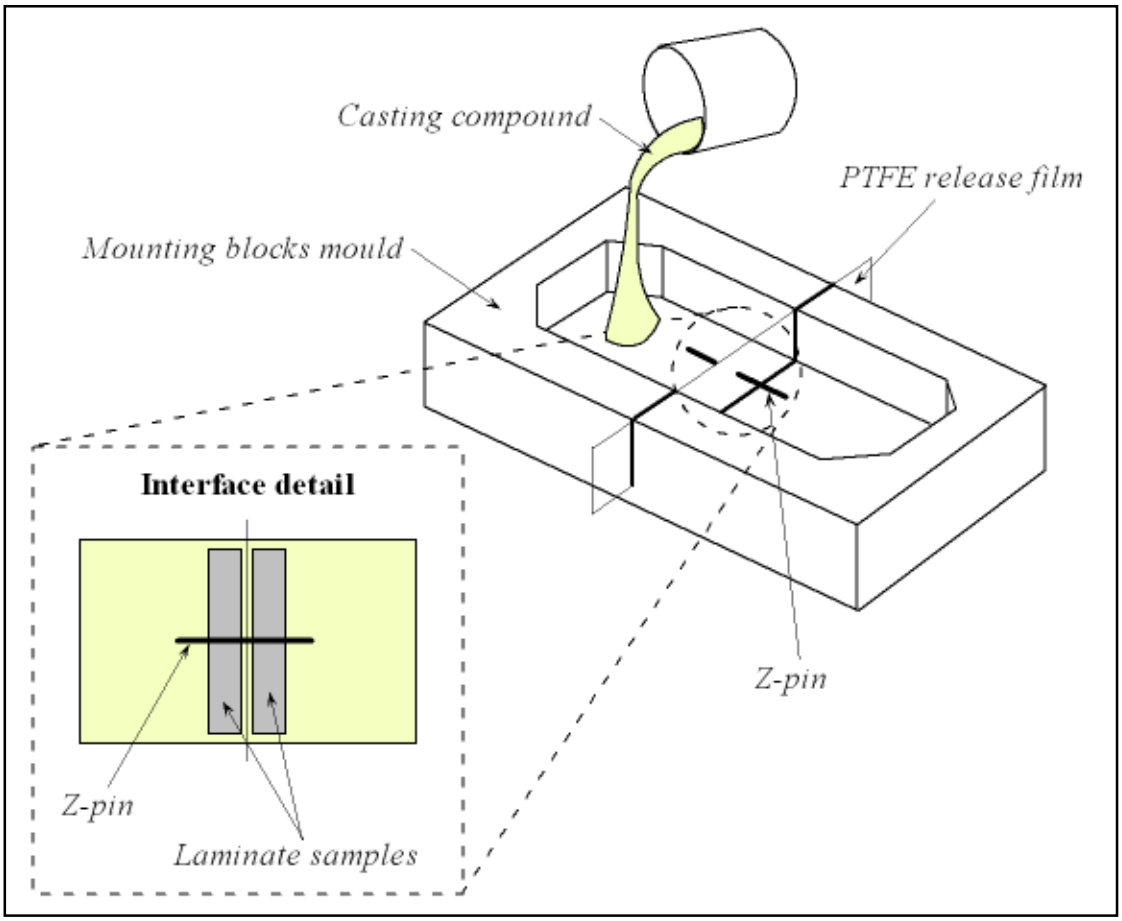

Figure 9.5 – New proposal for mounting z-pins in the Z-shear jig

9.3 Developing the modelling approach

This work has shown that the interface element based modelling approach can be used successfully for the analysis of composite structures. Closer agreement between the ultimate failure load values generated by the FE I-section model and the experimental tests will be obtained as the input data collection methodologies are refined. Comparison of these results highlights the limit to the capability of the current modelling approach and that is the influence of micromechanical z-pin effects on the laminate fracture. The plateau seen in the experimental tests for the z-pinned joints is caused by micro-scale damage effects which induce an earlier than expected failure. The current model is not built to analyse these micromechanical damage effects.

Possible causes for this early failure, which require additional investigation, might be the empty holes left in the laminate following pin-pull producing a ‘notched’ laminate scenario which is known to produce result in reduced in-plane strength. Another possibility is that the z-pins, in suppressing delamination propagation, cause the tensile failure in the weakest ply to induce premature failure of adjacent plies. Tensile fracture is usually catastrophic and therefore, interply delamination is actually beneficial in tension loaded laminates as the individual plies become uncoupled from each other and are hence less susceptible to damage caused by fracture of an adjacent ply. The location of failure in this case is likely to occur at the delamination boundary, such as at the edge of the z-pin reinforced patch.

The current model would benefit from the inclusion of a more advanced method of failure monitoring than the Hoffman criterion. The preferred option would be the Tsai-Wu failure criterion. In order for this to be implemented, a full set of tension, compression and shear test data, for the 914 / 6K5H / T300 material system, are required in order to fully describe failure.

The current modelling approach assumes that each z-pin is perfectly aligned in the through-thickness direction. As has been shown in Chapter 4 this is not representative of the real z-pinned laminate. The pin orientation will affect the z-pin response and therefore, to fully represent the distribution of orientations, test data must be obtained for each pin orientation angle in each material system used. If this could be completed, then z-pinning responses corresponding to the distribution of pin orientations measured by Chang et al [95] could be applied across the interface elements. Similarly, a distribution of pin damage could be incorporated to take account of the rodstock quality variations observed in this work.

The modelling approach developed in this work could be transferred to other through-thickness reinforcement technologies. This approach would be most applicable to modelling of the interfacial responses of tufting or stitching. For z-pin reinforced core constructions the modelling approach used here is not suitable for assessing the pin performance. The use of interface elements could be used to model the core to skin

adhesion but not the pins; for reinforced core structures the pin geometry needs to be represented. However, this interface element centred modelling approach is in keeping with Marasco's [152] unit cell representation of pin reinforced core structures. Marasco's unit cell approach intended to provide a user friendly tool for design in the same way as the interface elements used in this work. These basic through thickness reinforcement 'building blocks' can be assigned to larger structures in order to assess the effects of these reinforcement technologies on the global structural response.

The idea that pin reinforcement can be tailored for specific structures, as for z-pinning, is also directly transferable to pin reinforced core structures. During the manufacture of pin reinforced core panels in this work, the author has proposed some ideas where tailored pinned core design could provide attractive options. Firstly, modifying the pin arrangement around holes in core structures could allow clamping forces from bolts to be carried by vertically aligned pins to prevent core crushing. These highly stressed areas could be further designed to distribute the stress into the rest of the structure through a graded pin arrangement away from the hole. During a visit to Albany Int. in 2007 the author learned that vertically aligned pins around bolt holes had already been adopted. Albany Int. refer to this design feature as 'densification'.

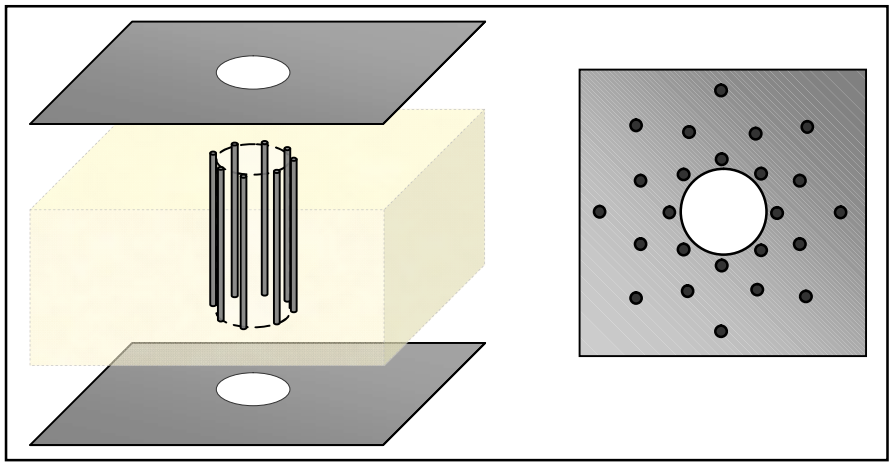

Figure 9.6 – Optimisation and stress management around bolt holes in sandwich structures by tailored pin reinforcement arrangement

For large sandwich constructions such as those used in the marine industry, the core area is made from multiple pieces. When this occurs, the join lines represent areas of weakness and high stress concentration. Use of a locally optimised arrangement of pin

reinforcement could be employed to bridge discontinuities such as these. High stress concentrations could be diffused into the global sandwich structure by grading the pin reinforcement density away from the discontinuity.

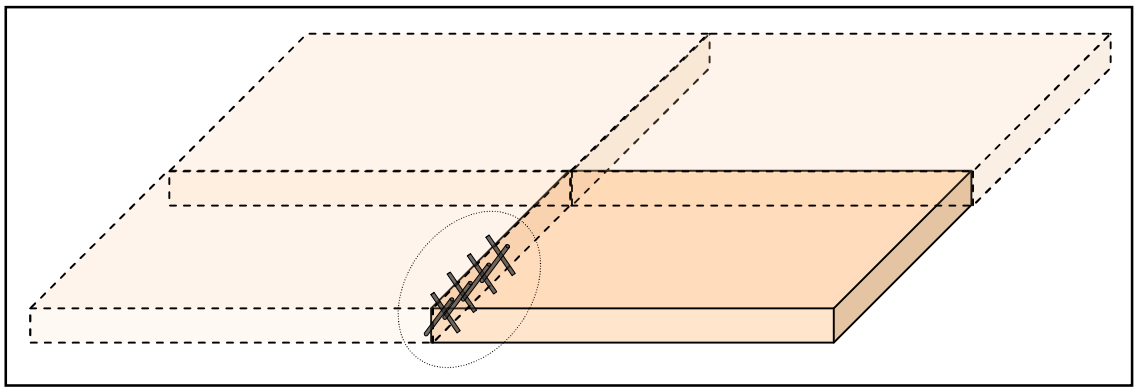

Figure 9.7 – Pin reinforcement to manage stress and transfer load across core discontinuities

In the author's opinion the most exciting opportunity for tailored core design is the production of panels with variable stiffness along the panel length. The pin arrangement in any given zone can be used to produce a desired stiffness and/or a desired ratio of compression to shear properties. This would allow the stiffness of the core structure to be tailored to loads applied at multiple locations. The deformed shape of the core structure under loading is be related to the pin arrangement and could be specifically designed. These possibilities may be beneficial to components subjected to aerodynamic loads; deformation could be encouraged to produce a more aerodynamically efficient profile.

In conclusion, this work has reported some important developments in the mode II testing of z-pins and has developed new analysis for the ELS test. The shear testing of aerospace grade, woven pre-preg composite laminates, and extensive comparison made to a UD control material, will assist in the future development of analysis methods specific to woven composites. Furthermore, the unique opportunity to produce z-pin products from the raw rodstock material has allowed an in depth understanding of the complexities associated with the manufacture of z-pinned structures to be obtained and reported. A modelling methodology has been developed and tested which is intended to promote the much needed consideration of the z-pinning technology during the design stage of composite structure development.

Chapter 10

Conclusions and suggestions for further work

10.1 Conclusions

1. Z-pin preforms and pin reinforced foam core constructions have been manufactured using a 6-axis robotic arm system. This capability has enabled the manufacture of non-standard z-pin arrangements in both cases.

2. The consolidation and full wetting out of the fibres in the rodstock has been identified as needing attention.

3. Splitting of z-pins has been observed following insertion into opaque glass / epoxy laminates. This loss of pin integrity affected 20 % of a small sample set manufactured in this case; the onset of splitting will be dependent on the resistance to insertion offered by the pre-preg as well as the z-pin quality.

4. Z-pinning can improve the ultimate load carrying capability of I-section patched joint structures. Additionally, z-pinning provides a damage tolerant I-section patch joint design.

5. The specific energy absorption of carbon / epoxy laminates is improved by the addition of z-pin reinforcement in the case of cylindrical crash tube structures. It is believed that z-pinning promotes a greater degree of laminate fragmentation which increases the energy absorbed.

6. The performance of the z-pinned I-section joints and crash tubes in this work would be enhanced by a tailored z-pinning arrangement specific to each structure.

7. Unexpected changes in the failure mode of z-pinned structures have been observed. The need for design tools to predict both the local and structural effects of z-pinning at the design stage has been highlighted.

8. For structures prone to delamination there is a critical quantity of z-pins which will retard this delamination and promote alternative failure at a new location and/or a new failure mode. Calculating this critical pin quantity and tailoring the z-pin arrangement will provide the optimal design solution.

9. A novel, beam theory based analysis for determining the sliding displacement relative to the original crack tip position has been developed. This analysis facilitates the generation of composite laminate interfacial traction responses to be obtained directly from the ELS test.

10. Pure, mode II shear responses with zero opening displacement have been obtained for single 0.51 mm diameter z-pins. The response for 0.28 mm diameter z-pins is deduced from additional mode II testing of multi-pin specimens.

11. A user friendly FE modelling approach, based on interface elements, to be used as a tool for designing with z-pins has been developed. This modelling approach has been used to assess a predominantly shear loaded z-pinned joint.

10.2 Suggestions for further work

As a priority, for improving the FE based design tool developed in this work, the SEM compatible and instrumented shear test discussed in Chapter 9 should be developed. The FE modelling work detailed in Chapter 8 showed the sensitivity of the simulated results to the traction response profiles which describe the behaviour of the interface elements in the model. These need to be more precisely measured to improve the overall accuracy of this modelling approach.

The Z-shear test jig has performed well in providing mode II z-pin data. The mounting of the z-pin in the test jig needs to be modified to be able to include a range of foundations which will provide a larger database to be used with the developed model.

Validation of whether a mixed mode z-pin response can be simulated by combining the pure mode I and II interface element responses is required. It is rare that any structure experiences a pure mode loading case so generally both modes of z-pin response will be required. If the overlaying of z-pin mode I and II responses can be confirmed, then the interface element methods used here will be ideally suited and this modelling approach can be extended to a much larger range of composite structural geometries and loading cases.

The design solutions that this modelling approach can assist in developing could be put into practice with greater ease by improving current facility used for manufacturing the z-pin preforms. The in-house manufacture of z-pin preform, and pin reinforced core constructions, has been limited by the software capabilities of the control system. A means by which the control program could be fed with the insertion co-ordinates from a Computer Aided Design (CAD) package would offer huge advantages over the current system. The manufacture of pinned foam cores in particular would be greatly assisted by the incorporation of an X-Y gantry system to reorient the core when necessary. The required movements of the robotic arm at present are such that only small areas of pin reinforced core can be manufactured. An X-Y gantry would reduce the movement requirements on the robotic arm and increase manufacture speed.

In the case of pin reinforced cores these two suggestions would greatly enhance the ability to insert into 3D shapes. Furthermore, it has been realised over the course of this work that the current system does not have the positional accuracy required for producing pin reinforced cores to the standards set by Albany Int. The tolerances related to the pin reveal length, in particular, are too tight for the current robot arm / insertion head system. More capable, precise machinery is required to correct this.

Appendices

Appendix A – Z-pin preform code

```
.PROGRAM z_pinning_robot()
      CALL sr_resetvariabl
      SIGNAL -49,-50,-51,-56
      OUTSPEED 0
      FLOWRATE OFF
      TOOL zpinhead
      WEIGHT 15
      ACCEL 100 ALWAYS
      DECEL 100 ALWAYS
      ONI -1034 CALL sr_safetyjkl,127
      PRINT /C,"****** Z-PINNING ROBOT MAIN PROGRAM ******"
      PRINT "---------- Created by J K Lander ----------"
      PRINT /C,"               MAIN MENU               "
001   PRINT /C,"Please choose an option from the following list..."
      PRINT /C,"1 - Manufacture a z-pin preform"
      PRINT "2 - Manufacture an X-Cor or K-Cor panel"
      PRINT "3 - Modified X/K-Cor panel (JKL)"
      PRINT "4 - Exit"
      PROMPT "Option: ",mainoption
      CASE mainoption OF
      VALUE 1:
      CALL sr_startpinloca
      CALL sr_preformarea
      CALL sr_pinpreform_v
      VALUE 2:
      CALL sr_xcorarea
      CALL sr_arraytable
      CALL sr_pinxcor
      VALUE 3:
      CALL sr_xcorarea
      CALL sr_arraytable
      CALL sr_jklcor
      VALUE 4:
      GOTO 002
      ANY :
      GOTO 001
002   END
.END


.PROGRAM sr_resetvariabl()
      mainoption = 0
      newposition = 0
      continue = 0
      setlengthinput = 0
      setlengthcode = 0
      xspacing = 0
      yspacing = 0
      xdistance = 0
      ydistance = 0
      nopinsx = 0
      nopinsy = 0
      arrayacceptable = 0
```

```
insertcount = 1
pinxcount = 1
fiftymmdiff = 0
stampcount = 0
pinycount = 1
returndistancex = 0
nopinsin50mm = 0
extrastamp = 0
pincount = 0
corethickness = 0
reveallength = 0
noofpasses = 0
xspacing1 = 0
yspacing1 = 0
xrotation1 = 0
yrotation1 = 0
nopinsx1 = 0
nopinsy1 = 0
thick = 0
x = 0
y = 0
a = 0
i = 0
b = 0
ii = 0
iii = 0
pinlength1 = 0
keeppinlength1 = 0
arrayacceptable = 0
xoffsetdist2 = 0
yoffsetdist2 = 0
xspacing2 = 0
yspacing2 = 0
xrotation2 = 0
yrotation2 = 0
nopinsx2 = 0
nopinsy2 = 0
x2 = 0
y2 = 0
a2 = 0
i2 = 0
b2 = 0
ii2 = 0
iii2 = 0
pinlength2 = 0
keeppinlength2 = 0
arrayacceptable = 0
insertcount1 = 0
insertcount2 = 0
fiftymmdiff1 = 0
fiftymmdiff2 = 0
pinycount1 = 1
pinycount2 = 1
returndistx1 = 0
returndistx2 = 0
nopinsin50mm1 = 0
nopinsin50mm2 = 0
extrastamp1 = 0
extrastamp2 = 0
```

```
      stampcount1 = 0
      stampcount2 = 0
      pincount1 = 0
      pincount2 = 0
      xoffsetdist3 = 0
      xoffsetdist4 = 0
      xoffsetdist5 = 0
      xoffsetdist6 = 0
      yoffsetdist3 = 0
      yoffsetdist4 = 0
      yoffsetdist5 = 0
      yoffsetdist6 = 0
      xspacing3 = 0
      xspacing4 = 0
      xspacing5 = 0
      xspacing6 = 0
      yspacing3 = 0
      yspacing4 = 0
      yspacing5 = 0
      yspacing6 = 0
      nopinsx3 = 0
      nopinsx4 = 0
      nopinsx5 = 0
      nopinsx6 = 0
      nopinsy3 = 0
      nopinsy4 = 0
      nopinsy5 = 0
      nopinsy6 = 0
      xrotation3 = 0
      xrotation4 = 0
      xrotation5 = 0
      xrotation6 = 0
      yrotation3 = 0
      yrotation4 = 0
      yrotation5 = 0
      yrotation6 = 0
      pinlength3 = 0
      pinlength4 = 0
      pinlength5 = 0
      pinlength6 = 0
.END


.PROGRAM sr_safetyjkl()
      PRINT /C,"--------------- SAFETY PROGRAM CALLED ! --------------
      -"
      HOLD.STEP ON
      PRINT ""
      PRINT /S,"A motion alarm has been triggered. Make sure all
      obstacles"
      PRINT " are cleared from the path of the robot"
      PRINT ""
      PRINT /S,"To resume program execution type CONTINUE.."
      PRINT " To completely end program execution type KILL"
.END


.PROGRAM sr_startpinloca()
      PRINT /C,"--------------- SET STARTING POSITION ---------------"
```

```
301   PRINT /C,"The last used starting position has been stored."
      PRINT "You can use this stored position or set a new one."
      PRINT ""
      PRINT /S,"Do you want to set a new starting position?"
      PROMPT " Press Yes (1) or No (2) and Enter: ",newposition
      CASE newposition OF
      VALUE 1:
      GOTO 302
      VALUE 2:
      GOTO 303
      ANY :
      GOTO 301
      END
302   PRINT ""
      PRINT /S,"Move the insertion head to the desired starting
      position,"
      PRINT " the base of the stamper should just touch the foam
      surface."
      PRINT /C,"Press the green CYCLE START button to continue..."
      PAUSE
      ALIGN
      BREAK
      HERE #startposition
      GOTO 304
303   PRINT ""
      PRINT /S,"Make sure that the orange MOTOR POWER button is on,"
      PRINT /S," the key is turned to REPEAT and the switch is set to
      RUN."
      PRINT " On the hand-held display turn TEACH LOCK off."
      PRINT /C,"Press the green CYCLE START button to continue..."
      PAUSE
      JMOVE #startposition
      BREAK
304   PRINT /C,"The robot will start pinning from the current TCP
      location."
      PRINT ""
      PRINT /S,"Do you wish to continue?"
      PROMPT " Press Yes (1) or No (2) and Enter: ",continue
      CASE continue OF
      VALUE 1:
      GOTO 305
      VALUE 2:
      GOTO 301
      ANY :
      GOTO 304
305   END
.END


.PROGRAM sr_preformarea()
      PRINT /C,"---------------- PREFORM DESIGN ----------------"
      PRINT ""
100   PRINT /S,"Enter the length of z-pin that you require against
      Code 0 in the"
      PRINT /S," wall mounted control box"
      PRINT ""
      PRINT "Press the Green CYCLE START button to continue..."
      PAUSE
      SIGNAL -52,-53,-54,-55
```

```
      SIGNAL 56
101   PRINT ""
      PRINT /S,"Enter the required x spacing (mm) between pins"
      PROMPT " (max. 7): ",xspacing
      IF xspacing>7 OR xspacing<0 THEN
      GOTO 101
      END
102   PRINT ""
      PRINT /S,"Enter the required y spacing (mm) between pins"
      PROMPT " (max. 10): ",yspacing
      IF yspacing>10 OR yspacing<0 THEN
      GOTO 102
      END
103   PRINT ""
      PRINT /S,"Enter the distance (mm) to be pinned along"
      PROMPT " the x-axis (max. 500): ",xdistance
      IF xdistance>500 OR xdistance<0 THEN
      GOTO 103
      END
104   PRINT ""
      PRINT /S,"Enter the distance (mm) to be pinned along"
      PROMPT " the y-axis (max. 500): ",ydistance
      IF ydistance>500 OR ydistance<0 THEN
      GOTO 104
      END
      nopinsx = INT(xdistance/xspacing)+1
      nopinsy = INT(ydistance/yspacing)+1
      PRINT /C,"Your preform will have the following z-pin array..."
      TYPE /C,"Length of z-pins: ",(setlengthinput)," mm"
      TYPE "Pin-to-pin spacing in the x-axis: ",(xspacing)," mm"
      TYPE "Pin-to-pin spacing in the y-axis: ",(yspacing)," mm"
      TYPE /S,"Z-pinned area: ",(xdistance)," mm"
      TYPE " by ",(ydistance)," mm"
      TYPE "Total no. of pins in the x direction: ",(nopinsx),""
      TYPE "Total no. of pins in the y direction: ",(nopinsy),""
105   PRINT ""
      PRINT /S,"Is this array acceptable?"
      PROMPT " Press Yes (1) or No (2) and Enter: ",arrayacceptable
      CASE arrayacceptable OF
      VALUE 1:
      GOTO 106
      VALUE 2:
      GOTO 100
      ANY :
      GOTO 105
106   END
.END


.PROGRAM sr_pinpreform_v()
      PRINT /C,"--------------- PREFORM MANUFACTURE ---------------"
      PROMPT "Enter the pin number in X that you wish to start from:
",nx
      PROMPT "Enter the pin number in Y that you wish to start from:
",ny
      PRINT /C,"Press the green CYCLE START button to begin
manufacture..."
      PAUSE
      PRINT /C,"--------------- CAUTION - Manufacture in progress ----
```

```
      -----------"
      POINT startpoint = #startposition
      xstart = (nx-1)*xspacing
      ystart = (ny-1)*yspacing
      POINT startpoint = SHIFT(startpoint BY xstart,ystart,0)
      LMOVE startpoint
      BREAK
      IF nx<>1 OR ny<>1 THEN
            PRINT /C,"Manufacture will re-start from this temporary
            start position..."
            PRINT /C,"If this is correct press the green CYCLE START
            button to continue..."
            PAUSE
      END
401   HERE #pinpoint
      POINT pinpoint = #pinpoint
      IF xdistance<=50 THEN
            FOR i = nx TO nopinsx
                  CALL sr_jkl_sig50
                  POINT pinpoint = SHIFT(pinpoint BY xspacing,0,0)
                  LMOVE pinpoint
                  BREAK
            END
            POINT pinpoint = SHIFT(startpoint BY 50,0,0)
            LMOVE pinpoint
            BREAK
            FOR i = nx TO nopinsx
                  CALL sr_jkl_sig51
                  POINT pinpoint = SHIFT(pinpoint BY xspacing,0,0)
                  LMOVE pinpoint
                  BREAK
            END
      ELSE
            nopinsin50mm = 1+INT(50/xspacing)
            extrastamp = nopinsx+6
            WHILE nx<nopinsin50mm DO
                  CALL sr_jkl_sig50
                  POINT pinpoint = SHIFT(pinpoint BY xspacing,0,0)
                  LMOVE pinpoint
                  BREAK
                  nx = nx+1
            END
            WHILE nx>=nopinsin50mm AND nx<=nopinsx DO
                  CALL sr_jkl_sig50
                  CALL sr_jkl_sig51
                  POINT pinpoint = SHIFT(pinpoint BY xspacing,0,0)
                  LMOVE pinpoint
                  BREAK
                  nx = nx+1
            END
            WHILE nx>nopinsx AND nx<=extrastamp DO
                  CALL sr_jkl_sig51
                  POINT pinpoint = SHIFT(pinpoint BY 10,0,0)
                  LMOVE pinpoint
                  BREAK
                  nx = nx+1
            END
      END
      nx = 1
```

```
      DRAW 0,0,20
      BREAK
      WHILE ny<nopinsy DO
            POINT startnewline = #startposition
            yshift = ny*yspacing
            POINT startnewline = SHIFT(startnewline BY 0,yshift,0)
            LMOVE startnewline
            BREAK
            TYPE /C,"Pinning line ",(ny+1)," of ",(nopinsy)
            ny = ny+1
            GOTO 401
      END
      PRINT /C,"------------ Preform manufacture complete ------------
"
.END


.PROGRAM sr_jkl_sig50()
0050  IF SIG(1050) THEN
      IF SIG(-1049) THEN
      PRINT /C,"Feeding rod-stock..."
      TWAIT 5
      END
      SIGNAL 50
      SWAIT -1049
      SIGNAL -50
      SWAIT 1049
      ELSE
      PRINT /C,"Rod-stock sensor has detected a fault and manufacture
is paused..."
      PRINT /C,"Once fixed press the green CYCLE START button to
resume manufacture"
      PAUSE
      GOTO 0050
      END
.END


.PROGRAM sr_jkl_sig51()
      SIGNAL 51
      TWAIT 0.5
      SIGNAL -51
      TWAIT 0.5
.END
```

Appendix B – Pin reinforced core code

```
.PROGRAM sr_xcorarea()
      PRINT /C,"---------- X/K-Cor DESIGN -----------"
      CALL sr_startpinloca
      PRINT ""
      PRINT "---------- X/K-Cor PANEL SIZING ----------"
600   PRINT ""
      PROMPT "Enter the thickness of the foam core (max. 13mm):
      ",corethickness
      IF corethickness>13 OR corethickness<0 THEN
      PRINT ""
      PRINT "Please re-enter - value outside acceptable limits"
      GOTO 600
      END
601   PRINT ""
      PROMPT "Enter the desired Z-pin reveal length (max. 3mm):
      ",reveallength
      IF reveallength>3 OR reveallength<0 THEN
      PRINT ""
      PRINT "Please re-enter - value outside acceptable limits"
      GOTO 601
      END
602   PRINT ""
      PRINT /S,"Enter the distance (mm) to be pinned along the"
      PROMPT " X-axis (max. 500): ",xdistance
      IF xdistance>500 OR xdistance<0 THEN
      PRINT ""
      PRINT "Please re-enter - value outside acceptable limits"
      GOTO 602
      END
603   PRINT ""
      PRINT /S,"Enter the distance (mm) to be pinned along the"
      PROMPT " Y-axis (max. 500): ",ydistance
      IF ydistance>500 OR ydistance<0 THEN
      PRINT ""
      PRINT "Please re-enter - value outside acceptable limits"
      GOTO 603
      END
      PRINT ""
      PRINT "---------- X/K-Cor PANEL DESIGN ----------"
      PRINT ""
604   PRINT /S,"Enter the number of passes you wish to make"
      PROMPT "(ie. the no. of different pin orientations in the
      panel): ",noofpasses
      CASE noofpasses OF
      VALUE 1:
      CALL sr_1pass
      VALUE 2:
      CALL sr_2passes
      ANY :
```

```
      PRINT ""
      PRINT "Please re-enter - value outside acceptable limits"
      GOTO 604
      END
.END


.PROGRAM sr_arraytable()
      PRINT /C,"--------------- X/K-Cor PARAMETERS ---------------"
      PRINT ""
            PRINT
      "*************************************************************
      ***"
      TYPE "* Core thickness (mm):    ",(corethickness)
      TYPE "* Reveal length (mm):     ",(reveallength)
      TYPE "* Total core height (mm): ",(thick)
      TYPE "* X distance (mm):        ",(xdistance)
      TYPE "* Y distance (mm):        ",(ydistance)
      PRINT "*-----------------------------------------------------------
      --------*"
      PRINT "* Pass No.:               1      2      3      4      5
      6   *"
      PRINT "*-----------------------------------------------------------
      --------*"
      PRINT /S,"* X origin offset (mm):  n/a"
      TYPE /S,"    ",(xoffsetdist2)
      TYPE /S,"     ",(xoffsetdist3)
      TYPE /S,"    ",(xoffsetdist4)
      TYPE /S,"    ",(xoffsetdist5)
      TYPE "    ",(xoffsetdist6)
      PRINT /S,"* Y origin offset (mm):  n/a"
      TYPE /S,"    ",(yoffsetdist2)
      TYPE /S,"     ",(yoffsetdist3)
      TYPE /S,"    ",(yoffsetdist4)
      TYPE /S,"    ",(yoffsetdist5)
      TYPE "    ",(yoffsetdist6)
      PRINT /S,"* X spacing (mm):"
      TYPE /S,"       ",(xspacing1)
      TYPE /S,"    ",(xspacing2)
      TYPE /S,"    ",(xspacing3)
      TYPE /S,"    ",(xspacing4)
      TYPE /S,"    ",(xspacing5)
      TYPE "    ",(xspacing6)
      PRINT /S,"* Y spacing (mm):"
      TYPE /S,"       ",(yspacing1)
      TYPE /S,"    ",(yspacing2)
      TYPE /S,"    ",(yspacing3)
      TYPE /S,"    ",(yspacing4)
      TYPE /S,"    ",(yspacing5)
      TYPE "    ",(yspacing6)
      PRINT /S,"* Rotation X (deg.)"
      TYPE /S,"     ",(xrotation1)
      TYPE /S,"    ",(xrotation2)
      TYPE /S,"    ",(xrotation3)
      TYPE /S,"    ",(xrotation4)
      TYPE /S,"    ",(xrotation5)
      TYPE "    ",(xrotation6)
      PRINT /S,"* Rotation Y (deg.)"
      TYPE /S,"     ",(yrotation1)
```

```
      TYPE /S,"    ",(yrotation2)
      TYPE /S,"    ",(yrotation3)
      TYPE /S,"    ",(yrotation4)
      TYPE /S,"    ",(yrotation5)
      TYPE "    ",(yrotation6)
      PRINT /S,"* X no. of pins:"
      TYPE /S,"        ",(nopinsx1)
      TYPE /S,"   ",(nopinsx2)
      TYPE /S,"   ",(nopinsx3)
      TYPE /S,"   ",(nopinsx4)
      TYPE /S,"   ",(nopinsx5)
      TYPE "   ",(nopinsx6)
      PRINT /S,"* Y no. of pins:"
      TYPE /S,"        ",(nopinsy1)
      TYPE /S,"    ",(nopinsy2)
      TYPE /S,"    ",(nopinsy3)
      TYPE /S,"    ",(nopinsy4)
      TYPE /S,"    ",(nopinsy5)
      TYPE "    ",(nopinsy6)
      PRINT "*-----------------------------------------------------
      --------*"
      PRINT /S,"* Z-pin length (mm):"
      TYPE /S,"    ",(pinlength1)
      TYPE /S,"    ",(pinlength2)
      TYPE /S,"    ",(pinlength3)
      TYPE /S,"    ",(pinlength4)
      TYPE /S,"    ",(pinlength5)
      TYPE "    ",(pinlength6)
      PRINT
      "*****************************************************************
      ***"
      PRINT ""
      PRINT /S,"Enter the Z-pin length values into the wall mounted"
      PRINT " Z-pinning head control box"
      PRINT ""
      PRINT "Each value should be assigned to the corresponding input
      code..."
      PRINT "eg. Pass 1 --> Code 1, Pass 2 --> Code 2 etc."
      PRINT /C,"Press the green CYCLE START button once completed..."
      PAUSE
.END


.PROGRAM sr_pinxcor()
      PRINT /C,"--------------- X/K-COR MANUFACTURE ---------------"
      PRINT /C,"Press the green CYCLE START button to begin
      manufacture..."
      PAUSE
      PRINT /C,"---------- CAUTION - Manufacture in progress ---------
      -"
1300  SIGNAL 52,-53,-54,-55
      SIGNAL 56
      TDRAW ,,,xrotation1,yrotation1
      IF xdistance<=50 THEN
1301  FOR insertcount1 = 1 TO nopinsx1
      SIGNAL 50
      TWAIT 2
      SIGNAL -50
      DRAW xspacing1
```

```
      BREAK
      END
      fiftymmdiff1 = 50-(xspacing1*(nopinsx1-1))-xspacing1
      DRAW fiftymmdiff1
      BREAK
      FOR stampcount1 = 1 TO nopinsx1
      SIGNAL 51
      TWAIT 0.5
      SIGNAL -51
      DRAW xspacing1
      BREAK
      END
      WHILE pinycount1<nopinsy1 DO
      returndistx1 = nopinsx1*xspacing1*2+fiftymmdiff1
      DRAW -returndistx1,yspacing1
      BREAK
      pinycount1 = pinycount1+1
      GOTO 1301
      END
      ELSE
1302  nopinsin50mm1 = INT(50/xspacing1)
      extrastamp1 = nopinsx1+nopinsin50mm1-1
      FOR pincount1 = 0 TO extrastamp1
      WHILE pincount1>=0 AND pincount1<nopinsin50mm1 DO
      SIGNAL 50
      TWAIT 2
      SIGNAL -50
      DRAW xspacing1
      BREAK
      pincount1 = pincount1+1
      END
      WHILE pincount1>=nopinsin50mm1 AND pincount1<nopinsx1 DO
      SIGNAL 49
      TWAIT 2
      SIGNAL -49
      DRAW xspacing1
      BREAK
      pincount1 = pincount1+1
      END
      WHILE pincount1>=nopinsx1 AND pincount1<=extrastamp1 DO
      SIGNAL 51
      TWAIT 0.5
      SIGNAL -51
      DRAW xspacing1
      BREAK
      pincount1 = pincount1+1
      END
      END
      WHILE pinycount1<nopinsy1 DO
      returndistx1 = (extrastamp1+1)*xspacing1
      DRAW -returndistx1,yspacing1
      BREAK
      pinycount1 = pinycount1+1
      GOTO 1302
      END
      END
1303  IF noofpasses>1 THEN
      ALIGN
      JMOVE #startposition
```

```
      TWAIT 4
      ALIGN
      SIGNAL -56
      SIGNAL -52,53,-54,-55
      SIGNAL 56
      TDRAW ,,,xrotation2,yrotation2
      DRAW xoffsetdist2,yoffsetdist2
      IF xdistance<=50 THEN
1304  FOR insertcount2 = 1 TO nopinsx2
      SIGNAL 50
      TWAIT 2
      SIGNAL -50
      DRAW xspacing2
      BREAK
      END
      fiftymmdiff2 = 50-(xspacing2*(nopinsx2-1))-xspacing2
      DRAW fiftymmdiff2
      BREAK
      FOR stampcount2 = 1 TO nopinsx2
      SIGNAL 51
      TWAIT 0.5
      SIGNAL -51
      DRAW xspacing2
      BREAK
      END
      WHILE pinycount2<nopinsy2 DO
      returndistx2 = nopinsx2*xspacing2*2+fiftymmdiff2
      DRAW -returndistx2,yspacing2
      BREAK
      pinycount2 = pinycount2+1
      GOTO 1304
      END
      ELSE
1305  nopinsin50mm2 = INT(50/xspacing2)
      extrastamp2 = nopinsx2+nopinsin50mm2-1
      FOR pincount2 = 0 TO extrastamp2
      WHILE pincount2>=0 AND pincount2<nopinsin50mm2 DO
      SIGNAL 50
      TWAIT 2
      SIGNAL -50
      DRAW xspacing2
      BREAK
      pincount2 = pincount2+1
      END
      WHILE pincount2>=nopinsin50mm2 AND pincount2<nopinsx2 DO
      SIGNAL 49
      TWAIT 2
      SIGNAL -49
      DRAW xspacing2
      BREAK
      pincount2 = pincount2+1
      END
      WHILE pincount2>=nopinsx2 AND pincount2<=extrastamp2 DO
      SIGNAL 51
      TWAIT 0.5
      SIGNAL -51
      DRAW xspacing2
      BREAK
      pincount2 = pincount2+1
```

```
      END
      END
      WHILE pinycount2<nopinsy2 DO
      returndistx2 = (extrastamp2+1)*xspacing2
      DRAW -returndistx2,yspacing2
      BREAK
      pinycount2 = pinycount2+1
      GOTO 1305
      END
      END
      END
      PRINT /C,"---------- X/K-Cor Manufacture Complete ----------"
.END


.PROGRAM sr_jklcor()
      PRINT /C,"---------- JKL MODIFIED X/K-Cor PANEL MANUFACTURE ----
      ------"
      PRINT /C,"Press the green CYCLE START button to begin
      manufacture..."
      PAUSE
      PRINT /C,"---------- CAUTION - Manufacture in progress ---------
      -"
1300  SIGNAL 52,-53,-54,-55
      SIGNAL 56
      TDRAW ,,,xrotation1,yrotation1
      1301    FOR insertcount1 = 0 TO nopinsx1
      1302        IF SIG(1050) THEN
      SIGNAL 50
      SWAIT -1049
      SIGNAL -50
      SWAIT 1049
      DRAW xspacing1
      BREAK
      IF SIG(-1049) THEN
      TWAIT 5
      END
      ELSE
      PRINT /C,"Rod-stock sensor has detected a fault and manufacture
      is paused..."
      PRINT /C,"Once fixed, press the green CYCLE START button to
      resume manufacture"
      PAUSE
      GOTO 1302
      END
      END
      WHILE pinycount1<nopinsy1 DO
      returndistx1 = (nopinsx1+1)*xspacing1
      DRAW ,,15
      DRAW -returndistx1,yspacing1
      DRAW ,,-15
      BREAK
      pinycount1 = pinycount1+1
      GOTO 1301
      END
      DRAW ,,150
.END
```

Appendix C – ELS test correction factors

Evaluation of the correction factors F and N for the end loaded split (ELS) geometry from [169].

Large displacement correction: $$F = 1 - \theta_1 \left(\frac{\delta}{L} \right)^2 - \theta_2 \left(\frac{\delta l_1}{L^2} \right)$$

End-block correction: $$N = 1 - \theta_3 \left(\frac{l_2}{L} \right)^3 - \theta_4 \left(\frac{\delta l_1}{L^2} \right) - \theta_5 \left(\frac{\delta}{L} \right)^2$$

$$\theta_1 = \frac{3}{20} \left[\frac{15 + 50 \left(\frac{a}{L} \right)^2 + 63 \left(\frac{a}{L} \right)^4}{\left[1 + 3 \left(\frac{a}{L} \right)^3 \right]^2} \right]$$

$$\theta_2 = \frac{-2 \left(\frac{L}{a} \right) \left(1 + 3 \left(\frac{a}{L} \right)^2 \right)}{1 + 3 \left(\frac{a}{L} \right)^3}$$

$$\theta_3 = \frac{4}{1 + 3 \left(\frac{a}{L} \right)^3}$$

$$\theta_4 = \frac{-9\left[\left(1-\left(\frac{a}{L}\right)\right)\left(1+3\left(\frac{a}{L}\right)^3\right)+4\left(\frac{a}{L}\right)^2\left(1-\left(\frac{l_2}{a}\right)^2\right)\left(1+3\left(\frac{a}{L}\right)^2\right)\right]}{4\left(1+3\left(\frac{a}{L}\right)^3\right)^2}$$

$$\theta_5 = \frac{36}{35}.\frac{1+\frac{3}{8}\left(\frac{a}{L}\right)^3\left(35+70\left(\frac{a}{L}\right)^2+63\left(\frac{a}{L}\right)^4\right)}{\left(1+3\left(\frac{a}{L}\right)^3\right)^3}$$

Appendix D – ELS laminate interface response FORTRAN subroutines

The example traction response subroutine shown here is for the 914 / 6K5H / T300 material, von Mises version. The inputs which alter for different materials and between different versions are highlighted.

```
      subroutine ucohesive(d,etot,e,s,send,ngens,relop,dt,dtdl,ncycle,
     $                     mdum,nn,kcus,matus,cohprop)
c
c     ** Start of generated type statements **
      real*8 beta, beta2, cohprop, d, dt, dtdl, e, eend, etot, g_c
      integer i, kcus, loading, matus, mdum, ncycle, ngens, nn
      real*8 relop, s, send, sigmac, tstar, vcurr, v_c, v_m
      real*8 energy_elastic, energy_current, sigma_aver, sigma1
      real*8 v_jkl, v_jklstar, plateau
c     ** End of generated type statements **
c
c... User subroutine to define the material behavior for interface
c... elements (MSC.Marc element types 186 to 193).
c...
c... Meaning of variables:
c...
c...  d         relation between stresses and relative displacements
c...            (stress-strain law)
c...  etot      accumulated total relative displacements at beginning
c...            of increment
c...  e         current incremental relative displacements
c...  s         accumulated stress at beginning of increment
c...  send      total stress at end of increment
c...  ngens     number of stress components
c...  relop(1)  equivalent relative opening displacement
c...  relop(2)  damage parameter
c...  dt        state variables
c...  dtdl      incremental state variables
c...  ncycle    current cycle number
c...  mdum(1)   user element number
c...  mdum(2)   internal element number
c...  nn        integration point number
c...  kcus(1)   layer number
c...  kcus(2)   internal layer number
c...  matus(1)  user material identifier
c...  matus(2)  internal material identifier
c...  cohprop   cohesive material properties defined via model
definition
c...            option cohesive
c
c... The variables d and send must be defined in this subroutine.
c... During the first assembly of an increment (ncycle equals zero),
```

```
c... the incremental relative displacements are estimated values and
c... it is recommended to keep the total stress at the end equal to.
c... the begin increment value
c
      dimension d(ngens,ngens),etot(*),e(*),s(*),send(*),
     $          dt(*),dtdl(*),kcus(*),matus(*),cohprop(*),
     $          relop(*)
c
      dimension eend(3)
c
c... set energy release rate (g_c), critical opening displacement c...
c... (v_c),
c... maximum opening displacement (v_m) and normal-shear weighting
c... factor (beta)
      g_c=4.113
      v_c=0.001104
      v_jkl=0.253820
      v_m=0.325
      plateau=5.50
      beta=1
c
      beta2=beta*beta
c
c... set total relative displacements; determine current equivalent
c... relative displacement
      if (ncycle==0) then
        do i=1,ngens
          eend(i)=etot(i)
        end do
      else
        do i=1,ngens
          eend(i)=etot(i)+e(i)
        end do
      end if
      if (eend(1)<0.0d0) then
        vcurr=beta2*eend(2)**2
      else
        vcurr=eend(1)**2+beta2*eend(2)**2
      end if
      if (ngens==3) vcurr=vcurr+beta2*eend(3)**2
      vcurr=sqrt(vcurr)
c
c... update maximum effective relative displacement; set loading flag
      if (vcurr>=relop(1)) then
        relop(1)=vcurr
        loading=1
      else
        if (relop(1)<=v_c) then
          loading=1
        else
          loading=0
        end if
      end if
c
c... assume linear model
      sigmac=2.0d0*g_c/v_m
      v_jklstar=((plateau*v_c)-(sigmac*v_jkl))/(plateau-sigmac)
      if (loading==1) then
        if (vcurr<=v_c) then
```

```
          d(1,1)=sigmac/v_c
        end if
        if ((vcurr>v_c).and.(vcurr<=v_jkl)) then
          d(1,1)=sigmac*(v_jklstar-vcurr)/(vcurr*(v_jklstar-v_c))
        end if
        if ((vcurr>v_jkl).and.(vcurr<=v_m)) then
          d(1,1)=sigmac*(v_jklstar-v_jkl)/(vcurr*(v_jklstar-v_c))
        end if
        if (vcurr>v_m) then
          d(1,1)=0
        end if
      else
        if (relop(1)<=v_c) then
          tstar=sigmac*relop(1)/v_c
        end if
        if ((relop(1)>v_c).and.(relop(1)<=v_jkl)) then
          tstar=sigmac*(v_jklstar-relop(1))/(v_jklstar-v_c)
        end if
        if ((relop(1)>v_jkl).and.(relop(1)<v_m)) then
          tstar=sigmac*(v_jklstar-v_jkl)/(v_jklstar-v_c)
        end if
        if (relop(1)>v_m) then
          tstar=0
        end if
        d(1,1)=tstar/relop(1)
      end if
      d(2,2)=beta2*d(1,1)
      if (ngens.eq.3) d(3,3)=beta2*d(1,1)
      if (eend(1)<0.0d0) d(1,1)=sigmac/v_c
c
      send(1)=d(1,1)*eend(1)
      send(2)=d(2,2)*eend(2)
      if (ngens.eq.3) send(3)=d(3,3)*eend(3)
c
c... fill damage parameter
      if (relop(1)>v_c) then
        energy_elastic=0.5d0*sigmac*v_c
        if (relop(1)>=v_m) then
          energy_current=g_c
        else
          sigma1=sigmac*(v_m-relop(1))/(v_m-v_c)
          sigma_aver=0.5d0*(sigma1+sigmac)
          energy_current=energy_elastic+
     $                   sigma_aver*(relop(1)-v_c)
        end if
        relop(2)=(energy_current-energy_elastic)/(g_c-energy_elastic)
      else
        relop(2)=0.0d0
      end if
c
      return
      end
```

Appendix E – FORTRAN subroutine code to generate ELS crack length

The example subroutine shown here is for the 914 / 6K5H / T300 material, von Mises version and includes the traction response code from Appendix D.

```
      subroutine
ucohesive(d,etot,e,s,send,ngens1,relop,dt,dtdl,ncycle1,
     $                     mdum,nn,kcus,matus1,cohprop)

c
c     ** Start of generated type statements **
      real*8 beta, beta2, cohprop, d, dt, dtdl, e, eend, etot, g_c
      integer i, kcus, loading, matus1, mdum, ncycle1, ngens1, nn
      real*8 relop, s, send, sigmac, tstar, vcurr, v_c, v_m
      real*8 energy_elastic, energy_current, sigma_aver, sigma1
      real*8 v_jkl, v_jklstar, plateau


c     ** End of generated type statements **
c
c... User subroutine to define the material behavior for interface
c... elements (MSC.Marc element types 186 to 193).
c...
c... Meaning of variables:
c...
c...  d         relation between stresses and relative displacements
c...            (stress-strain law)
c...  etot      accumulated total relative displacements at beginning
c...            of increment
c...  e         current incremental relative displacements
c...  s         accumulated stress at beginning of increment
c...  send      total stress at end of increment
c...  ngens     number of stress components
c...  relop(1)  equivalent relative opening displacement
c...  relop(2)  damage parameter
c...  dt        state variables
c...  dtdl      incremental state variables
c...  ncycle    current cycle number
c...  mdum(1)   user element number
c...  mdum(2)   internal element number
c...  nn        integration point number
c...  kcus(1)   layer number
c...  kcus(2)   internal layer number
c...  matus(1)  user material identifier
c...  matus(2)  internal material identifier
c...  cohprop   cohesive material properties defined via model
                definition
c...            option cohesive
c
```

```
c... The variables d and send must be defined in this subroutine.
c... During the first assembly of an increment (ncycle equals zero),
c... the incremental relative displacements are estimated values and
c... it is recommended to keep the total stress at the end equal to
c... the begin increment value.
c
      dimension d(ngens1,ngens1),etot(*),e(*),s(*),send(*),
     $          dt(*),dtdl(*),kcus(*),matus1(*),cohprop(*),
     $          relop(*)
c
      dimension eend(3)
c
c... set energy release rate (g_c), critical opening displacement
c... (v_c),
c... maximum opening displacement (v_m) and normal-shear weighting
c... factor (beta)
      g_c=4.113
      v_c=0.001104
      v_jkl=0.253820
      v_m=0.325
      plateau=5.50
      beta=1
c
      beta2=beta*beta
c
c... set total relative displacements; determine current equivalent
c... relative displacement
      if (ncycle1==0) then
        do i=1,ngens1
          eend(i)=etot(i)
        end do
      else
        do i=1,ngens1
          eend(i)=etot(i)+e(i)
        end do
      end if
      if (eend(1)<0.0d0) then
        vcurr=beta2*eend(2)**2
      else
        vcurr=eend(1)**2+beta2*eend(2)**2
      end if
      if (ngens1==3) vcurr=vcurr+beta2*eend(3)**2
      vcurr=sqrt(vcurr)
c
c... update maximum effective relative displacement; set loading flag
      if (vcurr>=relop(1)) then
        relop(1)=vcurr
        loading=1
      else
        if (relop(1)<=v_c) then
          loading=1
        else
          loading=0
        end if
      end if
c
c... assume linear model
      sigmac=2.0d0*g_c/v_m
      v_jklstar=((plateau*v_c)-(sigmac*v_jkl))/(plateau-sigmac)
```

```
      if (loading==1) then
        if (vcurr<=v_c) then
          d(1,1)=sigmac/v_c
        end if
        if ((vcurr>v_c).and.(vcurr<=v_jkl)) then
          d(1,1)=sigmac*(v_jklstar-vcurr)/(vcurr*(v_jklstar-v_c))
        end if
        if ((vcurr>v_jkl).and.(vcurr<=v_m)) then
          d(1,1)=sigmac*(v_jklstar-v_jkl)/(vcurr*(v_jklstar-v_c))
        end if
        if (vcurr>v_m) then
          d(1,1)=0
        end if
      else
        if (relop(1)<=v_c) then
          tstar=sigmac*relop(1)/v_c
        end if
        if ((relop(1)>v_c).and.(relop(1)<=v_jkl)) then
          tstar=sigmac*(v_jklstar-relop(1))/(v_jklstar-v_c)
        end if
        if ((relop(1)>v_jkl).and.(relop(1)<v_m)) then
          tstar=sigmac*(v_jklstar-v_jkl)/(v_jklstar-v_c)
        end if
        if (relop(1)>v_m) then
          tstar=0
        end if
        d(1,1)=tstar/relop(1)
      end if
      d(2,2)=beta2*d(1,1)
      if (ngens1.eq.3) d(3,3)=beta2*d(1,1)
      if (eend(1)<0.0d0) d(1,1)=sigmac/v_c
c
      send(1)=d(1,1)*eend(1)
      send(2)=d(2,2)*eend(2)
      if (ngens1.eq.3) send(3)=d(3,3)*eend(3)
c
c... fill damage parameter
      if (relop(1)>v_c) then
        energy_elastic=0.5d0*sigmac*v_c
        if (relop(1)>=v_m) then
          energy_current=g_c
        else
          sigma1=sigmac*(v_m-relop(1))/(v_m-v_c)
          sigma_aver=0.5d0*(sigma1+sigmac)
          energy_current=energy_elastic+
     $                   sigma_aver*(relop(1)-v_c)
        end if
        relop(2)=(energy_current-energy_elastic)/(g_c-energy_elastic)
      else
        relop(2)=0.0d0
      end if


      return
      end
```

```
            SUBROUTINE
PLOTV(V,S,SP,ETOT,EPLAS,ECREEP,T,M,NN,KCUS,NDI1,
     +                 NSHEAR1,JPLTCD)
            IMPLICIT REAL *8 (A-H, O-Z)
            include '../common/concom'
            include '../common/elmcom'
            include '../common/dimen'
            include '../common/array2'
            include '../common/space'
            include '../common/strvar'
            include '../common/blnk'
            include  '../common/creeps'
            include  '../common/spacevec'

      common//v1
      dimension v1(3000,100)
c... 3000 corresponds to the maximum no. of elements in the model
c... 100 corresponds to the maximum no. of increments to analyse the
     model

      common//crack_length
      dimension crack_length(100)
c... 100 corresponds to the maximum no. of increments to analyse
     the model

      common//writtenfile


            DIMENSION S(1),SP(1),ETOT(1),
     +           EPLAS(1),ECREEP(1),M(2),KCUS(2)
      dimension CNOD(12),DNOD(12)

                  crack_threshold=0.253820
            elem_length=1.0


            JRDPRE = 0
            CALL VECFTC (CNOD, XORD_D, NCRDMX, NCRD, LM(1),JRDPRE, 2,
            1)
            xnode1=CNOD(1)
            ynode1=CNOD(2)
            JRDPRE = 0
            CALL VECFTC (DNOD, DSXTS_D, NDEGMX, NDEG, LM(1),JRDPRE, 2,
            5)
            dxnode1=DNOD(1)
            dynode1=DNOD(2)
            JRDPRE = 0
            CALL VECFTC (CNOD, XORD_D, NCRDMX, NCRD, LM(2),JRDPRE, 2,
            1)
            xnode2=CNOD(1)
            ynode2=CNOD(2)
            JRDPRE = 0
            CALL VECFTC (DNOD, DSXTS_D, NDEGMX, NDEG, LM(2),JRDPRE, 2,
            5)
            dxnode2=DNOD(1)
            dynode2=DNOD(2)
            JRDPRE = 0
            CALL VECFTC (CNOD, XORD_D, NCRDMX, NCRD, LM(3),JRDPRE, 2,
            1)
```

```
      xnode3=CNOD(1)
      ynode3=CNOD(2)
      JRDPRE = 0
      CALL VECFTC (DNOD, DSXTS_D, NDEGMX, NDEG, LM(3),JRDPRE, 2,
      5)
      dxnode3=DNOD(1)
      dynode3=DNOD(2)
      JRDPRE = 0
      CALL VECFTC (CNOD, XORD_D, NCRDMX, NCRD, LM(4),JRDPRE, 2,
      1)
      xnode4=CNOD(1)
      ynode4=CNOD(2)
      JRDPRE = 0
      CALL VECFTC (DNOD, DSXTS_D, NDEGMX, NDEG, LM(4),JRDPRE, 2,
      5)
      dxnode4=DNOD(1)
      dynode4=DNOD(2)


      X1=xnode1+dxnode1
      Y1=ynode1+dynode1

      X2=xnode2+dxnode2
      Y2=ynode2+dynode2

      X3=xnode3+dxnode3
      Y3=ynode3+dynode3

      X4=xnode4+dxnode4
      Y4=ynode4+dynode4

      Theta=ATAN((Y2-Y1)/(X2-X1))

      Cs=COS(Theta)
      Sn=SIN(Theta)


      X1new=0
      Y1new=0

      X2new=(X2-X1)*Cs+(Y2-Y1)*Sn
      Y2new=-(X2-X1)*Sn+(Y2-Y1)*Cs

      X3new=(X3-X1)*Cs+(Y3-Y1)*Sn
      Y3new=-(X3-X1)*Sn+(Y3-Y1)*Cs

      X4new=(X4-X1)*Cs+(Y4-Y1)*Sn
      Y4new=-(X4-X1)*Sn+(Y4-Y1)*Cs
      dif=(xnode3-xnode2)**2+(xnode1-xnode4)**2+
     +          (ynode3-ynode2)**2+(ynode1-ynode4)**2
      if (mats==2) then
            V=ABS(X3new-X2new+X4new-X1new)/2
            v1(LM(1),INC)=ABS(X4new-X1new)
            v1(LM(2),INC)=ABS(X3new-X2new)
            v1(LM(3),INC)=ABS(X3new-X2new)
            v1(LM(4),INC)=ABS(X4new-X1new)
            if (lovl==7) then
                  if (V>=crack_threshold) then
                  crack_length(INC)=crack_length(INC)+
```

```
                  elem_length/2
                  end if
            end if
      else
            V=0
            v1(LM(1),INC)=0
            v1(LM(2),INC)=0
            v1(LM(3),INC)=0
            v1(LM(4),INC)=0
      end if

      if (lovl==7) then
            if (CPTIM+TIMINC>0.9999.AND.writtenfile<999) then
                  OPEN (11,FILE='d:\crack.txt',STATUS='REPLACE')
                  DO I=1,INC
                        Write (11,*) I,crack_length(I)
                  END DO
                  writtenfile=1000
            end if
      end if

      RETURN
 END


 SUBROUTINE UPSTNO(NQCODE,NODEID,VALNO,NQNCOMP,NQTYPE,
+      NQAVER,NQCOMPTYPE,NQDATATYPE,NQCOMPNAME)
      IMPLICIT REAL*8 (A-H,O-Z)
      DIMENSION VALNO(*)
      CHARACTER*24 NQCOMPNAME(*)
      include '../common/concom'
      include '../common/elmcom'
      include '../common/dimen'
      include '../common/array2'
      include '../common/space'
      include '../common/strvar'
      include '../common/blnk'
      include  '../common/creeps'
      include  '../common/spacevec'
      common//v1
      dimension v1(3000,100)
      if (nqcode==-1) then
            NQTYPE=0
            NQNCOMP =1
            VALNO(1) = V1(NODINT(NODEID),INC)
      end if
      RETURN
      END
```

References

1. Cartié, D. D. R. (2000), *Effect of Z-Fibres™ on the Delamination Behaviour of Carbon Fibre / Epoxy Laminates* (PhD thesis), Cranfield University, Cranfield, UK.

2. Troulis, E. (2003), *Effect of Z-Fiber® Pinning on the Mechanical Properties of Carbon Fibre/Epoxy Composites* (PhD thesis), Cranfield University, Cranfield, UK.

3. Bitsianis, N. (1999), *The Influence of Z-Pinning on Fracture Toughness & Compression After Impact Strength of Carbon Fibre Reinforced Polymers* (MSc thesis), Cranfield University, Cranfield, UK.

4. Alessandrini, A. (2003), *Delamination Behaviour of Z-Pinned Laminates Under Shear Loading* (MSc thesis), Cranfield University, Cranfield, UK.

5. Bonnet, C. (2005), *Effect of Through-the-Thickness Reinforcement on the Resistance of Delamination of Composite Structures Under Fatigue Loading Conditions* (MSc thesis), Cranfield University, Cranfield, UK.

6. Vilette, M. (2004), *Optimisation of "Z-Shear" Test* (MSc thesis), Cranfield University, Cranfield, UK.

7. Negre, P. (2000), *Compression-After-Impact Performance of Z-Pinned Carbon Fiber/Epoxy Laminates* (MSc thesis), Cranfield University, Cranfield, UK.

8. Graftieaux, B. P. H. (1999), *Investigation of Delamination of Z-Pinned Composite Laminates Under Mode I and Mode II Cyclic Loading* (MSc thesis), Cranfield.

9. Vaillant, C. (1997), *Manufacturing Z-Fiber Pinned Composite Structures* (MSc thesis), Cranfield University, Cranfield, UK.

10. Langer, J. D. (2000), *Impact, Compression After Impact and Strain Development in Z-Pinned Samples of IM7/8552 Composite* (MSc thesis), Cranfield University, Cranfield, UK.

11. Hounslow, L. E. (2000), *The Influence of Z-Pinning on Low Velocity Impact Performance of Laminated Carbon Composites* (MSc thesis), Cranfield University, Cranfield, UK.

12. McKensie, M. *Unpublished Work* (MSc thesis), Cranfield University, Cranfield, UK.

13. Kinloch, A. J. and Young, R. J. (1983), *Fracture Behaviour of Polymers*, Applied Science Publishers, London, UK.

14. Utracki, L. A. (2002), *Polymer Blends Handbook*, Kluwer Academic Publishers, Dordrecht.

15. Pearson, R. A. and Yee. A. F. (1985), 'The Effect of Cross-Link Density on the Toughening Mechanism of Elastomer-Modified Epoxies', in *Tough Composite Materials* , Noyes Publications, Park Ridge, pp. 157-177.

16. Akay, M. and Cracknell, J. G. (1985), 'Epoxy Resin-Polyethersulphone Blends', *Applied Polymer Science*, Vol. 52, No. 5, pp. 663-688.

17. Bucknall, C. B. and Gilbert, A. H. (1989), 'Toughening Tetrafunctional Epoxy Resins Using Polyetherimide', *Polymer*, Vol. 30, No. 2, pp. 213-217.

18. Bucknall, C. B. and Partridge, I. K. (1983), 'Phase Separation in Epoxy Resins Containing Polyethersulphone', *Polymer*, Vol. 24, No. 5, pp. 639-644.

19. Bucknall, C. B. and Partridge, I. K. (1986), 'Phase Separation in Cross-Linked Resins Containing Polymeric Modifiers', *Polymer Engineering & Science*, Vol. 26, No. 1, pp. 54-62.

20. Pascault, J. P. and Williams, R. J. J. (2000), 'Formulation and Characterization of Thermoset-Thermoplastic Blends', in *Polymer Blends* , Vol. 1, Wiley-Interscience, New York, USA, pp. 379-416.

21. Altstädt, D., Gerth, D., Stängle, M., and Recker, H. G. (1993), 'Interlaminar Crack Growth in Third-Generation Thermoset Prepreg Systems', *Polymer*, Vol. 34, No. 4, pp. 907-909.

22. Partridge, I. K. and Cartié, D. D. R. (2003), 'Suppression of Initiation of Delamination Cracking in Unidirectional Composites by Self-Same Resin Interleaving', in European Structural & Integrity Society (ESIS) *Application of Fracture Mechanics to Polymers, Adhesives and Composites*, Vol. 33.

23. Aksoy, A. and Carlsson, L. A. (1992), 'Interlaminar Shear Fracture of Interleaved Graphite/Epoxy Composites', *Composites Science & Technology*, Vol. 43, No. 1, pp. 55-69.

24. Ozdil, F. and Carlsson, L. A. (1992), 'Mode I Interlaminar Fracture of Interleaved Graphite/Epoxy', *Composite Materials*, Vol. 26, No. 3, pp. 432-459.

25. Kaw, A. K. and Goree, J. G. (1990), 'Effect of Interleaves on Fracture of Laminated Composites: Part 1 - Analysis', *Applied Mechanics*, Vol. 57, No. 1, pp. 168-174.

26. Kaw, A. K. and Goree, J. G. (1990), 'Effect of Interleaves on Fracture of Laminated Composites: Part 2 - Solution and Results', *Applied Mechanics*, Vol. 57, No. 1, pp. 175-181.

27. Ishai, O., Rosenthal, H., Sela, N., and Drukker, E. (1988), 'Effect of Selective Adhesive Interleaving on Interlaminar Toughness of Graphite/Epoxy Composite Laminates', *Composites*, Vol. 19, No. 1, pp. 49-54.

28. Sela, N., Ishai, O., and Banks-Sills, L. (1989), 'The Effect of Adhesive Thickness on Interlaminar Fracture Toughness of Interleaved CFRP Specimens', *Composites*, Vol. 20, No. 3, pp. 257-264.

29. Singh, S. and Partridge, I. K. (1995), 'Mixed-Mode Fracture in an Interleaved Carbon-Fibre/Epoxy Composite', *Composites Science & Technology*, Vol. 55, No. 4, pp. 319-327.

30. Hillermeier, R. W. and Seferis, J. C. (2001), 'Interlayer Toughening of Resin Transfer Moulding Composites', *Composites Part A: Applied Science & Manufacturing*, Vol. 32, No. 5, pp. 721-729.

31. Lo Faro, C., Aldridge, M., and Maskell, R. (2003), 'Epoxy Soluble Thermoplastic Fibres: Enabling the Technology for Manufacture of High Toughness Aerospace Primary Structures Via Liquid Resin Infusion Process', in Drechsler, K. (Editor), *"Advanced Composites: The Balance Between Performance and Cost" Proceedings of the 24th International SAMPE Europe Conference* at Paris, France; pp. 321-332.

32. Lo Faro, C., Aldridge, M., and Maskell, R. (2004), 'New Developments in Resin Infusion Materials Using Priform® Technology: Stitching', in *"Material & Process Technology - the Driver for Tomorrow's Improved Performance" 25th Jubilee International SAMPE Europe Conference* at Paris, France; pp. 378-385.

33. Lo Faro, C., Doyle, M., Blackburn, R., and Maskell, R. (2005), 'Low Cost Manufacturing Using Novel Preforming and Resin Infusion Technologies', in *"Nanotechnology Assists Leadership and Success of the Composite Technology" Proceedings of the 26th International SAMPE Europe Conference* at Paris, France; pp. 143-149.

34. Cytec Engineered Materials *Priform*®, available at: www.cytec.com/business/engineered materials/Priform.shtm (accessed 2008).

35. Dawson, D. K. (2006), 'Composite Spoilers Brake Airbus for Landing', *High-Performance Composites*, Vol. 14, No. 4, pp. 52-55.

36. Mouritz, A. P., Bannister, M. K., Falzon, P. J. , and Leong, K. H. (1999), 'Review of Applications for Advanced Three-Dimensional Fibre Textile Composites', *Composites Part A: Applied Science & Manufacturing*, Vol. 31, No. 12, pp. 1445-1461.

37. Tong, L., Mouritz, A. P., and Bannister, M. K. (2002), *3D Fibre Reinforced Polymer Composites*, Elsevier, Amsterdam, Holland.

38. Bogdanovic, A. and Mungalov, D. (2002), 'Recent Advancements in Manufacturing 3-D Braided Preforms and Composites', in Bandyopadhyay, S. (Editor), *Composite Systems - Macrocomposites, Microcomposites, Nanocomposites ACUN - 4 International Composites Conference*, Sydney, Australia, pp. 61-72.

39. Greenhalgh, E. and Hiley, M. J. (2003), 'The Assessment of Novel Materials and Processes for the Impact Tolerant Design of Stiffened Composite Aerospace Structures', *Composites Part A: Applied Science & Manufacturing*, Vol. 34, No. 2, pp. 151-161.

40. Chou, S., Chen, C., and Wu, C. C. (1992), 'BMI Resin Composites Reinforced With 3D Carbon-Fibre Fabrics', *Composites Science & Technology*, Vol. 43, No. 2, pp. 117-128.

41. Guénon, V. A., Chou, T. W., and Gillespie Jr., J. W. (1989), 'Toughness Properties of a Three-Dimensional Carbon-Epoxy Composite', *Materials Science*, Vol. 24, No. 11, pp. 4168-4175.

42. Callus, P. J., Mouritz, A. P., Bannister, M. K., and Leong, K. H. (1999), 'Tensile Properties and Failure Mechanisms of 3D Woven GRP Composites', *Composites Part A: Applied Science & Manufacturing*, Vol. 30, No. 11, pp. 1277-1287.

43. Kamiya, R., Cheeseman, B. A., Popper, P., and Chou, T. W. (2000), 'Some Recent Advantages in the Fabrication and Design of Three-Dimensional Textile Preforms: a Review', *Composites Science & Technology*, Vol. 60, No. 1, pp. 33-47.

44. Bannister, M. K., Herszberg, I., Nicolaidis, A., Coman, F., and Leong, K. H. (1998), 'The Manufacture of Glass/Epoxy Composites With Multilayer Woven Architectures', *Composites Part A: Applied Science & Manufacturing*, Vol. 39, No. 3, pp. 293-300.

45. Ruan, X. and Chou, T. W. (1996), 'Experimental and Theoretical Studies of the Elastic Behaviour of Knitted-Fabric Composites', *Composites Science & Technology*, Vol. 56, No. 12, pp. 1391-1403.

46. Williams, D. (1987), 'New Knitting Methods Offer Continuous Structures', *Engineering*, Vol. 227, No. 6, pp. 12-13.

47. McCarthy, R. J. (1991), 'Braiding of Hybrid Composite Propeller Blades', *Composite Polymers*, Vol. 4, No. 2, pp. 112-126.

48. McCarthy, R. J., Haines, G. H., and Newley, R. A. (1994), 'Polymer Composite Applications to Aerospace Equipment', *Composites Manufacturing*, Vol. 5, No. 2, pp. 83-93.

49. Abe, T., Hayashi, K., Sato, T., Yamane, S., and Hirokawa, T. (2003), 'A-VARTM Process and Z-Anchor® Technology for Primary Aircraft Structures', in Drechsler, K. (Editor), *"Advanced Composites: The Balance Between Performance and Cost" Proceedings of the 24th International SAMPE Europe Conference* at Paris, France; pp. 87-94.

50. Aoki, Y., Nagao, Y., Ishikawa, T., and Takeda, F. (2006), 'Experimental Evaluation and Consideration of Numerical Method of Z-Anchor CFRP® Laminates', in *Comptest 2006, Composites Testing and Model Identification* at Porto, Portugal; pp. 70-71.

51. Schneider, M. (2006), 'Carbon-Fibre Sewing Yarn for Composites', *JEC Composites*, Vol. 24, pp. 63-65.

52. Schneider, M. and Wohlmann, B. (2005), 'Carbon Fibre Sewing Yarn and Binder Yarn for Preform Applications', in *"Nanotechnology Assists Leadership and Success of the Composite Technology" Proceedings of the 26th International SAMPE Europe Conference 2005* at Paris, France; pp. 34-39.

53. Dransfield, K. A., Baille, C., and Mai, Y.-W. (1994), 'Improving the Delamination Resistance of CFRP by Stitching - A Review', *Composites Science & Technology*, Vol. 50, No. 3, pp. 305-317.

54. Mouritz, A. P. and Cox, B. N. (2000), 'A Mechanistic Approach to the Properties of Stitched Laminates', *Composites Part A: Applied Science & Manufacturing*, Vol. 31, No. 1, pp. 1-27.

55. Summerscales, J. (1987), 'High Performance Reinforcement Fabrics', *Progress in Rubber & Plastic Technology*, Vol. 3, No. 3, pp. 20-32.

56. Matsuhisa, Y., Hiramatsu, T., and Nishimura, A. (1988), 'Z-Directional Laminate Reinforcing Material High Performance "Torayca Carbon Stitching Thread"', in *33rd International SAMPE Symposium* , Vol. 33 at Anaheim, USA; pp. 91-103.

57. Langley Research Center *The Advanced Stitching Machine: Making Composite Wing Structures of the Future*, available at: oea.larc.nasa.gov/PAIS/ASM.html (accessed 2008).

58. Dransfield, K. A., Jain, L. K., and Mai Y-W. (1998), 'On the Effects of Stitching in CFRP - I: Mode I Delamination Toughness', *Composites Science & Technology*, Vol. 58, No. 6, pp. 815-827.

59. Sankar, B. V. and Sharma, S. K. (1997), 'Mode II Delamination Toughness of Stitched Graphite/Epoxy Textile Composites', *Composites Science & Technology*, Vol. 57, No. 7, pp. 729-737.

60. Jain, L. K., Dransfield, K. A., and Mai, Y.-W. (1998), 'On the Effects of Stitching in CFRP - II: Mode II Delamination Toughness', *Composites Science & Technology*, Vol. 58, No. 6, pp. 829-837.

61. Jain, L. K. and Mai, Y.-W. (1995), 'Determination of Mode II Delamination Toughness of Stitched Laminate Composites', *Composites Science & Technology*, Vol. 55, No. 3, pp. 241-253.

62. Jain, L. K. and Mai, Y.-W. (1994), 'On the Effect of Stitching on Mode I Delamination Toughness of Laminated Composites', *Composites Science & Technology*, Vol. 51, pp. 331-345.

63. Gunnion, A. J., Scott, M. L., Thomson, R. S., and Hachenberg, D. (2004), 'Thickness Effects on the Compressive Stiffness and Strength of Stitched Composite Laminates', *Composite Structures*, Vol. 66, No. 1 - 4, pp. 479-486.

64. Sun, X., Tong, L., Wood, M. D. K., and Mai, Y.-W. (2004), 'Effect of Stitch Distribution on Mode I Delamination Toughness of Laminated DCB Specimens', *Composites Science & Technology*, Vol. 64, No. 7 - 8, pp. 967-981.

65. Cox, B. N., Massabó, R., and Kedward, K. T. (1996), 'Suppression of Delaminations in Curved Structures by Stitching', *Composites Part A: Applied Science & Manufacturing*, Vol. 27, No. 12, pp. 1133-1138.

66. Massabó, R., Mumm, D. R., and Cox, B. N. (1998), 'Characterizing Mode II Delamination Cracks in Stitched Composites', *Fracture*, Vol. 92, No. 1, pp. 1-38.

67. Mouritz, A. P., Leong, K. H., and Herszberg, I. (1997), 'A Review of the Effect of Stitching on the in-Plane Mechanical Properties of Fibre-Reinforced Polymer Composites', *Composites Part A: Applied Science & Manufacturing*, Vol. 28, No. 12, pp. 979-991.

68. Farley, G. L., Smith, B. T., and Maiden, J. (1992), 'Compression Response of Thick Layer Composite Laminates With Through-the-Thickness Reinforcement', *Reinforced Plastics & Composites*, Vol. 11, pp. 787-810.

69. Pang, F., Wang, C. H., and Bathgate, R. G. (1997), 'Creep Response of Woven-Fibre Composites and the Effect of Stitching', *Composites Science & Technology*, Vol. 57, No. 1, pp. 91-98.

70. Hosure, M. V., Vaidya, U. K., Ulven, C., and Jeelani, S. (2004), 'Performance of Stitched/Unstitched Woven Carbon/Epoxy Composites Under High Velocity Impact Loading', *Composite Structures*, Vol. 64, No. 3 - 4, pp. 455-466.

71. Klopp, K., Moll, K. U., and Wulfhorst, B. (2000), 'Stitching Process With One-Sided Approach of the Textile for the Production of Reinforcing Textiles for Composites and Other Technical Textiles.', in *TexComp 5, The 5th International Conference on Textile Composites* at Leuven, Belgium.

72. Wittig, J. (2003), 'Development in Stitching Systems for the Production of Dry Fiber Pre-Forms', in Drechsler, K. (Editor), *"Advanced Composites: The Balance Between Performance and Cost" Proceedings of the 24th International SAMPE Europe Conference* at Paris, France; pp. 499-504.

73. Ogale, A. and Mitschang, P. (2004), 'Tailoring of Textile Preforms for Finbre-Reinforced Polymer Composites', *Industrial Textiles*, Vol. 34, No. 2, pp. 77-96.

74. Stueve, J., Henkel, F., and Gries, T. (2006), 'Complex Near-Net Shape Reinforcement Structures - Textile Preforms for CFRP', in *"Latest Advancements of Applied Composite Technology" Proceedings of the 27th International SAMPE Europe Conference* at Paris, France; pp. 266-271.

75. EADS *Working with Needle and Thread*, available at: www.eads.com/1024/en/pressdb/innovation_topic/CFK%20N%C3%A4hen.html (accessed 2008).

76. Keilmann, R. (2003), 'Innovative Processing Techniques for Carbon-Fibre Materials', *JEC Composites*, No. 5, pp. 81-82.

77. Brandt, J., Geßler, A., and Filsinger, J. (2002), 'New Approaches in Textile and Impregnation Technologies for the Cost Effective Manufacturing of CFRP Aerospace Components', in *ICAS 23rd International Congress of Aeronautical Sciences* at Toronto, Canada; pp. 634.1 - 634.9.

78. Wittig, J. (2001), 'Recent Developments in the Robotic Stitching Technology for Textile Structural Composites', *Textile & Apparel, Technology & Management*, Vol. 2, No. 1, pp. 1-8.

79. Dell'Anno, G. (2007), *Effect of Tufting on the Mechanical Behaviour of Carbon/Epoxy Composites* (PhD thesis), Cranfield University, Cranfield, UK.

80. Bauer, D. W. and Kotlensky, W. V. (1973), 'Relationship Between Structure and Strength for Carbon Infiltrated Substrates: Part 2 - Three Dimensional Woven, Tufted and Needled Substrates', *SAMPE Quarterly*, Vol. 4, No. 2, pp. 10-20.

81. KSL *Stitching Solutions for Composites*, available at: www.ksl-lorsch.de/ksl-lorsch/pdf/kslcomposites_e.pdf (accessed 2008).

82. Wittig, J. (2002), 'In-Mold-Reinforcement of Preforms by 3-Dimensional Tufting', in *47th International SAMPE Symposium and Exhibition* at Long Beach, USA; pp. 1043-1051.

83. Turner, G. F. (2001), 'More From the Recent Paris JEC/SAMPE Event - New Flexible Robotic Composite Stitching', *Advanced Materials & Composites News*, Vol. 23, No. 516, pp. 6.

84. Thurm, T. (2005), 'Applications of One-Sided Stitching Techniques for Resin Infusion Preforms and Structures', *SAMPE*, Vol. 41, No. 1, pp. 64-67.

85. Wittig, J. and Rattay, F. (2001), 'Robotic Three-Dimensional Stitching Technology', in *46th International SAMPE Symposium and Exhibition* at Long Beach, USA; pp. 2433-2444.

86. Wittig, J. and Rattay, F. (2001), 'Reinforcement of Carbon Fiber Composite Materials by Robotic Stitching', in Griffiths, G. R. and McCarthy, R. J. (Editor), *Proceedings of the 22nd International SAMPE Europe Conference* at Paris, France; pp. 317-327.

87. Hogg, P. J. and Wittig, J. (2002), 'Robotic Stitching Technology for Textile Structural Composites', in *9th International Fibre Reinforced Composites Conference* at Newcastle, UK; pp. 95-103.

88. Cartié, D. D. R., Dell'Anno, G., Poulin, E., and Partridge, I. K. (2006), '3D Reinforcement of Stiffener-to-Skin T-Joints by Z-Pinning and Tufting', *Engineering Fracture Mechanics*, Vol. 73, No. 16, pp. 2532-2540.

89. Poulin, E. (2004), *Reinforcement of a T-Joint by Z-Fiber® Pinning and 'Tufting'* (MSc thesis), Cranfield University, Cranfield, UK.

90. Mouritz, A. P. (2007), 'Review of Z-Pinned Composite Laminates', *Composites Part A: Applied Science & Manufacturing*, Vol. 38, No. 12, pp. 2383-2397.

91. Huang, S. L., Richey, R. J., and Deska, E. W. (1978), 'Cross Reinforcement Ina GR/EP Laminate', in *Proceedings of the American Society of Mechanical Engineers' Winter Annual Meeting* at San Francisco, USA;

92. Freitas, G. A., Fusco, T. M., Campbell, T., Harris, J. J., and Rosenberg, S. (1996), 'Z-Fiber Technology and Products for Enhancing Composite Design', in *Proceedings of the 83rd Meeting of the AGARD SMP Conference on Bolted/Bonded Joints in Polymeric Composites* at Florence, Italy;

93. Boyce, J.S., Freitas, G.A., Magee, C.L., Fusco, T.M., Harris, J.J. and Kunkel, E. (inventors) (1998), *Ultrasonic Fastening System and Method*. WO 98/29243.

94. Chang, P. (2006), *The Mechanical Properties and Failure Mechanisms of Z-Pinned Composites* (PhD thesis), RMIT University, Australia.

95. Chang, P., Mouritz, A. P., and Cox, B. N. (2006), 'Properties and Failure Mechanisms of Z-Pinned Laminates in Monotonic and Cyclic Tension', *Composites Part A: Applied Science & Manufacturing*, Vol. 37, pp. 1501-1513.

96. Dickinson, L. C., Farley, G. L., and Hinders, M. K. (1999), 'Prediction of Effective Three-Dimensional Elastic Constants of Translaminar Reinforced Composites', *Composite Materials*, Vol. 33, pp. 1002-1029.

97. McBeath, S. (2002), 'Safety Pins', *Racecar Engineering*, Vol. 12, No. 12, pp. 56-62.

98. Steeves, C. A. and Fleck, N. A. (2006), 'In-Plane Properties of Composite Laminates with Through-Thickness Pin Reinforcement', *Solids & Structures*, Vol. 43, pp. 3197-3212.

99. Partridge, I. K., Cartié, D. D. R., and Bonnington, T. (2003), 'Manufacture and Performance of Z-Pinned Composites', in Shonaike, G. O. and Advani, S. G. (Editor), *Advanced Polymeric Materials*, CRC Press LLC, USA, pp. 103-137.

100. Farley, G. L. and Dickinson, L. C. (1992), 'Removal of Surface Loop From Stitched Composites Can Improve Compressive and Composite-After-Impact Strengths', *Reinforced Plastics & Composites*, Vol. 11, pp. 633-642.

101. Leong, K. H., Ramakrishna, S., Bibo, G. A., and Huang, Z. M. (2000), 'The Potential for Knitting for Engineering Composites - a Review', *Composites Part A: Applied Science & Manufacturing*, Vol. 31, pp. 197-220.

102. Cox, B. N., Dadkah, M. S., Inman, R. V., Morris, W. L., and Zupon, J. (1992), 'Mechanisms of Failure in 3D Composites', *Acta Metallurgica et Materialia*, Vol. 40, pp. 3285-3298.

103. Stringer, L. G. and Hiley, M. J. (2003), 'Through Thickness Reinforcement of Composites: Z-Pinning, Stitching and 3-D Weaving', in *Proceedings of the 14th International Conference on Composite Materials* at San Diego, USA; pp. Paper no. 1312.

104. Sweeting, R. D. and Thomson, R. S. (2004), 'The Effect of Thermal Mismatch on Z-Pinned Laminated Composite Structures', *Composite Structures*, Vol. 66, pp. 189-195.

105. Freitas, G. A., Magee, C. L., Dardzinski, P., and Fusco T. M. (1994), 'Fibre Insertion Process for Improved Damage Tolerance in Aircraft Laminates', *Advanced Materials*, Vol. 25, pp. 36-43.

106. Vaidya, U. K., Duncan, B., and Kopacz, J. (2001), 'Affordable Processing and Characterization of Multi-Functional Z-Pin Reinforced VARTM Composites', in *Proceedings of the 13th International Conference on Composite Materials* at Beijing, China.

107. Barrett, D. J. (1996), 'The Mechanics of Z-Fibre Reinforcement', *Composite Structures*, Vol. 36, pp. 23-32.

108. Cartié, D. D. R. and Partridge, I. K. (1999), 'Delamination Behaviour of Z-Pinned Laminates', in *Proceedings of the 12th International Conference on Composite Materials* at Paris, France.

109. Cartié D. D. R. , Cox. B. N. , and Fleck, N. A. (2004), 'Mechanisms of Crack Bridging by Composite and Metallic Rods', *Composites Part A: Applied Science & Manufacturing*, Vol. 34, pp. 1325-1336.

110. Graftieaux, B. P. H., Rezai, A., and Partridge, I. K. (2000), 'Effects of Z-Pin Reinforcement on the Delamination Toughness and Fatigue Performance of Uni-Directional AS4/8552 Composite', in *Proceedings of ECCM-9* at Brighton, UK.

111. Partridge, I. K., Cartié, D. D. R., Troulis, E., Grassi, M., and Zhang, X. (2003), 'Evaluating the Mechanical Effectiveness of Z-Pinning', in *Proceedings of the 35th ISTC SAMPE Technical Conference* at Dayton OH, USA.

112. Dai, S.-C., Yan, W., Liu, H. Y., and Mai, Y.-W. (2004), 'Experimental Study on Z-Pin Bridging Law by Pull-Out Test', *Composites Science & Technology*, Vol. 64, pp. 2451-2457.

113. Rugg, K. L., Cox, B. N., and Massabó, R. (2002), 'Mixed Mode Delamination of Polymer Composite Laminates Reinforced Through the Thickness by Z-Fibres', *Composites Part A: Applied Science & Manufacturing*, Vol. 33, pp. 177-190.

114. Liu, H.-Y., Yan, W., and Mai, Y.-W. (2003), 'Z-Pin Bridge Force in Composite Delamination', in Blackman, B. R. K. et al. (Editor), *Fracture of Polymers, Composites and Adhesives II*, Elsevier.

115. Grassi, M. and Zhang, X. (2003), 'Finite Element Analyses of Mode I Interlaminar Delamination in Z-Fibre Reinforced Composite Laminates', *Composites Science & Technology*, Vol. 63, pp. 1815-1832.

116. Yan, W., Liu, H.-Y., and Mai, Y.-W. (2003), 'Numerical Study of the Mode I Delamination Toughness of Z-Pinned Laminates', *Composites Science & Technology*, Vol. 63, pp. 1481-1493.

117. Yan, W., Liu, H.-Y., and Mai, Y.-W. (2004), 'Mode II Delamination Toughness of Z-Pinned Laminates', *Composites Science & Technology*, Vol. 64, pp. 1937-1945.

118. Grassi, M. and Zhang, X. (2002), 'Numerical Modelling of Z-Fibre Effects on Mode-I Interlaminar Delamination', in *Proceedings of ECCM-10* at Brugge, Belgium.

119. Evans, D. A. and Boyce, J. S. (1989), 'Transverse Reinforcement Methods for Improved Delamination Resistance', in *Proceedings of the 34th International SAMPE Symposium & Exhibition* pp. 271-282.

120. Childress, J. J. and Freitas, G. A. (1992), 'Z-Direction Pinning of Composite Laminates for Increased Survivability', in *Proceedings of the AIAA Aerospace Design Conference* at Irvine, USA; pp. 92-109.

121. Rugg, K. L., Cox, B. N., Ward, K. E., and Sherrick, G. O. (1998), 'Damage Mechanisms for Angled Through-Thickness Rod Reinforcement in Carbon-Epoxy Laminates', *Composites Part A: Applied Science & Manufacturing*, Vol. 29, pp. 1603-1613.

122. Cox, B. N. (1999), 'Constitutive Model for a Fibre Tow Bridging a Delamination Crack', *Mechanics of Composite Materials & Structures*, Vol. 6, pp. 117-138.

123. Cox, B. N. (1999), 'Mechanisms and Models for Delamination in the Presence of Through-Thickness Reinforcement', *Advanced Composite Letters*, Vol. 8, pp. 249-256.

124. Cox, B. N. and Sridhar, N. (2002), 'A Traction Law for Inclined Fibre Tows Bridging Mixed Mode Cracks', *Mechanics of Composite Materials & Structures*, Vol. 9, pp. 299-331.

125. Massabó, R. and Cox, B. N. (1999), 'Concepts of Bridged Mode II Delamination Cracks', *Physics & Mechanics of Solids*, Vol. 47, pp. 1265-1300.

126. Troulis, E., Cartié, D. D. R., Bartattoni, L., and Partridge, I. K. (2001), 'Z-Pinned Woven Laminates: Interlaminar Fracture Results and Pinning Quality Considerations', in *Proceedings of the 6th International Conference on Deformation & Fracture of Composites* at Manchester, UK.

127. Liu, H.-Y., Yan, B., Gu, B., Dai, S.-C., and Mai, Y.-W. (2003), 'Z-Pinning Reinforcement and Its Bridging Law', in *Proceedings of the 8th Japan International SAMPE Symposium* at Tokyo, Japan; pp. 389-392.

128. Liu, H.-Y., Yan, W., Yu, X.-Y., and Mai, Y.-W. (2004), 'Experimental Study on Z-Pinned DCB Mode I Delamination', in *Proceedings of the International Conference on Structural Integrity & Fracture* at Brisbane, Australia.

129. Ratcliffe, J. G. and O'Brien, T. K. (NASA) (2004), *Discrete spring model for predicting delamination growth in z-fibre reinforced DCB specimens*, NASA Report NASA/TM-2004-213019.

130. Tong, L. and Sun, X. (2003), 'Effect of Through-Thickness Reinforcement Bending on Delamination Toughness of Composite Laminates', in *Proceedings of the 35th International SAMPE Technical Conference* at Dayton, USA.

131. Tong, L. and Sun, X. (2004), 'Bending Effect of Through-Thickness Reinforcement Rods on Mode I Delamination Toughness of DCB Specimen: I - Linearly Elastic and Rigid-Perfectly Plastic Models', *Solids & Structures*, Vol. 41, pp. 6831-6852.

132. Robinson, P. and Das, S. (2004), 'Mode I DCB Testing of Composite Laminates Reinforced With Z-Direction Pins: a Simple Model for the Investigation of Data Reduction Strategies', *Engineering Fracture Mechanics*, Vol. 71, pp. 345-364.

133. Birman, V. and Byrd, L. W. 'Strain Energy Release Rate of Co-Cured Z-Pinned Composite Double Cantilever Beams', *Aerospace Engineering (in Press)*,

134. Birman, V. and Byrd, L. W. (2005), 'Effect of Z-Pins on Fracture in Composite Cocured Double Cantilever Beams', *Aerospace Engineering*, Vol. 18, pp. 51-59.

135. Byrd, L. W. and Birman, V. (2005), 'The Estimate of the Effect of Z-Pins on the Strain Energy Release Rate, Fracture and Fatigue in a Composite Co-Cured Z-Pinned Double Cantilever Beam', *Composite Structures*, Vol. 68, pp. 53-63.

136. Byrd, L. W. and Birman, V. (2006), 'Effectiveness of Z-Pins in Preventing Delamination of Co-Cured Composite Joints on the Example of a Double Cantilever Test', *Composites Part B: Engineering*, Vol. 37, pp. 365-378.

137. Rezai, A., Cartié, D. D. R., Partridge, I. K. , Irving, P., Ashton, T., Negre, P., and Langer, J. D. (2001), 'Interlaminar Damage Resistance of Z-Fiber™ Reinforced Structural CFRP', in *Proceedings of the 13th International Conference on Composite Materials* at Beijing, China.

138. Partridge, I. K. and Cartié, D. D. R. (2005), 'Delamination Resistant Laminates by Z-Fiber® Pinning: Part I Manufacture and Fracture Performance', *Composites Part A: Applied Science & Manufacturing*, Vol. 36, pp. 55-64.

139. Cox, B. N. (2005), 'Snubbing Effects in the Pullout of a Fibrous Rod from a Laminate', *Mechanics of Advanced Materials & Structures*, Vol. 12, pp. 85-98.

140. Clarke, A., Greenhalgh, E., Meeks, C., and Jones, C. (2003), 'Enhanced Structural Damage Tolerance of CFRP Primary Structures by Z-Pin Reinforcement', in *Proceedings of the 44th AIAA Structures, Structural Dynamics and Materials Conference* at Norfolk; pp. Paper no. AIAA-2003-1679.

141. Grassi, M., Clarke, A., Khermiri, N., and Gaitonde, M. (2004), 'Analysis of Through-Thickness Reinforcements Effects on the Failure Modes of a Composite Rib Foot', in *Proceedings of ECCM-11* at Rhodes, Greece.

142. Zhang, X., Hounslow, L. E., and Grassi, M. (2003), 'Improvement to Low-Velocity Impact and Compression-After-Impact Performance of Z-Fibre Pinning', in *Proceedings of the 14th International Conference on Composite Materials* at San Diego, USA.

143. Grassi, M., Zhang, X., and Meo, M. (2002), 'Prediction of Stiffness and Stresses in Z-Fibre Reinforced Composite Laminates', *Composites Part A: Applied Science & Manufacturing*, Vol. 33, pp. 1653-1664.

144. Grassi, M. (2000), *Numerical Modelling of Composite Laminates With Through-Thickness-Reinforcements* (PhD thesis), Cranfield University, Cranfield, UK.

145. Chang, P., Mouritz, A. P., and Cox, B. N. (2007), 'Flexural Properties of Z-Pinned Laminates', *Composites Part A: Applied Science & Manufacturing*, Vol. 38, pp. 224-251.

146. Steeves, C. A. (2001), *Mechanics of Failure in Composite Structures* (PhD thesis), University of Cambridge, Cambridge, UK.

147. Mouritz, A. P. (2007), 'Compression Properties of Z-Pinned Composite Laminates', *Composites Science & Technology*, Vol. 67, No. 15 - 16, pp. 3110-3120.

148. O'Brien, T. K. and Krueger, R. (2006), 'Influence of Compression and Shear on the Strength of Composite Laminates With Z-Pinned Reinforcement', *Applied Composite Materials*, Vol. 13, pp. 173-189.

149. Hall, T. (2002), *Automation of Z-Fiber for Complex Shapes*, available at: cmtc.scra.org/pubs/fall_2002.pdf (accessed 2008).

150. Wallace, B. T., Sankar, B. V., and Ifju, P. G. (2001), 'Pin Reinforcement of Delaminated Sandwich Beams Under Axial Compression', *Sandwich Structures & Materials*, Vol. 3, pp. 117-129.

151. Wallace, B. T., Sankar, B. V., and Ifju, P. G. (2000), 'Effect of Z-Pinning on Buckling Delaminated Sandwich Panels', in *41st AIAA/ASME/AHS/ASC Structures, Structural Dynamics and Materials Conference and Exhibit* at Atlanta, USA; pp. 539-543.

152. Marasco, A. I. (2005), *Analysis and Evaluation of Mechanical Performance of Reinforced Sandwich Structures: X-Cor and K-Cor* (PhD thesis), Cranfield University, Cranfield, UK.

153. Carstensen, T., Cournoyer, D., Kunkel, E., and Magee, C. L. (2001), 'X-Cor Advanced Sandwich Core Material', in *Proceedings of the 33rd International SAMPE Technical Conference* at Seattle, USA.

154. Vaidya, U. K. (2002), 'Multifunctional Sandwich Composites', in *Proceedings of the SPIE Conference: Smart Materials, Structures and Systems* at Bangalore, India.

155. Sypeck, D. J. (2005), 'Cellular Truss Core Sandwich Structures', *Applied Composite Materials*, Vol. 12, pp. 229-246.

156. Wallach, J. C. and Gibson, L. J. (2001), 'Mechanical Behaviour of a Three-Dimensional Truss Material', *Solids & Structures*, Vol. 38, pp. 7181-7196.

157. Marasco, A. I., Cartié, D. D. R., Partridge, I. K., and Rezai, A. (2005), 'Mechanical Properties Balance in Novel Z-Pinned Sandwich Panels: Out-of-Plane Properties', *Composites Part A: Applied Science & Manufacturing*, Vol. 37, pp. 295-302.

158. Robinson, P. and Das, S. (2004), 'Erratum to "Mode I DCB Testing of Composite Laminates Reinforced With Z-Direction Pins: a Simple Model for the Investigation of Data Reduction Strategies"', *Engineering Fracture Mechanics*, Vol. 71, pp. 345-364.

159. Yan, W., Liu, H.-Y., and Mai, Y.-W. (2004), 'Numerical Study on Buckling of Z-Pinned Composite Laminates', in *Proceedings of the 4th Australasian Conference on Composite Materials* at Sydney, Australia; pp. 307-312.

160. Allegri, G. and Zhang, X. (2004), 'Delamination/Debond Growth in Z-Fibre Reinforced Composite T-Joints: a Finite Element Simulation', in *Proceedings of the ECCM-11 Conference* at Rhodes, Greece.

161. Allegri, G. and Zhang, X. (2007), 'On the Delamination and Debond Suppression in Structural Joints by Z-Fibre Pinning', *Composites Part A: Applied Science & Manufacturing*, Vol. 38, pp. 1107-1115.

162. Chang, P., Mouritz, A. P., and Cox, B. N. (2006), 'Properties and Failure Mechanisms of Pinned Composite Lap Joints in Monotonic and Cyclic Tension', *Composites Science & Technology*, Vol. 66, No. 13, pp. 2163-2176.

163. Tong, L. and Sun, X. (2007), 'Bending Effect of Through-Thickness Reinforcement Rods on Mode II Delamination Toughness of ENF Specimen: Elastic and Rigid-Perfectly Plastic Analyses', *Composites Part A: Applied Science & Manufacturing*, Vol. 38, No. 2, pp. 323-336.

164. Blackman, B. R. K., Kinloch, A. J., and Paraschi, M. (2003), 'On the Mode II Loading of Adhesive Joints', *European Structural Integrity Society (Elsevier Science)*, Vol. 32, pp. 293-304.

165. Brunner, A. J. and Blackman, B. R. K. (2003), 'Delamination Fracture in Cross-Ply Laminates: What Can Be Learned From Experiment?', *European Structural Integrity Society (Elsevier Science)*, Vol. 32, pp. 433-444.

166. Davies, P., Blackman, B. R. K., and Brunner, A. J. (2001), 'Mode II Delamination', *European Structural Integrity Society (Elsevier Science)*, Vol. 28, pp. 307-333.

167. Blackman, B. R. K., Brunner, A. J., and Davies, P. (2001), 'Delamination Fracture of Continuous Fibre Composites: Mixed-Mode Fracture', *European Structural Integrity Society (Elsevier Science)*, Vol. 28, pp. 335-359.

168. Brunner, A. J., Blackman, B. R. K., and Davies, P. (2008), 'A Status Report on Delamination Resistance Testing of Polymer-Matrix Composites', *Engineering Fracture Mechanics*, Vol. 75, No. 9, pp. 2779-2794.

169. Blackman, B. R. K., Brunner, A. J., and Williams, J. G. (2006), 'Mode II Fracture Testing of Composites: a New Look at an Old Problem', *Engineering Fracture Mechanics*, Vol. 73, No. 16, pp. 2443-2455.

170. Blackman, B. R. K., Kinloch, A. J., and Paraschi, M. (2005), 'The Determination of the Mode II Adhesive Fracture Resistance, G_{IIc}, of Structural Adhesive Joints: an Effective Crack Length Approach', *Engineering Fracture Mechanics*, Vol. 72, No. 6, pp. 811-812.

171. Allegri, G. and Zhang, X. 'An Explicit Analytical Constitutive Model of Z-Fibre Response Under Mode II Loading', *Mechanics of Materials (Submitted)*.

172. Samaras, Z. *Unpublished Work* (PhD thesis), Cranfield University, Cranfield, UK.

173. Hexcel Composites *Hexply® 8552 Epoxy Matrix Product Data*, (accessed 2008).

174. Watmough, T. (Aircelle, UK) (2005), *Private Communication.*

175. Huntsman *Araldite® 420 A/B Data Sheet*, available at: http://www.huntsmanservice.com/Product_Finder/ui/PSDetailProductList.do?pInfoSBUId=9&PCId=4697 (accessed 2008).

176. Cytec Engineered Materials *Cycom® 5250-4 RTM Resin System*, (accessed 2008).

177. Huntsman *RenInfusion® 8615R Resin*, (accessed 2008).

178. RenShape Solutions *RenInfusion™ 8606/Ren® 8606*, (accessed 2008).

179. Greve, L., Pickett, A. K., and Payen, F. (2008), 'Experimental Testing and Phenomenological Modelling of the Fragmentation Process of Braided Carbon/Epoxy Composite Tubes Under Axial and Oblique Impact', *Composites Part B: Engineering*, Vol. 39, pp. 1221-1232.

180. Zarei, H. R. and Kröger, M. (2006), 'Multiobjective Crashworthiness Optimization of Circular Aluminium Tubes', *Thin-Walled Structures*, Vol. 44, pp. 301-308.

181. Bisagni, C., Di Pietro, G., Fraschini, L., and Terletti, D. (2005), 'Progressive Crushing of Fiber-Reinforced Composite Structural Components of a Formula One Racing Car', *Composite Structures*, Vol. 68, pp. 491-503.

182. International Standards Organisation (ISO) (98), *Fibre-Reinforced Plastic Composites - Determination of Flexural Properties*, ISO 14125: 1998, British Standards Institute (BSI), London, UK.

183. European Structural & Integrity Society (ESIS) (2002), *Fibre-Reinforced Plastic Composites - Determination of Apparent Mode II Interlaminar Toughness, G_{IIc}, for Unidirectionally Reinforced Materials*, Version 01-04-02, Task Committee 4 (TC4) on fracture of composites and polymers.

184. Turmel, D., Szpicak, J., Singh, S., and Partridge, I. K. (1995), 'Crack Initiators and Pre-Cracking Techniques for Fracture Testing of Polymer Matrix Composites', in *Deformation and Fracture of Composites (DFC-3)* at Guildford, UK.

185. Thornton, P. H. (1979), 'Energy Absorption in Composite Structures', *Composite Materials*, Vol. 13, pp. 247-262.

186. Farley, G. L. (1983), 'Energy Absorption of Composite Materials', *Composite Materials*, Vol. 17, pp. 267-279.

187. Thornton, P. H. and Jeryan, R. A. (1988), 'Crash Energy Management in Composite Automotive Structures', *Impact Engineering*, Vol. 7, No. 2, pp. 167-180.

188. Zeng, T., Fang, D., and Lu, T. (2005), 'Dynamic Crashing and Impact Energy Absorption of 3D Braided Composite Tubes', *Materials Letters*, Vol. 59, pp. 1491-1496.

189. Melo, J. D. D., Silva, A. L. S., and Villena, J. E. N. (2008), 'The Effect of Processing Conditions on the Energy Absorption Capability of Composite Tubes', *Composite Structures*, Vol. 82, pp. 622-628.

190. Ochelski, S. and Gotowicki, P. (2009), 'Experimental Assessment of Energy Absorption Capability of Carbon-Epoxy and Glass-Epoxy Composites', *Composite Structures*, Vol. 87, pp. 215-224.

191. Warrior, N. A., Turner, T. A., Robitaille, F., and Rudd, C. D. (2003), 'Effect of Resin Properties and Processing Parameters on Crash Energy Absorbing Composite Structures Made by RTM', *Composites Part A: Applied Science & Manufacturing*, Vol. 34, pp. 543-550.

192. Warrior, N. A., Turner, T. A., Robitaille, F., and Rudd, C. D. (2004), 'The Effect of Interlaminar Toughening Strategies on the Energy Absorption of Composite Tubes', *Composites Part A: Applied Science & Manufacturing*, Vol. 35, pp. 431-437.

193. Yuan, Q., Kerth, S., Karger-Kocsis, J., and Friedrich, K. (1997), 'Crash and Energy Absorption Behaviour of Interleaved Carbon-Fibre Reinforced Epoxy Tubes', *Materials Science Letters*, Vol. 16, pp. 1793-1796.

194. Al Galib, D. and Limam, A. (2004), 'Experimental and Numerical Investigation of Static and Dynamic Axial Crushing of Circular Aluminium Tubes', *Thin-Walled Structures*, Vol. 42, pp. 1103-1137.

195. Williams, B. W., Oliveira, D. A., Simha, C. H. M., Worswick, M. J., and Mayer, R. (2007), 'Crashworthiness of Straight Section Hydroformed Aluminium Tubes', *Impact Engineering*, Vol. 34, pp. 1451-1464.

196. Federation Internationale de L'Automobile *2008 Formula One Technical Regulations*, available at: http://www.fia.com (accessed 2008).

197. Profeta, F. P. (2006), *Mechanical Properties of Hybrid Composite Laminates - Management of Failure Modes in Z-Pinned Composite Structures* (Italian Laurea thesis), Pisa University, Pisa, Italy.

198. Kalchman, L. (2007), *Incorporation of Mode II Z-Pin Response into a Composite Design Tool* (MSc thesis), Cranfield University, Cranfield, UK.

199. Harper, P. W. and Hallett, S. R. (2008), 'Cohesive Zone Length in Numerical Simulations of Composite Delamination', *Engineering Fracture Mechanics*, Vol. 75, pp. 4774-4792.

200. Mi, Y., Crisfield, M. A., Davies, G. A. O., and Hellweg, H.-B. (1998), 'Progressive Delamination Using Interface Elements', *Composite Materials*, Vol. 32, pp. 1246-1272.

201. Petrossian, Z. and Wisnom, M. R. (1998), 'Prediction of Delamination Initiation and Growth from Discontinuous Plies Using Interface Elements', *Composites Part A: Applied Science & Manufacturing*, Vol. 29, pp. 503-515.

202. Chen, J., Crisfield, M. A., Kinloch, A. J., Busso, E. P., Matthews, F. L., and Qiu, Y. (1999), 'Predicting Progressive Delamination of Composite Material Specimens Via Interface Elements', *Mechanics of Composite Materials & Structures*, Vol. 6, pp. 301-317.

203. Crisfield, M. A. and Alfano, G. (2000), 'Finite Element Interface Models for the Delamination Analysis of Laminated Composites: Mechanics and Computational Issues', *Numerical Methods in Engineering*, Vol. 50, pp. 1701-1736.

204. Camanho, P. P., Davila, C. G., and De Moura, M. F. (2003), 'Numerical Simulation of Mixed-Mode Progressive Delamination in Composite Materials', *Composite Materials*, Vol. 37, No. 1415–1424.

205. Pinho, S. T., Ianucci, L., and Robinson, P. (2006), 'Formulation and Implementation of Decohesion Elements in an Explicit Finite Element Code', *Composites Part A: Applied Science & Manufacturing*, Vol. 37, pp. 778-789.

206. Jiang, W. G., Hallett, S. R., Green, B. G., and Wisnom, M. R. (2007), 'A Concise Interface Constitutive Law for Analysis of Delamination and Splitting in Composite Materials and Its Application to Scaled Notched Tensile Specimens', *Numerical Methods in Engineering*, Vol. 69, pp. 1982-1995.

207. Dantuluri, V., Maiti, S., Geubelle, P. H., Patel, R., and Kilic, H. (2007), 'Cohesive Modelling of Delamination in Z-Pin Reinforced Composite Laminates', *Composites Science & Technology*, Vol. 67, pp. 616-631.

208. Camanho, P. P., Davila, C. G., and Pinho, S. T. (2003), 'Fracture Analysis of Composite Co-Cured Structural Joints Using Decohesion Elements', *Fatigue & Fracture of Engineering Materials & Structures*, Vol. 27, pp. 745-757.

209. Blackman, B. R. K., Hadavinia, H., Kinloch, A. J., and Williams, J. G. (2003), 'The Use of a Cohesive Zone Model to Study the Fracture of Fibre Composites and Adhesively-Bonded Joints', *Fracture*, Vol. 119, pp. 25-46.

210. Li, S., Thouless, M. D., Waas, A. M., Schroeder, J. A., and Zavattieri, P. D. (2006), 'Mixed-Mode Cohesive-Zone Models for Fracture of an Adhesively Bonded Polymer-Matrix Composite', *Engineering Fracture Mechanics*, Vol. 73, pp. 64-78.

211. Goyal, V. K., Johnson, E. R., and Goyal, V. K. (2008), 'Predictive Strength-Fracture Model for Composite Bonded Joints', *Composite Structures*, Vol. 82, pp. 434-446.

212. MSC.Software (2005), *MSC.Marc® Volume B: Element Library* (unpublished electronic manual).

213. Timoshenko, S. P. and Gere, J. M. (1972), *Mechanics of Materials* (1st edition), van Nostrand Reinhold Company Ltd., New York, USA.

214. Jaussaud, J. A. M. (1992), *Toughness Transfer Between Unreinforced Matrix and Fiber Composites* (PhD thesis), Cranfield University, Cranfield, UK.

215. Zimmerman, R. S. and Adams, D. F. (NASA) (1985), *Mechanical properties testing of candidate polymer matrix materials for use in high performance composites*, 177970, NASA, Langley Research Center, Virginia USA.

216. Hexcel Composites *Hexply® 914 Product Data*, available at: http://www.hexcel.com/NR/rdonlyres/23CE6ED9-3587-43D4-BFE1-65E5DC1D96DE/0/HexPly_914_eu.pdf (accessed 2008).

217. Torayca® *T300 Data Sheet*, available at: http://www.torayusa.com/cfa/pdfs/T300DataSheet.pdf (accessed 2008).

218. Soden, P. D., Hinton, M. J., and Kaddour, A. S. (1998), 'Lamina Properties, Lay-Up Configurations and Loading Conditions for a Range of Fibre-Reinforced Composite Laminates', *Composites Science & Technology*, Vol. 58, pp. 1011-1022.

219. Turon, A., Davila, C. G., Camanho, P. P., and Costa, J. (2007), 'An Engineering Solution for Mesh Size Effects in the Simulation of Delamination Using Cohesive Zone Models', *Engineering Fracture Mechanics*, Vol. 74, pp. 1665-1682.

220. Turon, A., Costa, J., Camanho, P. P., and Davila, C. G. (2007), 'Simulation of Delamination in Composites under High-Cycle Fatigue', *Composites Part A: Applied Science & Manufacturing*, Vol. 38, pp. 2270-82.

221. Bacon, D. (2008), 'Private E-Mail Communication from Albany Engineered Composites Ltd.'.

222. Treiber, J. (2008), 'Private Communication'.